Growth Defects in CrN/NbN Coatings Deposited by HIPIMS/UBM technique

Barnali Biswas

A thesis submitted in partial fulfilment of the requirements of

Sheffield Hallam University

for the degree of Doctor of Philosophy

In collaboration with The National HIPIMS technology Centre, UK at Sheffield Hallam

University and Zimmer Biomet

October 2017

To my Family: Mother, Father and Sister

আমার মা, বাবা এবং দিদিকে

Declaration

I hereby declare that this thesis is my own work and effort and that it has not been submitted anywhere for any award apart from that of Doctor of Philosophy at Sheffield Hallam University.

Where other sources of information have been used, they have been acknowledged.

Barnali Biswas   Date - 13.10.2017

Abstract

In recent years, high power impulse magnetron sputtering (HIPIMS) has caught the attention of users due to its ability to produce dense coatings. However, microscopic studies have shown that HIPIMS deposited coatings can suffer from some surface imperfections even though the overall number of defects can be significantly lower compared to, for example, arc deposited coatings of similar thickness.

Defects can degrade the coating performance thus any kind of defect is undesirable. To better understand the nature of these imperfections and the science of their formation, three sets of chromium nitride/niobium nitride (CrN/NbN) coatings were deposited using HIPIMS technique combined with unbalanced magnetron sputtering (UBM) by varying the deposition parameters, i.e. deposition time (t = 15 to 120 min), bias voltage (U_b = - 40 to - 150 V) and chamber pressure (P = 0.2 to 1 Pa). For each set, one parameter was varied and other two were kept constant. All these experiments were carried out with chamber conditions close to those found in industrial environment. The study revealed that the generated defects were similar for all the coatings and with the increase in deposition time/bias voltage/chamber pressure the surface area covered by optically visible defects (surface defect density) was increased. These defects were categorised as flakes related defects (nodular, open void and cone-like defects) and defects associated with substrate pits (pinhole defects). Depending on their types, the defects influenced the corrosion and tribological properties of the coatings. As the origins of most defects were flakes (generated from the chamber components), an additional study was conducted to understand the influence of chamber cleanliness on defect generation. As expected, surface defect density of the coating produced in a comparatively clean chamber was reduced noticeably (from 3.18 % to 1.37 % after cleaning). Coatings with lower surface defects performed significantly well during corrosion and tribological tests. However, the comparison between pure UBM and combined HIPIMS/UBM deposited coatings suggested that along with the defects, coating structure also had a major role in corrosion, wear and friction mechanisms. Even for deposition conditions where HIPIMS coatings showed higher surface defects, owing to their microstructures, their corrosion resistance and tribological behaviour were superior to the UBM deposited coatings.

Acknowledgements

Advanced studies

During the course of the studies for this thesis, the following conferences and workshops were attended:

- MERI Research Symposium 2017, Sheffield, UK, May 2017.

- 5th HIPIMS conference, Sheffield, UK, June 2014.

- SVC Courses - 323 High Power Impulse Magnetron Sputtering, 333 Practice and Applications of High Power Impulse Magnetron Sputtering (HIPIMS), 338 Application of Reactive Sputtering, Sheffield, UK, June 2014.

Oral Presentations

- Study of Coating Defects and their Influence on Corrosion and Tribological Properties of HIPIMS Deposited CrN/NbN Coatings, SVC TechCon 2017, Providence, Rhode Island, USA, April 29 - May 4, 2017.

- Wear and Failure mechanism of HIPIMS deposited nanostructured coating, Three minutes thesis competition 2016, Sheffield Hallam University, Sheffield, UK, May 24, 2016.

- Influence of deposition parameters on defect growth in CrN/NbN coatings produced by HIPIMS, MERI Research Symposium 2016, Sheffield, UK, May 17 – 18, 2016.

Poster Presentations

- Effect of chamber environment (cleanliness) on defect generation and their influence on corrosion and tribological properties of HIPIMS deposited CrN/NbN Coatings, 8th HIPIMS conference, Braunschweig, Germany, June 13 – 14, 2017.

- Impact of growth defects on the corrosion behaviour of CrN/NbN coatings deposited by HIPIMS/UBM, 7th HIPIMS conference, Sheffield, UK, June 29 - July 03, 2016.

- Performance of HIPIMS deposited CrN/NbN nanostructured coatings exposed to 650°C in pure steam environment, EBT 2016 International Conference, Varna, Bulgaria, June 13 -18, 2016.

- Characterisation of Growth Defects in PVD Coatings, MERI Research Symposium 2015, Sheffield, UK, May 19 – 20, 2015.

Publication

1. B. Biswas, Y. Purandare, A. Sugumaran, I. Khan, P.E. Hovsepian, Effect of chamber pressure on defect generation and their influence on corrosion and tribological properties of HIPIMS deposited CrN/NbN coatings, Surf. Coatings Technol. (2017). doi:10.1016/j.surfcoat.2017.08.021.

2. B. Biswas, Y. Purandare, A.A. Sugumaran, D.A.L. Loch, S. Creasey, A.P. Ehiasarian, P.E. Hovsepian, I. Khan, Defect growth in multilayer chromium nitride/niobium nitride coatings produced by combined high power impulse magnetron sputtering and unbalance magnetron sputtering technique, Thin Solid Films. 636 (2017) 558–566. doi:10.1016/j.tsf.2017.06.027.

3. P.E. Hovsepian, A.P. Ehiasarian, Y.P. Purandare, B. Biswas, F.J. Pérez, M.I. Lasanta, M.T. De Miguel, A. Illana, M. Juez-Lorenzo, R. Muelas, A. Agüero, Performance of HIPIMS deposited CrN/NbN nanostructured coatings exposed to 650°C in pure steam environment, Mater. Chem. Phys. 179 (2016) 110–119. doi:10.1016/j.matchemphys.2016.05.017.

Submitted to Surface and Coatings Technology

1. B. Biswas, Y. Purandare, I. Khan, P.E. Hovsepian, Influence of substrate bias voltage on defect generation and their influence on corrosion and tribological properties of HIPIMS deposited CrN/NbN Coatings.

Contents

List of Abbreviations

PVD	Physical Vapour Deposition
DC	Direct Current
DCMS	Direct Current Magnetron sputtering
UBM	Unbalanced Magnetron or Unbalanced Magnetron Sputtering
CFUBMS	Closed Field Unbalanced Magnetron Sputtering
HIPIMS	High Power Impulse Magnetron Sputtering
CA	Cathodic Arc
ABS	Arc Bond Sputtering
SS	Stainless Steel
HSS	High Speed Steel
XRD	X-Ray Diffraction
BB	Bragg–Brentano
GA	Glancing Angle
LA	Low Angle
SEM	Scanning Electron Microscope
FIB	Focused Ion Beam
AFM	Atomic Force Microscope
COF	Coefficient of Friction
COW	Coefficient of Wear
EDX	Energy Dispersive X-Ray
H - H	Samples etched using HIPIMS and deposited using combined HIPIMS and UBM techniques
H - U	Samples etched using HIPIMS and deposited using UBM technique

List of figures

Fig. 2.14. Different types of multilayer coatings: (a) small number of single layers, e.g. TiC/Ti(CN)/TiN, (b) high number of non-isostructural single layers, e.g. TiC/TiB2, (c) high number of isostructural single layers (superlattice), e.g. TiC/TiN [81].

Fig. 2.15. The mechanical properties as the functions of bilayer thickness [92].

Fig. 2.16. SEM image of the titanium ion etched surface of HSS sample [100].

Fig. 2.17. Plan view (a,b,c,d,h), cross-sectional SEM (e,g,i,j,k) and FIB images (f,l) of the following types of defects: (a) circular flat-topped morphological features at carbide inclusions in ASP30 tool steel (b) irregular flat-topped morphological features at carbide inclusions in D2 tool steel, (c) nodular or flake defect, (d) foreign particles preventing etching of the surface covered by them (e) cross-section of flake defect (f) FIB image of flake cross-section, (g) open void defect, (h) dish-like craters (i,j) cone-like defects (k) SEM image of pin-hole fracture cross-section (l) FIB image of pin-hole cross-section [2].

Fig. 2.18. Effect of bias voltage on the microstructure of TiN coatings deposited with different source combinations: (a) Pure UBM, U_b = - 75 V, (b) 1HIPIMS+ 3UBM, U_b = - 75 V, (c) 2HIPIMS+ 2UBM, U_b = - 50 V, (d) Pure HIPIMS, U_b = - 50 V, and (e) 1HIPIMS+ 3UBM, U_b = - 50 V [46].

Fig. 2.19. The coating surface (a) before and (b) after 128 cycles using the alumina ball. (c) Coefficient of friction (μ) versus the number of ball cycles [4].

Fig. 2.20. SEM images of the nodular defects in the wear track. The defects were subjected to 1 to 128 sliding cycles (a-f) [4].

Fig. 2.21. Schematic diagram outlining the corrosion mechanisms of macroparticle and growth defects (reaction 2 and 3) and the galvanic corrosion of the substrate associated

with these (reaction 4) and other defects, such as droplet shrinkage pinholes (reaction 1) [7].

.

List of tables

1 Introduction

1.1 Motivation

In the last few decades, the use of Physical Vapour Deposition (PVD) technique has increased significantly owing to its capability to deposit metals, alloys, ceramic and polymer thin films onto a wide range of substrate materials [1]. However, one major drawback of PVD process is that deposited coatings are not free from growth defects or imperfections [2–10]. Any kind of growth defect is undesirable because it can degrade the coating performance. The most commonly and industrially used PVD technique, arc-PVD (also known as cathodic arc deposition), itself creates droplets which initiate defects generation in the coatings [5–7,11–13]. During corrosion tests, these growth defects act as potential sites for localised pitting corrosion [14]. Also, hard metal droplets increase the wear during tribological tests [11].

Recently, High Power Impulse Magnetron Sputtering (HIPIMS) technique has been proven useful in depositing droplet free hard (which is comparable with arc -PVD) coatings [15]. This novel technique boosts the generation of metal ions and ions of reactive gases in the plasma which is free from droplet phase when operated under carefully selected parameters such as the right frequency, pulse width and arc suppression settings [15,16]. Previous studies have shown that defects in PVD coatings can be generated due to external factors. For example, contamination of the depositing surface with dust (loose particles of metal/metal-compounds) often generated due to the thermal expansion of chamber components (common for any coating technique associated with vacuum chambers) and substrate irregularities like pits can initiate defect formation [2,3,9,10]. Defects generated during coating growth using HIPIMS have not yet been discussed in detail. However, this is of particular interest for HIPIMS

as high power densities are used for etching and also the plasma during deposition is highly ionised thus reactive.

To study the defect formation during HIPIMS process, the CrN/NbN coating was considered because of its wide industrial applications in recent years as a protective material due to the high hardness, good wear resistance and anticorrosive properties [14,17–20]. However, the constant development of coating industries demands improved and long-lasting coatings for advanced applications, such as coating on biomedical devices. Therefore, a thorough investigation of the coating defects is much required to aid better understanding of their influence on the overall coating performance. With this motivation, the present thesis is focused on the study of the defects associated with HIPIMS process.

1.2 Aims and Objectives

The aim of this project is to identify the source of the defects, understand their formation and discuss possible ways to control their growth. Along with this, we also investigate the influence of these defects on coating performance.

The objectives of the present work are as follows:

- To study the influence of deposition time, bias voltage, chamber pressure and chamber cleanliness on defects generation during HIPIMS processes.

- To study the effects of these defects on corrosion and tribological properties of the coatings.

- To study the effects of defects and deposition techniques on performances of the coatings deposited by two different PVD processes; pure UBM and HIPIMS/UBM.

2 Literature Review

2.1 Thin film deposition techniques

There are several deposition technologies for thin film deposition, such as electroplating, spray coating, chemical vapour deposition (CVD) and physical vapour deposition (PVD). Depending on the application requirements, coatings are produced using the appropriate deposition technique. For this study, CrN/NbN coatings were deposited by sputtering which is one type of PVD technique. In the following section, this particular deposition technique is discussed in detail.

2.2 Physical Vapour Deposition (PVD)

PVD is the transformation of solid material into a vapour phase via physical process. The deposition of vaporised material on the substrate creates the coating. In order to avoid impurities, PVD processes are usually performed in a vacuum or low-pressure environment.

PVD techniques evolved with the evolution of vacuum, electronics, magnetism, and plasma technologies as well as with the advances of gaseous chemistry. A combination of numerous achievements and inventions in those fields opened the door for industrial applications of PVD. In 1930s, cathode sputtering was employed for the fabrication of coatings (Furth 1932), while sputtering by ion bombardment was reported for commercial application in the 1950s (Wehner 1955). Evaporation techniques were also developing in parallel. Nowadays, complicated PVD techniques are used to produce nanostructured, single -, and multilayer coatings with improved properties [21].

The term PVD includes an extensive group of different deposition processes [22], such as

- thermal evaporation

- electron beam (e-beam) evaporation and reactive electron beam evaporation

- sputtering (planar magnetron, cylindrical magnetron, dual magnetron, high-power pulsed magnetron, unbalanced magnetron, closed field magnetron, ion beam sputtering, diode, triode) and reactive sputtering

- filtered and unfiltered cathodic arc deposition (non-reactive and reactive)

- ion plating

- pulsed laser deposition

Followings are the variations of these processes:

- bias sputtering

- ion-assisted deposition

- hybrid processes

Among them, the hybrid processes combine the best attributes of each PVD process, which are:

- magnetron sputtering and e-beam evaporation

- magnetron sputtering and filtered cathodic arc deposition

- e-beam evaporation and filtered cathodic arc deposition [22]

The common PVD processes are evaporation, cathodic arc deposition (arc-PVD) and sputtering. In the case of thermal evaporation, the following sequential basic steps take place: (i) a vapour is generated by boiling or subliming a source material, (ii) the vapour is transported from the source to the substrate, and (iii) the vapour is condensed to a solid film on the substrate surface [23]. The advantage of this method is the possibility to obtain a high deposition rate; however, this process is hard to control. Also, materials

with low melting temperature cannot be used as the source (target). Fig. 2.1 shows a schematic drawing of thermal evaporation process.

Another common PVD coating technology is the cathodic arc deposition or arc-PVD. This is very likely the oldest PVD process. In contrast to thermal evaporation, cathodic arcs can operate near room temperature thus it can be used to produce coatings of the materials with low melting points. As the name suggests, cathodic arcs are determined by the arcing processes at the cathode where arcs are identified as electrical discharges characterized by relatively high current (greater than 1 A) and low burning voltage (less than 50 V) [24]. The arcing generates highly ionized plasma of cathode material. A simple schematic diagram of the basic arc-PVD process is shown in Fig. 2.2.
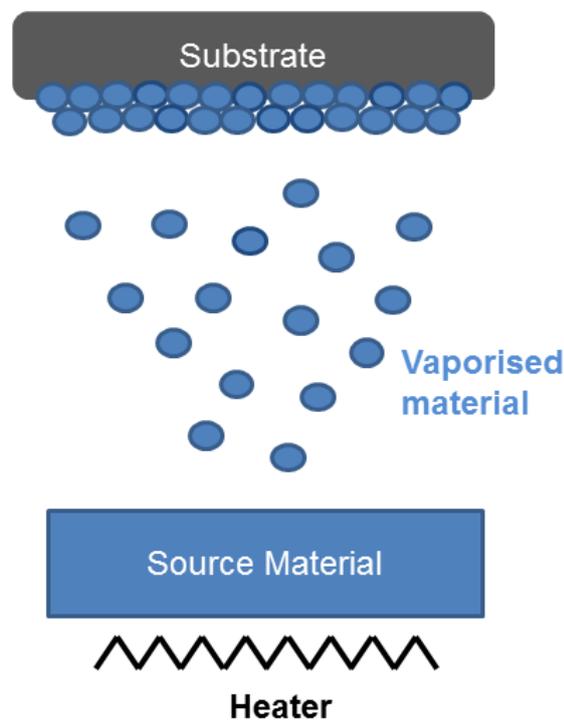
Fig. 2.1. Schematic drawing of thermal evaporation.
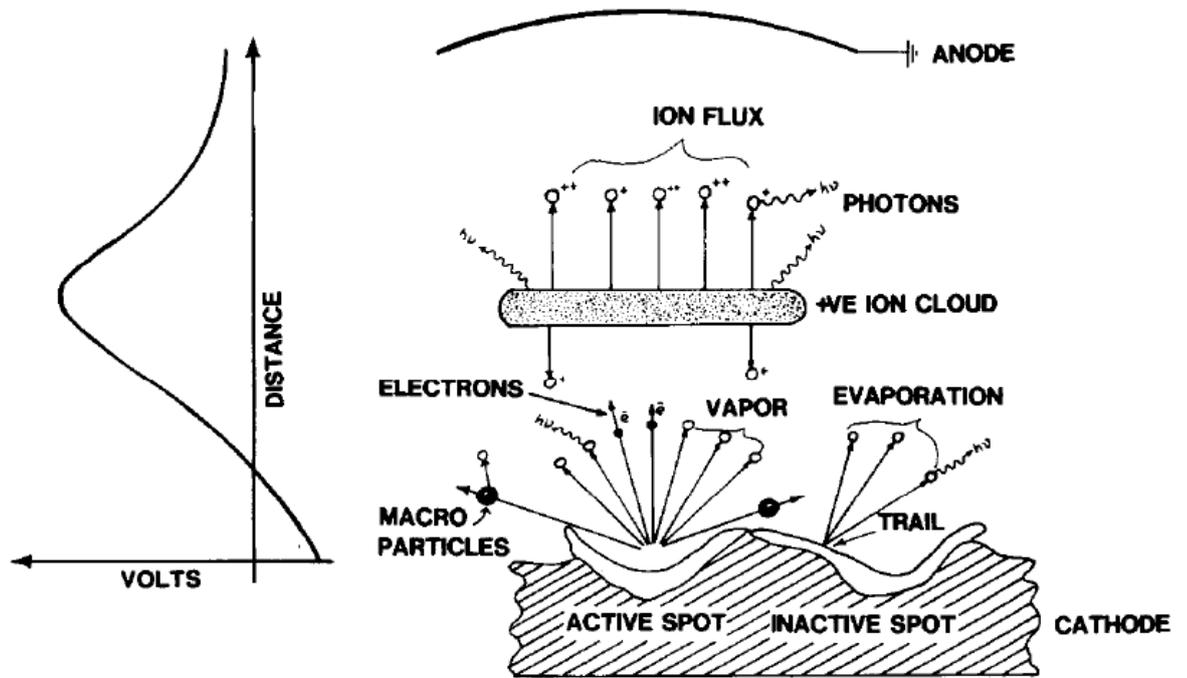
Fig. 2.2. Arc-PVD process [25].

In cathodic arc vaporisation the high current density arc moves over a solid cathodic electrode causing local heating and vaporisation [26]. The arc movement may be random or "steered" using a magnetic field. In many cathodic arc vapour deposition systems multiple cathodic arc sources are used to perform deposition over large areas. The vaporised plasma is generated at one or several locations called 'cathode spots' on the cathode. The operation of cathodic arc spots can be considered as a rapid sequence of microexplosions. In these explosive events, large amounts of electrons can overcome the potential barrier. The cathode material in the vicinity of the spot experiences phase transformations, ultimately resulting in fully ionized, rapidly expanding plasma [24]. However, the sudden increase in temperature at the cathode spot melts the cathode materials which are ejected as droplets or macroparticles (Fig. 2.2) [25,26]. The formation of these droplets is highly undesirable because they can initiate defect formation in the coatings if they deposit on the substrates or in growing coatings. These

droplets create bumps, which, when dislodged, create pinholes [26]. Such defects are potential sites for localised corrosion [8,14]. The pores created due to the separation of droplets from the coating can provide the direct diffusion passes for corrosion medium [8]. The differences of binding energy and chemical composition between coating matrix and droplet can cause galvanic corrosion [8]. Moreover, the roughness of the final coating increases due to the accumulation of droplets during the deposition [14]. This is undesirable for engineering and commercial applications such as cutting tools and artificial jewellery where the smoothness of the finished surface is of prime importance [27].

The other very commonly used PVD process is called sputtering. Unlike arc-PVD, this process involves collisional bombardment of a target material by heavy atoms. If the energy of the incoming atoms is sufficient, they can eject a particle from the target surface. This process minimises the chance of target melting and droplet generations. In this current work, only the technologies based on sputtering phenomena will be discussed.

2.2.1 Sputtering

Sputtering is simply the process of erosion of the surface, namely target, by the energetic particles. It is a sort of atomistic sandblasting [23]. The ejected target materials travel towards a nearby sample (known as a substrate) and create a layer, i.e. coating by condensing on it. This coating deposition process is called sputter deposition. In 1852, Sir W. R. Grove used sputtering to deposit a coating on a silver surface. This was the first reported study on sputter deposition [26].

A schematic drawing of sputtering process and coating deposition is shown in Fig. 2.3.
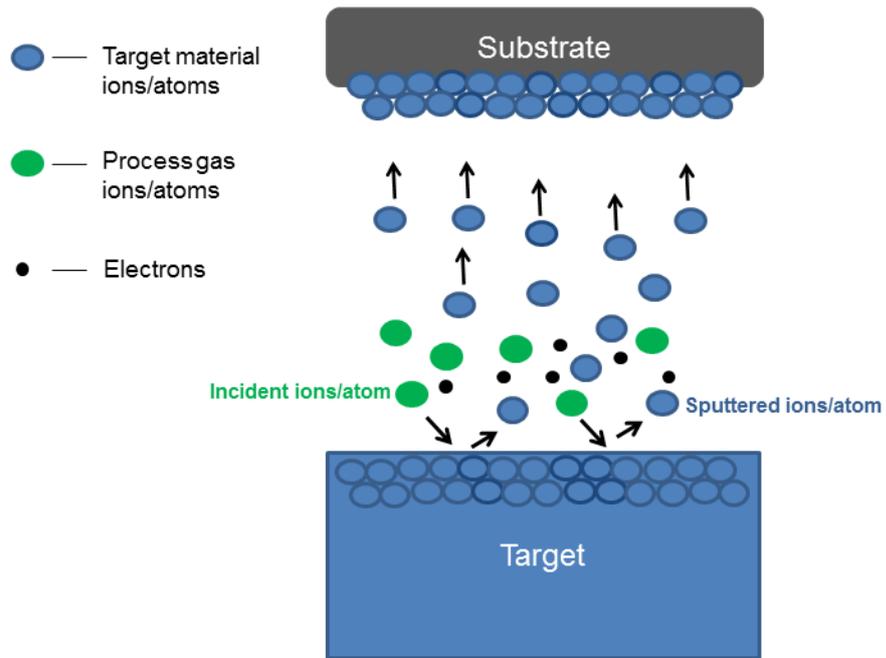
Fig. 2.3. Schematic drawing of sputtering process.

The target can be powered in different ways, ranging from dc for conductive targets, to rf for non- conductive targets, to a variety of different ways of applying current and/or voltage pulses to the target [28]. The target acts as the cathode and the substrate acts as the anode and Argon gas is used as a sputtering medium. Ions form naturally in the gas via collision processes and radiation. In conventional sputter deposition, the target is connected to a DC power supply. By applying a potential difference between the two electrodes the positively charged gas ions are attracted toward the target (cathode) and the electrons are attracted towards the substrate (anode). Accelerated particles collide with other atoms creating more ions. This ionization process can be described as

$$\text{Atom} + \text{e-} \rightarrow \text{Ion} + \text{2e-} \qquad \text{Eq. 2.1}$$
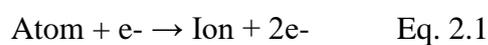
When an ion collides with the target, the kinetic energy of the ion is transferred to the atom of the target. The series of collisions within the target, generated by this primary collision at the surface, is known as a collision cascade [29]. This collision cascade may lead to the sputter ejection of an atom from the surface depending on the energy of the impinging ions. If the energy of incoming ions is sufficient, the atomic bonds are broken and atoms are ejected from the surface. A useful parameter of the sputtering process is the sputtering yield (S) which is defined as the number of atoms (or molecules) ejected per incident ion. The sputtering yield depends on various parameters, such as masses of the incident and target atoms, surface binding energy of the target material and the energy of the incident atoms/ions [28]. It is also sensitive to the angle-of-incidence of the bombarding particle. By applying sufficiently high negative voltage to the cathode, i.e. the target, positively charged ions are attracted from the plasma towards the target. The ions gain energy in the electric field and bombard the target with sufficient energy to initiate sputtering. Thus, the energy of the incident ions depends on the voltage applied to the target. As a result, the voltage applied to the target indirectly influences the sputtering yield.

2.2.2. DC Magnetron Sputtering

The conventional sputtering technique has some limitations, such as low ionisation efficiencies and low deposition rates. In the sputtering process, emitted secondary electrons can recombine with ions and some of them are drained from the plasma via the chamber walls. As a result, the ion/electron density in the plasma is decreased and subsequently the sputtering rate is reduced.

To overcome this problem, the magnetron sputtering process is introduced. By placing the magnets behind the cathode, the plasma is confined to the near-target region. According to the Lorentz force formula, the magnetic fields reshape the trajectories of

the secondary electrons into spiral-like patterns and trap the secondary electrons in the near-target region.

$$\vec{F} = q\,[(\vec{E} + (\vec{v_\perp} \times \vec{B})] \qquad \text{Eq. 2.2}$$

Where q is the charge of the particle, $\vec{E}$ is the electric field, $\vec{v_\perp}$ is the velocity of the charged particle perpendicular to the magnetic field, $\vec{B}$ and $\vec{F}$ is the force experienced by the particle.

Due to such magnetic arrangement, ionisation rate increases with consequent improvements in sputtering and coating deposition rates as compared to conventional sputtering technique. Fig. 2.4 represents the schematic drawing of magnetic field lines in magnetron sputtering setup.
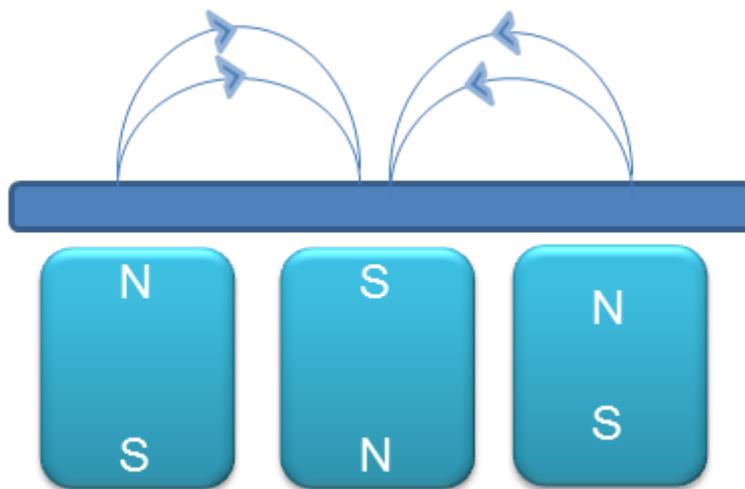
Fig. 2.4. Schematics of balanced field lines in magnetron sputtering.

2.2.3 Unbalanced Magnetron Sputtering

In a conventional magnetron, the magnetic strengths are balanced which confine the plasma mainly to the target region. However, by strengthening the outer magnets compared to the central magnet, the magnetic field lines are directed away from the target region. As a result, some of the charged particles are no longer confined near the target but they are able to follow the magnetic field lines and flow out towards the substrate [30]. In this configuration ion bombardment at the substrate is increased with a consequent improvement in coating structure [30].

Fig. 2.5 shows the schematic drawing of magnetic field lines in an unbalanced magnetron sputtering setup.
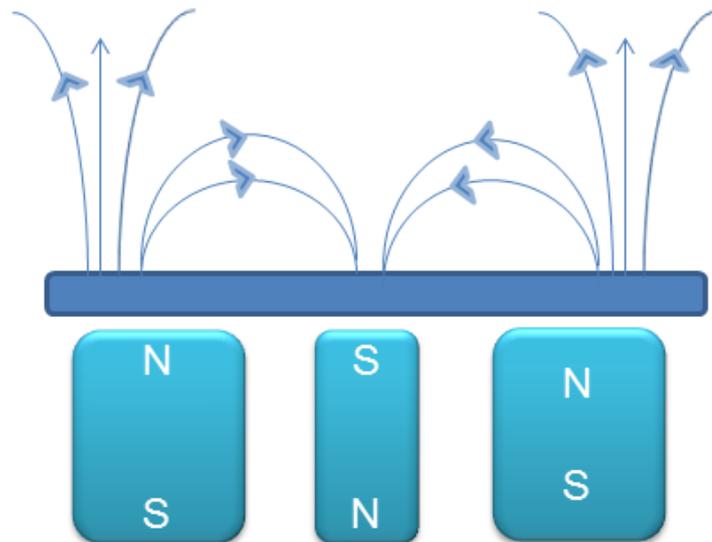
Fig. 2.5. Schematic of magnetic field lines in unbalance magnetron sputtering.

In the previous setup (Fig. 2.4), the magnetic strengths are balanced. In this current set up (Fig. 2.5), the magnetic strengths of the outer magnets are higher compared to the central magnet. This magnetic configuration directs the charged particles towards the

substrate. As a result, ion bombardment at the substrate is increased and the structure of the depositing coating is improved.

The plasma properties can be further improved by arranging UBM cathodes into Closed Field Unbalanced Magnetron Sputtering (CFUBMS) configuration [31]. Fig. 2.6 represents such CFUBMS configuration. In this configuration, magnetic fields trap the electrons between the magnets. As a result, the electron absorption through the walls of the chamber is reduced. The trapped electrons intensify the plasma by colliding with the atoms. The use of CFUBMS leads to improvements in the structure and properties of the sputtered coating [32].
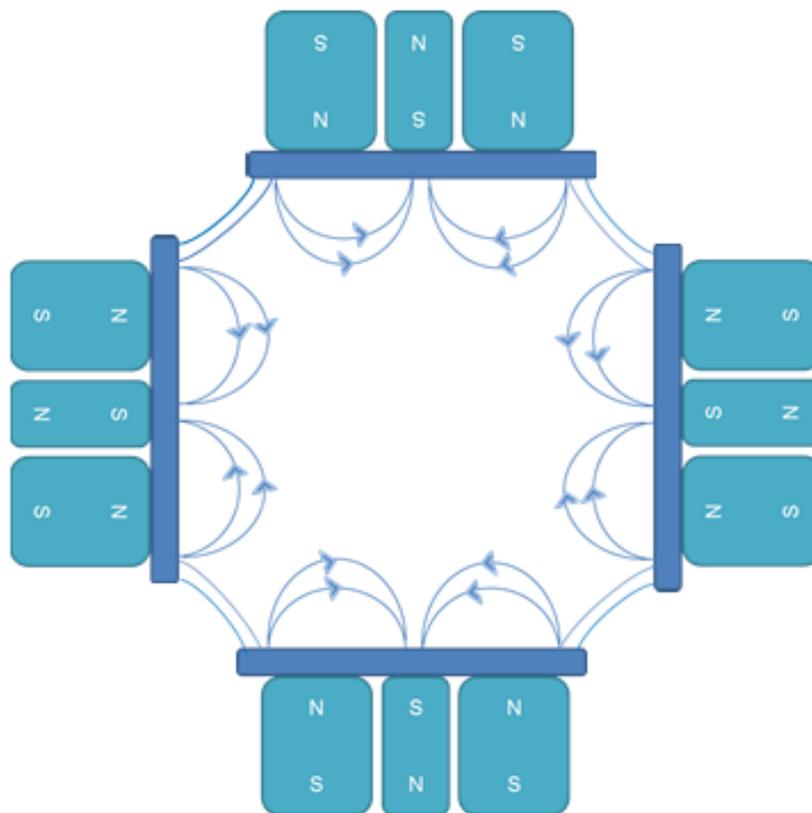
Fig. 2.6. A schematic of the magnet arrangement and field lines in CFUBMS.

2.2.4 High Powered Impulse Magnetron Sputtering (HIPIMS)

DCMS systems are widely used for coating deposition. But these systems need to be operated at low power to prevent cathodes from overheating and melting. The typical cathode power densities during DCMS process are less than 50 Wcm^{-2} [33]. However, a higher target power density of up to 900 Wcm^{-2} can be obtained using pulsed DC [34].

HIPIMS is also a pulsed sputtering technology that utilises much higher peak target power. The peak power exceeds the average power by typically two orders of magnitude [35]. Stable high power discharges with peak powers in the range of 100 – 500 kW (target powers densities of 0.6 – 2.8 $kWcm^{-2}$) was achieved using this pulsed magnetron sputtering technique [33]. The supply of immense high power in very short pulses (impulse) enhances the generation of metal ions (M^+) and the lower average power prevents the targets from melting. Because of higher ionisation, the deposited coatings become dense as compared to conventional magnetron sputtering [35–38]. High ratio of ion to neutral benefits the technique in more ways. The trajectories of ions can be controlled by applying external electric and magnetic fields. Thus, utilising the benefit of higher ionisation during HIPIMS process homogeneous coatings can be produced on complex-shaped substrates which is not achievable by conventional sputtering deposition due to its anisotropic deposition flux [39,40]. Dense and homogeneous microstructure enhances the properties of HIPIMS deposited coating. Application of HIPIMS results in denser microstructure, smaller grain size, lower surface roughness, higher hardness, improved adhesion, excellent wear and corrosion resistance [41–43].

In addition, HIPIMS deposited coatings are free from droplet related defects [15]. Droplets are produced due to the melting of target and they can initiate defects in the depositing coatings [44]. HIPIMS utilises lower average power which prevents droplet formation.

HIPIMS plasma can also be used to pre-treat the substrate before coating deposition [16]. This pre-treatment step enhances the adhesion of the coating with the substrate [16,35,45]. As a result, the mechanical properties of the coatings improve.

Combined High Power Impulse Magnetron Sputtering and Unbalance Magnetron Sputtering technique (HIPIMS/UBM)

The higher ion content in HIPIMS plasma also has a disadvantage. The back attraction of the positively charged metal ions to the cathode reduces the deposition rate during HIPIMS process. It has been widely published that the HIPIMS technique is an excellent tool to deposit coatings with very dense structure without inter-columnar voids but shows a relatively lower deposition rate. On the other hand, the conventional UBM technique has higher deposition rate but can produce porous coatings [15,35,46–48]. A combination of both techniques, however can eradicate these problems and produce coatings with a high deposition rate and very dense structure [46,49].
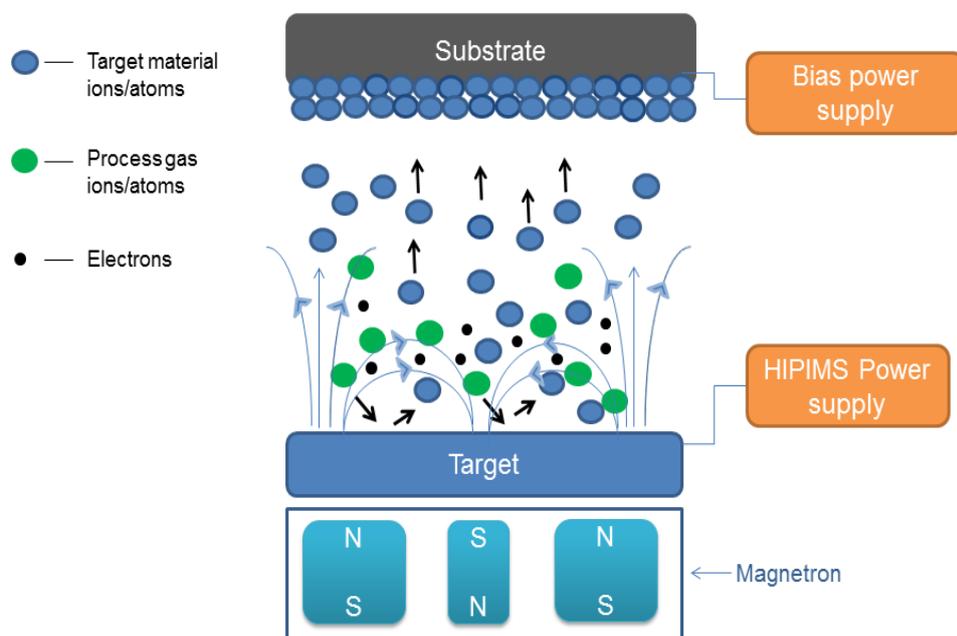
Fig. 2.7. A schematic of HIPIMS process.

Reactive Sputtering

Reactive sputtering is a sputtering process which allows compounds to be deposited by introducing reactive gases into the plasma. During the reactive sputtering process the reactive gas is "activated" by the plasma and chemically reacts with the target materials. Using this process a wide range of compounds (oxides, nitrides, carbides, fluorides) thin films can be produced [50–52].

In this current work, CrN/NbN coatings were produced by sputtering the Chromium and Niobium targets in reactive gas atmosphere of Argon (inert gas) and Nitrogen (reactive gas) using HIPIMS/UBM technique.

2.3 Microstructure of Thin Films

In thin films, growth process controls the microstructure evaluation [53]. This process can be divided into several phases, from nucleation to growth of continuous film structure.
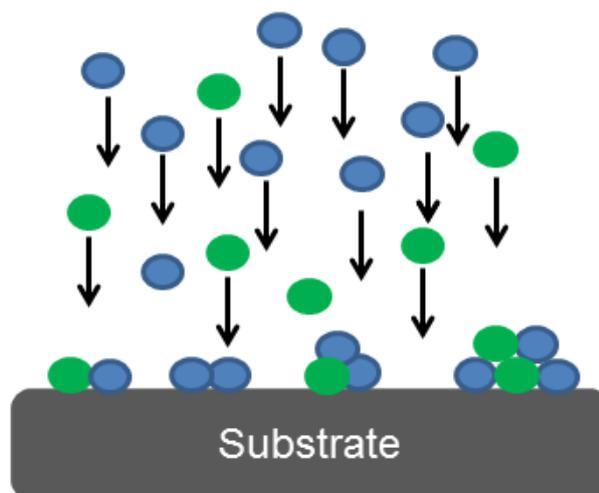
Fig. 2.8. Condensation and nucleation of the adatoms

The growth process hence the microstructure of thin films deposited by PVD technique is influenced by a number of deposition conditions and process parameters such as substrate temperature, substrate bias, substrate rotation, target arrangement, target power, chamber pressure, ion to neutral ratio and ion bombardment energy [40,53–67]. By varying these parameters systematically, the microstructure and thus the properties of PVD coatings can be modified as required for a specific application. For this unique feature, PVD has become a very important thin film deposition technique.

The influence of process parameters on microstructure evaluation in PVD coatings has been studied by several scientists. In 1969, Movchan and Demchishin introduced the concept of structure zone model (SZM) for the first time [68]. Their SZM described the influence of substrate temperature (represented by the ratio of substrate temperature T_s to the melting point of the material T_m) on the coating morphology. The proposed model can be divided into three zones (Fig. 2.9). Zone 1 ($T_s \ll T_m$) exhibits a porous structure associated with insufficient adatom surface mobility. With increasing substrate temperature, the adatom mobility increases. As a result, the structure becomes densified (zone 2). In zone 3 (when T_s is very close to T_m), the high substrate temperature allows bulk diffusion and recrystallisation resulting in a very dense coating structure.

In 1974, this model was extended by Thornton for sputtered coatings [69]. In this new model, the effect of gas (Argon) pressure was added and a new zone, namely Transition (T) zone, was introduced. Zone T consists of densely packed fibrous grain, which is wider at low Ar pressure (Fig. 2.10). With the increase in Ar pressure this zone narrows. The high-energy neutrals bombarded from the sputtering target create this zone.
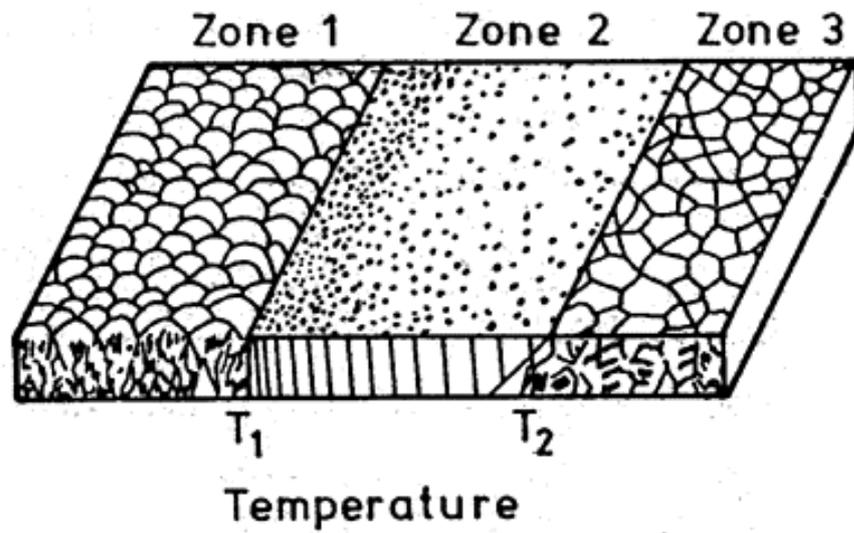
Fig. 2.9. Structure zone model according to Movchan and Demchishin, showing the

influence of substrate temperature on microstructure for evaporated films [68].
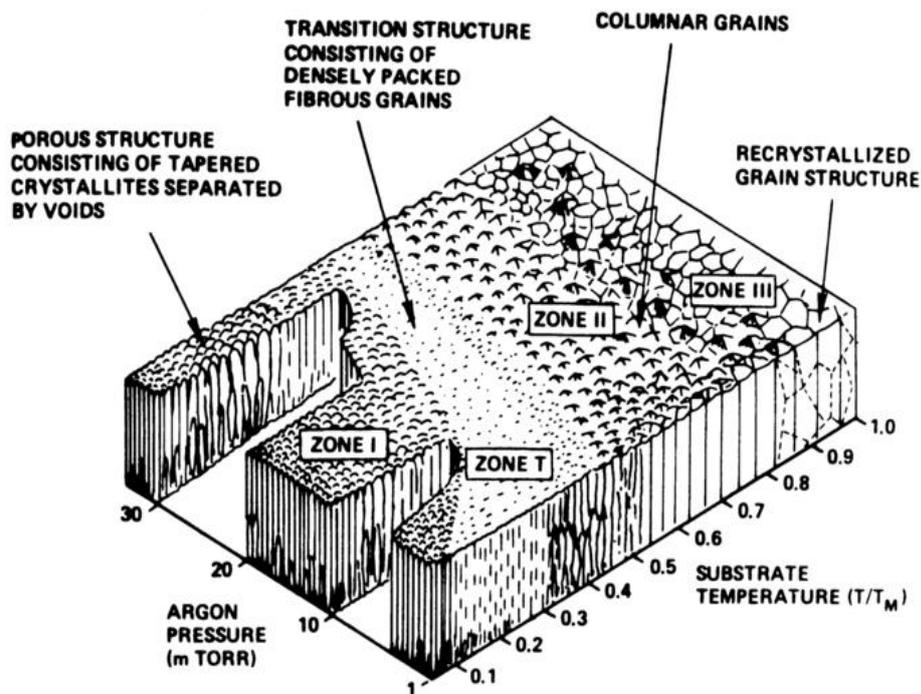
Fig. 2.10. Structure zone model by Thornton showing the influences of substrate

temperature and Ar pressure on microstructure for sputter-deposited films [69].

In 1984, the Structure-zone model (by Thornton) was further modified by Messier, Giri and Roy [70]. They replaced the pressure axis by the substrate bias axis. With the increase in bias voltage the adatom mobility increases, this subsequently suppresses the formation of zone 1. At higher bias voltage, zone 1 transforms to zone T even at very low temperature (Fig. 2.11).
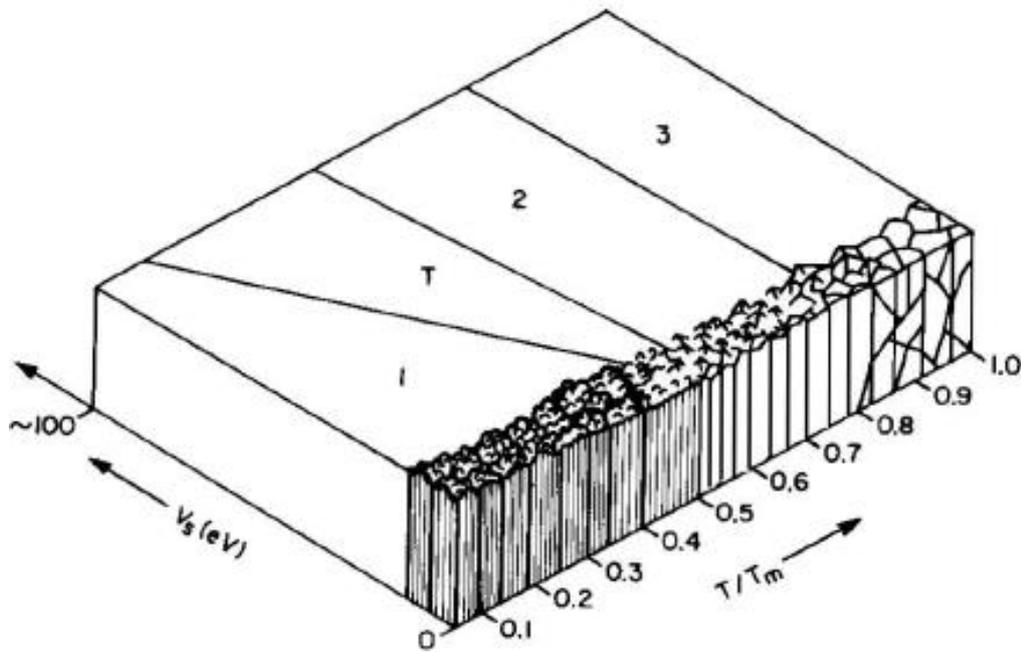
Fig. 2.11. Structure zone model by Messier, Giri and Roy showing the influences of substrate temperature and bias voltage on microstructure for sputter-deposited films [70].

In 1998, Barna and Adamik analysed the structure zone models published in the literature [68–70]. Based on that fundamental structure forming phenomena, they discussed the structure evolution in polycrystalline thin films with the thickness [71]. Fig. 2.12 shows the summarised structure zone model proposed by them.

ZONE I.   ZONE T.   ZONE II.
competitve texture   restructuration texture

T_s/T_m
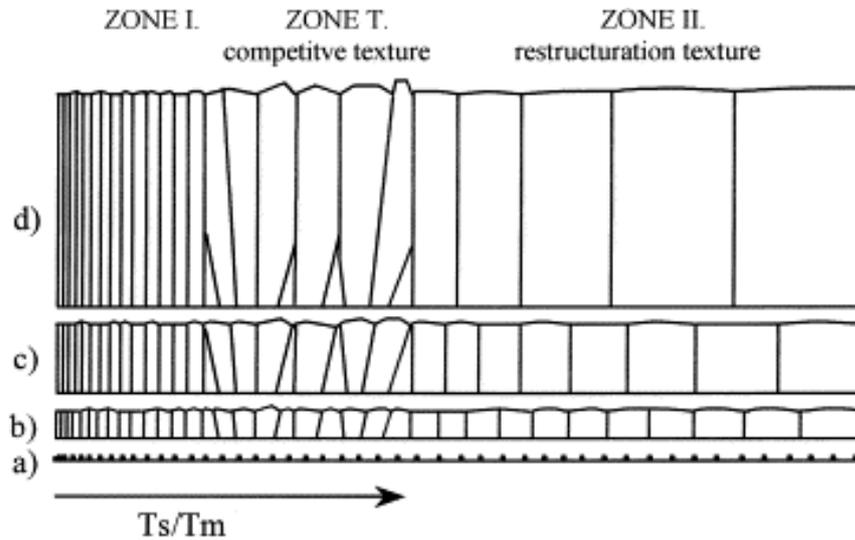
Fig. 2.12. Basic structure zone models at various film thickness [71].

Figure shows that the zone 1 is homogeneous along the thickness of the film. This zone is composed of fibres of small diameter (1 – 10 nm). With the increase in substrate temperature zone 1 converts to Zone T. In zone T, the structure is inhomogeneous along the film thickness. It is fine crystalline at the substrate, composed of V-shaped grains in the next thickness range while can be columnar in the upper part of thick films. In zone 2, grain boundaries are almost perpendicular to the film plane and the structure is homogeneous along the thickness. Due to the higher substrate temperature, randomly oriented small grains (of zone T) dissolve gradually by the grain coarsening and produce the wide columnar structure of zone 2. Further increase in substrate temperature results in recrystallisation. This structure (zone 3) is characterised by equiaxed globular three dimensional grains with random orientations (Fig. 2.9, 2.10, 2.11).

With the development in sputtering technology, the structure zone model was revised and modified for CFUBMS by Kelly and Arnell in 1998 [72]. This model describes the

coating morphology as a function of ion flux (ion to neutral ratio, J_i/J_a) along with the bias voltage and substrate temperature. Fig. 2.13 shows the schematic of the structure zone model for CFUBMS.
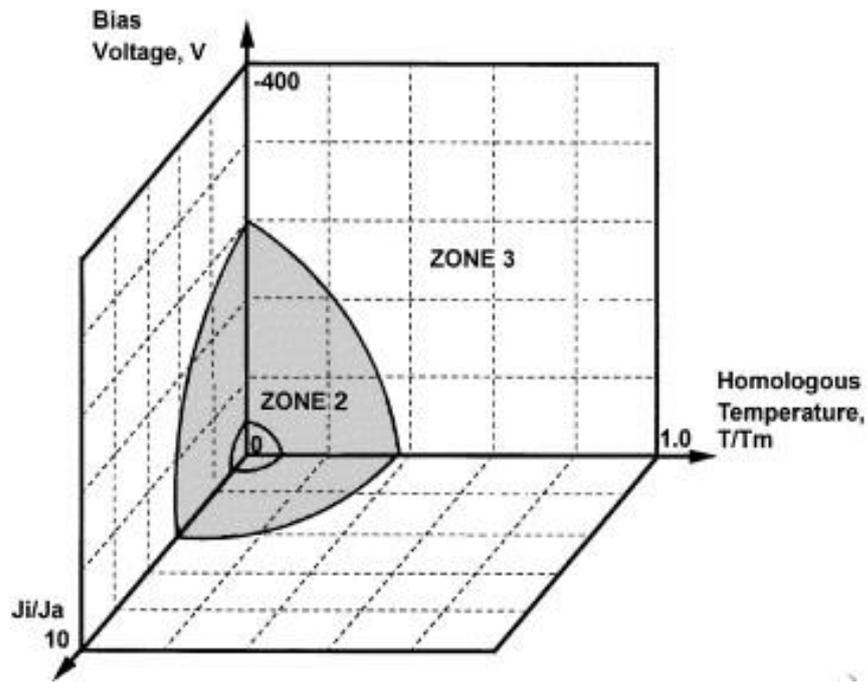
Fig. 2.13. Schematic of the structure zone model, proposed by Kelly and Arnell for CFUBMS [72].

As seen from the figure, this three-dimensional SZM only has zone 2 and zone 3. Zone 1 could not be identified because CFUBMS configuration develops a highly ionised condition by trapping the electrons within the plasma which subsequently suppresses the formation of porous columnar zone 1-type structures. There is a small boundary inside the zone 2 but that does not represent the zone 1 / zone 2 boundary. It shows the lower levels of each of the variables used and marks the lower limits of normal operating condition [31].

2.4 Coating Architecture

Recent advances in deposition techniques have allowed engineering of the materials to achieve unique properties which are often not obtainable in bulk materials. In many cases, coatings with a single monolithic layer have provided improved protection to the bulk substrate material. For industrial applications, hard transition metal nitride PVD coatings with a single monolithic layer have been used successfully. CrN, TiN and NbN coatings especially have shown notable protective properties against corrosion and wear [73–75]. Moreover, it has been reported that multilayer nitride coatings deposited by reactive magnetron sputtering can improve coating properties. For example, TiN/VN and TiN/NbN multilayer coatings have shown high coating hardness whereas, TiN/CrN and CrN/NbN both have improved corrosion resistance and reduced wear rates due to their multilayer structures [20,76–79].

In general, a multilayer structure represents a thin film system composed of layers of two different materials alternatively and repeatedly deposited on a substrate [80]. Multilayer PVD coating can be produced using a rotating substrate holder carousel which sequentially exposes the substrates to different targets for brief periods allowing layer by layer growth of the target materials.

According to the number of single layers and their arrangements, multilayer structure can be classified into three categories [81].

- **Coating with a limited number of single layers** (Fig. 2.14a)

- **Coating with a high number of non isostructural single layers** (Fig. 2.14b)

- **Superlattice coating** (Fig. 2.14c)
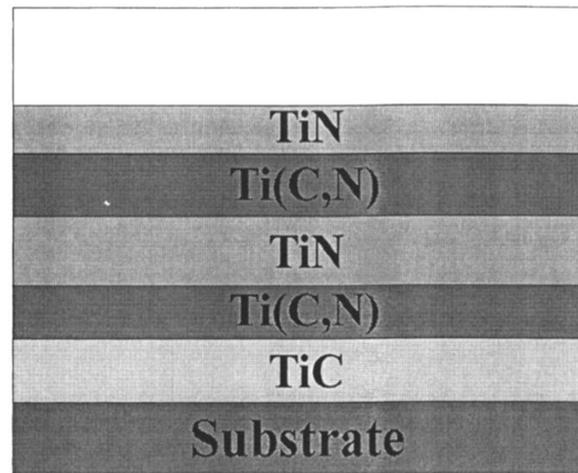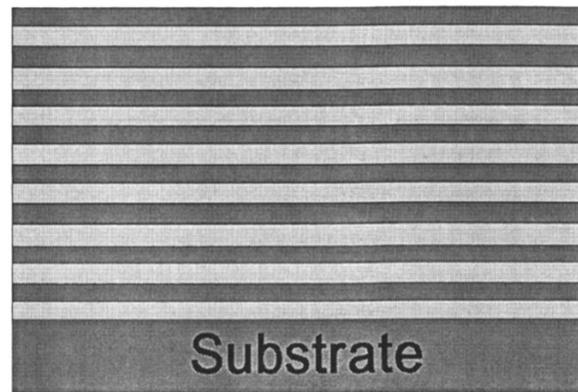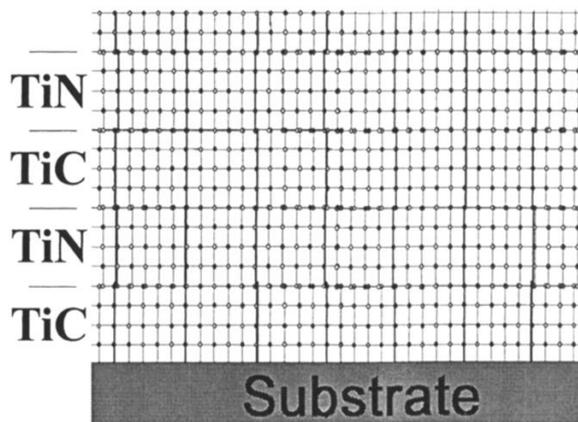
Fig. 2.14. Different types of multilayer coatings: (a) small number of single layers, e.g. TiC/Ti(CN)/TiN, (b) high number of non isostructural single layers, e.g. TiC/TiB₂, (c) high number of isostructural single layers (superlattice), e.g. TiC/TiN [81].

The main concept of multilayer coating is to prevent the columnar grain growth and to combine different materials for additional benefits. For example, NbN was combined with CrN (which was already an established coating for tribological applications) to improve the hardness and corrosion properties [82]. The resulting CrN/NbN multilayer coatings provided enhanced corrosion protection to the substrate when compared to CrN coatings. Also, the wear resistance was improved significantly [20,83,84].

These superior coating properties were achieved due to the combination of wear resistant Cr with chemically stable Nb. Moreover, CrN and NbN layers are isostructural, i.e. they have similar chemical bonding, similar atomic radii and lattice distances. As a result, superlattice CrN/NbN coatings were produced. The superlattice structure hardened the coating, suppressed the columnar growth, and increased the coating density. The large number of layers in superlattice coating protected the substrate more effectively than the bulk material or monolithic coating [84].

In 1970, Koehler suggested the ways to fabricate layer structure of two materials in order to design a strong solid [85] where he explained the reason for increasing hardness in layer structure. He said that the interfaces between the layers would act as diffusion barriers to the motion of 'dislocation', which are the line defects that are mainly responsible for the plastic deformation of crystalline solids. According to Koehler's model, the critical stress requires to move a dislocation across an abrupt interface is proportional to

$$Q = (G_A - G_B) / (G_A + G_B) \qquad \text{Eq. 2.3}$$

Where, G_A is the modulus of rigidity of layer A and G_B is that of layer B.

By choosing two materials having a large difference in modulus, multilayer coating with large critical stress, i.e. high hardness can be produced.

The benefit of superlattice multilayer coating is that it can provide unique properties which are not achievable using individual layer materials alone [81]. These properties can be further improved by changing the thickness of individual layers [81,86–93]. The layer thickness is a function of the deposition rate which depends mainly on the target current and target to substrate distance and on the rotation speed of the substrate arrangement [94]. By controlling the deposition parameters, the layer thickness and hence the coating properties can be modified.

For example, the bilayer thickness/period (the total thickness of two successive layers which is also known as superlattice spacing, Δ) of CrN/CrAlN nanoscale multilayer coatings was varied from 4.4 to 44.1 nm by controlling the rotation speed of the substrate holder [92]. The study showed that the wear behaviour, microstructure and mechanical properties of the coatings were dependent on the bilayer thickness. The coating with a bilayer thickness of 5.5 nm exhibited the best coating properties. This shows that a critical bilayer thickness is required to obtain good mechanical properties, such as high hardness and resistance to plastic deformation [92].

The properties deteriorate for the coatings with a bilayer thickness below or above that critical value. This behaviour can be explained using Koehler's model. In the case of a bilayer thickness lower than the critical value, the hardness reduces due to two following reasons [95]:

1. Small layers nearly interdiffuse and the modulus of each layer becomes the same thus no hardness enhancement can occur.

2. Very close interfaces can exert opposing forces on a dislocation at an interface which lowers the stress needed to move the dislocation.

However, in the case of large Δ, the dislocations can move within the individual layers which results in a decrease in hardness value.

Fig. 2.15 shows the variation in mechanical properties with the bilayer thickness of CrN/CrAlN nanoscale multilayer coatings deposited by CFUBMS.
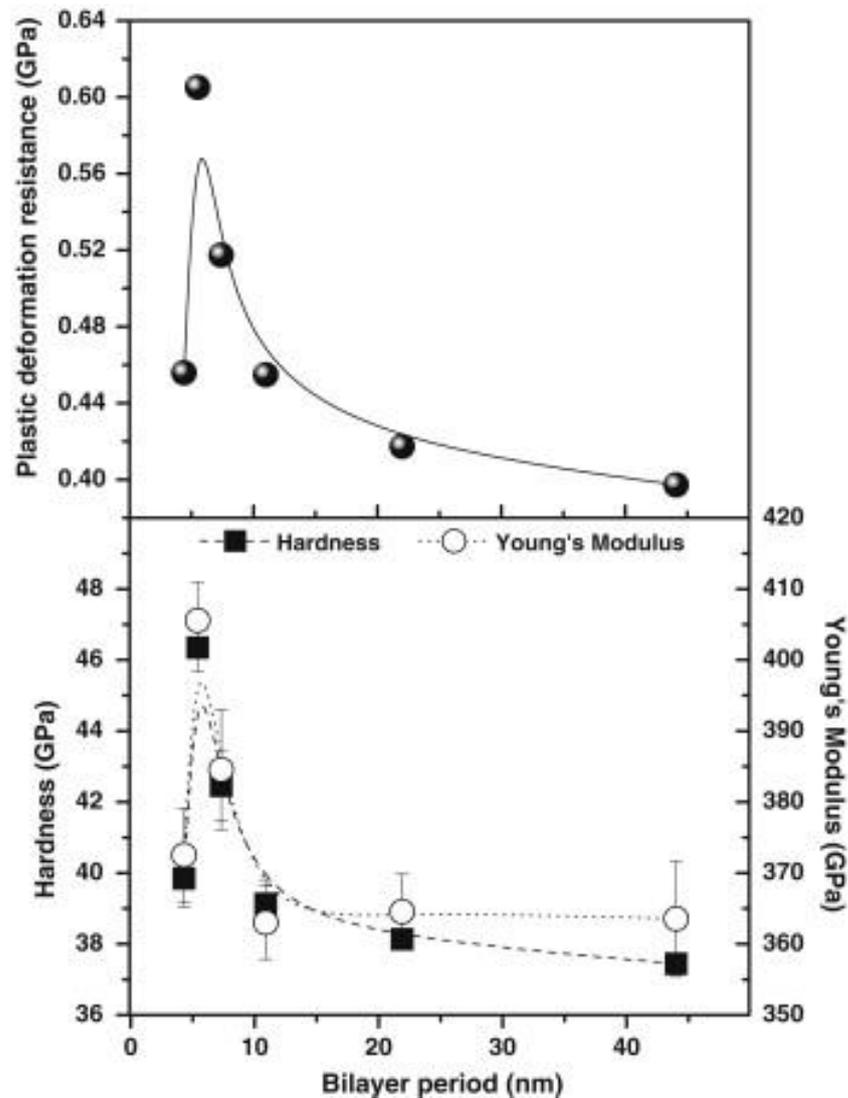
Fig. 2.15. The mechanical properties as the functions of bilayer thickness [92].

The studies on multilayer structure suggest that by controlling the deposition process, it is possible to produce coatings with improved properties over monolithic coatings. This widens the range of industrial applications for multilayer coatings.

2.5 Defects in PVD coatings

During the coating growth, different types of defects also grow within the coating. The most commonly and industrially used PVD technique, arc-PVD, itself creates droplets which initiate the defects generation in the coatings [5–7,11–13,27,96–98]. Apart from droplets, PVD coatings also suffer from surface imperfections associated with external factors. For example, contamination of the depositing surface with flakes and substrate irregularities like pits can initiate defect formation [2,3,9,10].

2.5.1 Types of defects

According to shape, size and growth mechanism defects can be categorised as follows:

Droplet related defects: Droplet related defects are very common in the coatings deposited by arc-PVD. These defects are also found in the coatings deposited by conventional DC sputtering where substrate surfaces are etched by high-energy metal ions prior to the coating deposition [99]. Due to the application of high bias voltage during etching, arcs are formed which subsequently initiate defect formation in the coatings.

Arcing liquefies the target at the arc spot. These liquid target materials are ejected from the target as droplets [13]. Instant solidification of the liquid materials on the substrate surface generates droplet related defects. These defects stick to the surface in the form of wide hemispheres with a flattened bottom (Fig. 2.16) [100].
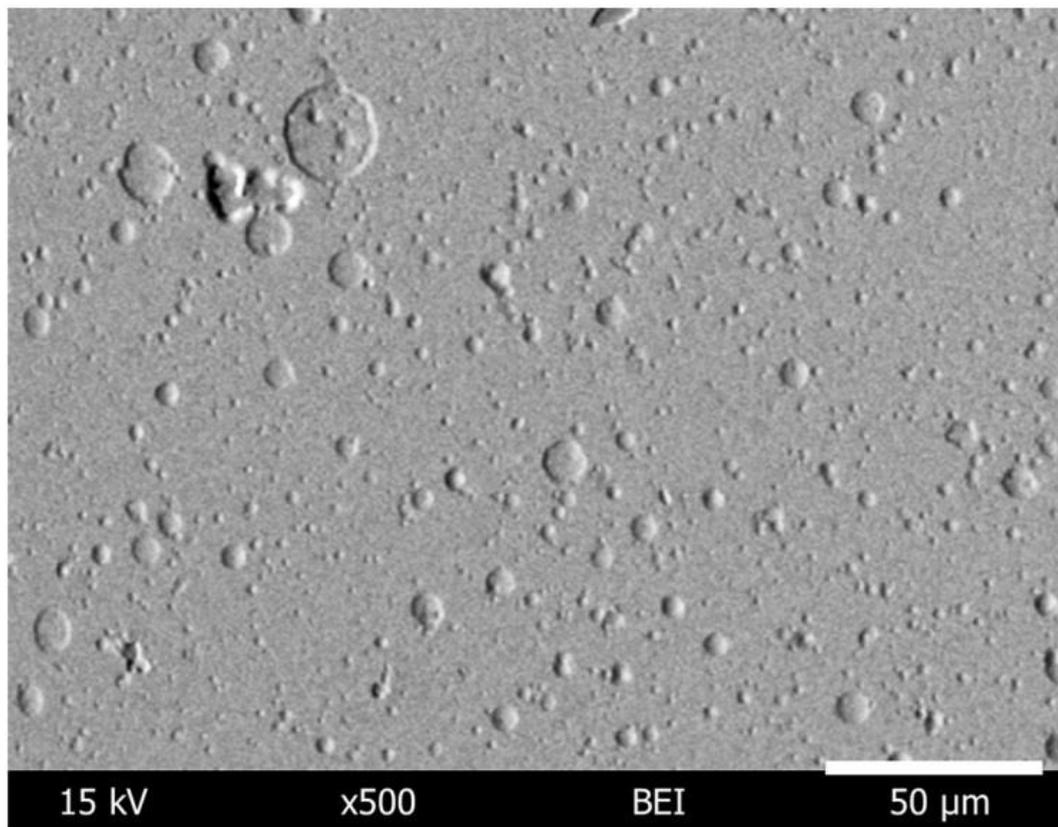
Fig. 2.16. SEM image of the titanium ion etched surface of HSS sample [100].

Flakes related defects: Flakes related defects can be found in any coating deposited in a vacuum chamber. During the fast pumping phase from the atmospheric pressure to the base pressure, turbulent flow may pick up some small particles from the chamber parts [101]. Some of the flakes generate due to the thermal and structural stresses on the chamber components (shields, heaters) during coating deposition [2]. Further sources for small seed particles and wear debris are the sputter flux bombardment on chamber (walls and other components) and the rotation of the substrates holders.

According to their appearance, these defects can be divided into subgroups:- nodular shaped defects, cone-like defects and open void defects [2].

Due to the deposition of coating materials on the flakes attached to the substrate, nodular shaped and cone-like defects are formed (Fig. 2.17c,j). Nodular shaped defects

start to grow at the intermediate stage during coating deposition whereas cone-like defects generate when relatively small foreign particles get attached to the substrate at a very initial stage of coating deposition. Due to the shadowing effects, these defects are weakly attached to the surrounding coating. Therefore, any kind of stresses (thermal or mechanical) can easily deform and delaminate these defects from the coating thus leave a void. These voids are called open void defects (Fig. 2.17g).

A significant difference between arc droplet and a flake-defect is that the coating grows over time on top of the flake whereas arc droplets either solidify outside the coating or on the surface instantaneously.

Pinhole defects: These defects generate due to the substrate surface imperfections, such as small craters, pits etc. During the condensation process, these pits and craters lead to the formation of pinhole defects [2]. Deposition of coating materials can cover most of the surface imperfections. However, larger cavities may not be closed fully and remain as voids within the coatings. These kinds of defects extend through the whole coating from substrate to the top surface of the coating (Fig. 2.17k).
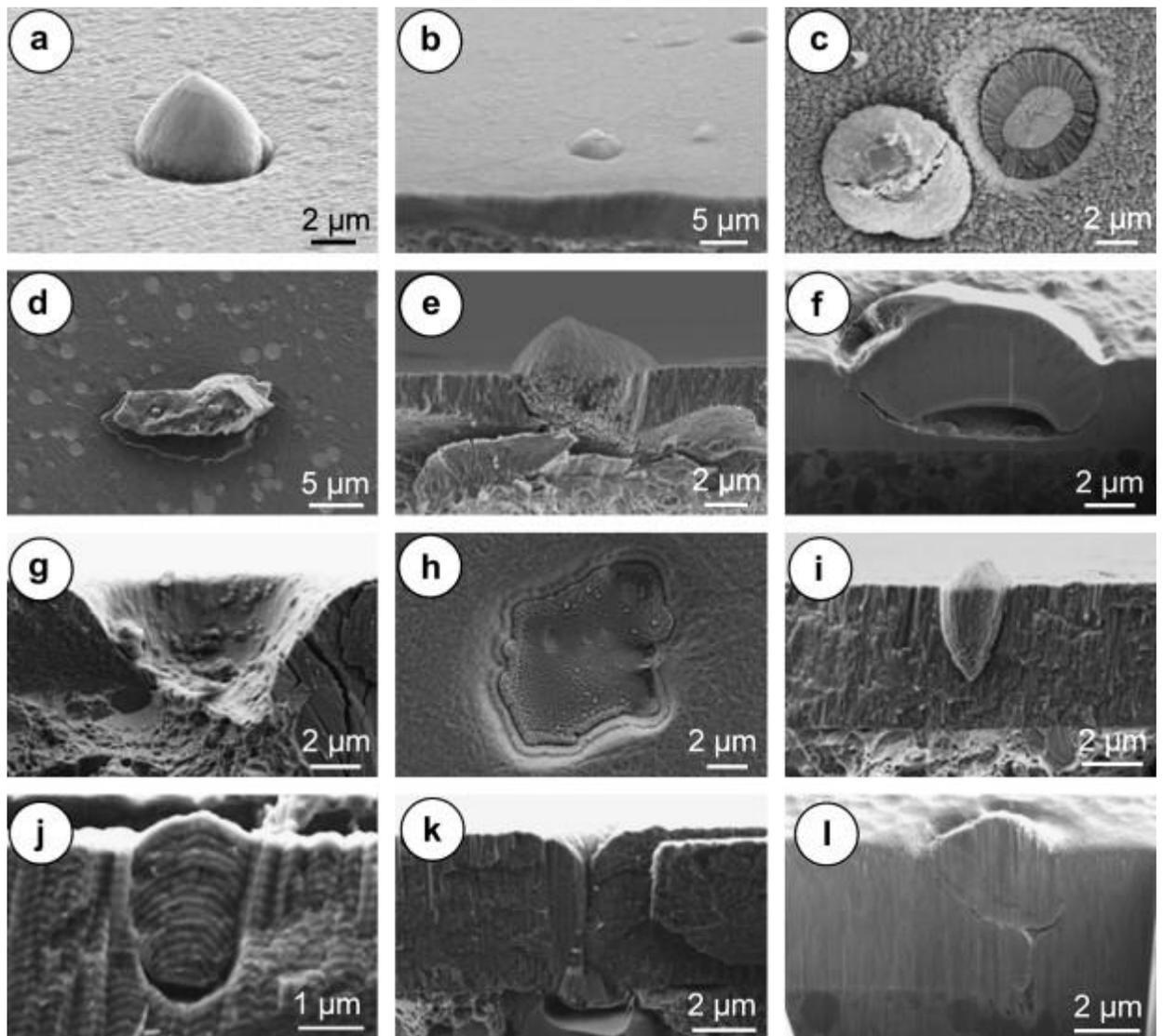
Fig. 2.17. Plan view (a,b,c,d,h), cross-sectional SEM (e,g,i,j,k) and FIB images (f,l) of the following types of defects: (a) circular flat-topped morphological features at carbide inclusions in ASP30 tool steel (b) irregular flat-topped morphological features at carbide inclusions in D2 tool steel, (c) nodular or flake defect, (d) foreign particles preventing etching of the surface covered by them (e) cross-section of flake defect (f) FIB image of flake cross-section, (g) open void defect, (h) dish-like craters (i,j) cone-like defects (k) SEM image of pin-hole fracture cross-section (l) FIB image of pin-hole cross-section [2].

Inter columnar voids are another type of coating imperfection. Unlike, pinhole defects which generate due to the pre-existence of the substrate pits, inter columnar voids are the drawbacks of coating technology. During low energy sputtering processes such as conventional UBM, these voids are created due to the lower adatom mobility [102]. The adatom mobility can be increased by suitably biasing the substrate to increase the energy of adatoms and/or by increasing the metal ion flux incident on the substrate surface [102]. In HIPIMS, the metal ion to neutral ratio is much higher which prevents the void formation and hence can be used to deposit void free dense coatings [35–37,102]. The benefits of using HIPIMS and a higher bias voltage can be observed from the Fig. 2.18.

The coating deposited by pure UBM (Fig. 2.18a) had a coarse microstructure with pronounced open column boundaries. In contrast, HIPIMS deposited coatings exhibited wide columnar structure with very smooth column tops (Fig. 2.18d) [46]. This study suggested that sufficiently high metal ionisation can eradicate these defects (i.e. technology related drawbacks).
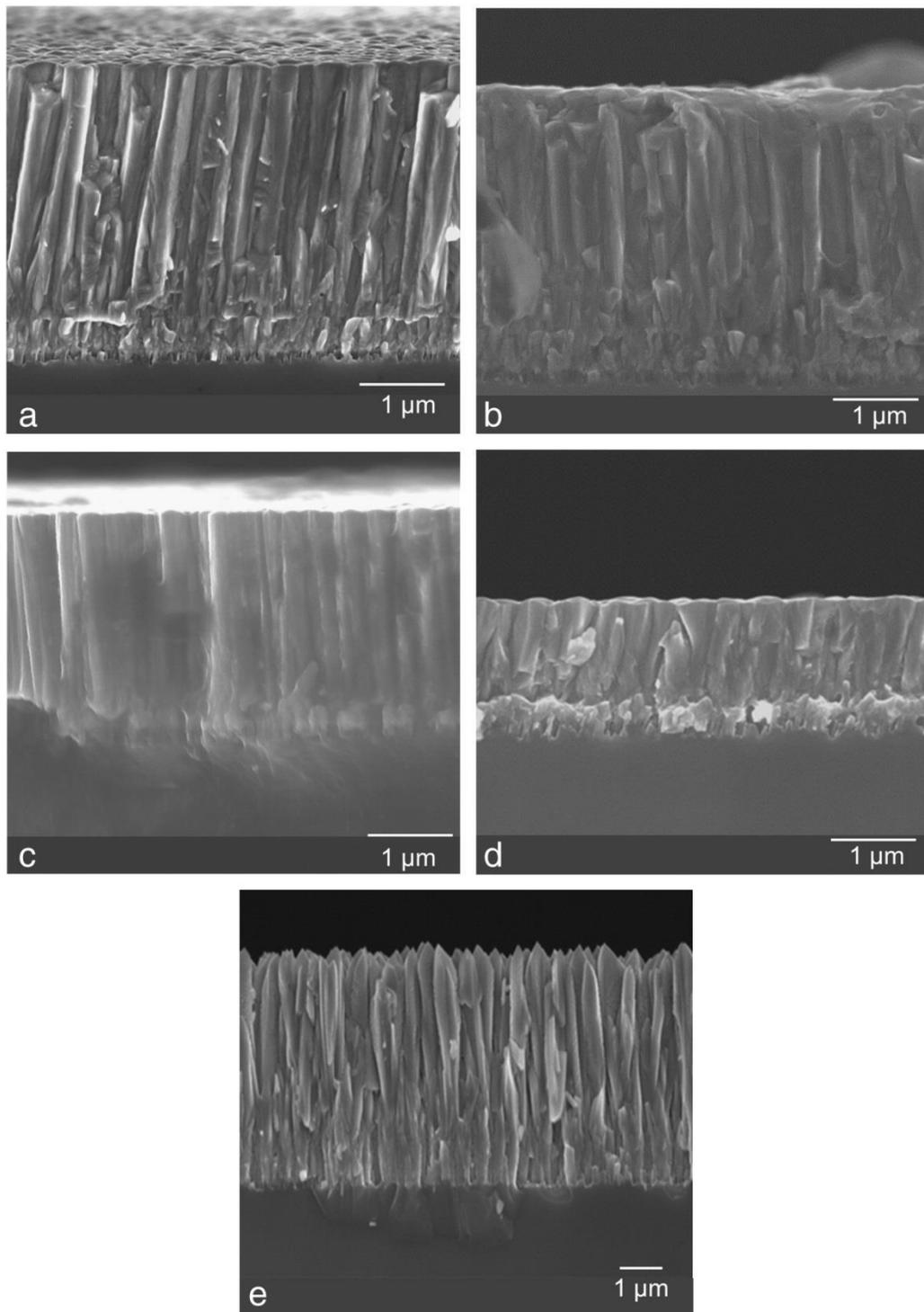
Fig. 2.18. Effect of bias voltage on the microstructure of TiN coatings deposited with different source combinations: (a) Pure UBM, $U_b = - 75$ V, (b) 1HIPIMS+ 3UBM, $U_b = - 75$ V, (c) 2HIPIMS+ 2UBM, $U_b = - 50$ V, (d) Pure HIPIMS, $U_b = - 50$ V, and (e) 1HIPIMS+ 3UBM, $U_b = - 50$ V [46].

2.5.2 Effect of defects on coating performance

Any kind of growth defects are undesirable as they can restrain the coating functionality [2,4,7,11,14,44,103]. They can affect the surface roughness and surface finish thus the tribological performance of the coatings can also be affected [4,103]. During sliding, the applied force can smash the defects onto the coating surface [4]. Subsequently the formation of debris increases due to the three body tribological contact mechanism [104]. This can affect the friction behaviour of the coatings. Fig. 2.19 shows the as deposited TiAlN coating surface (a), the same surface after 128 cycles using Alumina ball (b) and the dependence of friction coefficient on number of ball cycles (c).
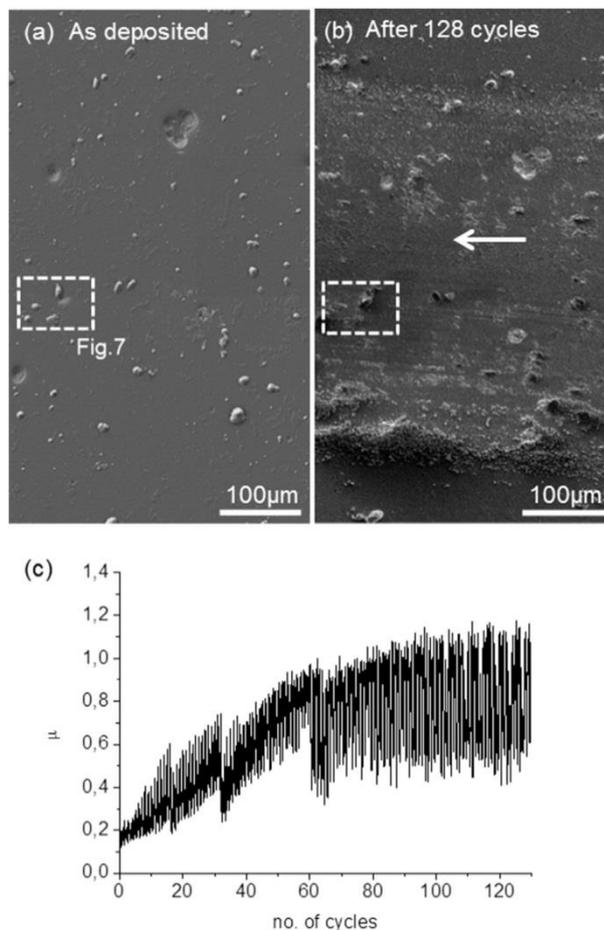
Fig. 2.19. The coating surface (a) before and (b) after 128 cycles using the alumina ball, and (c) Coefficient of friction (μ) as a function of number of ball cycles [4].

As seen from the figure, coefficient of friction (COF) was increased with the cycle. The breaking and the spallation of the nodular defects initiated the three body abrasion with a consequent increase in the COF value.

Fig. 2.20 shows the smashed defects within the wear track of TiAlN coating [4]. Cycle-to-cycle imaging shows the formation of fine abrasive particles and oxidation at the positions of the nodular defects.
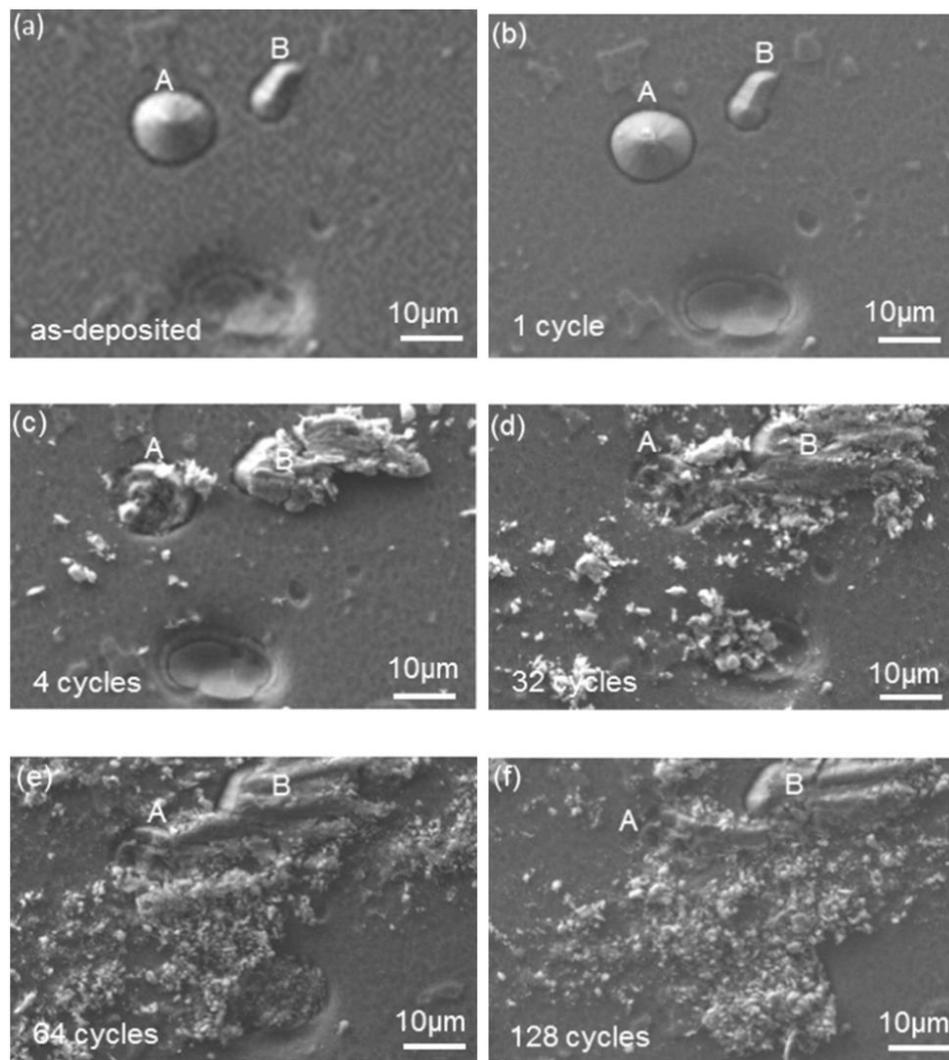
Fig. 2.20. SEM images of the nodular defects in the wear track. The defects were subjected to 1 to 128 sliding cycles (a-f) [4].

Also, hard metal droplets can damage the surfaces of both the coating and the counterpart (under the test) and increase the wear. For example, in case of Nb–Ti–N coatings deposited by cathodic arc from TiNb compound cathodes, the Nb rich metallic droplets increased the wear of the counterpart (UHMWPE) in hip simulator test liquid during wear tests [11].

Not only the tribological properties, the corrosion properties are also affected by the coating defects. The defects like pores, holes and voids can expose the substrate material to the corrosive media and accelerate the corrosion process [7,14]. Fig. 2.21 shows the schematic diagram of localised corrosion related to coating defects.
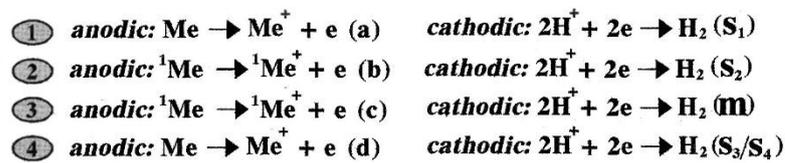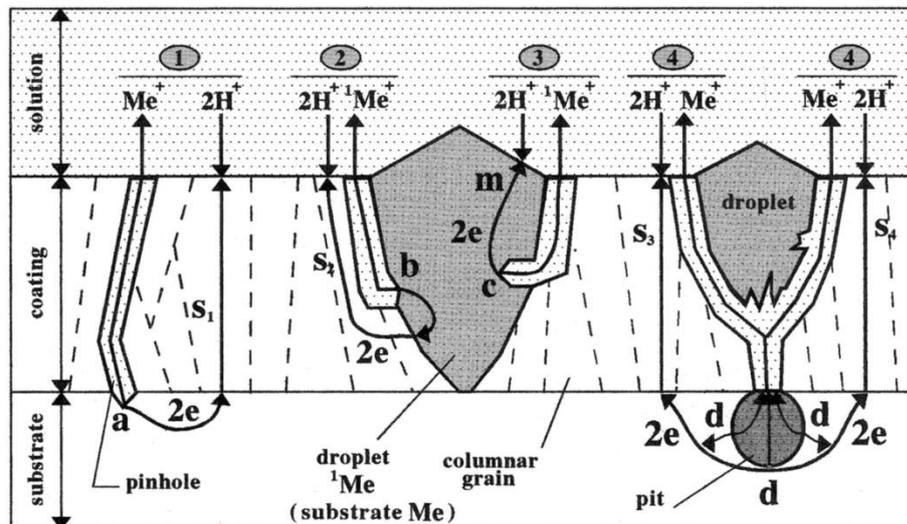
Fig. 2.21. Schematic diagram outlining the corrosion mechanisms of macroparticle and growth defects (reaction 2 and 3) and the galvanic corrosion of the substrate associated with these (reaction 4) and other defects such as droplet shrinkage pinholes (reaction 1) [7].

The cavitation erosion study of TiN coatings produced by arc-PVD revealed the important role of droplet-related defects on the cavitation erosion damage [100]. During the tests, deep cavities were formed by the detachment of conical droplets. Fig. 2.22 represents the schematic drawing of cavitation erosion damage on different droplet related defects.
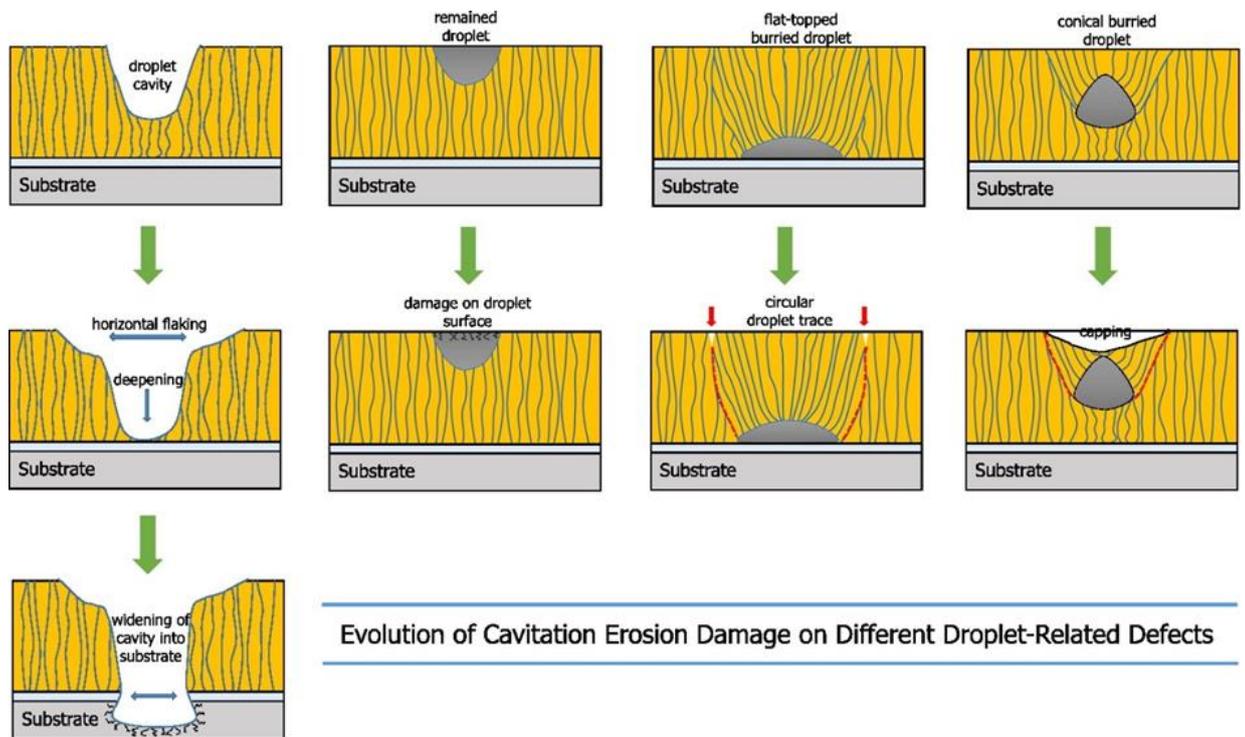
Fig. 2.22. Schematic presentation of the evolution of cavitation erosion damage on different droplet related defects [100].

In optical coatings, nodular defects were found to influence laser-induced damage [105–108]. Electric-field modelling had shown that the light intensified at the defect spots due to the geometric and interference nature of these defects [106]. Therefore, to minimise the localised damage, the defect-related absorption and hence the defect generation needs to be reduced.

All these studies suggested that coating defects deteriorate the coating properties in most cases. Thus, for improved and advanced industrial applications, such as biomedical, a detailed understanding about coating defects and their influence on coating performance is very crucial.

2.6 CrN/NbN coatings

To investigate the coating defects associated with HIPIMS, nanoscale multilayer CrN/NbN coatings are considered because these coatings have performed notably well in various applications (pump impellers, hydraulic valves, nozzles, pistons and sharp edges / cutting blades) where corrosion, oxidation and intense wear are expected [18–20]. Thus, in recent years, CrN/NbN coatings have become potential candidates for industrial applications [14,17,18].

Due to the high hardness, good wear resistance and anticorrosive properties, PVD CrN/NbN multilayer coatings have already substituted the electroplated hard chromium and PVD monolithic CrN [14,82]. Table 2.1 represents the properties of CrN/NbN coatings deposited by various techniques.

However, studies on arc-PVD CrN/NbN showed that the droplet related defects can deteriorate the corrosion performances of the coatings [7,14]. To prevent droplet formation, HIPIMS has been used. These recent studies demonstrated the benefits of using HIPIMS over conventional PVD to deposit CrN/NbN coatings [18,102]. HIPIMS etched and HIPIMS/UBM deposited (H-H) CrN/NbN coating exhibited better corrosion resistance as compared to the H-U (HIPIMS etched and UBM deposited) and ABS (arc etched and UBM deposited) coatings (Fig. 2.23) [102].

During erosion–corrosion analysis, the volume loss of H-H coating was found to be the lowest (Fig. 2.24) [18].
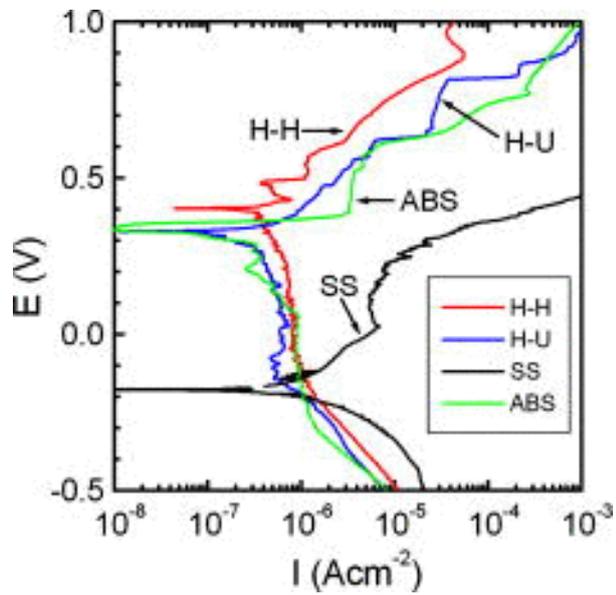
Fig. 2.23. Potentiodynamic polarization curves for the H-H, H-U, ABS coating, and uncoated SS polarized from -1000 to +1000 mV in a 3 % NaCl solution aerated for 25 min [102].
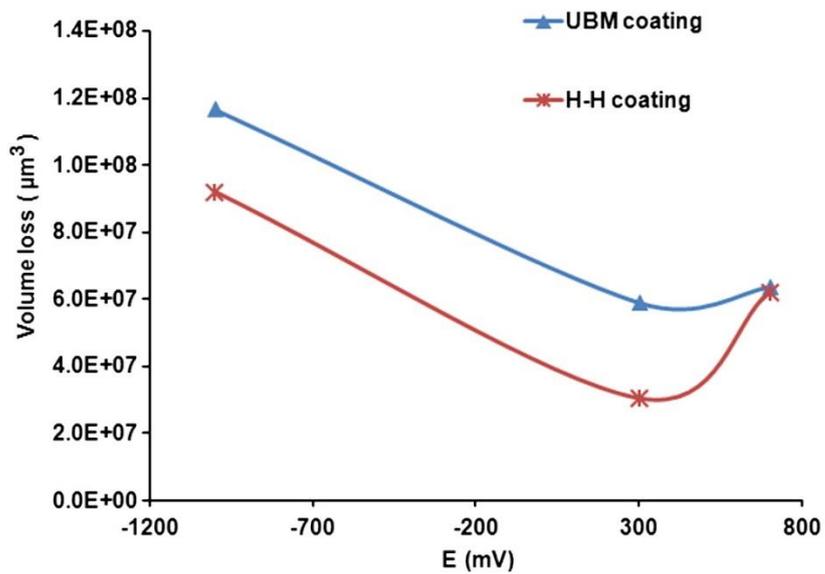
Fig. 2.24. Volume loss measured for nanoscale CrN/NbN multilayer coated substrates at different electrochemical potentials [18].

Nevertheless, the friction coefficient and wear rate of H-H coating were significantly lower than the H-U and ABS coatings [102]. The lower number of intercolumnar voids in the H-H case improved the tribological properties of the H-H coating over H-U and ABS coatings.

None of the studies mentioned the influence of defects in CrN/NbN coatings deposited using HIPIMS. However, it is important to study the formation of defects and their influence on the overall coating performance for advanced coating applications. To the best of our knowledge, there are very few literatures available on the defects associated with HIPIMS coatings. The present research investigates the effects of defects on HIPIMS deposited CrN/NbN coatings.

Ref	Deposition Process	Temp. (°C)	Deposition Time (min)	Bias Voltage (V)	Pressure (Pa)	Thickness (μm)	Crystal Structure	Hardness	Corrosion / Corrosion-erosion	Tribological properties	
										Friction	Wear
[20]	ABS +UBM, Cr-ion pre-etching (mentioned as CN45)	400	150	-75	0.31 to 0.38	4.23	FCC	3400 kgmm^{-2}	Pitting potentials was higher up to 500 mV compared with 304L steel substrate.		
[19]	ABS + UBM, Cr-ion pre-etching (mentioned as coating 1)	400	150	-75	0.35	6.6	FCC	3580 HK	Pitting potential (mV) was 230 mV in acetate buffer solution, pH 4.5 (where 30 mV was for 304L steel substrate).		

Ref	Deposition Process	Temp. (° C)	Deposition Time (min)	Bias Voltage (V)	Pressure (Pa)	Thickness (µm)	Crystal Structure	Hardness	Corrosion / Corrosion-erosion	Tribological properties	
										Friction	Wear
[7,109]	ABS + UBM (Ring samples, 32 mm o.d, 2 mm wall thickness, 10 mm height)		150		N₂, partial pressure of 0.11 to 0.18	5			Compared with the uncoated substrate, the coated sample had lower corrosion current values in 3.5% NaCl solution.		
[110]	UBM, special ion pre-treatment			-75		3.5		2700 Hv	Passivating current densities was lower than the uncoated substrates. The relative protection was dependent on the impact angle.		

Ref	Deposition Process	Temp. (°C)	Deposition Time (min)	Bias Voltage (V)	Pressure (Pa)	Thickness (μm)	Crystal Structure	Hardness	Corrosion / Corrosion-erosion	Tribological properties	
										Friction	Wear
[111]	UBM, special ion pre-treatment			-95		3		2488 HK, 25 GPa	The substrate surface appeared more damaged than the coated surface for all the potentials and impact angles.		
[112]	UBM			-120		4.5	FCC	33.3 GPa	The least corrosion resistance was provided by the UBM coating	0.95	9.2×10^{-15} $m^3N^{-1}m^{-1}$
	ABS			-100		5.8		35.3 GPa		0.3	6.2×10^{-15} $m^3N^{-1}m^{-1}$
	ARC			-120		4.5		36.3 GPa		0.9	5.0×10^{-15} $m^3N^{-1}m^{-1}$

Ref	Deposition Process	Temp. (°C)	Deposition Time (min)	Bias Voltage (V)	Pressure (Pa)	Thickness (μm)	Crystal Structure	Hardness	Corrosion / Corrosion-erosion	Tribological properties	
										Friction	Wear
[14]	ABS	250		-75		3.5	FCC	51 GPa	Increases in the bias voltage from -75 V to -95 V resulted in lower corrosion current density and higher pitting potential. The corrosion resistance of coatings were superior to the 304 steel substrate.		
				-95		3.25		69 GPa			

Ref	Deposition Process	Temp. (°C)	Deposition Time (min)	Bias Voltage (V)	Pressure (Pa)	Thickness (μm)	Crystal Structure	Hardness	Corrosion / Corrosion-erosion	Tribological properties	
										Friction	Wear
[83]	Reactive cathodic arc deposition	350		-160	N_2 pressure of 3	3.6	FCC	1690 HV_{50}, 35 GPa			Rotating wheel → 9107 $\mu m^3 N^{-1} mm^{-1}$ Ball-cratering → 290 $\mu m^3 N^{-1} mm^{-1}$
[94]	CFUBMS			-60, -100, -200				Samples with highest bias were hardest (~35 GPa).			

Ref	Deposition Process	Temp. (° C)	Deposition Time (min)	Bias Voltage (V)	Pressure (Pa)	Thickness (µm)	Crystal Structure	Hardness	Corrosion / Corrosion-erosion	Tribological properties	
										Friction	Wear
[84]	UBM deposition with a) Nb HIPIMS pre-treatment, b) Nb HIPIMS pre-treatment + Nb interlayer by HIPIMS, c) Nb CA pre-treatment + Nb interlayer by CA	400		-75	0.4	4	FCC	Hardness values were similar for all three coatings	Coating (b) showed high capability to protect the M2 HSS substrates		

Ref	Deposition Process	Temp. (°C)	Deposition Time (min)	Bias Voltage (V)	Pressure (Pa)	Thickness (µm)	Crystal Structure	Hardness	Corrosion / Corrosion-erosion	Tribological properties	
										Friction	Wear
[18]	HIPIMS					3.9	FCC	3526 ± 30 $HK_{0.25N}$, 34 ± 4.2 GPa	HIPIMS deposited coatings exhibited enhanced wear, erosion,corrosion and hence erosion–corrosion resistance compared with the UBM deposited coatings (Fig. 2.24).	0.46	1.22×10^{-15} $m^3N^{-1}m^{-1}$
	UBM							3049 ± 67 $HK_{0.25\,N}$, 31 ± 6.6 GPa		0.90	4.06×10^{-15} $m^3N^{-1}m^{-1}$

Ref	Deposition Process	Temp. (°C)	Deposition Time (min)	Bias Voltage (V)	Pressure (Pa)	Thickness (μm)	Crystal Structure	Hardness	Corrosion / Corrosion-erosion	Tribological properties	
										Friction	Wear
[102]	a) H-H (HIPIMS pre-treatment + HIPIMS/UBM deposition)	400		-75 V.		2.9	FCC	3025 HK$_{0.025}$	The coatings deposited by the H-H technique demonstrated better corrosion resistance as compared to the H-U and ABS coatings (Fig. 2.23).	0.32	1.8×10^{-15} m^{3}N^{-1}m^{-1}
	b) H-U (HIPIMS pre-treatment + UBM deposition)					4.2		2725 HK$_{0.025}$		0.46	3.0×10^{-15} m^{3}N^{-1}m^{-1}
	c) ABS					3.6		3300 HK$_{0.025}$		0.63	2.2×10^{-15} m^{3}N^{-1}m^{-1}

Ref	Deposition Process	Temp. (°C)	Deposition Time (min)	Bias Voltage (V)	Pressure (Pa)	Thickness (μm)	Crystal Structure	Hardness	Corrosion / Corrosion-erosion	Tribological properties		
										Friction		Wear
[113]	Cathodic arc, Rotation of substrate holder was varied					20 – 25	FCC	~ 3200 HV $\Delta = 4$ nm, ~ 2000 HV at $\Delta = 20$ nm		Low for $\Delta \leq 10$ nm. Highest at $\Delta = 20$ nm.		
[114]	PVD technique using magnetron sputtering	450				2.7	FCC	24 ± 3 GPa		Against Al$_2$O$_3$	0.01	2.6×10^{-7} mm^{3}N^{-1}m^{-1}
										Against 100Cr6	0.17	8.2×10^{-7} mm^{3}N^{-1}m^{-1}
										Against SiC	0.3	3.4×10^{-7} mm^{3}N^{-1}m^{-1}

Ref	Deposition Process	Temp. (°C)	Deposition Time (min)	Bias Voltage (V)	Pressure (Pa)	Thickness (μm)	Crystal Structure	Hardness	Corrosion / Corrosion-erosion	Tribological properties	
										Friction	Wear
[115]	CAPVD, Rotation of substrate holder was varied					15		~ 3200 HV at Δ = 4 nm ~ 1900 HV at Δ = 22 nm			
[116]	HIPIMS a) Low Nb-CrN/NbN #46 b) High Nb-CrN/NbN #46 c) High Nb-CrN/NbN #1000	400		-65		10 & 6	FCC		Thermogravimetric studies showed that in high temperature steam atmosphere all coatings had significantly higher corrosion resistance compared to the P92 steel substrate.		

Ref	Deposition Process	Temp. (°C)	Deposition Time (min)	Bias Voltage (V)	Pressure (Pa)	Thickness (μm)	Crystal Structure	Hardness	Corrosion / Corrosion-erosion	Tribological properties	
										Friction	Wear
[117]	PVD	200	180	-75	Ar : N$_2$ 25 : 6	1.3	FCC	28 GPa	CrN/NbN coating showed best corrosion resistance compared to CrAlTiN-coated and bare 304 SS samples. **COR (mm/year)** 2.688×10^{-3} - CrN/NbN 2.691×10^{-2} - CrAlTiN 3.23×10^{-1}- 304 SS	stable values between 0.5 and 0.55 (where it was 0.64 for bare 304 SS samples)	4.32 mm^3/m (where it was 6.65 mm^3/m for bare 304 SS samples)

Ref	Deposition Process	Temp. (°C)	Deposition Time (min)	Bias Voltage (V)	Pressure (Pa)	Thickness (μm)	Crystal Structure	Hardness	Corrosion / Corrosion-erosion	Tribological properties	
										Friction	Wear
[118]	UBM Cr:Nb:N was varied from 5.5:0:4.5 to 0:5.5:5.5			- 40		3	FCC	19.5 to 28 GPa		0.6 to 1	0.18 to 2.07 mm^3/m (maximum was for Cr:Nb:N = 0.5:4:5.5)
[119]	PVD + MPII *Not CrN/NbN coating, Nb ions were implanted into CrN PVD coating using MPII								After the Nb implantation, the I_{corr} value decreased from 1 $\times 10^{-7}$ to (2–3) $\times 10^{-8}$ Acm^{-2}		

Table 2.1. Properties of CrN/NbN coatings deposited by various processes.

3 Methodology

This chapter consists of two sections. Section 3.1 presents the specimen preparation procedures prior to the coating deposition and the coating deposition sequence. In section 3.2, coating characterisation techniques are described.

3.1 Specimen preparation and coating deposition

3.1.1 Substrate materials, specimen preparation

Substrate materials: 304 stainless steel (SS), M2 high speed steel (HSS) and Si wafer were used as the substrate materials. Table 3.1 represents the dimensions of these substrates and the tests for which they were used.

Substrate	Dimension	Test
304 stainless steel	ø 30 mm × 6 mm	XRD, SEM, AFM, Optical microscopy, Profilometry, Potentiodynamic polarisation, Raman.
M2 high speed steel	ø 30 mm × 6 mm	Nanohardness, Pin on disc, Raman, SEM, Optical microscopy.
Silicon wafer	15 mm × 5 mm × 0.3 mm	SEM.

Table 3.1. Substrate materials used for various tests and analytical methods.

Specimen preparation: The stainless steel and high-speed steel disks were ground with grit paper and then polished to a mirror finish using 1 μm diamond paste. Prior to the deposition process, the polished disks and the silicon wafers were cleaned in an automated ultrasonic cleaning line with industrial detergents (alkaline cleaning agents from Borer chemicals) to remove surface contaminants. Finally, all substrates were washed with de-ionized water, followed by drying in a heated vacuum dryer. After drying, samples were loaded into the PVD unit chamber immediately. This substrate cleaning is a very important part of the whole process because any kind of residual dust, dirt can lead to defect generation during coating growth.

3.1.2 Deposition technique and system geometry

The substrates were coated in an industrial sized machine (Hauzer 1000 four sources PVD system) at Sheffield Hallam University (Fig. 3.1). The machine has a chamber size of 1 m^3 with four rectangular planar targets (sized 600 x 200 mm). The system is fitted with a 250 m^3/h roots pump and a 500 m^3/h rotary vane pump, in addition to two Blazers TPH 2200 turbo molecular pumps used to evacuate the chamber. The machine is equipped with two HIPIMS power supplies (Hüttinger Elektronik Sp. z o.o., Warsaw, Poland), a dedicated bias power supply and active arc suppression units on cathode and substrate bias supplies. There is a sample holder carousel in the centre of the chamber which can operate with one-, two- or three-fold orbital rotational motion (Fig. 3.2). The machine is heated using two heaters located on the inside wall of the chamber doors, in between targets 1 and 2, and the other between targets 3 and 4. The system's doors and cathodes are water cooled during operation. Gas inlets allow the use of Ar as a sputtering medium, and N$_2$ as reactive gas during deposition.

Fig. 3.1. Hauzer 1000 four source PVD system.
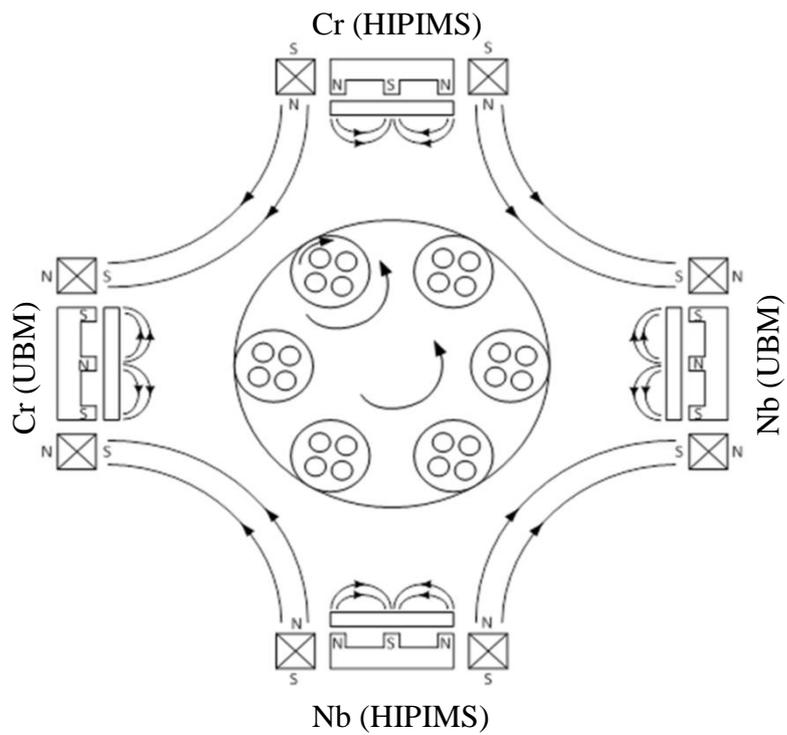
Fig. 3.2. Schematic cross section of the chamber of Hauzer 1000 four source PVD

system.

3.1.3 Deposition Process Sequence

3.1.3.1 Evacuation of the Chamber

In order to deposit coatings with a low level of impurities, it is necessary to evacuate the chamber to a relatively low pressure. The chamber was evacuated into two stages. First, the pressure was reduced to 8 Pa using the roots and rotary vane pumps. The final pressure of 7.5×10^{-3} Pa was obtained using turbo molecular pumps.

3.1.3.2 Heating

During processes, the temperature was maintained at 200 °C. Heating causes out-gassing of components within the chamber and thus increases the pressure. For these reasons, the chamber was heated up for a few hours before the deposition process commenced.

3.1.3.3 Target Cleaning

To sputter out the impurities and the contaminations from target surfaces, high cathode voltages were applied to the targets in an Ar atmosphere (with constant flow of 200 sccm). The targets were sputtered in two steps of 5 minutes, increasing the voltage in the second step. During this step, the shutters were placed in front of the targets to protect the substrates from impurities.

3.1.3.4 Metal Ion etching

Prior to the coating deposition, the substrate surfaces were pre-treated with a HIPIMS plasma discharge enriched with Cr ions. In this step, the substrate surfaces are bombarded with highly energised positive ions by applying high bias voltage of - 1200 V to the substrate. These bombardments remove the impurities which could not be removed during the sample cleaning process. Nevertheless, some metal ions are

implanted into the substrate during the process. Both surface cleaning and implantation improve the adhesion of the coating with the substrate [45].

3.1.3.5 Deposition of coatings

The multilayer coatings were deposited using all four targets in UBM or HIPIMS and UBM combination modes in a gas mix of Ar and N_2. In section 3.1.4, the deposition processes are described in detail.

3.1.3.6 Cooling down and venting the chamber

Before venting, the chamber was allowed to cool down to room temperature.

3.1.4 Deposition of CrN/NbN coating

3.1.4.1 HIPIMS/UBM coating

CrN/NbN nano-structured multilayer coatings were deposited using the combined HIPIMS/UBM technique. During this nanoscale multilayer coating deposition step, one Cr and one Nb target were operated in HIPIMS mode, while the other two targets (1 Cr and 1 Nb) were operated in UBM mode. The machine was operated in constant power mode and the average power on the individual cathode was maintained at 8 kW irrespective of the technology (UBM or HIPIMS). Rectangular pulses of 200 µs at a frequency of 100 Hz, with a duty cycle of 1 % were employed to generate the HIPIMS plasma for coating deposition. During depositions, Ar and N_2 (1:1) were used as the process gas. The deposition temperature was maintained at 200 °C. Three sets of coatings were deposited by varying deposition parameters, namely deposition time (t), bias voltage (U_b) and chamber total pressure (P). The details of the deposition

conditions are given in the table 3.2. For each set, coatings were produced by varying one parameter while other two parameters were kept fixed.

Coating	Varied Parameter	Fixed Parameters
Set 1	t = 0, 15, 30, 60, 120 min	U_b = - 65 V, P = 0.35 Pa
Set 2	U_b = - 40, - 65, - 100, - 150 V	t = 120 min, P = 0.35 Pa
Set 3	P = 0.2, 0.35, 1 Pa	t = 120 min, U_b = - 65 V

Table 3.2. Process parameters for HIPIMS/UBM CrN/NbN coating deposition.

3.1.4.2 UBM coating

During pure UBM coating deposition, all four targets were operated in UBM mode with 8 kW cathode power applied on each of them. The maximum deposition time for the coating was 100 min. During this process, the deposition temperature and chamber pressure were maintained at 200 °C and at 0.35 Pa respectively.

In this work, properties of the coatings deposited by HIPIMS/UBM and pure UBM coating are studied. Table 3.3 represents the process parameters for HIPIMS/UBM and pure UBM coatings which are compared in the result section 4.5.

Deposition technique	Deposition time (t) in min	Bias voltage (U_b) in V	Chamber total pressure (P) in Pa
HIPIMS/UBM	120	- 65	0.35
Pure UBM	100	- 65	0.35

Table 3.3. Process parameters for CrN/NbN coatings deposited by HIPIMS/UBM and pure UBM technique.

3.2 Characterisation Technique

3.2.1 X-Ray Diffraction Analysis

X-ray diffraction (XRD) technique is a non-destructive characterisation technique. This technique was used to determine the crystallographic structure and bilayer thickness of the deposited coatings.

Wavelengths of x-rays are approximately in the same range as the inter atomic spacing. When x-rays pass through a crystal, they are scattered in all directions by the electrons associated with each atom or ion that lies within the beam's path [120]. The scattered x-rays can interfere with each other and the resultant intensity distribution is modulated by this interaction. If the scattered x-rays are in phase, constructive interference occurs. In 1912, W. L. Bragg gave a relation which elucidates the condition for constructive interference. In that case, path length difference between two consecutive x-rays is equal to a wavelength (λ) or an integer number of wavelengths which is summarised in the following equation (Eq. 3.1).

$$n\lambda = 2d_{hkl}\sin\theta \qquad \text{Eq. 3.1}$$

This equation is called the Bragg's equation for X-ray diffraction. Here n is the order of reflection, λ is the wavelength, θ is the angle of diffraction and d_{hkl} is the interplanar spacing.
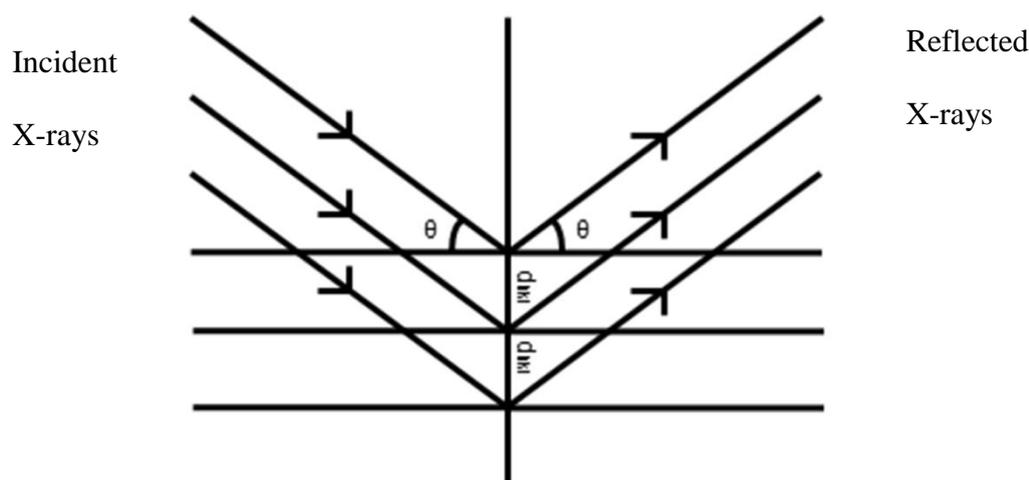
Fig. 3.3. A schematic drawing of X-rays scattering from the planes of atoms.

For practical reasons, the diffractometer measures an angle twice that of the θ angle. In diffractometers, the X-ray wavelength (λ) is fixed. Consequently, a family of planes produce a diffraction peak only at a specific angle θ.

In this study, a PANalytical Empyrean PIXcel 3D automated diffractometer in 2θ Bragg–Brentano (BB) and Glancing Angle (GA) beam geometry were used to determine the crystal structure configuration. The scanning range for BB XRD was selected as $2\theta = 20°$ to $120°$ with a step size of $0.26°$. For GA XRD the incident angle was fixed at $2°$ over a scanning range of $2\theta = 20°$ to $100°$ with a step size of $0.006°$. The

GA XRD technique is a convenient method for stress analysis and phase identification studies in the case of the nanostructured coatings. Due to the reduced penetration depth of the X-rays in GA geometry, the contribution related to the substrate is eliminated in comparison to standard X-ray diffraction [121]. In this geometry, the incidence angle (α) is fixed at typically between 1° and 3°. The angle between the incident beam and the diffracted beam (2θ) is varied, moving only the detector position. Thus, the incident beam penetrates shallow but gains information from a significant proportion of the coating which reinforces the diffraction pattern. The Miller indices for all the phases present in both the BB and GA XRD patterns were calculated by X'Pert HighScore Plus Software.

To measure the bilayer thickness (Δ) of the coating, BB XRD technique with low-angle (LA) geometry was used. The selected scan rage was 2θ = 2° - 10°. Using standard Bragg's law, the bilayer thickness was calculated.

$$\Delta = n\lambda/\ 2\sin\theta \qquad \text{Eq. 3.2}$$

For all the experiments, monochromatic Cu-Kα radiation with a wavelength of 1.5406 nm was used as the X-ray source. The voltage and current of the X-ray generation tube were 45 kV and 40 mA respectively.

3.2.2 Microstructural study of coating surface and defects

Scanning Electron Microscope (SEM) and Atomic Force Microscope (AFM) were used to study the microstructure and topography of the coating. Defect morphology was

investigated using Focused Ion Beam (FIB) and SEM. Optical Microscope was used to examine the coating surface and to quantify the defects.

3.2.2.1 Scanning electron microscopy

SEM is a widely employed coating characterization instrument. Electron beams having energies ranging from a few thousand to 50 keV, scan across the surface of the specimen. Upon impinging on the specimen, the electrons interact with the atomic electrons and then scatter due to inelastic and elastic collisions. Fig. 3.4 represents the schematic drawing of a scanning electron beam incident on a solid sample.
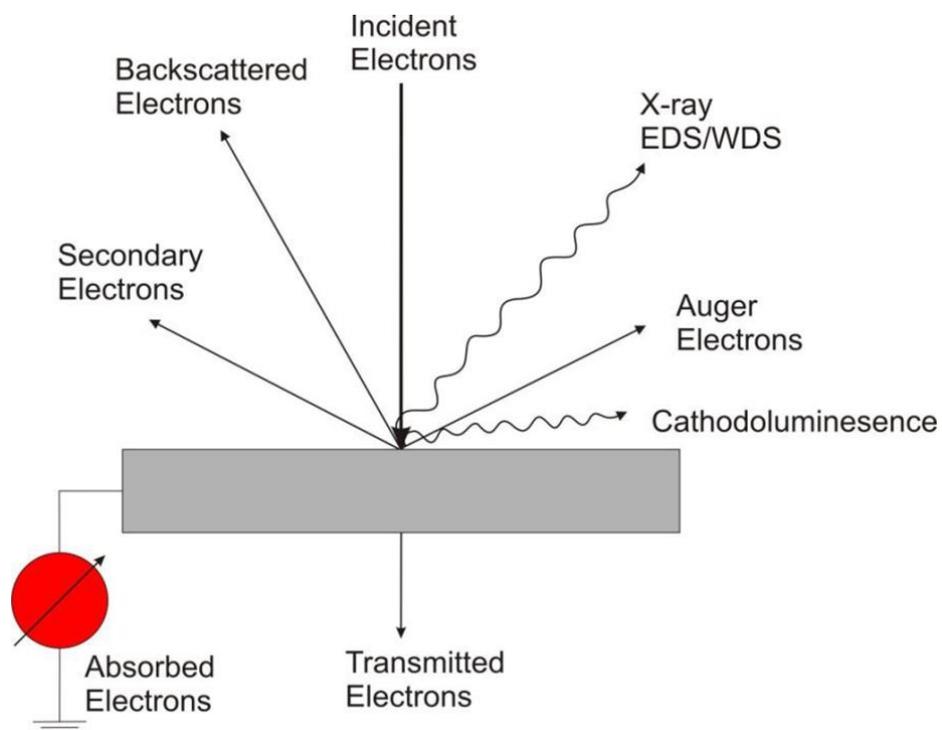
Fig. 3.4. Schematic drawing of a scanning electron beam incident on a solid sample [122].

Using a detector these deflected and emitted electrons are collected to map the topography and chemistry of a sample.

In this study, FEI-Nova NanoSEM 200 was used to capture the secondary electron (SE) images of planar and fractural cross-sectional view of the coatings. SE emission occurs due to the inelastic collisions. When an incident electron with sufficient energy collides with an atom, an electron can be ejected from that atom due to energy transfer from the incident electron. These emitted electrons have relatively low energies; therefore, only the electrons of the atoms at the surface escape from the sample and get detected. Thus, SE images provide necessary information (topography and density) about the coating surface. To capture the SE images ETD (Everhart-Thornley detector) was used at lower magnification whereas TLD (Through the Lens Detector) was used to capture images at higher magnification. The working distance was in the range of 4 to 5 mm and the beam voltage was in the range of 5 to 20 kV in the process to capture clear images.

Characteristic X-ray is generated due to the transition of electrons from a higher to a lower electron shell. The incident electron with sufficient energy can eject an inner shell electron from the specimen atom. As a result, the electron from outer shell transits to inner shell. In the process characteristic X-ray with a specific energy and wavelength is emitted. Due to this, each atom has its own characteristic X-ray radiation which can be used to identify the material composition. This characterisation technique is known as Energy Dispersive X-ray Spectrometry (EDS or EDX). Using Aztec software (OXFORD Instruments) EDX data were analysed to assess the chemical composition of the coating.

3.2.2.2 Focused Ion beam

Focused Ion beam (FIB) works in a similar fashion to SEM except it uses a finely focused beam of gallium ions rather than a beam of electrons. FIB is capable to capture images when operated at low beam currents. By applying high beam currents, it can be used for fast and precise milling of the specimen material. The milling reveals the internal structure of the coating specimen and sub-surface defects if exist. A combination of FIB and SEM, minimises any contamination effects, and produces clear, prominent images of cross sections which are sometimes not possible for fracture cross sections by conventional technique.
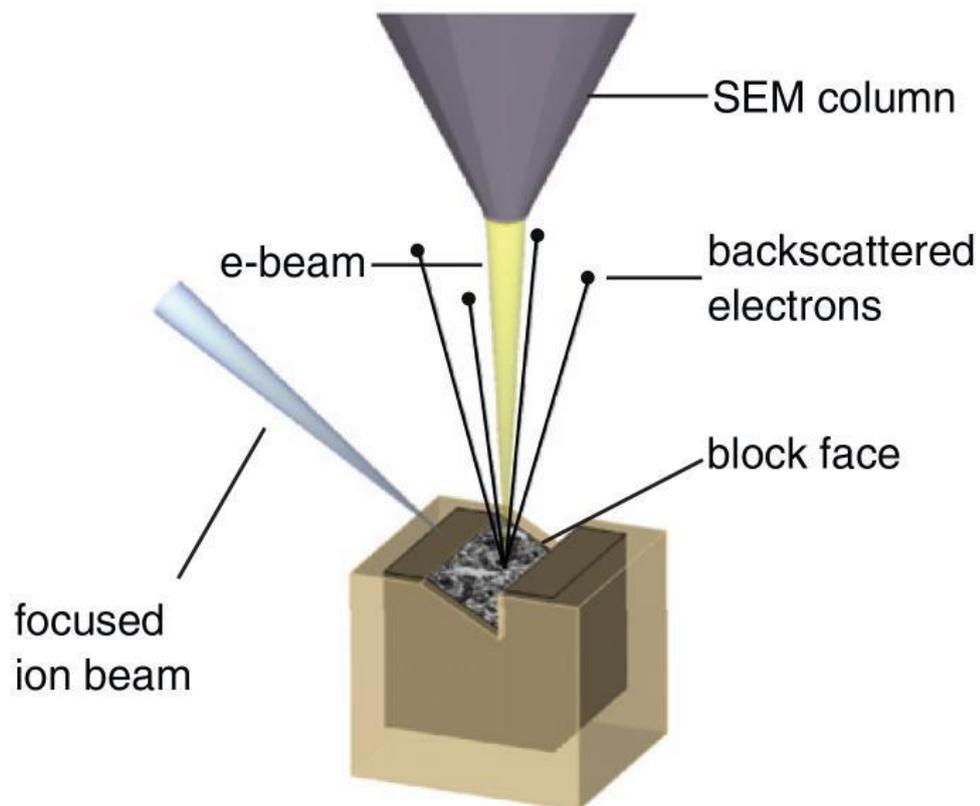
Fig. 3.5. Schematic drawing of focused ion beam milling scanning electron microscopy (FIB-SEM) [123].

In this study, FEI Quanta 650 3D Dual Beam FIB FEG-SEM was used to produce cross sections of specific growth defects on the surface and obtain high-quality images. The Quanta 3D used for this study is a combination of two systems: a focused ion beam (FIB) comprising of Gallium (Ga) ion gun system and a field emission gun (FEG). 30 kV voltage was applied during milling. After milling, ETD was used to capture the cross-sectional SEM images of the defects. The working distance was fixed at 10 mm and the applied voltage was 10 kV.

3.2.2.3 Atomic Force Microscopy

The Atomic Force Microscope (AFM) is one kind of scanning probe microscopes (SPM) [124]. A probe with a very fine sensor tip mounted on a flexible cantilever scans the surface of the sample (Fig. 3.6). The forces between the atoms on the surface of the sample and those on the tip cause the tip to deflect. The magnitude of the deflection depends on the separation between the surface atoms and the tip atoms and on the atomic forces (Van der Waals forces) between them. This deflection can be recorded in various ways, the most common of which uses a laser beam focused on the top of the cantilever and reflected onto photodetectors. The photodetector signals are used to map the surface topography of samples with resolutions down to the atomic and nanoscales. The feedback signal and position of the probe are electronically recorded to produce a three dimensional map of the sample. These AFM maps/images are suitable for further investigation of the surface such as measurement of surface roughness, analysis of particle and grain size etc. AFM can also be used to measure magnetic and electrical properties of the material [125].
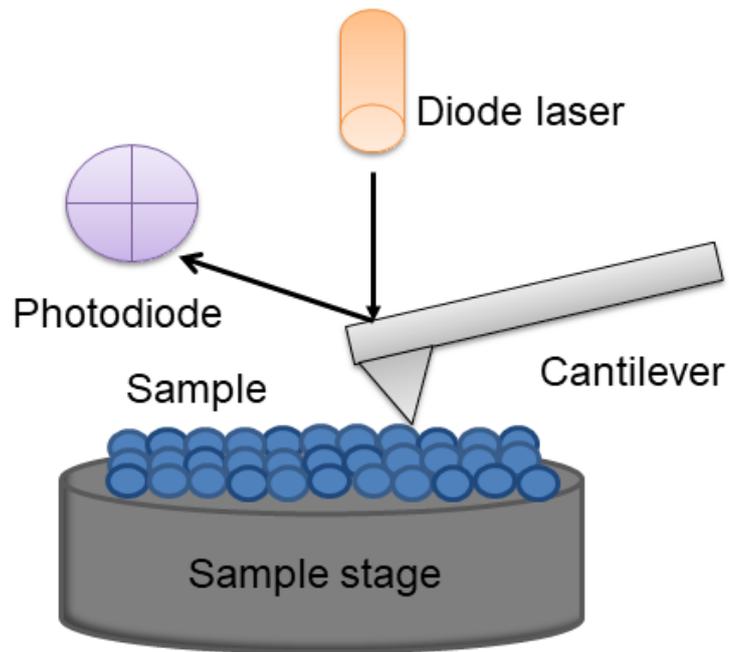
Fig. 3.6. Schematic drawing of an Atomic Force Microscope.

In this study, the Anton Paar - CSM atomic force microscope was used to examine the surface morphology. The AFM images were produced by scanning the sample surface using a silicon nitride stylus which was operated by CSM software.

3.2.2.4 Optical microscopy

An optical microscope is the primary tool to scientists and engineers for morphological characterization. It creates a magnified image of an object specimen with an objective lens and magnifies the image furthermore with an eyepiece. Microscope magnification is the multiplication of the lens magnification and the eyepiece magnification.

The resolution of a microscope is a function of its parameters and can be stated as:

$$R = \lambda / 2NA \qquad \text{Eq. 3.3}$$

Where NA = μ sin α is called the numerical aperture with μ is the index of refraction and α is the half-angle of the maximum cone of light that can enter or exit the lens. Optical microscopy is very useful for fast analysis of micro-structures and the influence of the destructive tests on the coating.

Unlike an optical microscope used for biological systems which works on transmitted light principle, the microscope for metallurgical systems is operated using the reflected light principle. Since the metal samples are non-transparent, they are illuminated by frontal lighting. Fig. 3.7 represents a schematic drawing of an optical microscope used in metallurgical study.
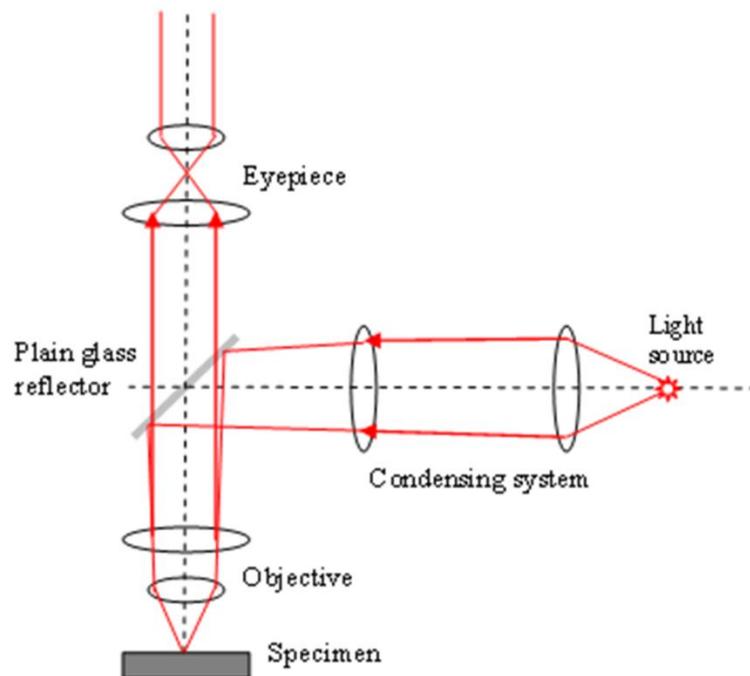
Fig. 3.7. A schematic drawing of optical microscope used for metallurgical systems [126].

To calculate **surface defect density**, a Huvitz 3D optical microscope and ImageJ software were used. In this study, surface defect density of the coating was estimated by analysing the fraction of surface area of the sample covered by the imperfections.

The optical microscope used to examine the surface of the coating was equipped with a Plan Fluor semi Apochromat optical lens with a magnification of 100 times. Then the images of the coating surfaces (130 μm × 90 μm) were captured using a digital camera at a magnification of 1000 times. Using ImageJ software, those optical microscope images were converted into black and white binary images. These conversions turned the surface defects into prominent black features with respect to the converted white background. Using the analysing tool of the software, the surface area occupied by the black features which represent the actual surface imperfection, was calculated. For each coating, this process was repeated for ten times to calculate the average surface defect density. This study was conducted to determine the effect of deposition parameters on defect formation.

3.2.3 Coating roughness measurement

The surface roughness of deposited coatings was measured by scanning a diamond stylus over the surface. The working principle of a profilometer is similar to AFM.

A contact profilometer uses a diamond stylus to measure the topological features of a sample. The stylus scans across the sample surface. Depending on the surface texture of the sample, the stylus experiences a vertical displacement which is converted into a height value in Z [127]. The mechanical movements of the stylus are then converted into an electrical signal by a transducer attached to it, and then amplified and

demodulated. Finally, the signal is passed to a computer where, by using the relevant software, it is analysed and stored.

In this study, a DEKTAK 150 was used to measure the surface roughness. The radius of the stylus was 12.5 μm and a 4 mg (39×10^{-6} N) load was applied on it during all scans. For each sample five scans were recorded. During these scans, the probe travelled a length of 1000 μm on the surface under examination with a spatial resolution of 0.033 μm and the surface roughness of the scanned profile was analysed by the associated software. Roughness values were calculated by averaging all five scans.
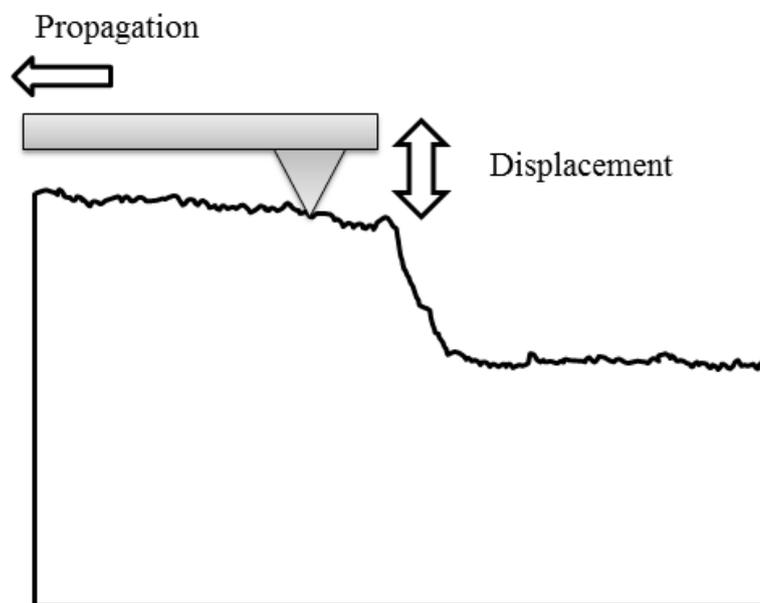
Fig. 3.8. A schematic of a profilometer tip in contact with a surface as it processes; the displacement due to the topography of the sample is recorded.

3.2.4. Nanohardness test

Hardness is a measure of the resistance to permanent deformation or damage. Young's modulus, also known as the elastic modulus, is a measure of the stiffness of a solid material.

The nanohardness and the elastic modulus of the coatings were measured using a CSM nanoindentation tester. A normal load of 20 mN was applied to the coated samples through the Berkovich diamond indenter. 15 indentations were conducted for each coating. To avoid substrate contribution, only those measurements were considered where the indentation depth was 10 % of the total coating thickness. Then the average values of nanohardness and the elastic modulus were calculated by the associated software using the Oliver and Pharr method from the resultant load–displacement curves. Fig. 3.9 shows the surface under maximum load and a typical load–displacement curve of nanoindentation test.

The necessary formulas for calculating hardness and Young's (elastic) modulus are given by

$$H = P_{max} / A(h_c) \qquad \text{Eq. 3.4}$$

$$E = \frac{1 - v_s^2}{\frac{1}{E_r} - \frac{1 - v_i^2}{E_i}} \qquad \text{Eq. 3.5}$$

Where P_{max} is the maximum load, $A(h_c)$ is the projected contact area; v_s is the Poisson's ratio of the sample, v_i is the Poisson's ratio of the indenter, E_r is the reduced modulus of the indentation contact and E_i is the Young's modulus of the indenter.
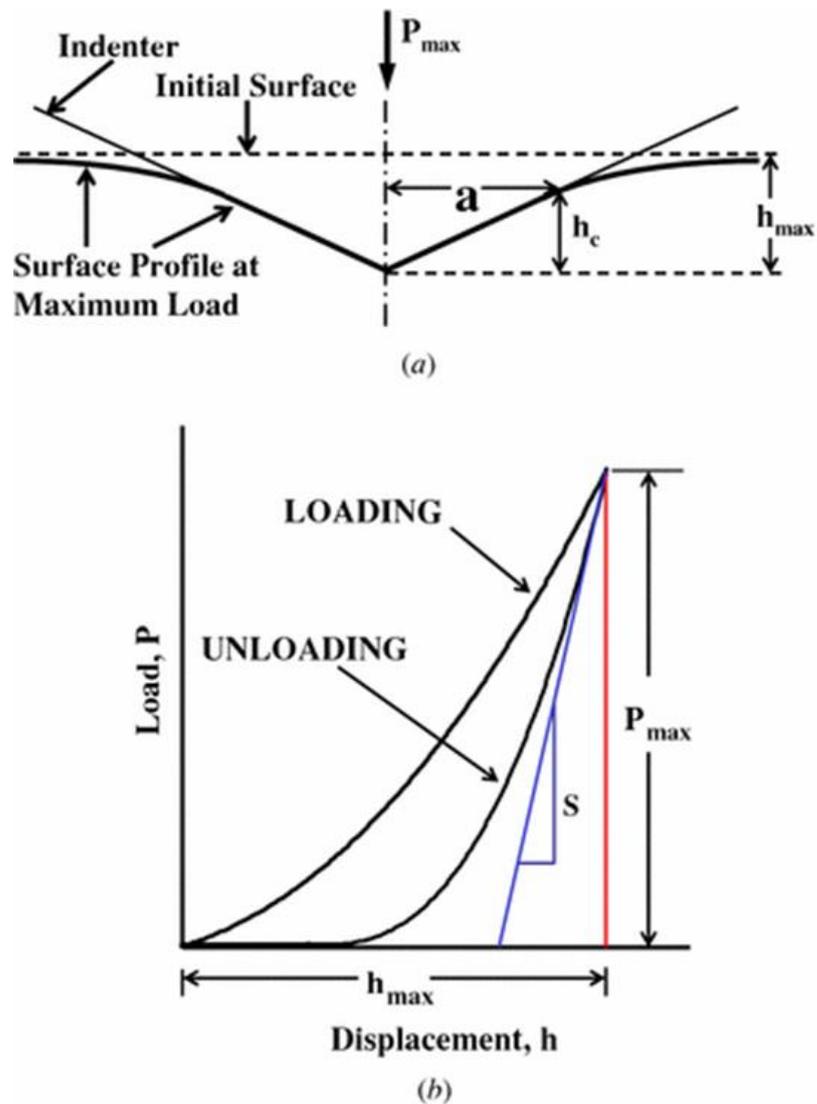
Fig. 3.9. Schematic illustrations of (a) the indentation geometry at maximum force for

an ideal conical indenter and (b) an indentation load–displacement curve [128,129].

3.2.5 Potentiodynamic polarisation corrosion test

Corrosion is based on the reaction of a metallic material or layer with its environment. The metal (M) atoms of a component change from the metallic state into an oxidized state. The driving force of this process has the tendency to lower the free energy of the system [130].

In the corrosion process, two types of reactions take place. In one type of reaction which is called anodic reaction (Eq. 3.6) metal atoms transform to ions by losing n number of electrons. In the other type of reaction, those free electrons are consumed by H_2, O_2 and H_2O. These reactions are known as cathodic reactions (Eq. 3.7, 3.8 and 3.9).

$$M \rightarrow M^{n+} + ne^- \qquad \text{Eq. 3.6}$$

$$H^+ + e^- \rightarrow H \qquad \text{Eq. 3.7}$$

$$2\,H \rightarrow H_2 \qquad \text{Eq. 3.8}$$

$$2\,H_2O + O_2 + 4e^- \rightarrow 4OH^- \qquad \text{Eq. 3.9}$$
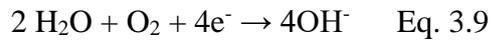
Equations 3.7 and 3.8 represent a two-step process in which hydrogen gas is formed. Hydrogen ions (H^+) are always present in water to a greater or less extent and therefore these two reactions (Eq. 3.7 and 3.8) are always possible. The reaction presented by the Eq. 3.9 depends upon the level of dissolved oxygen in solution. When the level of dissolved oxygen varies locally in a corrosion cell, differential-aeration corrosion may result [130].

When a sample is immersed in a corrosive solution in the absence of electrical connections, a potential relative to a reference electrode is generated due to the electrochemical reactions at the sample solution interface. This potential is called electrochemical corrosion potential (E_{corr}) which is also referred as 'open circuit potential'. At E_{corr} the rates of anodic reaction and cathodic reaction are exactly equal thus the net current flow is zero. The corrosion potential is a characteristic of the

specific sample-solution system since it is determined by the specific chemistry of the system.

As seen from the Eq. 3.5, the surface mass affected by a corrosion process is directly proportional to the generation of electrons. Thus, by measuring the flow of electrons, i.e. current, the corrosion activity (rate) at the sample can be obtained. The critical potential above which the current density increases suddenly is termed as pitting potential (E_{pit}). The damage in coating (pitting) can expose fresh metallic substrate surface and enhance the electrochemical reaction kinetics. Pitting can also occur at a potential below E_{pit} but those pits are metastable [131]. However, the pitting observed above E_{pit} is stable which continues to grow in a destructive fashion and results in a continuous increase in current density.

Fig. 3.10 shows a schematic diagram of wet corrosion cell used for the laboratory tests. This corrosion test involves three types of electrodes: a working electrode, a reference electrode, and two auxiliary electrodes. In this system, the coated sample represents the working electrode. For potentiodynamic experiments, the applied potential on the working electrode is increased with time and corresponding change in the current is constantly monitored.
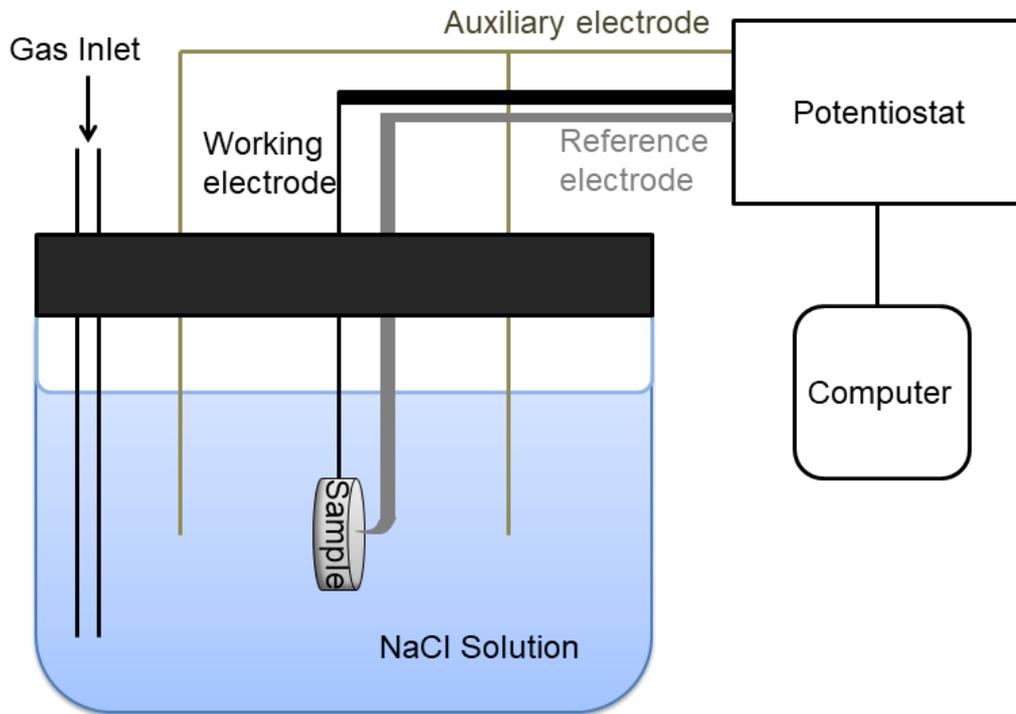
Fig. 3.10. A schematic drawing of a corrosion cell.

Fig. 3.11 represents a schematic "potential vs log current density (E/log i) plot" for a metal sample in a corrosive solution. This plot is known as potentiodynamic polarisation curve. In this plot, AB represents cathodic behaviour and B is the electrochemical corrosion potential. In the range BC, the metal is passive. Such a situation is regarded as exhibiting resistance to localised corrosion because the metal is well protected by its passive film [130]. In this passive zone, the current density is maintained at low and steady level, until breakdown of the protective film begins at C. This potential is called the breakdown potential. It is also known as pitting potential because at C, the pitting activity is likely to be the highest [130]. At potentials more positive than C, the current density begins to rise because more pits propagate. However, the current density can also increase due to the new anodic processes rather

than because of the pitting. In that situation the region CD is called transpassive region [130].
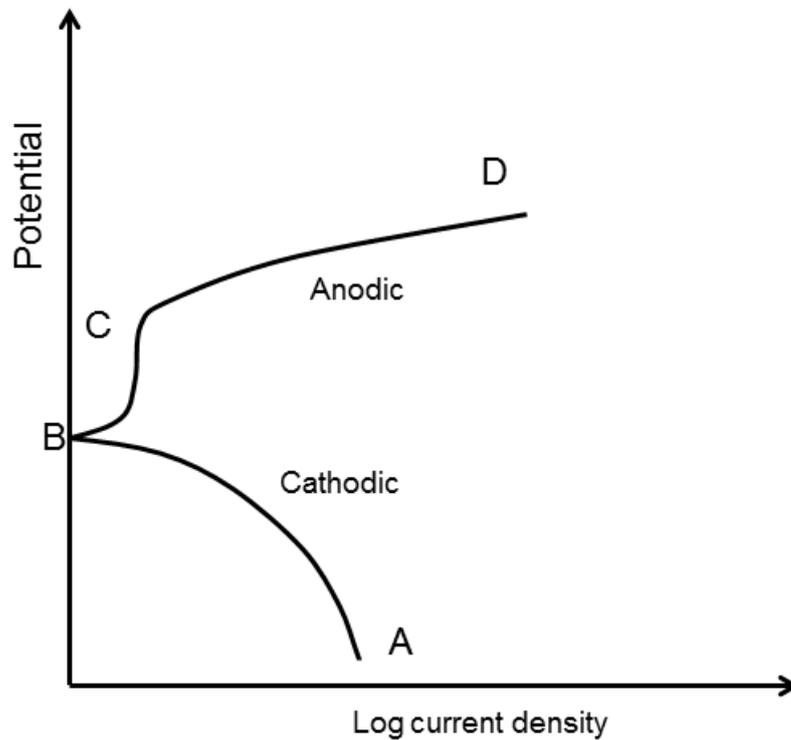
Fig. 3.11. An example of potentiodynamic polarisation curve showing stable passivity (after ref [130]).

The corrosion behaviour of the CrN/NbN coating was examined using a Gill AC Potentiostat. A saturated calomel electrode (SCE) was used as the reference electrode. At room temperature (25 °C), all the electrochemical experiments were conducted by polarising the sample from - 1000 mV to + 1000 mV at a scan rate of 0.5 mV per sec in 3.5 % NaCl solution. The exposed surface area of the coated CrN/NbN 304 stainless steels was 1 cm^2. The aim of these measurements was to study the role of coating defects on the corrosion resistance of the coatings.

3.2.6 Pin-on-disc test

The friction and sliding wear coefficients are important mechanical properties of the coating. Friction is the resistance to motion which occurs when one solid body slides over another [132]. The resistive force, which acts in a direction directly opposite to the direction of motion, is known as the friction force. Amonton's second law states that the friction force (F) is proportional to the normal load (W). Hence

$$F = \mu W \qquad \text{Eq. 3.10}$$

Where μ is the constant of proportionality and is known as the coefficient of friction. The value of μ depends on various factors, such as the intrinsic properties of the materials involved, operating conditions, sliding speed, load and lubricant.

Wear is defined as the progressive loss of substance from the operating surfaces as a result of relative motion. Tribological processes involve different kinds of wear. Most commonly referred wear mechanisms are: (1) adhesive wear, (2) abrasive wear, (3) surface fatigue and (4) corrosive wear [132].

1. Adhesive wear: When two surfaces are loaded together, they can adhere over some parts of the true contact area, to form friction junctions. If the relative sliding needs to take place, these junctions have to be broken. This wear mechanism is known as adhesive wear. Surface topography plays an important role in adhesive wear in the sense that the smoother are the surfaces, fewer are the interactions between them.

2. Abrasive wear: The term 'abrasive wear' covers two types of situations, which are known as two-body abrasion and three body abrasion. In two-body abrasion, a rough

surface slides against a relatively soft opposing surface, whereas in three body abrasion rough hard particles trapped between the two sliding surfaces cause one or both of them to be abraded.

3. Surface fatigue: Surface fatigue is associated with the formation of fatigue cracks due to repeated elastic and plastic deformations.

4. Corrosive wear: Corrosive wear is the removal of material due to electrochemical reactions.

To study the friction and wear behaviour of the deposited coatings in dry sliding condition, a CSM (Anton Paar) room temperature pin-on-disc tribometer was used. The tribometer consists of a stationary ball as counterpart, which slides against the coated disc sample clamped to a rotating sample holder under the influence of a static load. The ball is mounted in contact with the rotating sample via an elastic arm which can move laterally and therefore measure the tangential forces (friction) between sample and ball with a sensor [133].

The rotation of the disc creates a circular scar on the surface known as the wear track. The linear speed of rotation was fixed at 0.1 ms^{-1}. Al$_2$O$_3$ balls each of 6 mm diameter were used as counterpart. For all the experiments, the number of cycles was fixed at 20000 cycles and a 5 N load was used to measure the friction rates. The room temperature and the relative humidity recorded for the experiments were 25 °C and 15 % respectively. After the test, the wear coefficient (K$_C$) was calculated using Archard's equation, given by

$$K_C = \frac{F_N}{V \times d} \qquad \text{Eq. 3.11}$$

Where V is wear volume in m^3, F_N is normal load in Newtons and d is the sliding distance in meters.

The wear volume V was calculated as

$$V = 2\pi RA \qquad\qquad \text{Eq. 3.12}$$

Where R stands for wear track radius and A is cross-sectional area of the wear track. A Veeco Dektak 150 surface profilometer was used to measure R and A after the test.
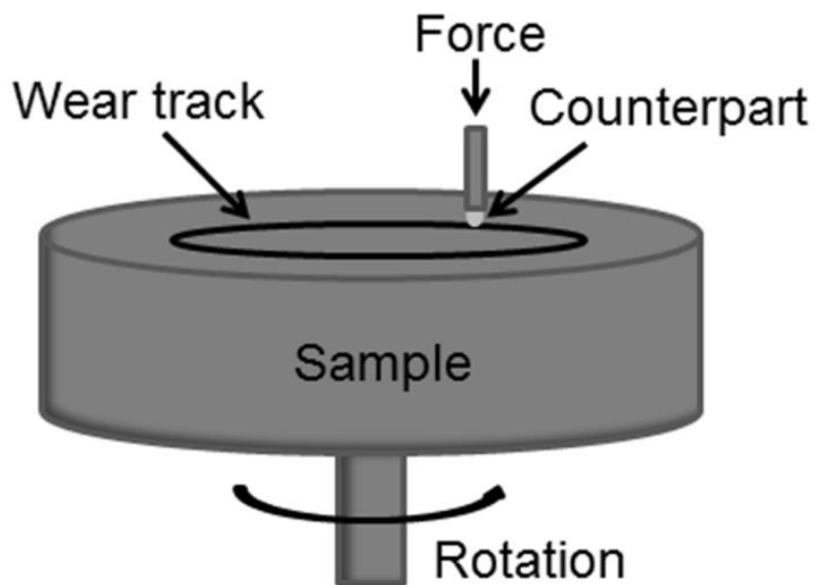
Fig. 3.12. A schematic drawing of pin-on-disk test

3.2.7. Raman spectroscopy

Raman spectroscopy was used to investigate the chemistry of the tribolayer formed during sliding. This technique is based on the 'Raman scattering' which is defined as the

inelastic scattering of a photon by the atoms of the samples [134]. The shift in the wavelength of photon radiation due to this inelastic scattering provides the chemical and structural information of the samples. Depending on the interaction between photon and atoms, the energy of the scattered photon can be higher or lower than the energy of the incident photon. Fig. 3.13 represents a simplified energy diagram of Raman scattering. If the energy of the scattered photon is lower than the energy of the incident photon, the scattering is called Stokes scattering. On the other hand, if the energy of the scattered photon is higher than that of the incident photon, the scattering is called Anti-Stokes scattering. Some of the incident photons do not interact with the atoms of the sample. Thus, they scatter from the sample with the same wavelength as the original incident wave. This is called Rayleigh scattering.
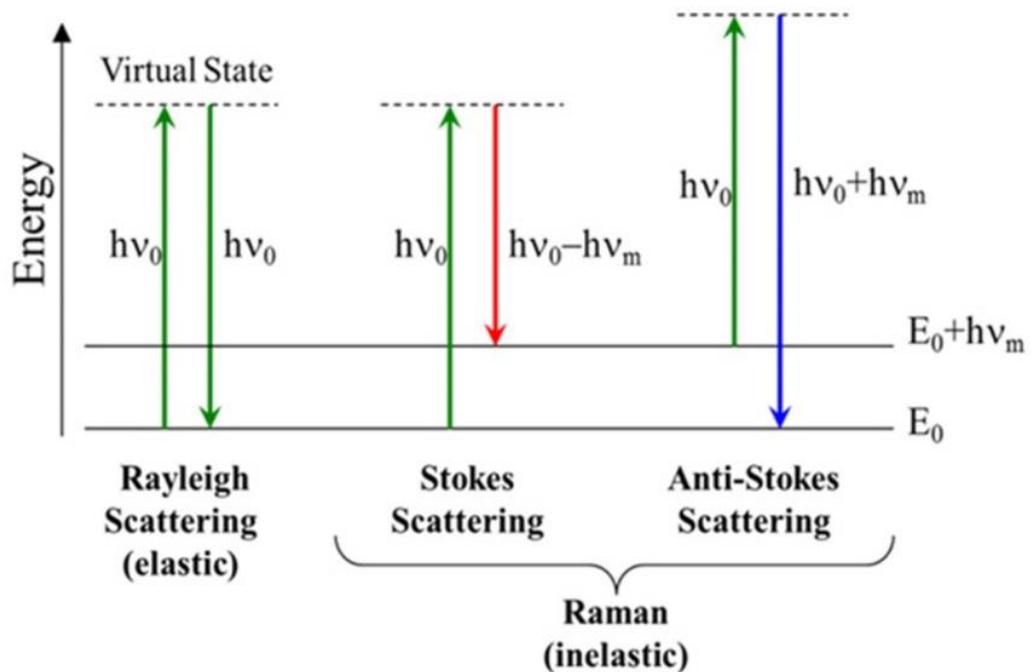
Fig. 3.13. Schematic illustration of Raman scattering (http://bwtek.com/raman-theory-of-raman-scattering).

The energy differences between scattered photon ($h\nu_s$) and incident photon ($h\nu_i$) for different types of scattering are given below.

For Rayleigh scattering,

$$h\nu_s - h\nu_i = h\nu_0 - h\nu_0 = 0 \qquad \text{Eq. 3.13}$$

For Stokes scattering,

$$h\nu_s - h\nu_i = (h\nu_0 - h\nu_m) - h\nu_0 = -h\nu_m \qquad \text{Eq. 3.14}$$

For Anti - Stokes scattering,

$$h\nu_s - h\nu_i = (h\nu_0 + h\nu_m) - h\nu_0 = h\nu_m \qquad \text{Eq. 3.15}$$

Each atom within the material is bonded to its neighbour; these bonds can be modelled as springs which resonate when energy is provided. Atoms within the lattice can therefore vibrate around their bonds. These vibrational modes can be quantised as energy levels. In the case of Stokes scattering (center diagram), the energy from the photon is absorbed and the target atom is promoted to a higher (virtual) energy state from ground state (E_0). The relaxation of this atom from virtual energy state to another energy state (higher than the ground state, ($E_0 + h\nu_m$)) causes radiation which is known Stokes scattering. Anti-Stokes scatter (diagram on right) results when an atom in an excited state ($E_0 + h\nu_m$) gains energy from the incident photon and then decays back to ground state (E_0). In this case, the scattered photon has the higher energy than the incident photon. At room temperature most atoms are in the ground state and hence the intensity of the Stokes peak is generally much greater than the Anti-Stokes and therefore more useful for measurements. In practice, during calibration, the Rayleigh line is centred at zero and the Stokes peaks detected are described as being Raman

shifted in wavelength (cm^{-1}) from the zero point. The vibrational modes of a molecule depend on the bond strength among the atoms, atomic size and molecular orientation. By analysing the Raman spectra, a specific bond structure thus the molecule can be identified. For this reason Raman Spectroscopy is a very useful tool to detect a wide range of compounds from inorganic to organic materials.

In this study, a Horiba-Jobin-Yvon LabRam HR800 integrated Raman spectrometer fitted with a green laser ($\lambda = 532$ nm) was used to collect the Raman spectra of the wear track and wear debris. To reduce the intensity of the incident beam and to avoid irradiation damage, a 10 % transmission filter was applied.

4 Result and discussion

This chapter is divided into five sections. The first four sections describe the effect of deposition time, substrate bias voltage, chamber total pressure and chamber cleanliness respectively on defect formation and their influences on corrosion and tribological properties of HIPIMS/UBM deposited CrN/NbN coatings. Comparison between coating defects in HIPIMS/UBM and pure UBM deposited coatings is discussed in the fifth chapter.

4.1 Influence of deposition time on HIPIMS/UBM deposited CrN/NbN coatings

4.1.1 Overview of the experiments

For this study, four sets of CrN/NbN coatings were deposited by varying deposition time (t) from 15 to 120 min. During all deposition processes, bias voltage (U_b) and chamber pressure (P) were maintained at - 65 V and at 0.35 Pa respectively. The aim of this study was to investigate the defect formation at different stages during the coating deposition. To recognise the sources of the defects and to better understand the coating growth and defect formation, Cr ion etched substrates were also examined in this study.

4.1.2 Coating thickness

The coatings thickness was measured on fractured Silicon wafer cross-sections using SEM. For each coating, five images were captured from which the average value of thickness was calculated.

Fig. 4.1 shows the coating thickness as a function of the deposition time. Relevant cross section SEM images are included in insets to support the thickness data. As expected, the coating thickness increased with the deposition time, exhibiting a linear relationship. This indicates constant coating deposition conditions and deposition rate, which was calculated to be 0.018 μm per min.
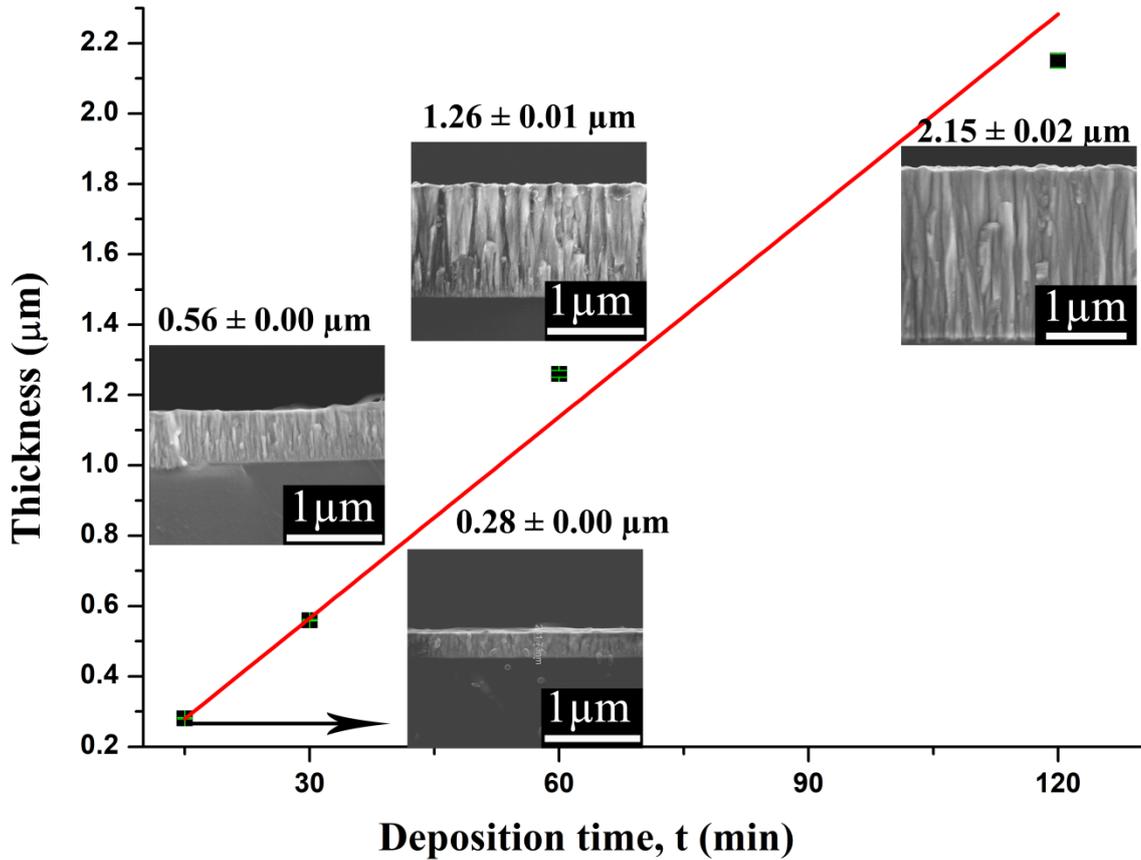
Fig. 4.1. Thickness variation of the HIPIMS/UBM coatings with the deposition time and the related cross-section SEM images.

4.1.3 Physical properties

4.1.3.1 Hardness

Table 4.1 shows the hardness and Young's Modulus values of the coatings. As observed, each coating has a nearly similar value in the hardness as well as in the

Young's Modulus. This result was expected as all the coatings were deposited at similar deposition process conditions apart from the deposition time. As the applied power on the sputtering sources, the total chamber pressure, substrate bias voltage as well as the primary rotation speed of the samples remained constant during all the depositions, coatings with similar stoichiometry and nanoscale multilayer structure were produced. Hence, the hardness value was not influenced by the coating deposition time. The hardness values of these coatings were lower than the previously reported results where coatings were deposited using similar technology i.e. combined HIPIMS and UBM [18,102]. However, note that there was no base layer and the thickness of these coatings was also lower as compared to the mentioned coatings (see the Table 2.1).

Deposition time (min)	Hardness (GPa)	Vickers (H_{vk})	Young's Modulus (GPa)
15	23.57 ± 0.6	1997 ± 62	295 ± 18
30	25.37 ± 3.2	2349 ± 303	298 ± 21
60	26.23 ± 3.5	2421 ± 330	304 ± 15
120	25.85 ± 2.4	2394 ± 228	312 ± 17

Table 4.1. Hardness, Vickers Hardness, Young's modulus values of deposited coatings.

4.1.3.2 Roughness

Table 4.2 presents the results from surface roughness (Ra) measurements of the polished substrate, etched substrate and deposited coating surfaces. The Ra value of the polished substrate was measured to be the lowest (0.012 µm). It increased rapidly to almost twice (Ra = 0.023 µm) when the samples were subjected to the etching process. This transformation can be explained by the substrate material removal due to the

sputtering produced by the bombardment with the high-energy ions generated in the HIPIMS discharge. This sputtering can be aggressive in some places, like grain boundaries or specific microstructural phases as compared to others, which give rise to an uneven surface on a nanometer scale.

During the analysis of 15 min deposited coating, it was observed that the roughness value initially decreased slightly to 0.021 μm due to covering of the uneven surface by the depositing material. However, further increase of the deposition time led to an increase of the surface roughness. For the maximum deposition time of 120 min, the roughness value, Ra was observed to be the highest (0.039 μm). This behaviour was attributed to the natural increase in column diameter and their dome shaped tops with the increase of the coating thickness which is typical for a competitive coating growth mechanism [135].

Samples	Roughness, R_a (µm)
Polished Substrate	0.012 ± 0.003
Etched Substrate	0.023 ± 0.000
Deposition time = 15 min	0.021 ± 0.002
Deposition time = 30 min	0.018 ± 0.001
Deposition time = 60 min	0.038 ± 0.002
Deposition time = 120 min	0.039 ± 0.002

Table 4.2. Roughness of the polished substrate, etched substrate and deposited coatings.

4.1.4 Crystallographic structure

The crystallographic structure of CrN/NbN coatings has been investigated using X-ray diffraction (XRD). BB XRD peak patterns of the coatings are shown in Fig. 4.2. These

XRD patterns revealed that all CrN/NbN nanoscale multilayer coatings had single phase fcc lattice structure. The diffraction pattern of the etched sample corresponds to the 304 stainless steel substrate. Coating reflections could be observed from a 15 min deposited coating. The thickness of this coating was 0.28 µm thus the contribution from the substrate was prominent.
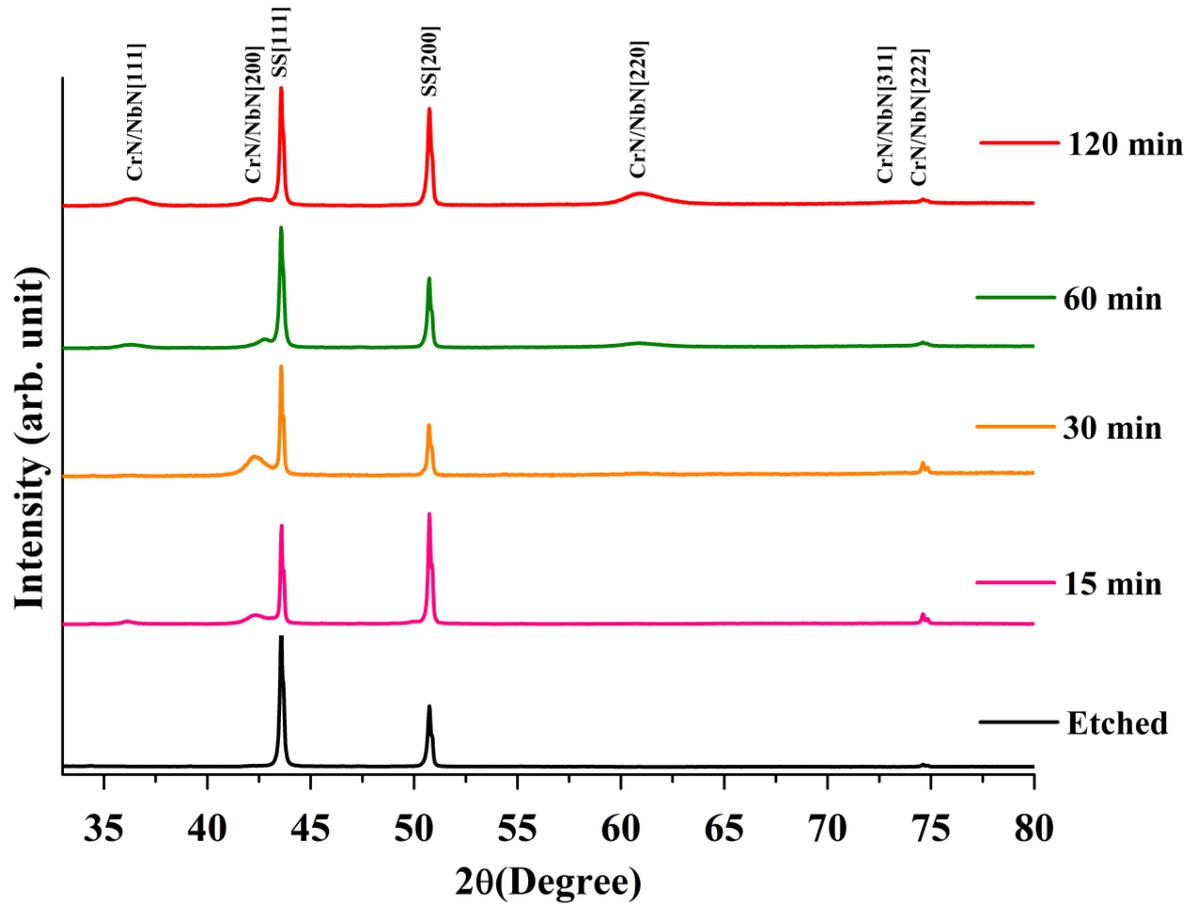
Fig. 4.2. BB Diffraction patterns of an etched substrate and CrN/NbN nanoscale multilayer coatings with different deposition time.
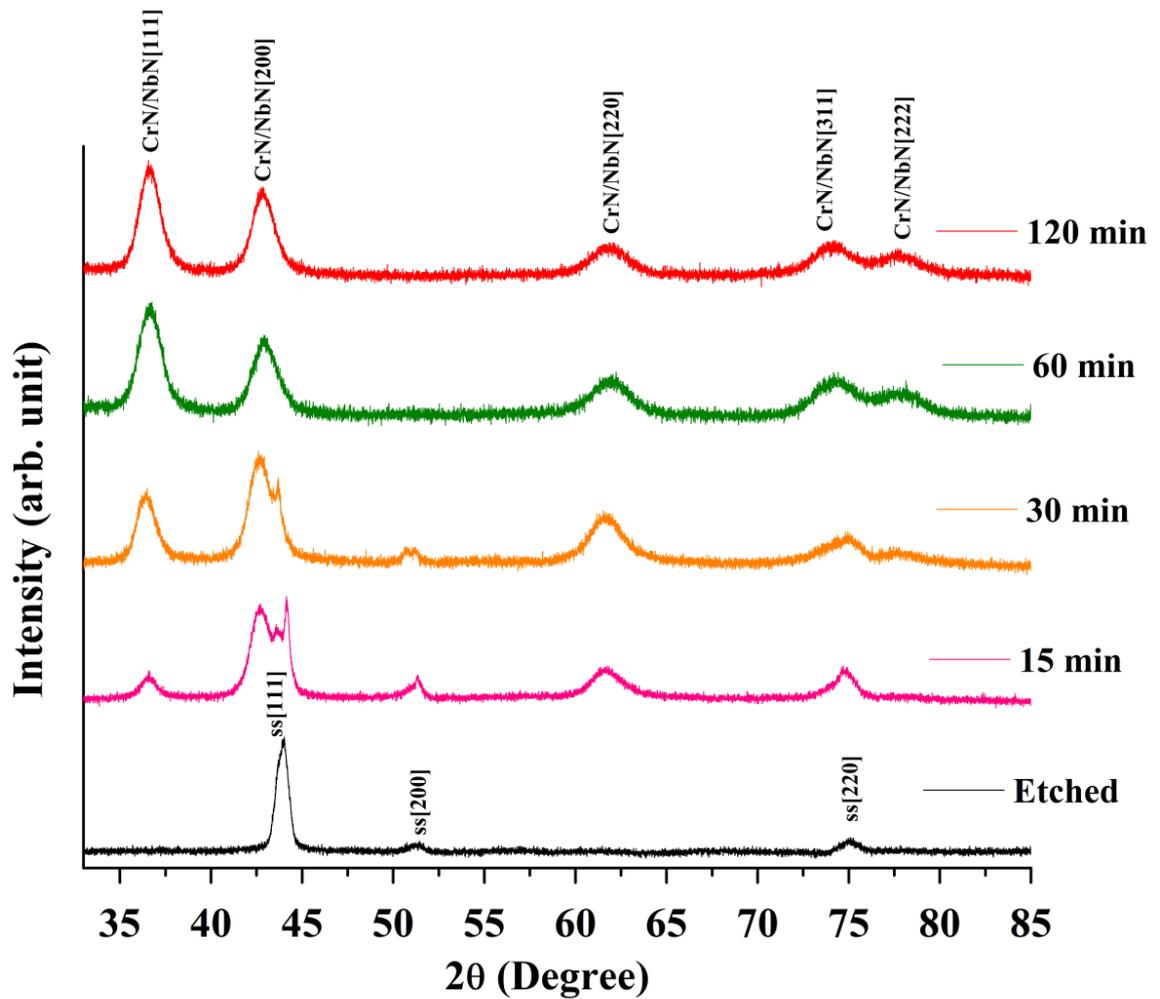
Fig. 4.3. GA Diffraction patterns of an etched substrate and CrN/NbN nanoscale

multilayer coatings with different deposition time.

To better understand the influence of the deposition time on the crystallographic structure, XRD data of CrN/NbN coatings were collected in GA mode. In this mode, due to the reduced penetration depth of the X-rays, contribution related to the substrate can be eliminated in comparison to standard BB XRD (Detail in sec 3.2.1) [136]. Fig. 4.3 shows GA XRD peak patterns of the CrN/NbN coatings, which clearly indicates that the intensity of the peaks increased with increase of coating deposition time, and hence with the coating thickness. This is an expected result. However, the coating structure did not change with the coating deposition time (or thickness) as the other coating

deposition parameters (power applied on the magnetrons, bias voltage, and chamber pressure as well as reactive gas partial pressure) remained constant for all deposition processes.

As seen from the Fig. 4.3, the XRD peaks of CrN/NbN multilayer coatings were incorporated with the reflections from both the CrN and NbN. For example, the peak around 36 ° corresponds to the combination of (111) reflections from CrN and NbN while the individual peak of CrN (111) and NbN (111) reflection occurs at 37.60 ° and 35.36 ° respectively.

4.1.5 Topography and Microstructure

Topography and microstructure of the etched substrate and the coating surface were studied using AFM and SEM techniques. Fig. 4.4a shows a 2D AFM image of the Cr ion etched substrate surfaces over an area of 20×20 µm^2. The colour intensity depicts the surface features of the coatings. In these AFM images, the lighter shaded regions represent the highest points and the darker shaded regions represent pores and cavities. Fig. 4.4a shows cavities and scratches produced during the mechanical polishing step of the samples. Although during the HIPIMS etching step, a thin surface layer of few nm thickness is removed by sputtering due to the bombardment of accelerated Cr ions, a complete removal of all surface imperfections is not achieved as the etching process itself is not meant to be very aggressive. Therefore, surface defects such as pinholes and scratches inherited from the substrate were apparently visible (Fig. 4.4a) even after the etching step. These defects are regarded as one of the main sources /sites for generation of growth defects [2,14].
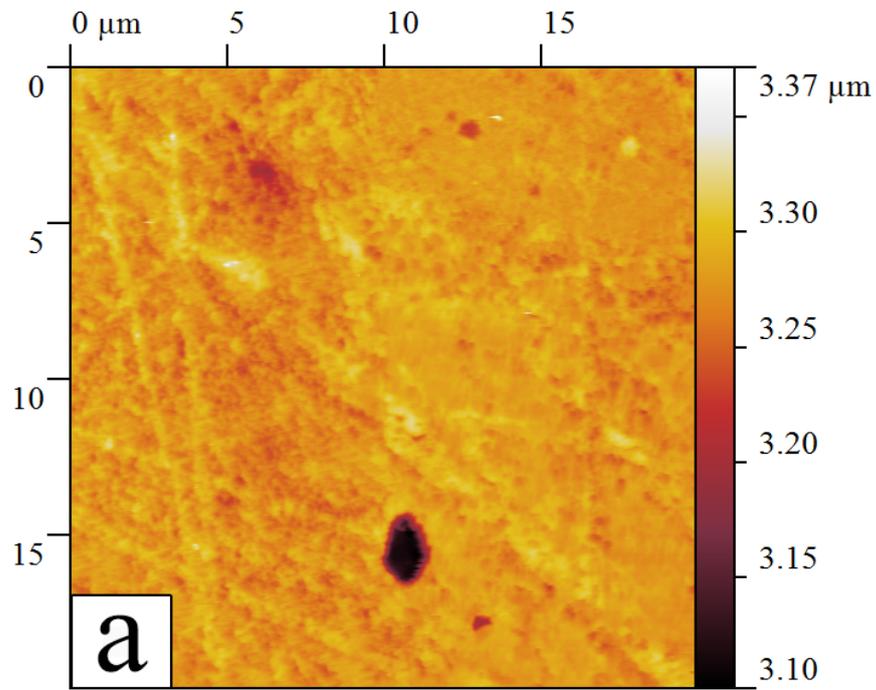
Fig. 4.4. (a) AFM image of ion etched sample.

Low magnification SEM image of the same ion etched substrate but a different area (Fig. 4.4b) shows no evidence of droplet formation when HIPIMS was used for etching. This is in stark contrast to an arc etched surface where, at the end of the etching step the surface is covered with droplets (Fig. 2.16) [5–7,100]. This superior surface finish after HIPIMS etching was a result of careful parameter selection and effective use of arc suppression units on cathodes and bias power supplies [15,35,46]. However, the surface roughness associated with the preferential etching of the grain boundaries and protruding grains was clearly visible in the high magnification SEM image (Fig. 4.4c).
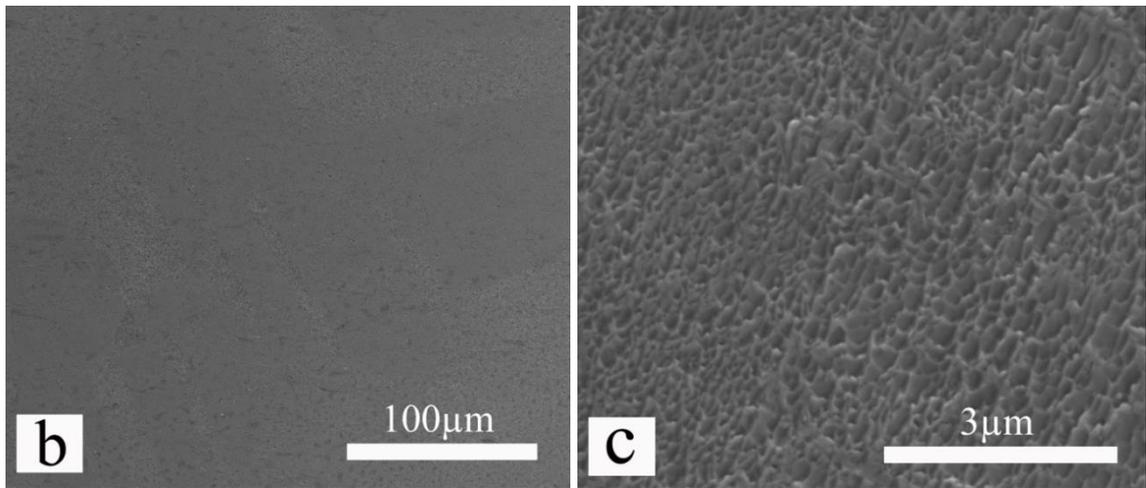
Fig. 4.4. (b) Low magnification and (c) high magnification SEM image of ion etched sample.

Fig. 4.5a-h show the AFM and SEM images of the coated surface deposited by HIPIMS/UBM with varying deposition time. For the 15 min deposited coating (Fig. 4.5a,b), it was evident that the coating deposition had started and covered the surface extensively. However, the imprints of preferential etching of the substrate can still be observed even after a coating thickness of 0.28 µm. Coating morphology, which was dependent on both the grain orientation and grain size of the substrate, suggested a high epitaxy in coating growth, which is a finger print of HIPIMS [15,35,46].

For 30 min deposition time (Fig. 4.5d), most of the surface was covered with coating flux engulfing most of the smaller substrate imperfections, however imprints of some of the deep scratches and pits were still visible (Fig. 4.5c) as the coating simply follows the topography. With an increase in the deposition time, for instance, for 60 min deposition (Fig. 4.5e,f), the majority of the surface imperfections were found to be covered and infused within the coating [2,3] and the morphology appeared more homogeneous. Growth of a columnar structure with rounded column tops, which is typical for sputter

coatings, could be observed from the plan view of the coating surface in Fig. 4.5f. However, all the coating structures were found to be homogeneous, densely packed, and fine grained in the cross-sectional microscopic studies (Fig. 4.1). This densification can be attributed to the high-energy ion bombardment from the HIPIMS plasma. This is significant since low substrate bias voltage (- 65 V) and low deposition temperature (200 °C) were used. Some evidence of contamination defects (explained in the following section) was also evident.

For 120 min deposition time (Fig. 4.5g,h), the basic columnar morphology remained unchanged, however the grain size increased noticeably; more peculiar dome shaped column tops were visible. In this study, two targets were running in HIPIMS mode and two other targets were operated in UBM mode. The benefit of using HIPIMS was clearly visible as the columns were found to be very densely packed (Fig. 4.1) than the columns of pure UBM coating deposited in similar conditions [102].

Although the coating morphology becomes homogeneous with the increase in deposition time, the larger cavities on the substrate surface may never get covered with the coating materials if the coating is thin especially when conditions such as atomic shadowing dominate. These cavities can be apparent on the surface of the fully-grown coating, as visible in the case of 120 min deposited coating (Fig. 4.5g).
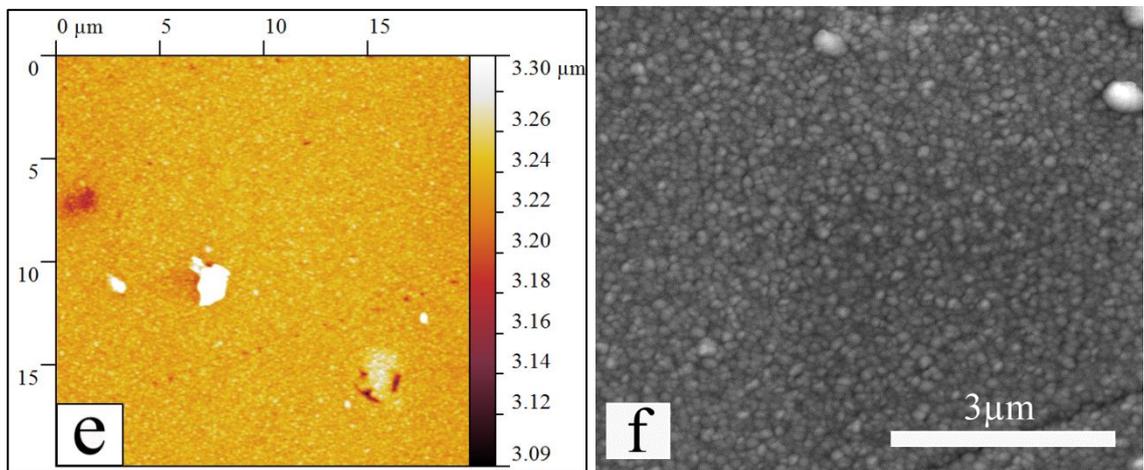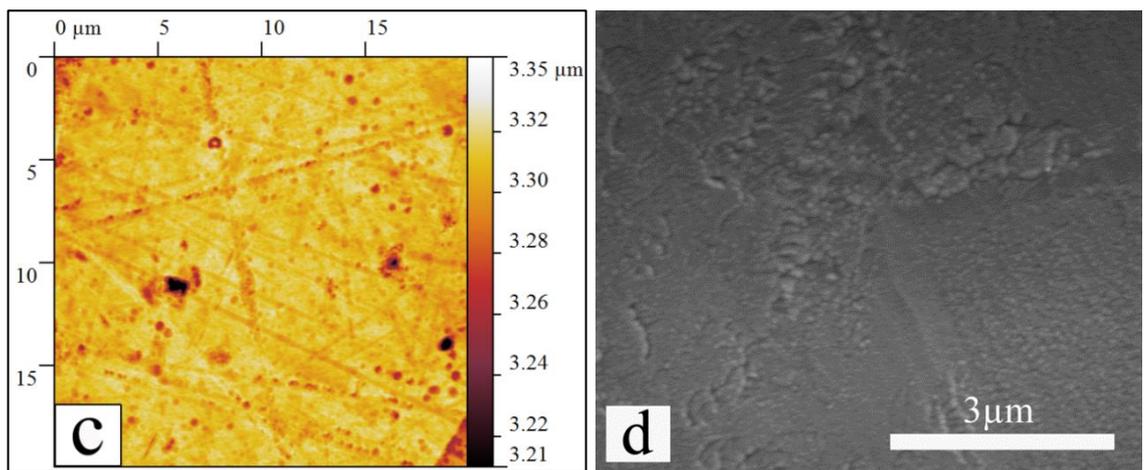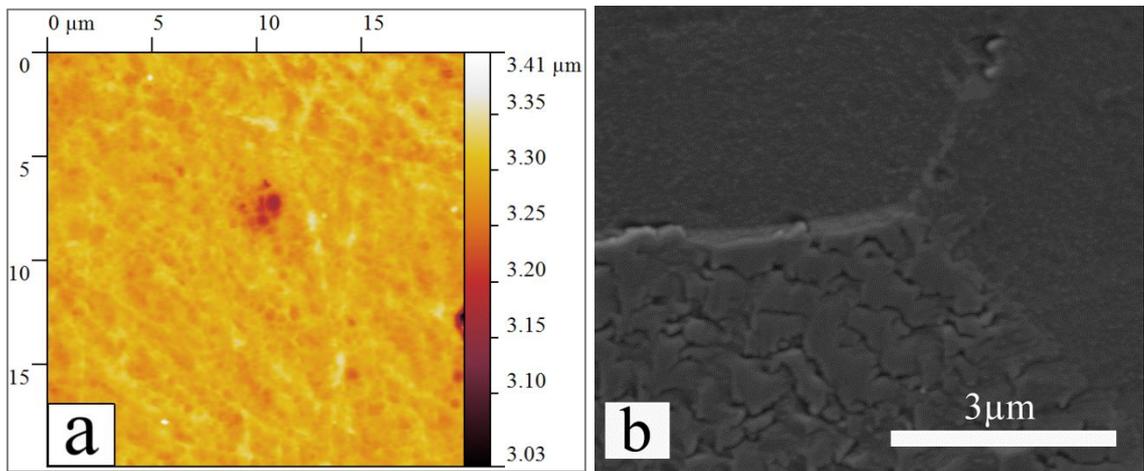
Fig. 4.5. (Continue)
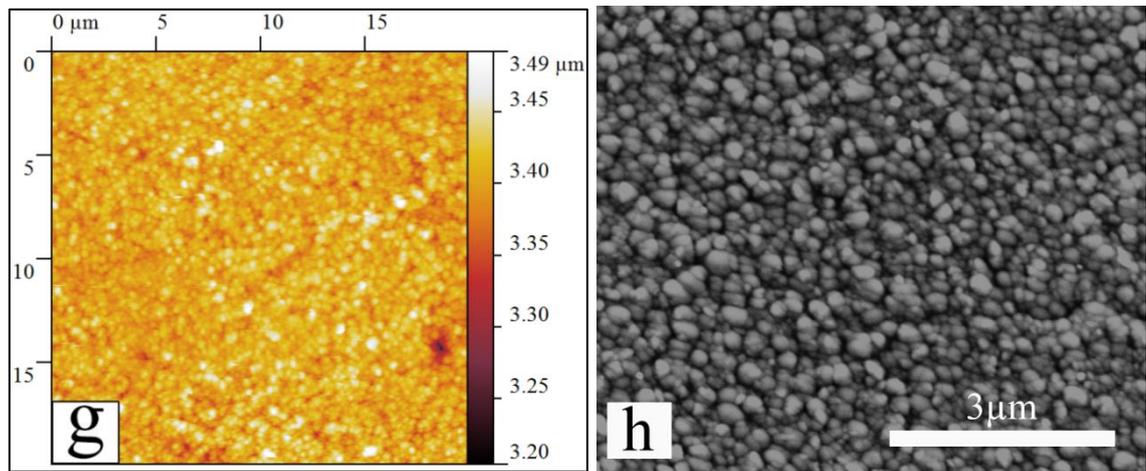
Fig. 4.5. (a) AFM image and (b) SEM image of 15 min deposited coating; (c) AFM

image and (d) SEM image of 30 min deposited coating; (e) AFM image and

(f) SEM image of 60 min deposited coating; (g) AFM image and (h) SEM image of 120

min deposited coating produced using HIPIMS/UBM.

4.1.6 Coating defects

4.1.6.1 Defect types

Defect formation and defect types associated with PVD coatings have been described

before by various authors [2,3,9,10]. In this research, extensive SEM studies were

conducted to investigate the defects in HIPIMS/UBM deposited CrN/NbN coatings. The

types of defects identified were very similar in nature to those reported earlier for

conventional magnetron sputtering processes and already described in detail in section

2.5.1.
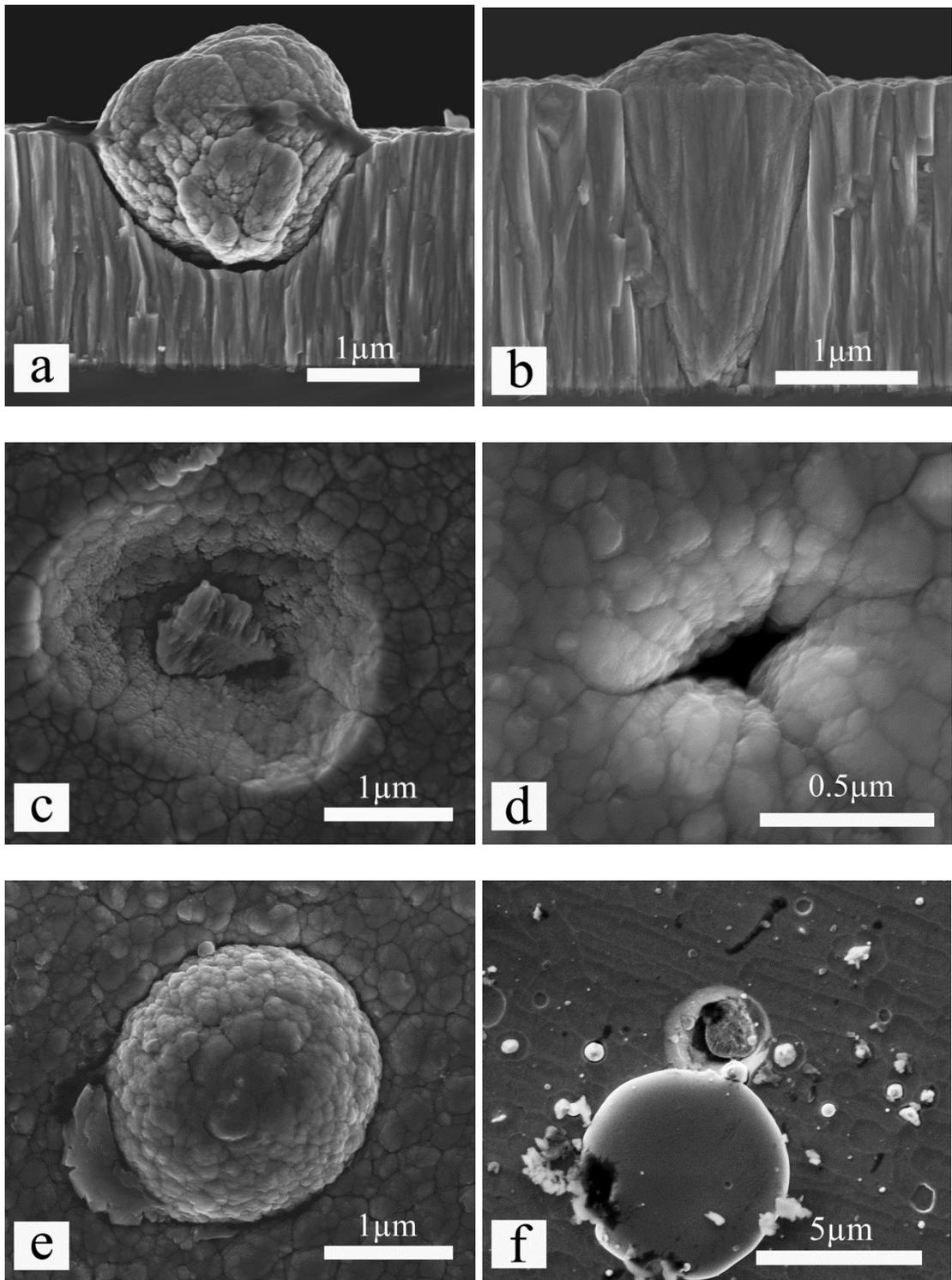
Fig. 4.6. (a) Cross section of nodular shaped defect and (b) cone-like defect; top view of

(c) open void defect, (d) pinhole defects (e) nodular/cone-like defect in HIPIMS/UBM

deposited coatings and (f) droplet in Arc-deposited coating (commercially available).

Fig. 4.6a-e shows the SEM images of different types of defects found in HIPIMS/UBM coatings. Depending on their origins, these defects were categorised into two groups; flakes related defects and defects associated with substrate pits. The flakes related defects include nodular shaped defect (Fig. 4.6a), cone-like defect (Fig. 4.6b) and open void defect (Fig. 4.6c), while pinhole defects (Fig. 4.6d) are associated with substrate pits. Fig. 4.6e shows a nodular/cone-like defect on the surface of HIPIMS/UBM deposited coating whereas Fig. 4.6f shows the top surface view of an arc droplet.

The detail observation of the SEM images of a nodular defect and cone-like defect of HIPIMS/UBM coating (Fig. 4.6a,b,e) demonstrate that the morphology of these defects and the coatings is similar. This indicated that the growth steps for the coatings and these defects were the same and most likely these defects were generated due to the deposition of coating materials on the top of foreign particles attached to the substrate. Thus, to verify the elemental compositions of these defects, EDX analysis was conducted. Fig. 4.7a,b shows SEM image of such flakes related defect and corresponding EDX spectra.
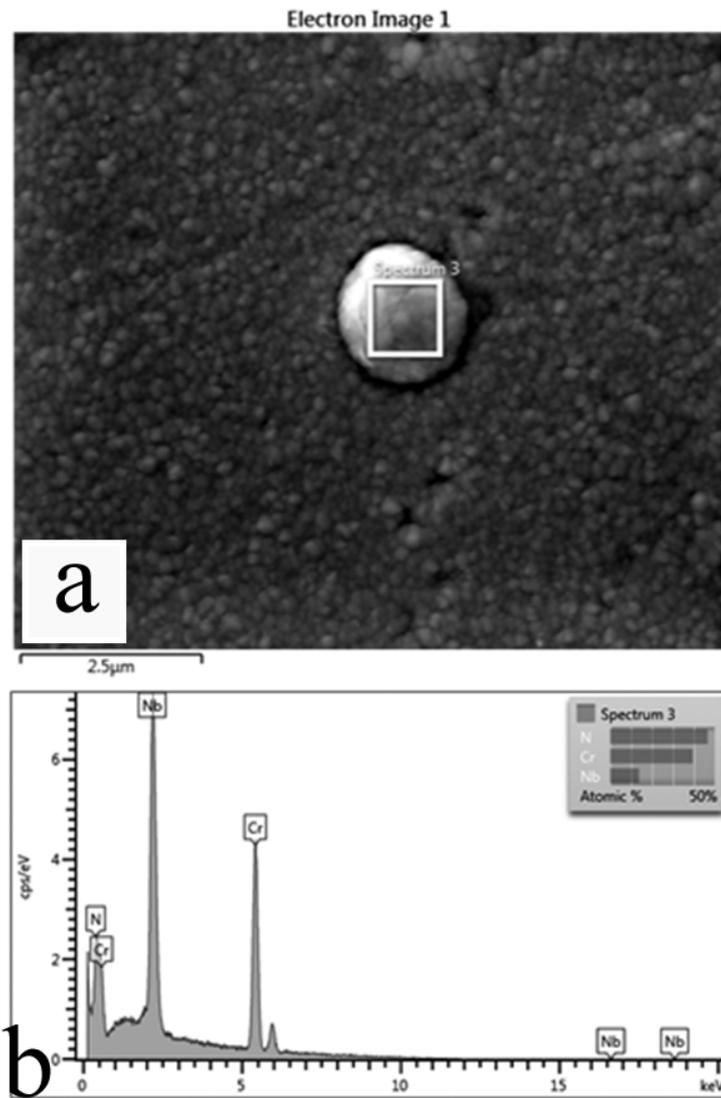
Fig. 4.7. (a) Flakes related defect in HIPIMS/UBM coating and (b) EDX spectra of the defect;

EDX analysis confirmed that the elemental compositions of the nodular defect were same as the coating. Atomic percentages of Cr, Nb and N were found to be 39 %, 14 % and 47 % respectively for both the coating and the nodular defect. This emphasised the fact that defects in HIPIMS/UBM coatings grow over the course of time due to the deposition of coating materials on flakes.

For comparison, SEM image of a droplet on commercially available arc-PVD CrN/NbN coating was taken. Significant differences in morphologies and sizes between arc droplet and nodular defect can be seen from the Fig. 4.6e,f and Fig. 4.7a,c. The arc droplets in the both cases were bigger in size and had a continuous solid structure whereas the grain boundaries and columnar coating growth could be clearly observed from the magnified image of the nodular defect (Fig. 4.6a,e).
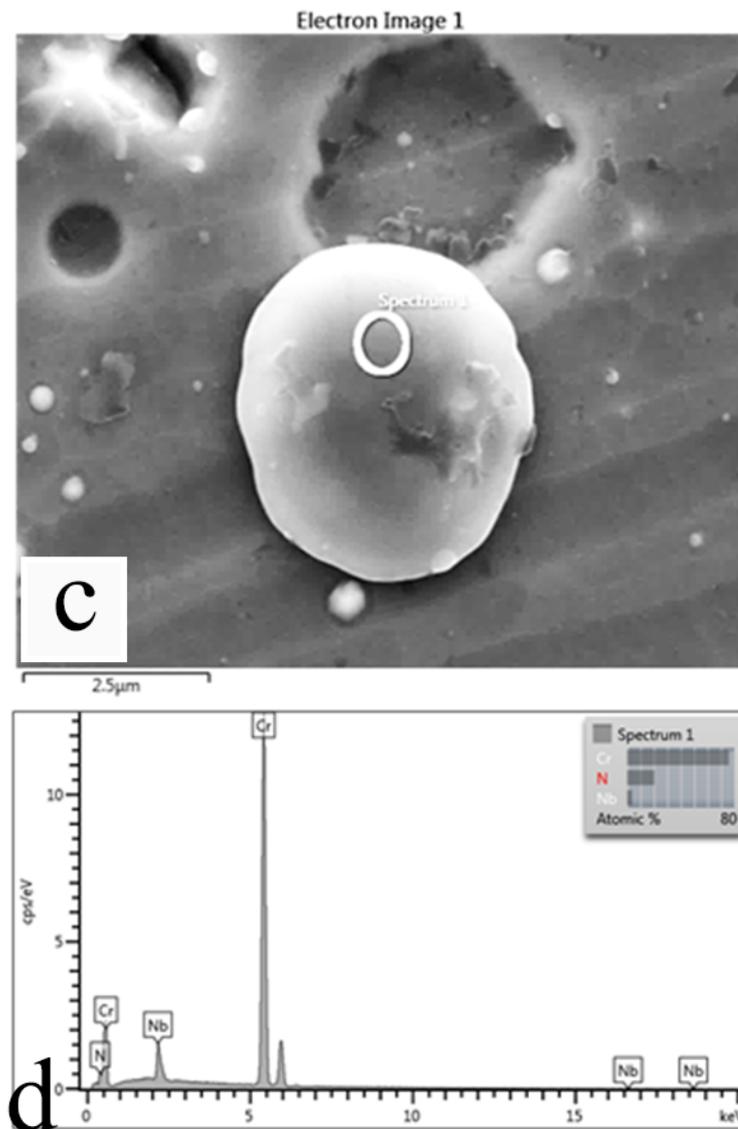
Fig. 4.7. (c) Droplet in Arc-deposited coating (commercially available) and (d) EDX spectra of the droplet.

Moreover, Fig.4.7c also exhibits the morphological differences between the arc deposited coating surface and arc droplet which suggests that the growth steps of the coating and the droplet were different. Arc droplet did not grow over the time rather an instant solidification of cluster of materials ejected from the target led to droplet formation in arc-PVD. EDX analysis (Fig. 4.7d) supported this growth mechanism of arc-droplet. As observed from the spectrum, the droplet was mostly made of Cr (atomic percentage 80 %) indicating that the droplet was generated due to the expulsion of Cr from Cr target at the cathode spot, which solidified instantly on the coating.

Microscopic images of the deposited coating surfaces (Fig. 4.5a-h) and a cross sectional view of a nodular defect (Fig. 4.6a) suggested that flakes related defects generated around the intermediate stages during coating growth, whereas, the voids associated with the substrate pits were more common for the coatings deposited for shorter time (Fig. 4.5a,c). Thus, an additional SEM study was conducted to understand the defect growth mechanism as a function of the deposition time.

Fig. 4.8a,b represents the SEM images of 15 min and 120 min deposited coating surfaces (planar surface view at low magnification) which indicates that the density of defects and type of defects present on the coatings vary with the deposition time. For 15 min deposited coatings, grooves and pits are visible whereas flakes related nodular defects are more noticable on 120 min deposited coatings.
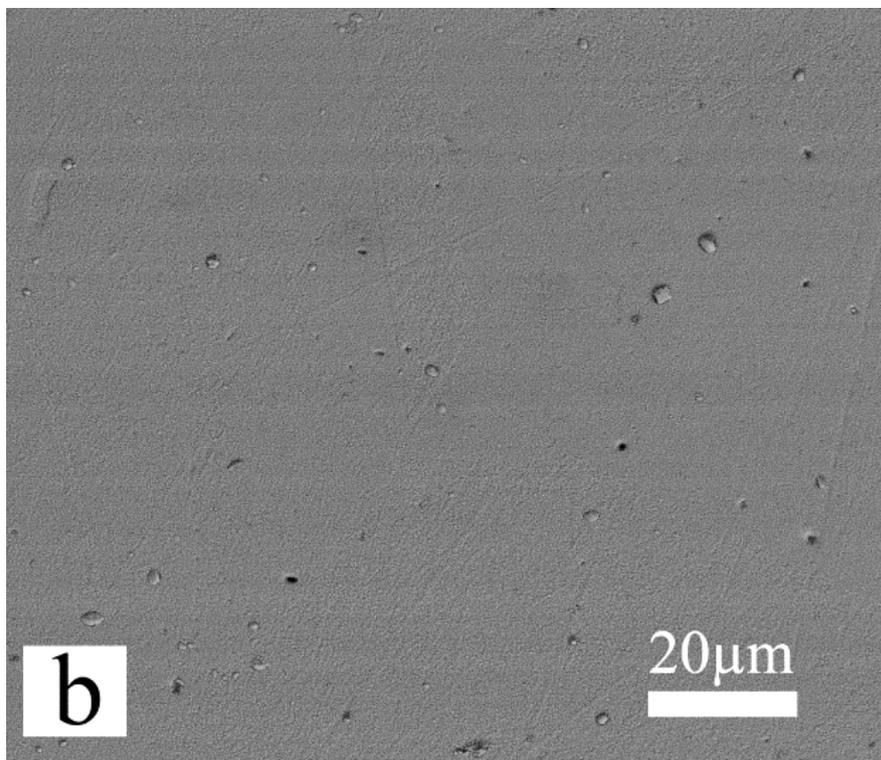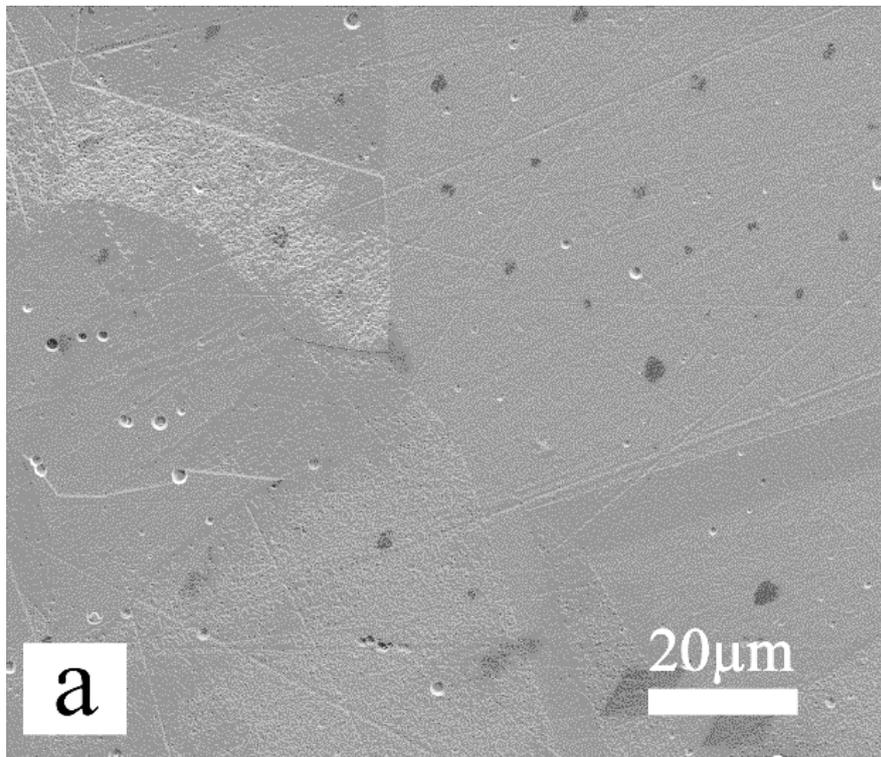
Fig. 4.8. (a) SEM image of 15 min deposited coating; (b) SEM image of 120 min deposited coating.
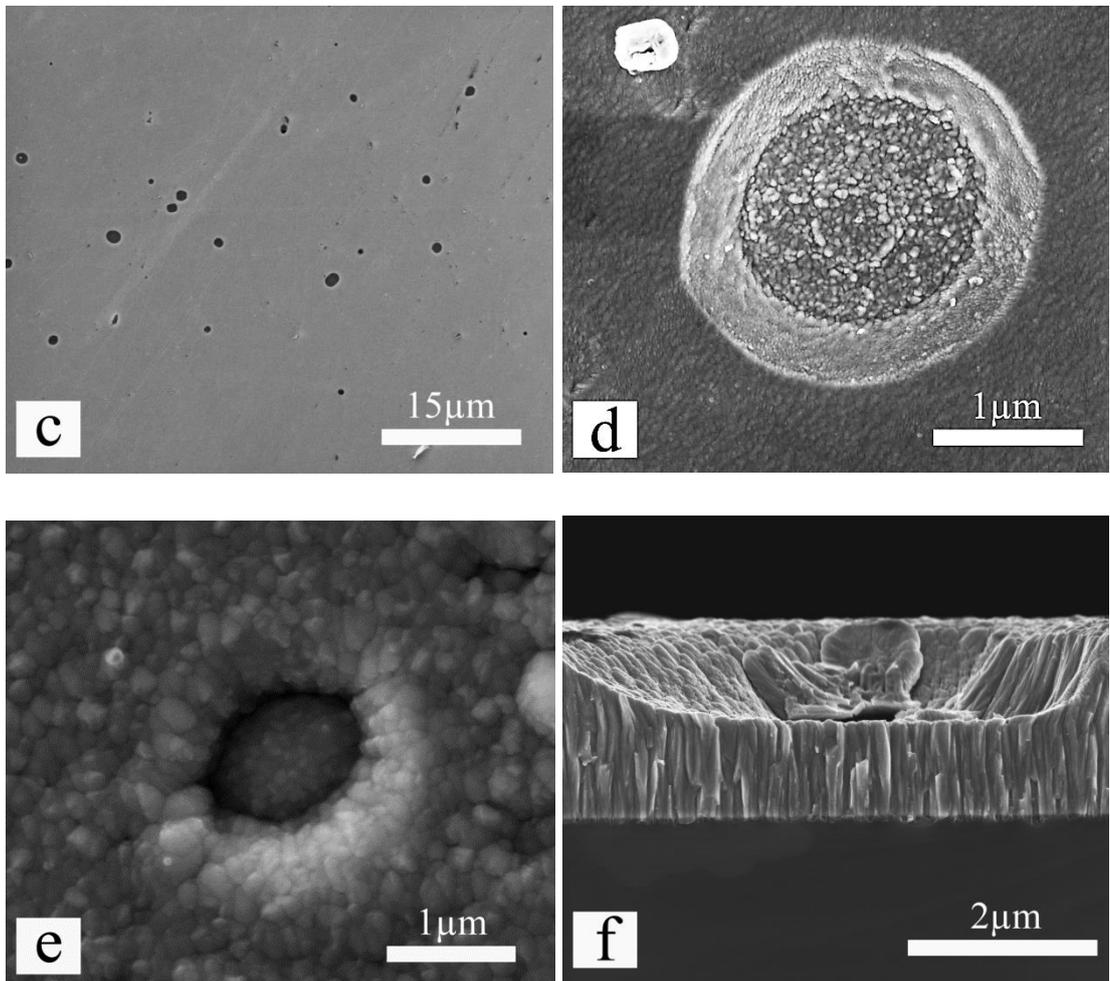
Fig. 4.8. (c) SEM image of stainless steel substrate showing substrate pits, (d) surface of 15 min deposited coating exhibiting substrate pit, (e) surface of 60 min deposited coating showing partially coved substrate pits and (f) Cross-sectional view of open void defects in 120 min deposited coating.

Fig. 4.8c shows the SEM image of the stainless steel substrate exhibiting the pits on it. With the deposition of coating materials, most of these pits get covered. The coating preferentially deposits to the flat front side of the substrate, while the deposition rate on the sidewall of the cavity is much smaller (shadowing effect) [2]. Thus for the 15 min deposited coating (Fig. 4.8d) the pit is more apparent as compared to that on 60 min deposited coating (Fig. 4.8e). Although, the size of these two pits (Fig. 4.8d,e) should

not be compared because the size of the initial substrate pits could be different. However, in Fig. 4.8e deposition of coating flux can been seen clearly. These two images imply that the longer deposition process/time could fill most of the substrate pits which are not very deep or large. In that case, they may not be fully closed even after 120 min of coating deposition and can exist as a pinhole (Fig. 4.6d).

Apart from the pinhole defects, another type of void can be seen on the coatings deposited for longer time. These voids are associated with the nodular defects. From Fig. 4.6a, it can be clearly seen that the nodular defects are very loosly attached to the surrounding coating thus it can be easily expelled and open void defects can form (Fig. 4.6c). These defects can degrade the coating barrier properties by decreasing the effective thickness of the coatings (Fig. 4.8f).

4.1.6.2 Surface defect density

The extensive SEM study on coating defects (section 4.1.6.1) suggested that the deposition time has an influence on defect formation. Thus, this study investigated the effect of deposition time on the surface defect density.
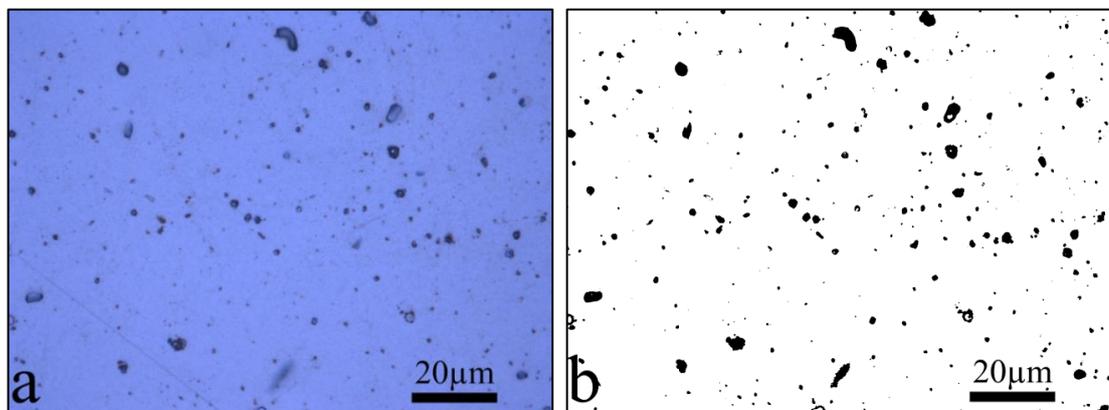
Fig. 4.9. (a) Optical microscopic image of coating surface and (b) Converted binary image of the same surface.

Images captured by the Huvitz microscope and the Image J software were used to study the relationship between the deposition time and defects visible on the surface. Fig. 4.9a shows the surface of the deposited coating captured by optical microscopy and Fig. 4.9b represents the converted binary image of the same surface.

In the optical images, the surface imperfections, i.e., both the protrusions and voids are seen as dark features. For comparison, optical images of polished steel substrate were also captured. In the previous section, the SEM images of stainless steel substrate surface (Fig. 4.8c) and 15 min deposited coating (4.8a) exhibited similar type of surface imperfections which were categorised as pits. The optical microscopic images also revealed that both the substrate and 15 min deposited coatings had similar types of dark dots on their surface. The surface defect density (A_d) of the coatings and the substrate was calculated as a percentage of the surface area covered by optically visible imperfections. The study indicated that the substrate and 15 min deposited coatings had similar A_d values, 0.39 ± 0.04 and 0.48 ± 0.02 respectively which were mainly due to the presence of pits on their surface. With the increase in deposition time, the number of dark features increased on the surfaces. Fig. 4.10 shows the percentage of surface area covered by optically visible defects as a function of the coating deposition time. It was clearly observed that there was a direct proportionality between these two factors; as the coating deposition time increased the area percentage of defects also increased. The increase in growth defects with time was believed to be due to the increase of the number of small flakes (seed) in the chamber during the deposition process. Some of the seed particles generate from the chamber components of the coating system due to thermal and structural stresses or flux-bombardment on them. A further source for small seed particles and wear debris is the rotation of the substrates holders. The number of flakes is increased in the chamber with time because of all these continuous processes. When flakes of significant size fall on the substrate, they may effectively alter the

coating growth direction as compared to that of the rest of the coating, thus forming nodular/cone-like defects [2,3]. During or after the deposition, some nodular defects can be expelled due to high compressive stresses present there creating a different type of defect, such as cavities (Fig. 4.6b, 4.8f).
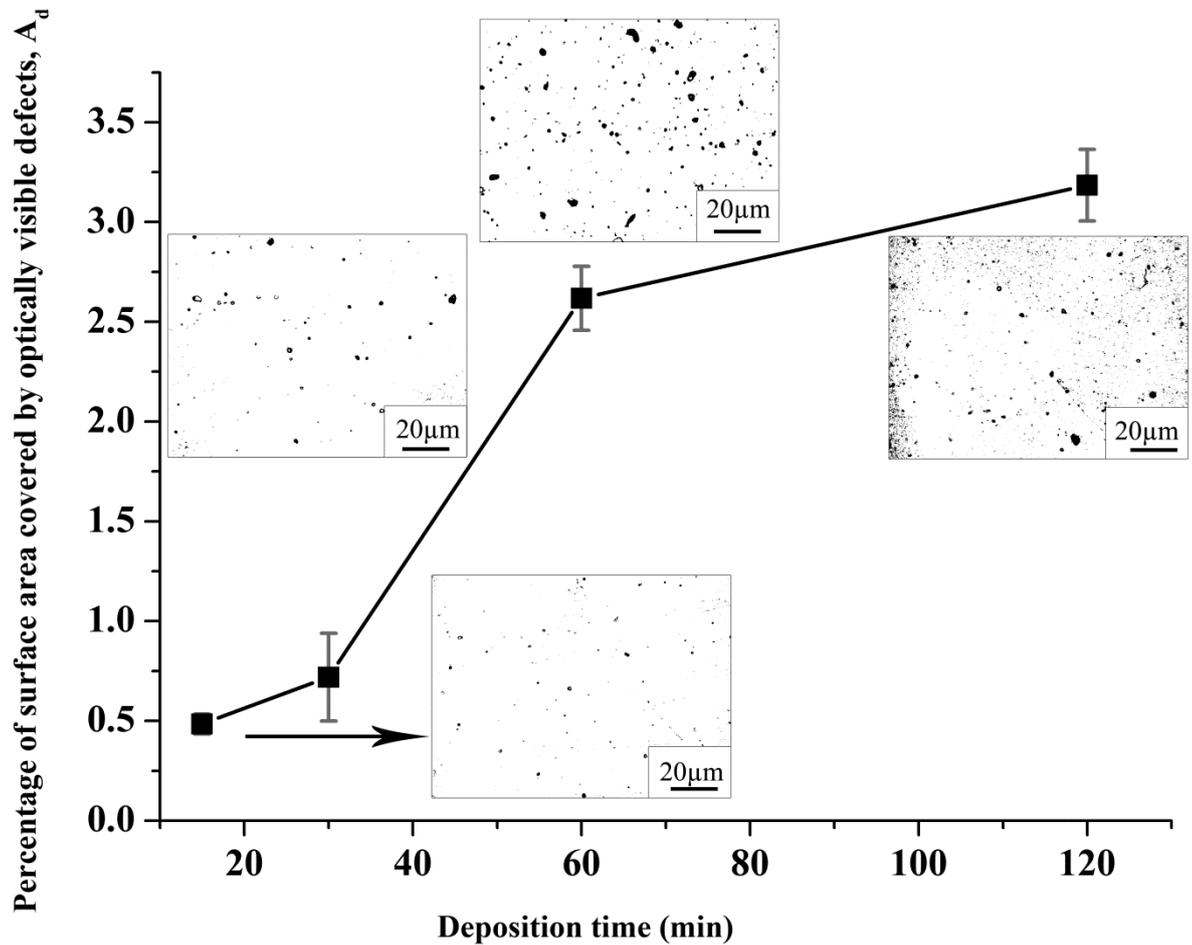
Fig. 4.10. Variation of surface area coved by optically visible defects as a function of deposition time.

4.1.7 Corrosion resistance

It has been suggested that, the corrosion properties of CrN/NbN superlatices are a function of their chemical compositions, residual stress levels and coating defects

[2,3,7,8,14,18–20,112,137]. Fig. 4.11 shows potentiodynamic polarisation curves for the CrN/NbN nano-scale multilayer coatings.
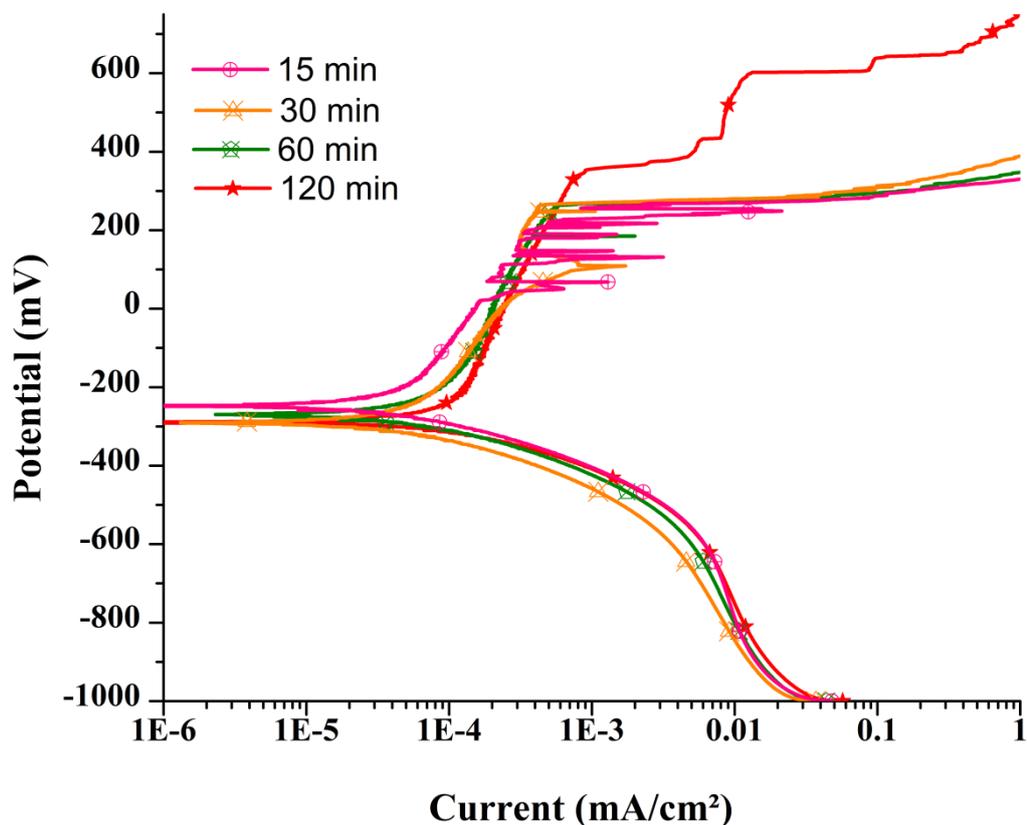
Fig. 4.11. Potentiodynamic polarisation curves for the HIPIMS/UBM CrN/NbN nano-scale multilayer coatings deposited by varying deposition time (min).

In general, all coated specimens above E_{corr} value exhibited an increase in corrosion currents with increasing anodic potentials. This can be attributed to the dissolution of Cr phase from the coating and/or the substrate as well as corrosion of the substrate, since Nb has been found to be passive at these conditions of pH and potentials [137].

All the coatings showed increased fluctuation in corrosion currents in the anodic potential ranges of around 50 mV and 400 mV. This fluctuation was observed to be

126

severe for the thinnest coating (15 min deposited and 0.28 µm thickness). Considering the thin and uneven nature of this coating (Fig. 4.5a,b and Fig. 4.8a,d), it can be speculated that with increasing anodic potential and hence time, there was an increase in the number of sites where coating dissolution took place leading to the exposure of the substrate. In optical microscopic images of the CrN/NbN, coating surfaces were found to be severely damaged with large pits visually evident (Fig. 4.12). Thus, the corrosion current fluctuation was a result of active dissolution, passivation, trans-passivation and re-passivation events happening on the newly exposed substrate surfaces through pits as well as the coating. With the increase of coating thickness, the rapid occurrence of these events was reduced. For example, the fluctuations in current density in 30 min and 60 min deposited coatings were occurred only a few times. These fluctuations were believed to be associated with the defects in the coatings, which were preferentially removed by the galvanic effects [18,112,137] and exposed the substrate surface to the corrosive media. The corrosion response observed in the 120 min deposited 2.15 µm thick coating was purely due to the events of the corrosion/passivation of the coating. As evident, though the number of defects increased with coating thickness, the corrosion tests suggested that these defects were not extended throughout the thickness rather originated during the intermediate stage of coating deposition. Any defect initiated at the substrate level, could act as a direct pathway for corrosive media to reach the substrate and increase the corrosion rate significantly.
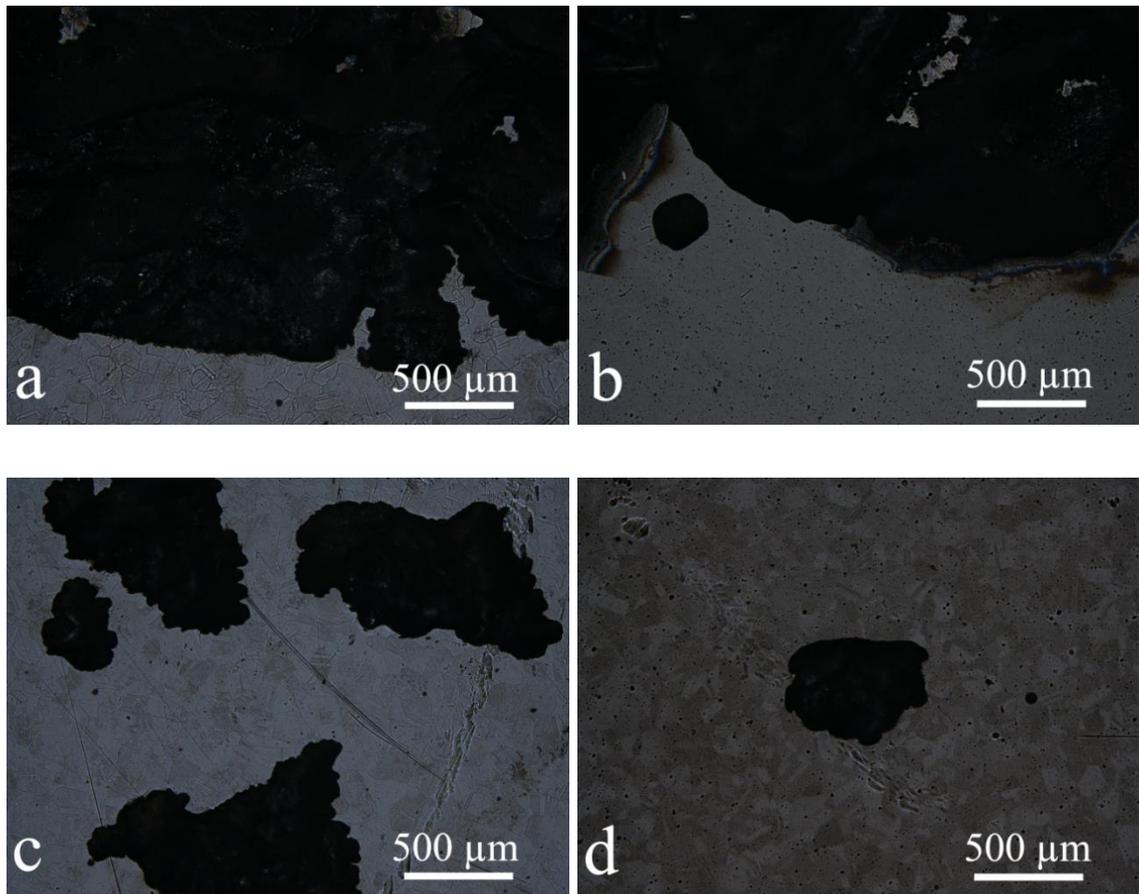
Fig. 4.12. Optical microscopic images of (a) 15 min deposited, (b) 30 min deposited, (c) 60 min deposited and (d) 120 min deposited coating surface after corrosion test.

4.1.8 Tribological properties

4.1.8.1 Determination of wear and friction coefficients

The wear and friction behaviour of CrN/NbN coatings were evaluated by pin on disc tests in dry sliding conditions. The friction coefficient, COF (μ) of CrN/NbN coatings and uncoated HSS substrate against number of revolutions (friction cycles) has been plotted in Fig. 4.13. Fig. 4.14 shows the wear tracks of the coatings deposited by varying deposition time and an uncoated HSS substrate.
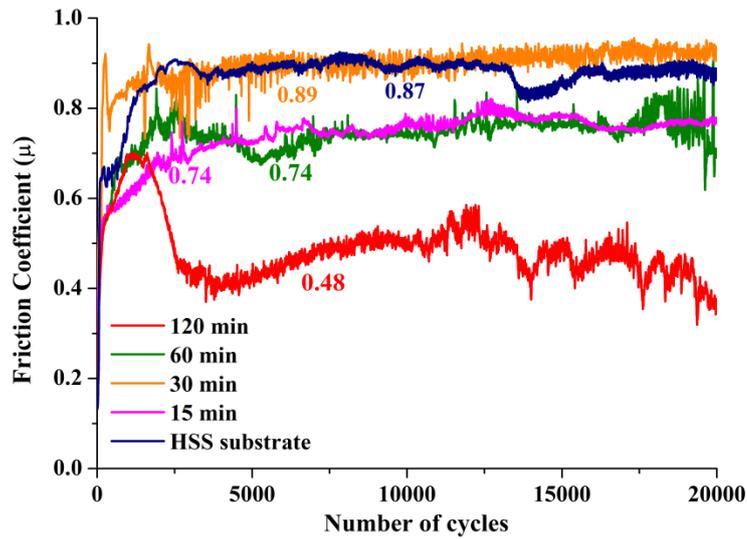
Fig. 4.13. Dependence of friction coefficient on number of revolutions (friction cycles) for the coatings deposited by varying deposition time and uncoated HSS substrate.
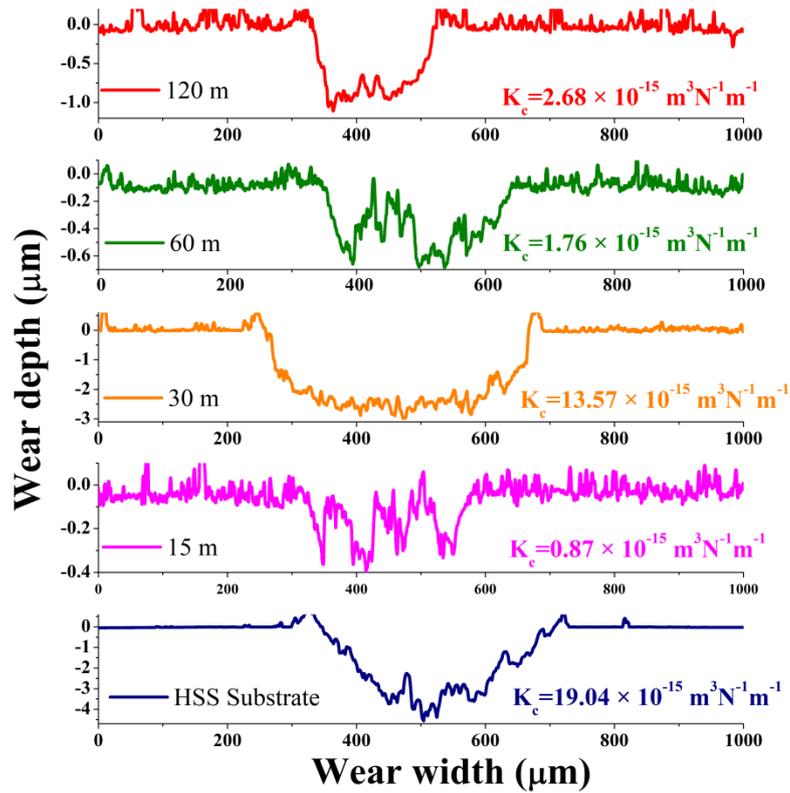
Fig. 4.14. Wear track profiles of the coatings deposited by varying deposition time and the uncoated HSS substrate.

As observed in the Fig. 4.13, the μ values of the coatings deposited for 15, 60 and 120 min were similar up to 1000 cycles. After that, μ of 120 min deposited coating decreased significantly to 0.4 at 3000 cycles and again increased to 0.5 at around 9000 cycles. Also, the fluctuation in μ value in the range of 10000 and 20000 cycles can be observed. The tribological behavior of this 120 min coating was a typical sliding wear process with a large amount of debris involved in a three body tribo-contact mechanism [104,138].

During the tribological test two types of wear are prevalent in coated samples. They are progressive (abrasive, adhesive) and catastrophic (spalling) wear [139]. Due to the competitive growth the stress within the coating increases with the thickness. This stress could result in the spallation of some parts from the top surface of the thickest coatings (120 min deposition and 2.15 μm thick) when load was applied. The wear particles trapped between the coating and the counterpart could initially decrease the friction by causing three body rolling mechanism. However, this coating had the highest number of surface defects (A_d = 3.18 %). During the tribology test, due to the interaction between the alumina ball and coating surface, loosely bonded defects could be expunged and these defects could increase the wear debris formation. The continuous generation of wear debris initiated the three body abrasive wear mechanism and ultimately raised the friction value. The μ value of this coating is comparable with the results reported by other authors [18,102,117].

For the other coatings, a two-body abrasive wear mechanism was found to be dominant and the COF increased continuously. For comparison, dependence of COF value on number of cycles in case of uncoated HSS substrate was also plotted. The similarly in μ values and the nature of the "dependence of μ values on friction cycles" between the uncoated HSS substrate and the CrN/NbN coated substrates (t ≤ 60 min) indicated that the friction behaviours of these coated substrates were influenced by the substrate

materials. It could also be confirmed from the wear track profiles of the coated substrates (Fig. 4.14) which shows the depths of the wear tracks were higher than the coating thickness for 15 min and 30 min deposited coatings. This implies that for these two coatings (t ≤ 30 min) the counterpart, Al_2O_3 ball reached the substrate during the tribo tests. Although, for 60 min deposited coatings the wear depth was less than the coating thickness, this coating still exhibited higher μ value. Thus to better understand the friction behaviour of the coatings, images of the wear tracks were captured using optical microscopy (Fig. 4.15).
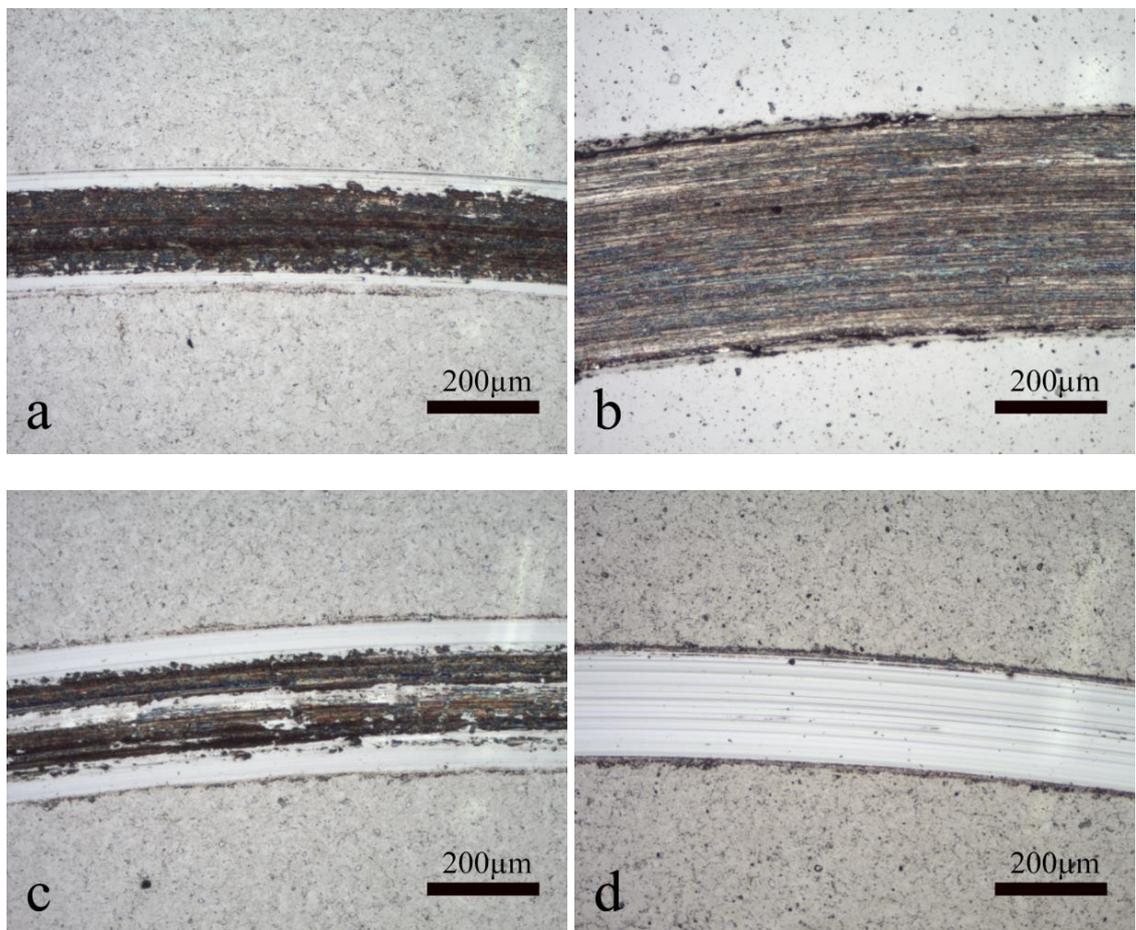
(Fig. 4.15. Continue)
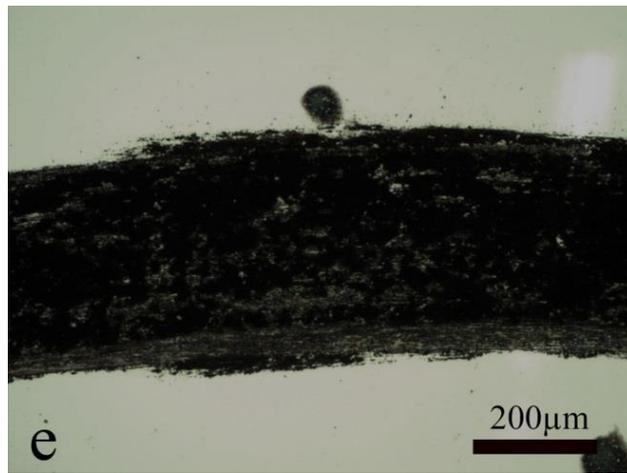
Fig. 4.15. Optical image of wear track of the (a) 15 min deposited, (b) 30 min deposited, (c) 60 min deposited, (d) 120 min deposited coating and (e) uncoated HSS substrate.

These optical microscopic images indicated that the μ values of the coatings deposited for $\leq$ 60 min were influenced by oxides produced within the wear tracks. Although the wear depth of 60 min deposited coating was less than the coating thickness, the sign of oxide formation could also be observed within the wear track of this coating. This could happen due to breakdown of the coating in some places during the test. In contrast, a smooth wear track with an unremarkable colour can be seen on the 120 min deposited coating (Fig. 4.15d) which indicates that the COF value of this coating was mainly due to the sliding properties of the CrN/NbN coating against Al_2O_3 ball and layer by layer material removal mechanism [17]. However, because of the three body wear mechanism the wear rate (K_C) of 120 min deposited coating was found to be higher ($K_C = 2.68 \times 10^{-15}$ $m^3N^{-1}m^{-1}$) than that of 15 and 60 min deposited coatings. Surprisingly, 30 min deposited coatings had the highest wear coefficient value ($K_C = 13.57 \times 10^{-15}$ $m^3N^{-1}m^{-1}$) with the highest wear depth of 3 μm and wear width of 400 μm. As discussed in the section 4.1.3.2, the roughness value of this coating was the lowest (0.18 μm) which could increase the contact area of the interfaces during the initial sliding passes and then

the wear track width and depth increased due to the continuous wear loss. Also, the nature of the oxides produced during the tribological test could affect the wear mechanism of this coating [114,118].

4.1.8.2 Raman Spectroscopy

To evaluate the nature of the oxides produced during the tribological test, Raman spectra were obtained from the wear tracks and debris. Fig. 4.16 shows the Raman spectra obtained from wear tracks for the coatings deposited for t ≤ 60 min and from the wear debris beside the wear track of 120 min deposited coating. Because for this coating (t = 120 min) there was no trace of wear debris formation within the wear track.
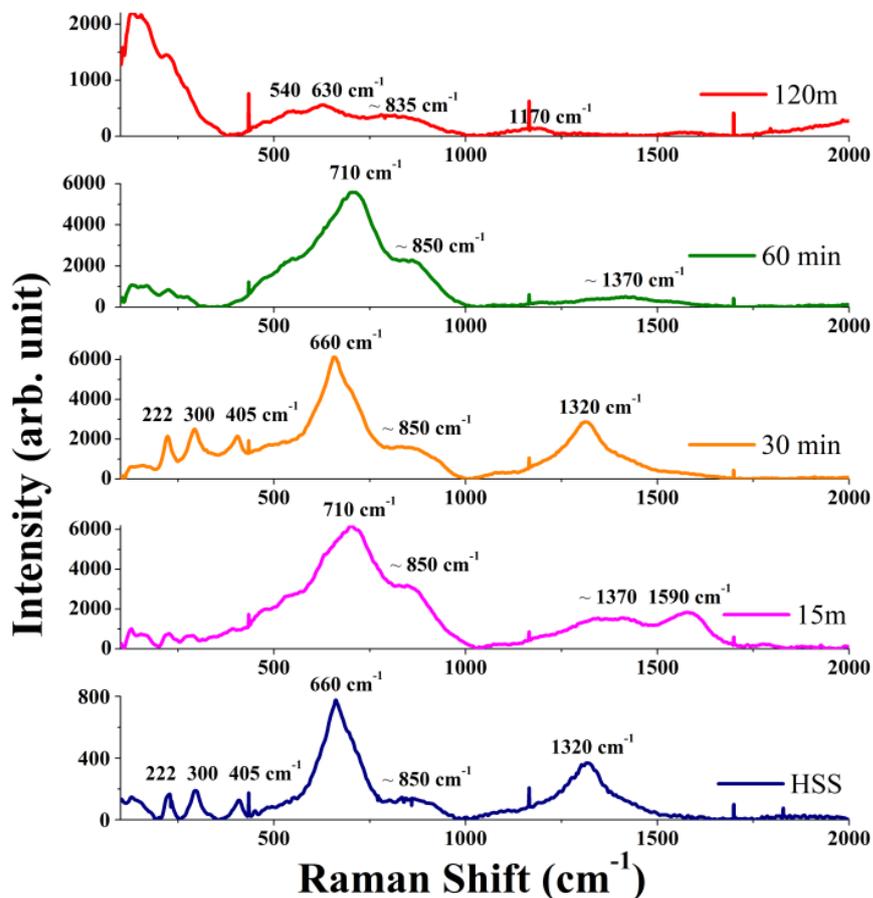
Fig. 4.16. Raman spectra of the tribolayer formed at the tribological contact.

In Fig 4.16 several intense peaks can be observed on the wear tracks of the coatings deposited for $\leq$ 60 min. The Raman spectra of 30 min deposited coating and the uncoated HSS substrate were exactly similar. Interestingly, their μ values were nearly equal (0.89 and 0.87 respectively). On the other hand, Raman spectra of 15 min and 60 min deposited coatings were same. In this case also their μ values were equal (0.74). This study confirmed that the μ values of these coatings were influenced by the oxides produced at the tribological contacts. The peaks (222, 300 405 and 660 cm^{-1}) observed for 30 min deposited coating and the substrate corresponds to Fe_2O_3 [140,141]. Iron oxides are known as non-protective oxides which justifies the higher μ values of the coating and the uncoated substrate. Although, D carbon peak at 1320 cm^{-1} was visible for both cases, produced iron oxides dominated the friction behaviours. As a result of its (Fe_2O_3) formations, wear track was badly damaged and the μ values of the coating and the substrate reached the higher values of 0.89 and 0.87.

For 15 and 60 min deposited coatings the formation of Fe_2O_3 was not very evident. Rather, both these coatings showed pronounced Raman peaks 710 cm^{-1}. This peak could result from the overlapping of several peaks. Most probably this peak corresponds to a mixture of oxides like Cr_2O_3, $CrNbO_4$ coming from the coatings and Fe_2O_3 coming from the substrate [118,140–142]. Along with Fe_2O_3 the formation of Cr-based oxides was beneficial for these coatings (because Cr_2O_3 is a protective oxide) [118]. As a result the μ values of these coatings decreased from 0.89 to a lower value of 0.74.

In addition, the 15 min deposited coating showed pronounced peaks at 1370 and 1590 cm^{-1} which correspond to D and G carbon peaks respectively [142,143] coming from the substrate. This carbon layer could act as a solid lubricant thus increasing the wear resistance ($K_C = 0.87 \times 10^{-15}$ m^{3}N^{-1}m^{-1}) of the 15 min deposited coating. Raman spectra of the wear debris of 60 min deposited coating did not show G carbon peak but it showed a peak at around 1370 cm^{-1} which correspond to D peak of carbon.

The wear track of the 120 min deposited coating did not show any intense peak like the wear tracks of the other coatings. Thus, to compare the nature of the wear debris of this coating with the virgin sample, Raman spectra were plotted in Fig. 4.17.
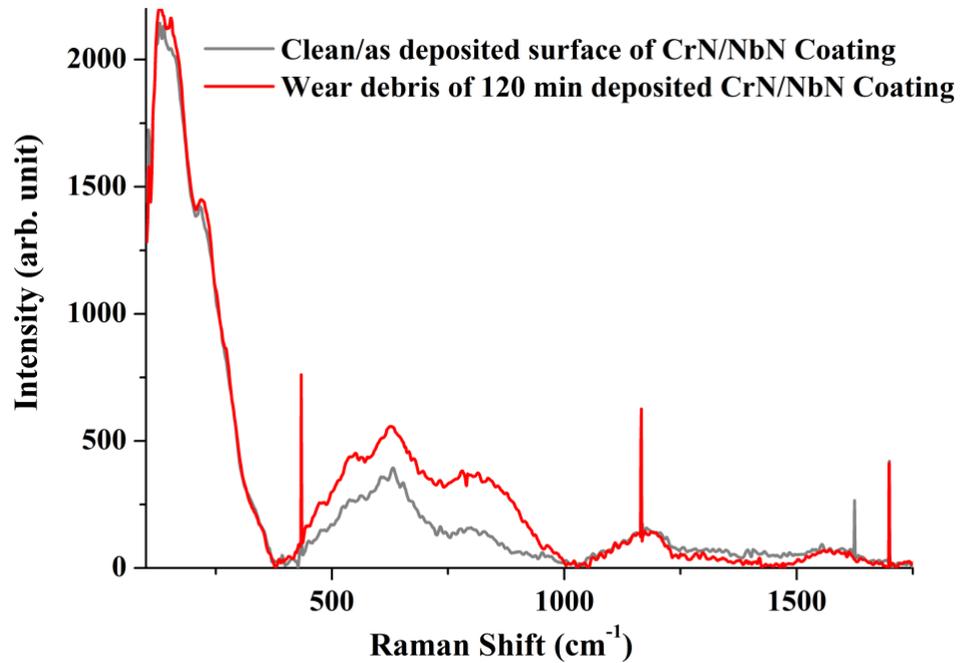
Fig. 4.17. Raman spectra of the wear track and the coating surface.

This figure shows that the Raman spectra obtained from the wear debris of 120 min deposited coating and the as deposited coating surface are very similar. This result confirmed that with the increase in the deposition time (or thickness) the coating provided better protection to the substrate during tribological tests.

4.1.9 Summary

- The microstructures of the nanoscale CrN/NbN coatings were influenced by the deposition time. However, SEM cross-sectional images confirmed that irrespective of the thickness, all the coatings were dense and free from inter-columnar voids.

- Comprehensive study of the coating surfaces and cross-sections suggested that defects were mostly generated due to the interruption of the systematic coating growth by external factors, such as chamber dust or substrate surface imperfections, such as pits or protrusions.

- Deposition time had a strong effect on defect formation. The critical time required for contamination related defects (foreign particles such as flake and chamber dust) to appear was between 30 and 60 min of deposition. However, the defects associated with substrate pit were reduced with the deposition time. Thus, the increase in surface defect density with the deposition time was mainly due of the formation of flakes related defects.

- Results from corrosion experiments revealed that though visible on the surface, these defects may not extend all the way to the substrate thereby providing effective barrier against a corrosive medium.

- Friction and wear values were mostly influenced by the coating deposition time (or thickness) and the nature of tribolayer produced during the tribological tests. The coting deposited for the longest time of 120 min had the highest surface defect density (A_d = 3.18 %) but due to the highest thickness (2.15 µm), it provided better protection and µ value of this coating was found to be the lowest value (µ = 0.48).

4.2 Influence of substrate bias voltage on HIPIMS/UBM deposited CrN/NbN coatings

4.2.1 Overview of the experiments

The substrate bias voltage is one of the most influential deposition parameter. This parameter directly controls the adatom mobility during the growth of the coating [53,55–58,61,62]. To study the influence of the bias voltage on the formation of morphological defects in the coating, four sets of CrN/NbN coatings were deposited by varying the bias voltage (U_b) from - 40 V to - 150 V. The chamber pressure (P) was maintained at 0.35 Pa and the deposition time was 120 min for all the coatings.

4.2.2 Coating thickness

The thickness of deposited coating was measured to study the influence of bias voltage on the deposition rate. The thickness values are summarised in Table 4.3.

Bias Voltage (V)	Thickness (µm)
- 40	2.02 ± 0.03
- 65	2.15 ± 0.02
- 100	2.05 ± 0.01
- 150	1.80 ± 0.04

Table 4.3. Coatings thickness as a function of substrate bias voltage.

This study revealed that the coating thickness slightly increased when the bias value was raised from - 40 V to - 65 V. Further increase of bias voltage resulted to the decrease in coating thickness. At the bias voltage of - 150 V, thinnest coating was

produced (1.80 µm). Similar behaviour was observed for CrN and other transition metal nitride coatings [55,144–146]. The decrease in the thickness was more likely due to the re-sputtering of the coating materials with the increasing bias voltage. The intention of applying negative bias voltage is to increase the adatom mobility in order to produce a dense coating. However, at the higher bias voltage of - 150 V, the re-emission of the deposited materials by the energetic neutral or ion bombardment caused the decrease the coating thickness.

4.2.3 Chemical composition

It was found in the previous section (sec 4.2.2) that there was a significant influence of bias voltage on coating deposition rate. Thus, chemical compositions of the coatings were evaluated to understand the effect of the bias voltage on the coating growth mechanism in more detail. From the Table 4.4, it is clear that the decrease in coating thickness was due to the decrease in metal ions concentration in the ingrowing coating. The highest metal to nitrogen ratio was achieved at the bias voltage of - 65 V and the coating produced at this bias voltage had the highest thickness value (2.15 µm).

Bias Voltage (V)	Chemical composition (Atomic %)		
	Cr	Nb	N
- 40	29.4 ± 0.3	13.7 ± 0.2	56.8 ± 0.6
- 65	39.51 ± 1.3	14.13 ± 0.5	46.36 ± 0.8
- 100	25.89 ± 0.4	13.30 ± 0.7	61.11 ± 0.5
- 150	19.15 ± 0.8	10.00 ± 0.5	70.84 ± 0.2

Table 4.4. Chemical compositions of the deposited coatings as a function of substrate bias voltage.

4.2.4 Physical properties

4.2.4.1 Hardness

Coating hardness and Young's Modulus were determined using CSM nano hardness tester. Table 4.5 presents the results from the hardness measurements of the coatings deposited at various bias voltages.

Bias Voltage (V)	Hardness (GPa)	Vickers (H_{Vk})	Young's Modulus (GPa)
- 40	19.74 ± 2.4	1828 ± 381	296 ± 16
- 65	25.85 ± 3.2	2394 ± 228	312 ± 27
- 100	27.39 ± 3.8	2537 ± 326	326 ± 45
- 150	26.04 ± 3.9	2412 ± 352	316 ± 48

Table 4.5. Hardness, Vickers Hardness, Young's modulus values of the coatings deposited by varying substrate bias voltage.

As seen from the table, the coating produced with the lowest bias voltage of - 40 V had the lowest hardness value (Hardness = 19.74 GPa). Further increase of bias voltage raised the bombarding energy which led to a higher adhesion between the sputtered atoms and the substrate. As a result, the hardness of the coatings was increased and reached the maximum value (Hardness = 27.39 GPa for U_b = - 100 V). However, a slight decrease in the hardness value was observed in case of the coating produced at - 150 V substrate bias. This could be due to the stress relaxation caused by the increased movements of the implanted atoms (adatom mobility) at higher bias voltage. The exclusion of bigger atoms (Nb) from the lattice can also reduce the stress (Table 4.4) and decrease the hardness of the coating deposited at - 150 V [147].

4.2.4.2 Roughness

The roughness values of the coatings are summarised in Table 4.6. As seen from the table, roughness values of the coatings deposited at bias voltages of - 40 V and - 65 V were similar. When the bias voltage increased from - 65 V to - 100 V, the roughness of the coating increased abruptly reaching the highest value (0.083 µm). Further increase in the bias voltage to - 150 V decreased the roughness to 0.073 µm. The initial increase in roughness with the increase in bias voltage is believed to be associated with the surface damage due to the intense re-sputtering. It is well known that the roughness value of the coating depends not only on the coating morphology but also on the surface defect density [53]. In later sections (4.2.6 and 4.2.7), the effects of bias voltage on coating morphology and defects generation were thoroughly studied.

Bias Voltage (V)	Roughness, Ra (µm)
- 40	0.040 ± 0.004
- 65	0.039 ± 0.002
- 100	0.083 ± 0.005
- 150	0.073 ± 0.001

Table 4.6. Roughness of the coatings deposited by varying substrate bias voltage.

4.2.5 Crystallographic structure

Fig. 4.18 shows the XRD patterns as a function of the substrate bias voltage during the deposition. This study revealed that the fcc lattice structure of the coatings remained same but the orientation of crystallographic planes changed with the variation of bias voltage. The coating deposited at - 65 V, displayed a pronounced (111) orientation of nitride phase whereas all other coatings (deposited at - 40 V, - 100 V, - 150 V) showed

(200) preferred orientation. The change in the chemical composition due to the preferential re-sputtering of coating materials at different bias voltage can cause the variation in the structure of the chromium nitride and niobium nitride layers (see Fig. 4.19) [94]. As a result, preferential crystallographic orientations of the coatings were changed.
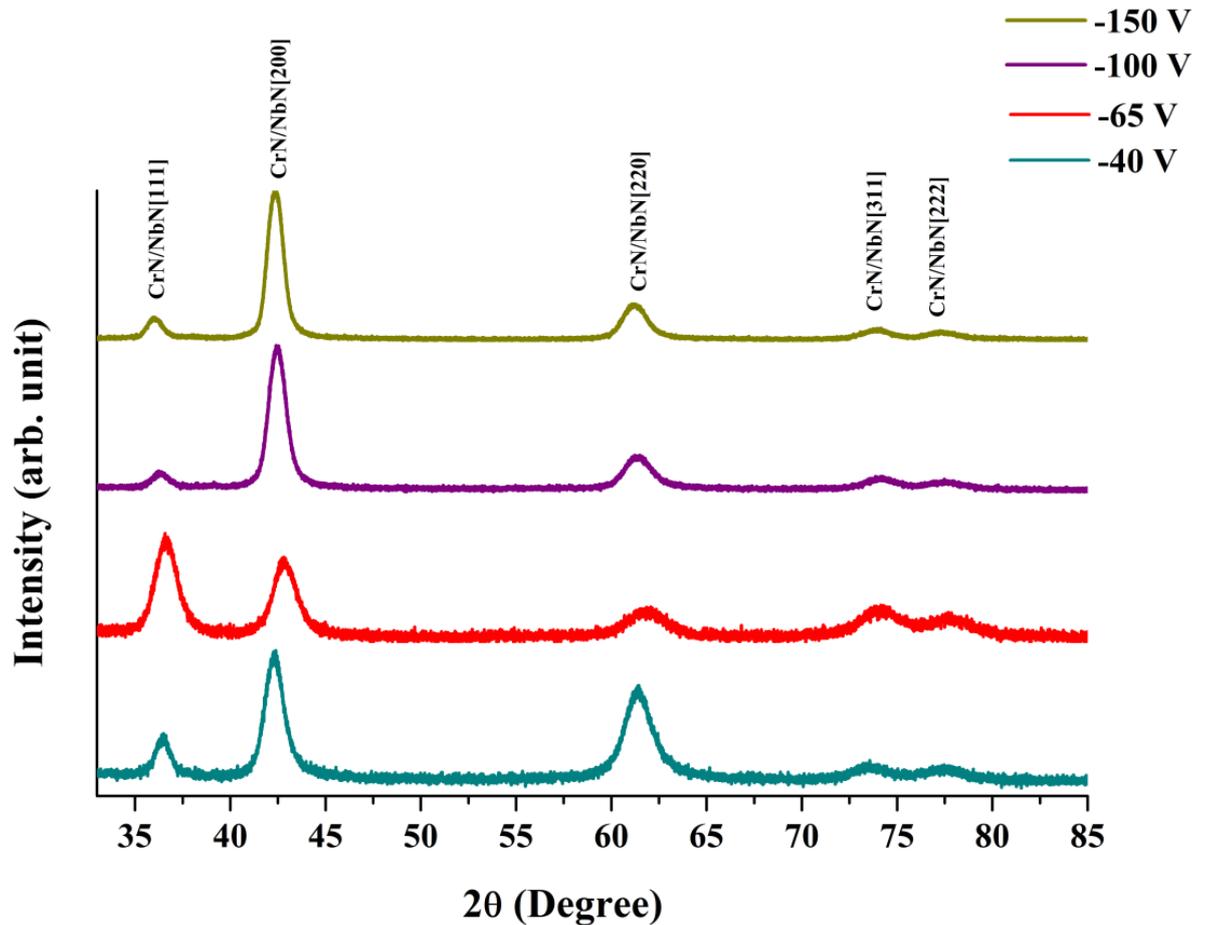
Fig. 4.18. XRD patterns CrN/NbN nanoscale multilayer coatings by varying substrate bias voltage.

To evaluate the effect of bias voltage on the bilayer thickness of the multilayer CrN/NbN coatings, Low Angle ($2\theta = 1°$ to $10°$) X-ray Diffraction (LAXRD) was used. Fig. 4.19 shows the LA XRD patterns of the coatings.

The superlattice spacing is a function of the deposition rate [94]. As discussed in this study, the bias voltage applied to the substrate influenced the deposition rate (sec 4.2.2). Subsequently, it caused similar variation in the bilayer thickness of the coatings.
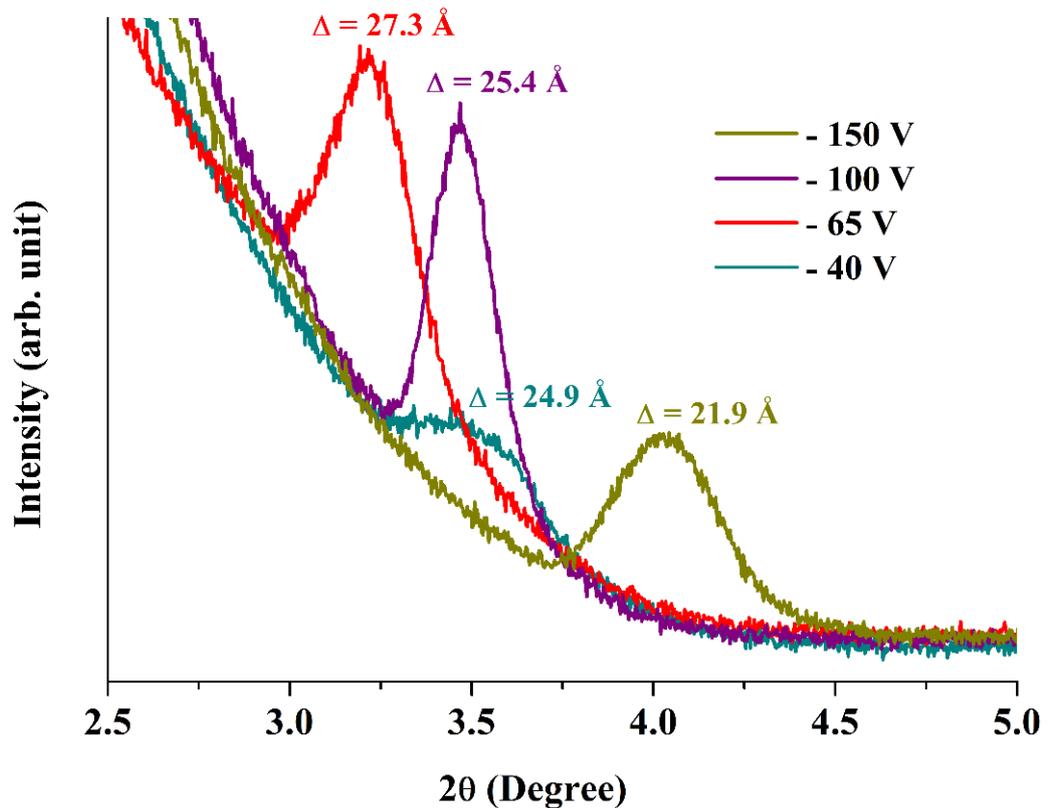
Fig. 4.19. Low angle diffraction peaks from the coatings deposited by varying substrate bias voltage.

4.2.6 Topography and Microstructure

SEM was used to study the coating morphology and microstructure. Fig. 4.20 (a-h) shows the planar and cross-sectional SEM images of the coatings.
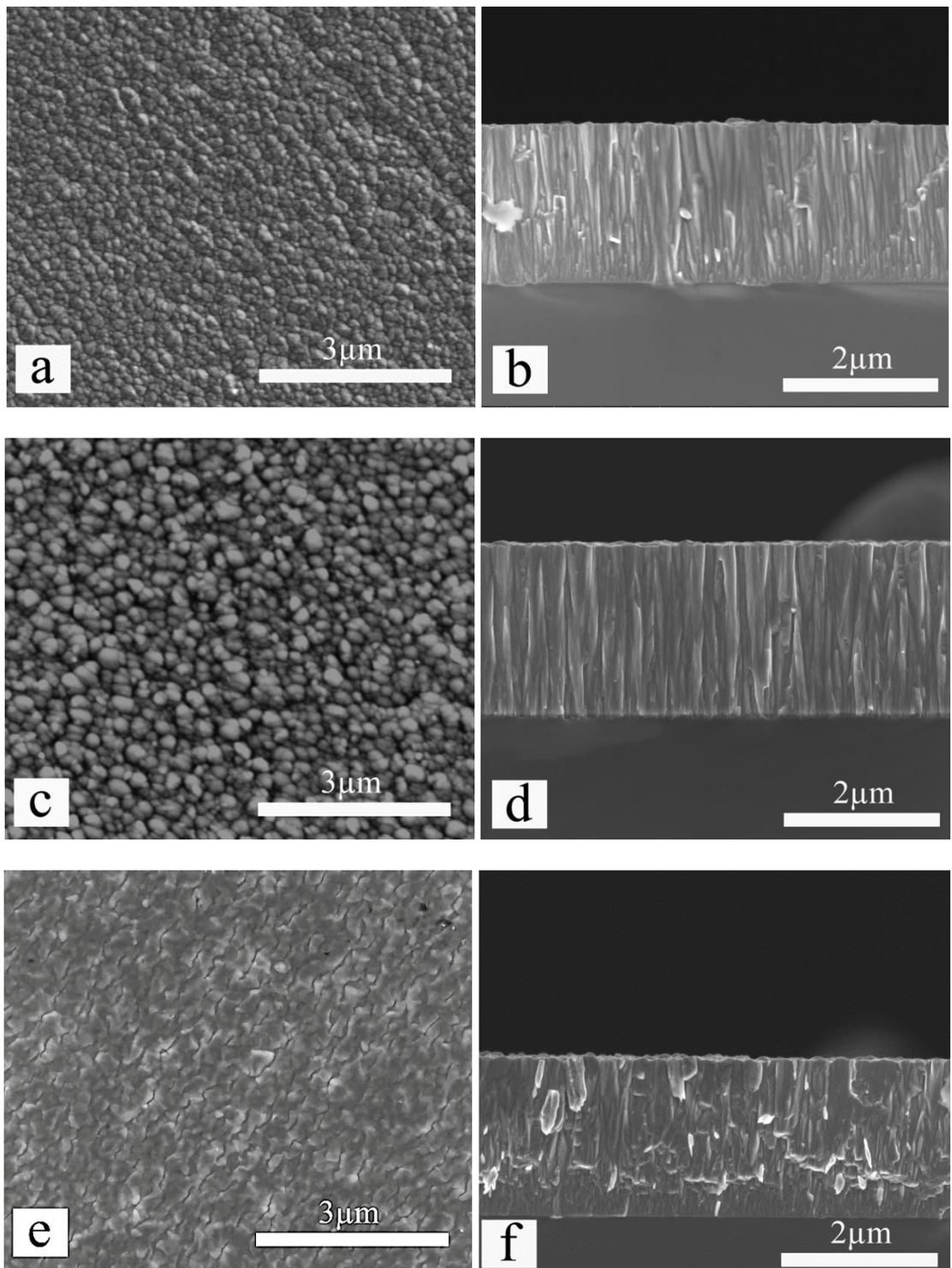
Fig. 4.20. (Continue)
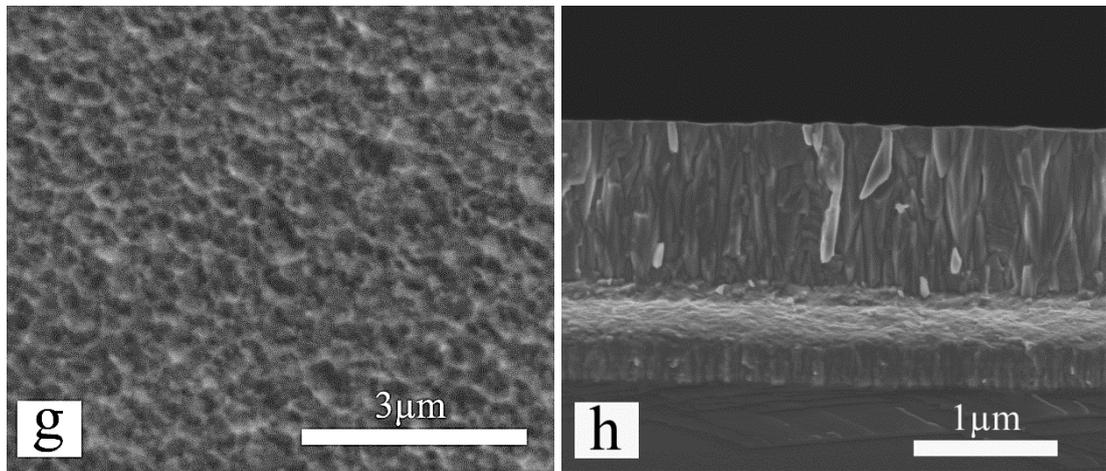
Fig. 4.20. (a) Planar and (b) cross-sectional SEM image of coating deposited at - 40 V;

(c) Planar and (d) cross-sectional SEM image of coating deposited at - 65 V; (e) Planar

and (f) cross-sectional SEM image of coating deposited at - 100 V; (g) Planar and (h)

cross-sectional SEM image of coating deposited at - 150 V bias voltage.

The coating deposited at - 40 V substrate bias exhibited a columnar structure with

rounded columnar tops (Fig. 4.20a,b). With an increase of bias voltage from - 40 V to

- 65 V, coalescence of adatoms increased leading to an increase in the columnar

densities (Fig. 4.20c); however, the columnar morphology remained same (Fig. 4.20d).

As the bias voltage was further increased to - 100 V, the columnar grains were dissolved

gradually by the grain coarsening process (Fig. 4.20e). Fig. 4.20f shows the cross-

sectional view of this coating (U_b = - 100 V) which clearly exhibits the influence of

increasing bias voltage on microstructure densification. The column microstructure in

the case of the coating deposited at U_b = - 150 V was even harder to resolve giving an

impression of a bulk material (Fig. 4.20g). The changes in the coating microstructure

and surface morphology with the bias voltage can be attributed to the increased surface

mobility of adatoms on the growing film [53,55–58,61,62]. This increased adatom

movement promoted the grain refinement by filling the voids between the grains,

breaking down the large columnar grain growth and creating more nucleation sites. As a result, columnar grain free, a very dense coating was produced at the highest bias voltage of -150 V.

The microstructural evolution of these coatings can be correlated nicely with the SZM proposed by Messier, Giri and Roy [70]. However, the HIPIMS/UBM deposition process is an energetic process [72,102], thus the zone 1 could not be traced. The coating deposited at U_b = - 40 V and - 65 V exhibited inhomogeneous structure along the film thickness (Fig 4.20b,d) which corresponds to Zone T. The upper parts of both coatings showed wide columnar structure while at the substrate, fine grains could be observed. However, with the increase of negative substrate bias from - 40 V to - 65 V, the adatom mobility was increased. As a result, the columns became wider for the coating deposited at U_b = - 65 V. Further increase in negative substrate bias from - 65 V to - 100 V promoted grain boundary migration which transformed the structure from Zone T to Zone 2. The coating deposited at U_b = - 150 V had randomly orientated grains (Fig. 4.20h) which was the result of recrystallisation process. The structure of this coating represented Zone 3 structure of SZM.

4.2.7 Surface defect density

SEM images revealed that all the coatings have similar type of defects (similar defects were discussed in sec 4.1.6), but the number of defects increased with the increase of bias voltage. To quantify the defect population, density of the coating defects was calculated using optical microscopy and Image J software (described in the earlier sections 3.2.2.4 and 4.1.6.2).
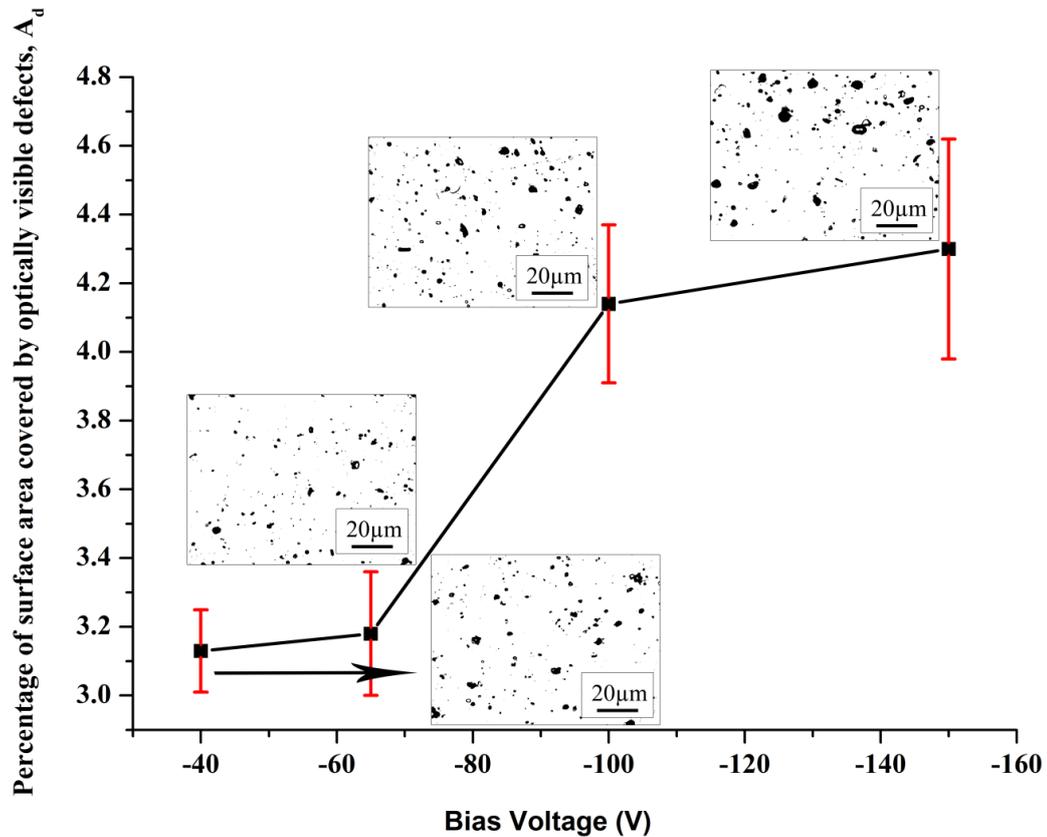
Fig. 4.21. Variation of surface area coved by optically visible defects as a function of substrate bias voltage.

The calculated defect densities (A_d) of the coatings deposited at bias voltages of - 40 V and - 65 V were similar (A_d = 3.13 % and 3.18 % respectively). Whereas, a sudden increase in A_d value (4.14 %) was observed when a higher bias voltage (U_b = - 100 V) was applied to the substrate. This result justifies the roughness values of the coatings (Table 4.6). The increase in surface defect density with the increase in bias voltage resulted in rougher surfaces. As a result, the roughness value suddenly increased from 0.039 to 0.083 µm. Although, there was a slight decrease in roughness value from 0.083 to 0.073 µm when bias voltage increased from - 100 V to - 150 V. This could be due to the densification of the coating as the grain boundaries and columnar morphology

146

disappeared at - 150 V substrate bias (Fig. 4.20g). Thus, the roughness of the coating was attributed to the surface defect density as well as the coating morphology.

The increase in surface defect density with the increase of substrate bias was associated with two factors. At higher bias voltages, the high-energy flux bombardments on chamber components can increase the flakes generation. These flakes can produce more defects in the coating. Nevertheless, re-sputtering phenomena can also be responsible for raising the surface defect density. At very high negative bias voltages, the extremely high-energy bombardment on the growing coatings can expose the already formed defects and hence increase the area under the defects. Also, some loosely bound nodular defects can be expelled from the coatings leaving more visible voids.

4.2.8 Corrosion resistance

Fig. 4.22 shows the Potentiodynamic polarisation curves of the coatings deposited at various bias voltages. It is clear from the curves that the increased substrate bias improved the corrosion resistance of the coatings. As observed from the SEM images, increased negative bias densified the coating. Thus, the higher corrosion resistance of the coatings was attributed to the densification of coatings with the increase of substrate bias voltage. The coatings produced by ABS technique also showed similar trend [14]. The increase in negative bias voltage from - 75 V to - 95 V improved the corrosion performance of the coatings.

In the anodic potential ranging from - 248 mV to + 475 mV, the corrosion current density was notably higher (one order of magnitude) for the coating deposited at - 40 V bias voltage than that of the coatings deposited at higher bias voltages (- 100 V, - 150 V). Although surface defect density of this coating (U_b = - 40 V) was the lowest (A_d = 3.13 %), the under-dense structure of the coating played the most important role in

determining corrosion resistance. The coatings deposited at higher substrate bias voltages ($\geq$ - 65 V) exhibited similar corrosion current values in the anodic potential ranging from 3.4 mV to + 358 mV which suggested that - 65 V can be used as the optimum bias voltage to produce dense coatings for corrosion applications.
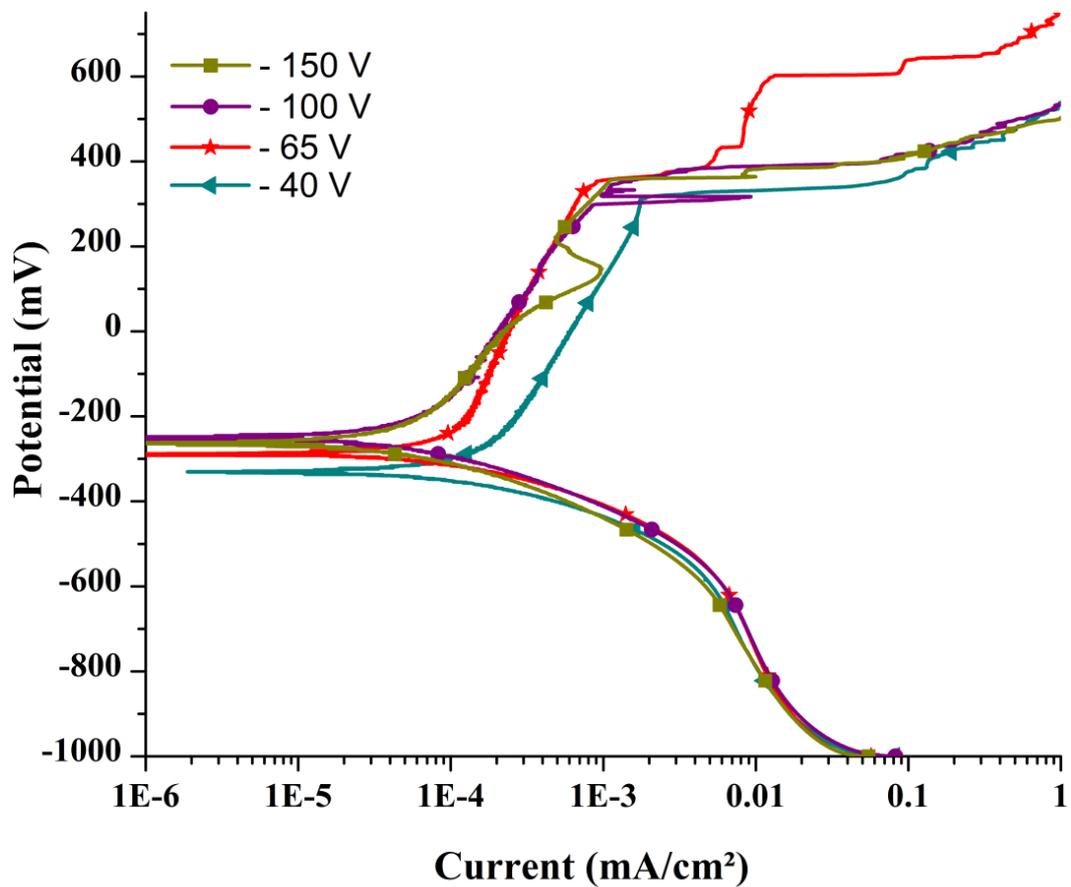
Fig. 4.22. Potentiodynamic polarisation curves of the coatings deposited at various bias voltages.

Apparently, the effect of the higher number of defects on coating corrosion performance was also observed. The coating deposited at bias voltage - 100 V and - 150 V had higher defect densities (A_d = 4.14 % and 4.30 %) and the polarisation curves of both coatings evidenced the formation of metastable pits which are believed to be associated with the

growth defects. The removal of nodular/cone-like defects can expose the fresh substrate surface to the corrosive media thus raise the electrochemical reaction kinetics which can be observed by the sudden increase in current densities at around 300 mV and 50 mV for the coatings deposited at $U_b = -100$ V and -150 V respectively.

4.2.9 Tribological properties

4.2.9.1 Determination of wear and friction coefficients

A room temperature Pin-on-disc tribometer was used to study the friction behaviour of the deposited coatings in dry sliding condition. Fig. 4.23 shows the dependence of friction coefficient on number of revolutions (friction cycles) for the coatings deposited at various bias voltages.
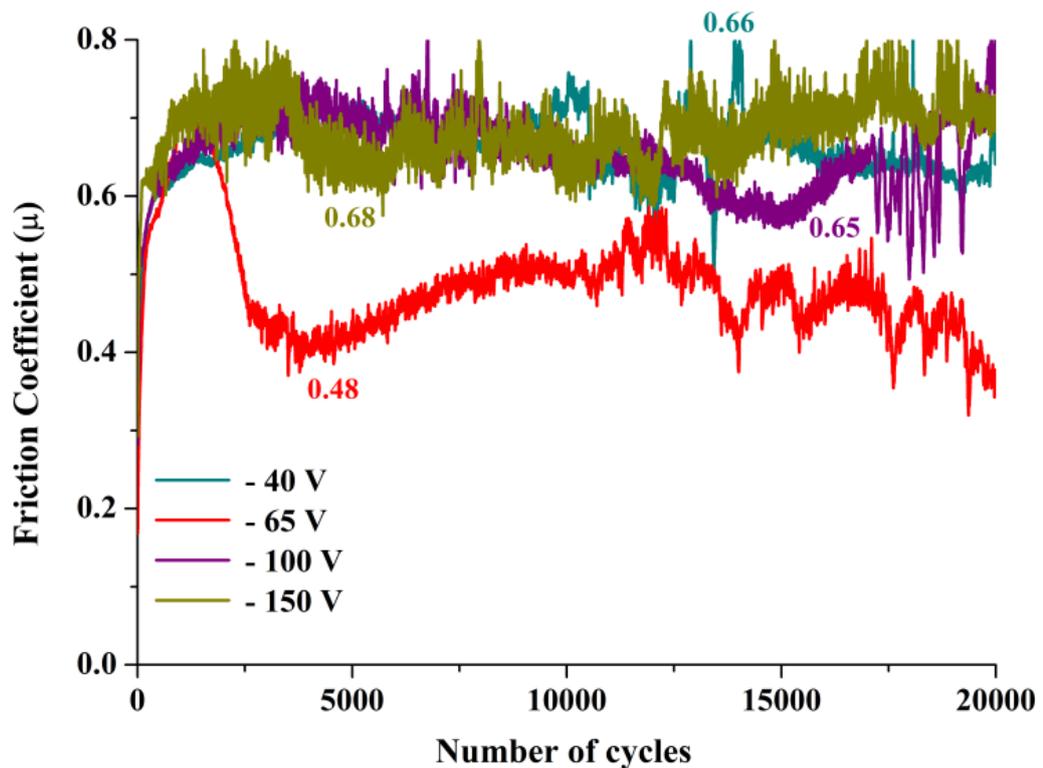
Fig. 4.23. Dependence of friction coefficient on number of revolutions (friction cycles) for the coatings deposited at various bias voltages.

Although, influence of surface defect density on friction values was not apparent; the fluctuation in friction values was observed for all the cases. These fluctuations are believed to be associated with coating defects. All these coatings had higher surface defect density ranging from 3.13 % to 4.30 %. Due to the height of the defects (nodular/cone-like), they are subjected to a full contact during sliding [4]. As a result, the nodular/cone-like defects experience high stresses which cause their fracture and spalling. The debris generated from the nodular defects creates tribological film within the wear tracks. The shape and the position of the film patches are not stable during the wear test and these phenomena probably cause the fluctuations in the COF values [4]. During sliding poorly attached nodular defects could be pulled out from the coating and create voids within the wear tracks. In corrosive environments these defects can act as potential sites for corrosive attacks. Fig. 4.24a represents the SEM image of the wear track showing voids, generated due to the removal of coating defects. High magnification SEM image of such void can be seen in Fig. 4.24b.
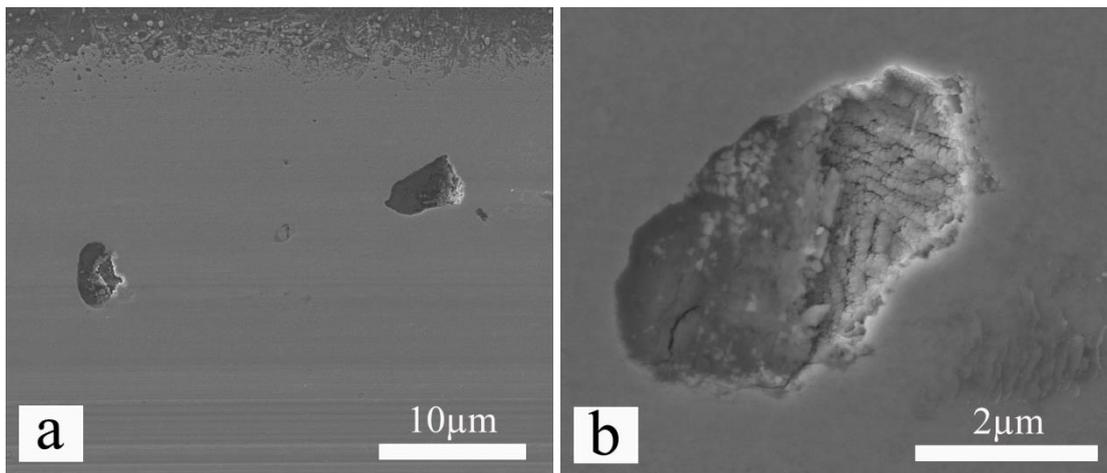
Fig. 4.24. (a) SEM image of the wear track and (b) void within the wear track.

Optical microscopic images of the wear tracks are shown in Fig. 4.25 which indicates that all the coatings experienced abrasive wear during sliding. Due to the three body ploughing action [104], narrow grooves of few nanometer in width were created. These grooves became more pronounced for the coatings deposited at higher bias volatages ($\geq$ - 100 V) (Fig. 4.25c,d). Also, a higher number of voids (black dots) can be seen within the wear tracks of these coatings. Higher bias voltages induced stress in the coatings. Thus, more defects from coatings deposited at higher bias volateges of - 100 V and - 150 V were expelled when load was applied during tribological tests. Also, the defect densities were higher for these coatings. The removal of large number of defects produced more wear debris, which subsequently damaged the surface more severely.
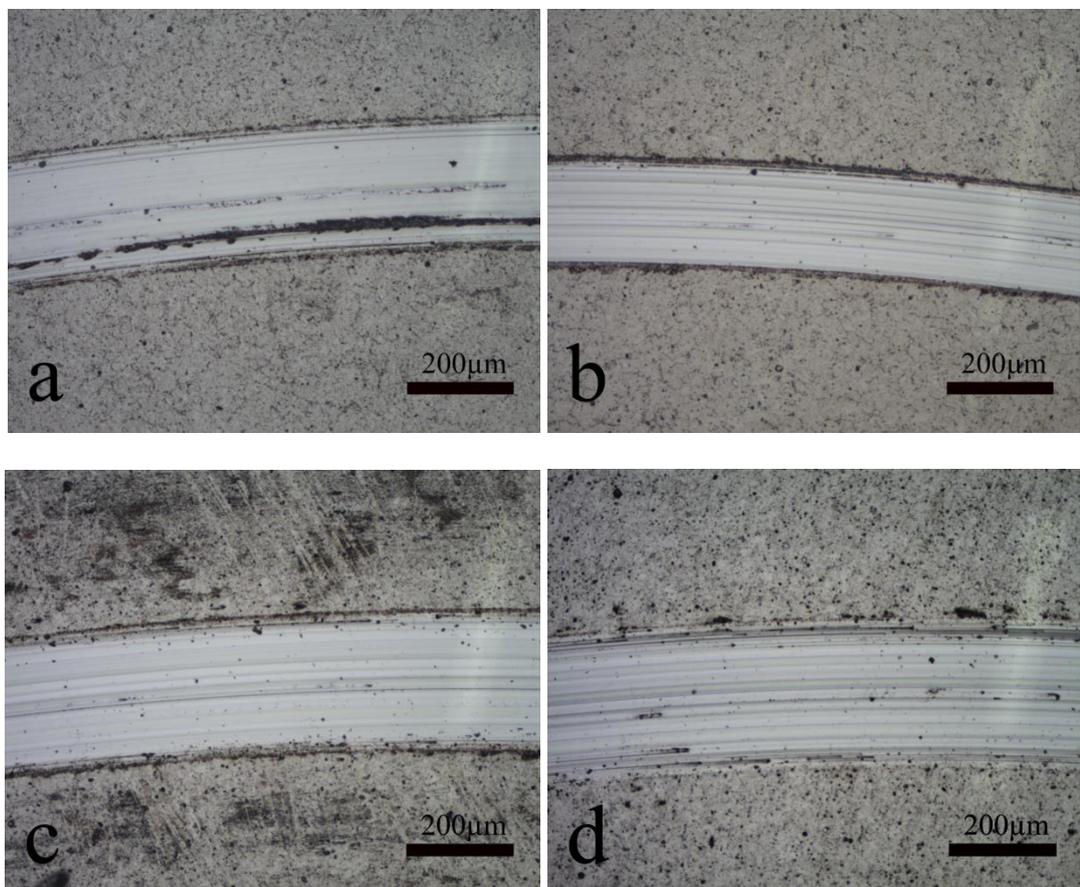
Fig. 4.25. Optical image of the wear track of the coating deposited at (a) - 40 V, (b) - 65 V, (c) - 100 V and (d) - 150 V.

Fig. 4.26 represents the wear track profiles analysed using a DEKTAK 150 profilometer. Coefficient of wear (K_C) was found to be the highest (4.19 $\times$ 10^{-15} $m^3N^{-1}m^{-1}$) for the coating deposited at the lowest bias voltage of - 40 V. The low hardness (19.74 GPa) and under-dense columnar structure of this coating could not defend the applied load. As a result, large amount of coating materials was removed during sliding. Fig. 4.25a shows the debris in the wear track (black line) produced due to the removal of coating materials.

With the increase of bias voltage from - 40 V to - 65 V, a significant improvement in wear resistance was observed (K_C = 2.68 $\times$ 10^{-15} $m^3N^{-1}m^{-1}$ for - 65 V). This could be attributed to the strong interaction between the columns which provided effective protection against cracking and plastic deformation thus reducing the material removal rate of the coating [104].

Further increase of the bias voltage was found to be ineffective in enhancing the wear resistance rather it degraded the wear properties. As discussed earlier, the application of higher bias voltage ($\geq$ - 100 V) increased the defect density. During the tribo test, a higher amount of defect removal (black dots in Fig. 4.25c,d) could increase the debris generation. As a result of these combined effects, wear rates for the coatings deposited at - 100 V and - 150 V substrate bias were increased to K_C = 3.36 $\times$ 10^{-15} $m^3N^{-1}m^{-1}$ and 3.85 $\times$ 10^{-15} $m^3N^{-1}m^{-1}$ respectively.

In addition, the bilayer thickness of the coatings can also influence the wear resistance [81,86–93]. As discussed in the sec 4.2.5, the bilayer thickness of the coating deposited at - 65 V substrate bias was higher (Δ = 27.3 Å) than the other coatings. Interestingly, this coating (U_b = - 65 V) provided the best resistance against wear. While for the coatings deposited at U_b = - 40 V, - 100 V, - 150 V, the bilayer thickness values were found to be lower (Δ = 24.9 Å, 25.4 Å and 21.9 Å respectively). This study indicated that relatively thicker (here 27.3 Å) hard layers reduced the plastic deformation and the

abrasive penetration in the metal layers. As a result, the wear volume of the coating was decreased to the lowest value.
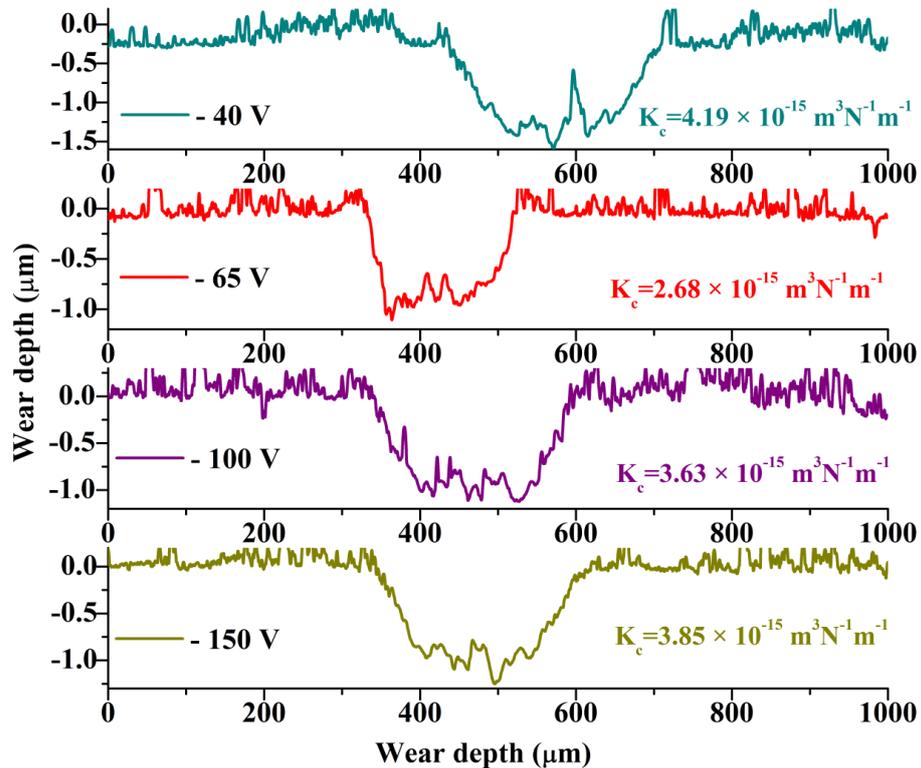
Fig. 4.26. Wear track profiles of the coatings deposited at various bias voltages.

4.2.9.2 Raman Spectroscopy

Although the coating defects influenced the wear mechanism, the friction values were not affected by it. As found in the sec 4.1.8.2, friction values can depend on the oxides formed during the tribological tests [114,118]. Hence, the Raman spectra from the wear tracks and wear debris were obtained using a Raman spectrometer (Horiba-Jobin-Yvon LabRam HR800). Fig. 4.27 represents the Raman spectra obtained from the wear debris beside the wear tracks of the coatings deposited at various bias voltages.

The wear debris of the coatings deposited at U_b = - 100 V, - 150 V exhibited a pronounced peak at 790cm^{-1} which is a characteristic of CrNbO$_4$ [118,142] and both the

coatings had similar friction values (μ = 0.65 and 0.68 respectively). The coatings produced at U_b = - 40 V and - 65 V showed similar types of Raman spectra however the intensity of the peak at around 835 cm^{-1} was higher for the coating deposited at U_b = - 40 V. This could be due to the production of Nb_2O_5 , nH_2O [118,142] which could also lead to an increase in μ value. However, the most possible reason for higher μ value of the coating deposited at U_b = - 40 V than the coating deposited at U_b = - 65 V was the difference in microstructure of these two coatings. Due to breakdown of the coating and formation of a tribological film within the wear track (Fig. 4.25a) the μ value of this coating (U_b = - 40 V) was increased to 0.66 as compared to μ = 0.48 for the coating deposited at U_b = - 65 V.
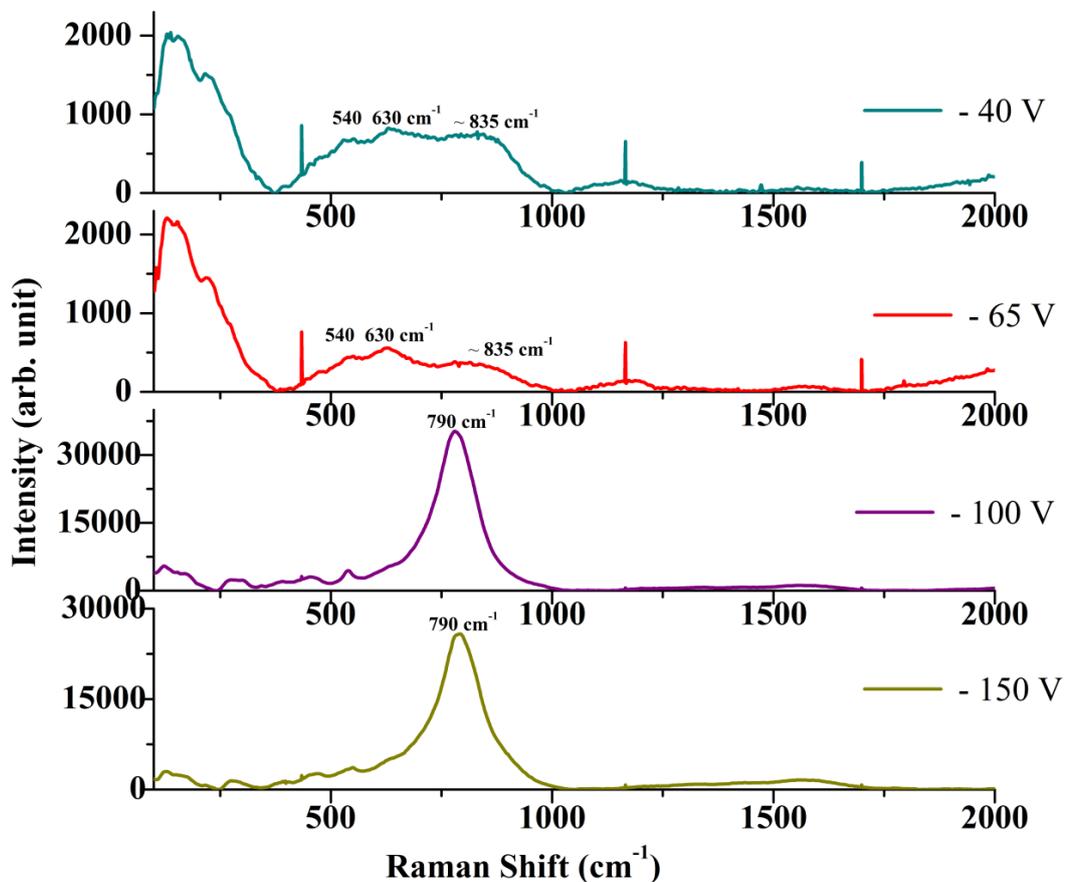
Fig. 4.27. Raman spectra obtained from the wear debris of the coatings deposited at various bias voltages.

4.2.10 Summary

- The microstructures, chemical compositions, crystallographic orientation, bilayer thickness and also the surface defect density of the nanoscale CrN/NbN coatings were influenced by the bias voltage applied to the substrate.

- The study of coating defects suggested that the increase in the surface defect density with the bias voltage was caused by the re-sputtering and the flakes generation due to the high-energy flux bombardment on chamber components.

- The corrosion study confirmed the positive influence of dense microstructure on the coating barrier properties. The effect of coating defects was also apparent. Corrosion curves of the coatings with higher defects exhibited sudden increases in current densities due to the removal of loosely bound defects.

- The wear mechanisms of the coatings were dominated by the removal of coating defects during the tests as well as by the bilayer thickness. The coating with the maximum bilayer thickness showed the lowest wear rate.

- Raman study on wear tracks and wear debris suggested that the tribological friction values of the coatings were dependant on the nature of the oxides produced during the tests. However, coating microstructure also influenced μ value.

- In this study, - 65 V was found to be the optimum bias voltage to produce coatings with low friction, low wear rate and higher corrosion resistance.

4.3 Influence of total chamber pressure on HIPIMS/UBM deposited CrN/NbN coatings

4.3.1 Overview of the experiments

The chamber pressure has a significant but complicated influence on the kinetics of plasma species in a sputtering system [148][149]. During the deposition, an increase in chamber pressure increases the number of available molecules to collide with electrons, resulting to more number of free electrons in the chamber. This could increase the sputtering rate as the plasma becomes more ionised (active) with the increase in chamber pressure.

On the other hand, higher chamber pressure can decrease the energy of the ions. The higher pressure increases the density of species in the chamber which subsequently decreases the mean free path of the electrons and the other elements (metal ions coming from the target) resulting in a decrease in the sputtering rate. Thus, optimisation of chamber pressure is required to produce coatings with the desired thickness and density. Nevertheless, in the case of reactive sputtering, N_2 partial pressure influences the coating properties remarkably [59,60,148,150–155]. For this reason, it is intriguing to examine the effect of total chamber pressure on the coating growth as well as on defect formation.

To study this, three sets of CrN/NbN nanoscale multilayer coatings were deposited at chamber pressures (P) of 0.2 Pa, 0.35 Pa and 1 Pa. During all the depositions, Ar and N_2 (1:1) were used as the process gas. The bias voltage (U_b) and deposition time (t) were fixed at - 65 V and 120 min respectively.

4.3.2 Coating thickness

SEM was used to measure the coating thickness. The variations in the coating thickness with the chamber pressure are summarised in table 4.7.

Chamber Pressure (Pa)	Thickness (µm)
0.2	3.65 ± 0.01
0.35	2.15 ± 0.02
1	2.18 ± 0.01

Table 4.7. Coatings thickness as a function of chamber pressure.

The table shows that the thickest coating (3.65 µm) was produced at the lowest chamber pressure (0.2 Pa). The thickness then decreased suddenly to 2.15 µm with the increase of chamber pressure to 0.35 Pa. The reason for decreasing thickness could be due to the re-sputtering of coated flux at high pressure. Also, the diffusive collisions of depositing species within the plasma and the target poisoning can decrease the deposition rate [40,156]. For reactive sputtering, target poisoning is a very common phenomenon [157]. Although, during these coating depositions, N_2 and Ar flow rates (sccm) were always fixed at 1:1, a slight increase in the ratio of the partial pressures of N_2 and Ar with the increase of the chamber pressure was observed. The ratio (P_{N_2} / P_{Ar}) was varied from 0.85 at 0.2 Pa to 0.95 at 1 Pa. The change in the partial pressures could slightly increase the target poisoning at the higher chamber pressures. Due to the formation of nitride layers on the target surfaces the sputter rate was reduced. Nevertheless, the mean free paths (ℓ) of the plasma species (neutral atoms, ions) were also reduced with the increase of chamber pressure. The reactive gas (Ar + N_2) atmosphere during HIPIMS process is highly ionised [48], which makes the kinetics of the atoms/ions extremely complex.

However, assuming the plasma atmosphere to be similar to the ideal gas atmosphere, the mean free paths at different chamber pressure were calculated (using Van der Waals radius (R) of Nitrogen = 1.55×10^{-10} m). At 0.2 Pa chamber pressure, the ℓ value was found to be 0.64 m. The ℓ value then decreased to 0.37 m at P = 0.35 Pa and 0.13 m at P = 1 Pa. This calculation clearly indicated that the collision frequency was higher at higher chamber pressures. Thus, the decrease in deposition rate at higher chamber pressure could be attributed to the combined effect of target poisoning and re-sputtering & diffusive collision of depositing materials.

Further increase in chamber pressure from 0.35 Pa to 1 Pa increased the thickness slightly from 2.15 µm to 2.18 µm. The complex nature of the plasma is believed to be the reason for this increase in thickness. The mechanisms stated in the sec 4.3.1 can explain this behaviour. At the chamber pressure of 1 Pa, plasma ionisation could be more intense than the diffusive collisions as compared to that of at P = 0.35 Pa. As a result, the sputtering rate was increased a little. Fig. 4.28 shows the variation of the coating thickness as a function of chamber pressure.
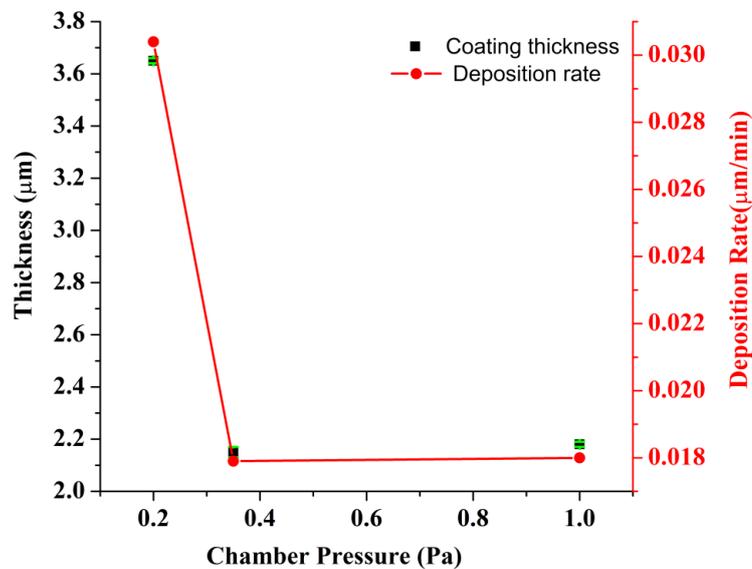
Fig. 4.28. Coating thickness and deposition rate as a function of chamber pressure.

4.3.3 Chemical composition

Using EDX, the chemical compositions of the coatings were evaluated. As seen from the Table 4.8, the change in the chamber pressure altered the atomic percentages of the elements in the deposited coatings. The coating deposited at the lowest chamber pressure of 0.2 Pa had the highest metal to nitrogen ratio ((Cr + Nb) / N). The longer mean free paths of the sputtered species at lower pressure increased the possibility of metal species (Cr + Nb) to reach the substrates without colliding with the gas species [40]. As a consequence, the coatings deposited at lower chamber pressure contained higher metal species.

With the increase in chamber pressure from 0.2 Pa to 1 Pa, atomic percentage of nitrogen increased from 44.83 % to 50.95 % due to the increase of nitrogen gas in the chamber [60]. At the highest chamber pressure of 1 Pa, preferential re-sputtering decreased the Cr percentage to the lowest value (34.10 %).

Chamber Pressure (Pa)	Chemical composition (Atomic %)		
	Cr	Nb	N
0.2	38.41 ± 0.3	16.76 ± 0.2	44.83 ± 0.4
0.35	39.51 ± 1.3	14.13 ± 0.3	46.36 ± 0.8
1	34.10 ± 1.3	14.94 ± 0.9	50.95 ± 1.2

Table 4.8. Chemical compositions of the deposited coatings as a function of chamber pressure.

4.3.4 Physical properties

4.3.4.1 Hardness

Hardness and Young's Modulus values of the coating are summarised in Table 4.9. As observed, the hardness value of the coating deposited at the lowest chamber pressure of 0.2 Pa was the highest (26.38 GPa). The higher hardness value of this coating could be associated with the higher coating thickness and the higher metal concentration.

Chamber Pressure (Pa)	Hardness (GPa)	Vickers (H_{Vk})	Young's Modulus (GPa)
0.2	26.38 ± 4.2	2442 ± 390	323 ± 30
0.35	25.85 ± 3.2	2394 ± 228	312 ± 27
1	23.45 ± 3.7	2172 ± 346	303 ± 43

Table 4.9. Hardness, Vickers Hardness, Young's modulus values of the coatings deposited at various chamber pressures.

4.3.4.2 Roughness

Table 4.10 represents the roughness values of the coatings deposited at various chamber pressures. In section 4.2.7, the roughness of the coating was found to be influenced by the coating morphology and surface defect density. Similarly, the change in roughness value with the chamber pressure is believed to be associated with the change in morphology and surface defect density with the variation of chamber pressure. In later section (4.3.6 and 4.3.7), coating morphology and the surface defect density have been studied which could help to understand the variation in roughness value with the chamber pressure.

160

Chamber Pressure (Pa)	Roughness, Ra (µm)
0.2	0.025 ± 0.001
0.35	0.039 ± 0.002
1	0.039 ± 0.000

Table 4.10. Roughness of the coatings deposited at various chamber pressures.

4.3.5 Crystallographic structure

XRD was used to determine the crystallographic orientations as well as the bilayer thickness of the coatings. High angle XRD peaks are shown in Fig. 4.29, whereas Fig. 4.30 represents the Low angle (LA) XRD.

This measurement revealed that the crystal structures of nanoscale CrN/NbN coatings were of a single phase fcc lattice. The coating deposited at the lowest chamber pressure of 0.2 Pa displayed a pronounced (200) orientation of nitride phase. With the increase of chamber pressure to 0.35 Pa, the preferred orientation was shifted from (200) to (111). For the highest chamber pressure of 1 Pa, the preferred orientation was again changed to (200). Similar behaviour was observed for CrN coatings when the nitrogen percentage was varied [158]. The change in the crystallographic orientation was attributed to the change in composition between the chromium nitride and niobium nitride layers in the structure [94] associated with the change in the nitrogen volume within the chamber. One satellite peak (sp) is visible at the left sides of the (200) for the coating deposited at P = 0.2 Pa. The existence of well-defined satellite peaks indicates good coating crystallinity, as well as good chemical modulation of the multilayer [81,91,113]. This study suggested that the higher hardness of this coating was the result of well-defined interfaces.

As seen from the Fig. 4.30, this coating had the highest bilayer thickness (Δ = 39.3 Å). For multilayer coatings, thickness of individual layers can affect hardness [67,81,86–93]. Thus, along with the good crystallinity and well defined interfaces, the higher bilayer thickness also increased the hardness.

With the increase of chamber pressure from 0.2 Pa to 0.35 Pa, the bilayer thickness decreased to a much lower value of 27.3 Å. Further increase in pressure from 0.35 Pa to 1 Pa slightly increased the Δ value to 31.1 Å showing the similar trend of increasing thickness from 2.15 µm to 2.18 µm.

However, the coating deposited at highest pressure of 1 Pa had the lowest hardness value of 23.45 GPa in spite of having a higher bilayer thickness than the coating deposited at 0.35 Pa. The reason could be the stress relaxation caused by the inclusion of smaller atoms (N) in the lattice [147] (as seen in the Table 4.8).
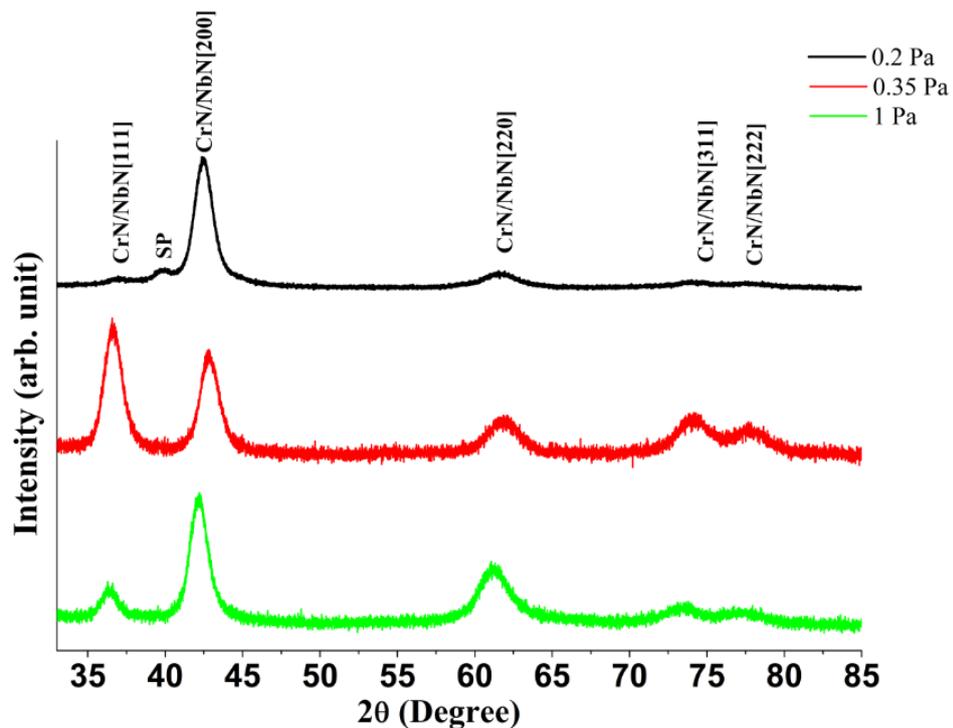
Fig. 4.29. XRD patterns of CrN/NbN nanoscale multilayer coatings deposited at various chamber pressures.
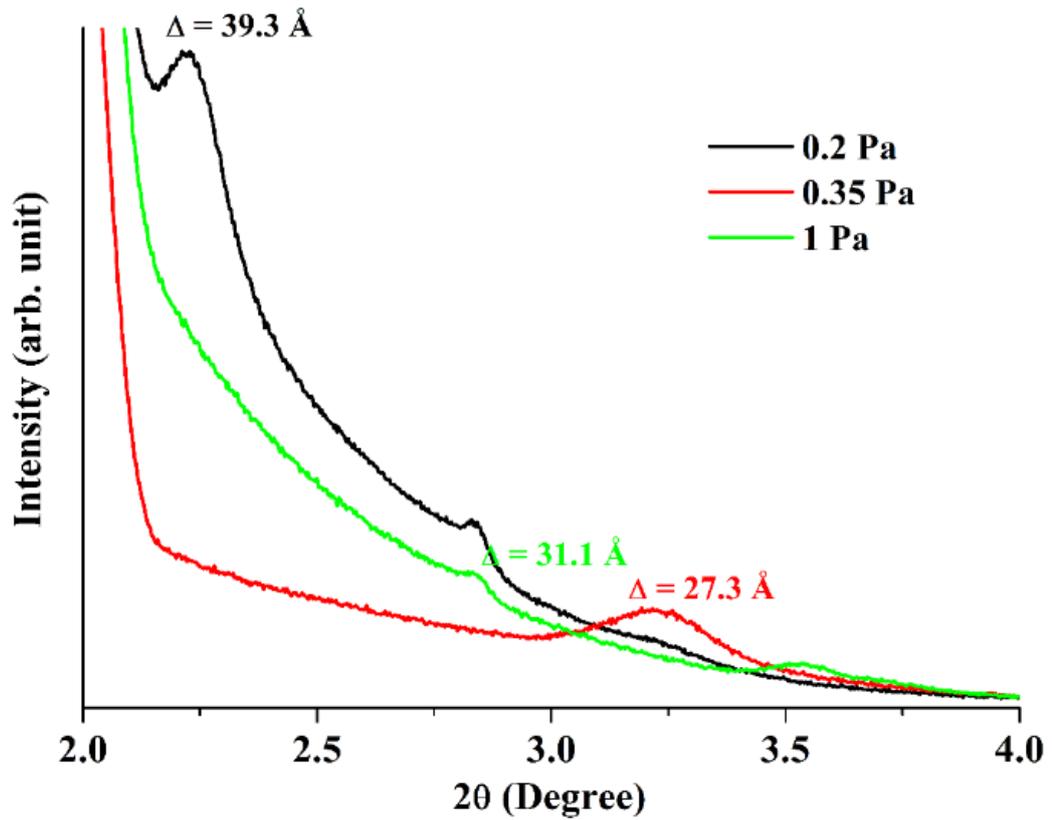
Fig. 4.30. Low angle diffraction peaks from the coatings deposited at various chamber

pressures.

4.3.6 Topography and Microstructure

Topography and microstructure of the coating surface were studied using SEM technique. Fig. 4.31 (a-f) shows the planar and cross-sectional SEM images of the coatings.

With the increase of chamber pressure, the coating morphology changed significantly. The coating produced at P = 0.2 Pa had very dense continuous structure (Fig. 4.31 a,b). The surface of this coating looks very smooth which explains the lower roughness value (Ra = 0.025 µm) of this coating.
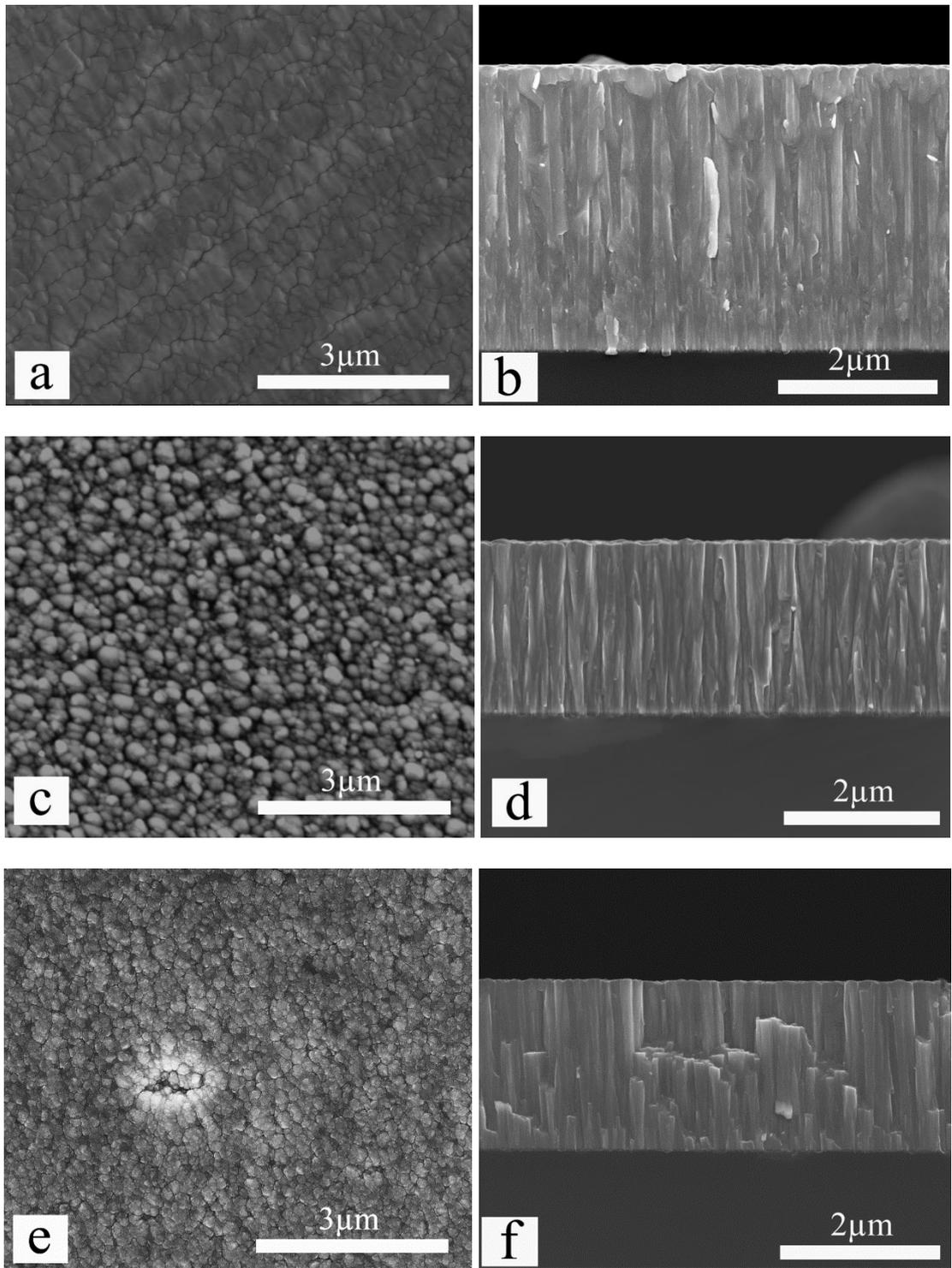
Fig. 4.31. (a) Planar and (b) cross-sectional SEM image of coating deposited at 0.2 Pa;

(c) Planar and (d) cross-sectional SEM image of coating deposited at 0.35 Pa; (e) Planar

and (f) cross-sectional SEM image of coating deposited at 1 Pa.

Increasing pressure from 0.2 Pa to 0.35 Pa changed the morphology to columnar structure with rounded columnar tops (Fig. 4.31c,d). Further increase in chamber pressure again modified the coating morphology. Although, similar columnar structure was still visible for the coating deposited at P = 1 Pa, the grain size decreased (Fig. 4.31e,f). The change in the coating morphology was associated with the variation in the ion energy with the chamber pressure.

4.3.7 Surface defect density

The study on coating morphology revealed the existence of several types of defects in the coatings (already discussed in sec 4.1.6). The density of these defects seemed to be influenced by the chamber pressure. So, the surface defect density calculation was conducted to understand the influence of chamber pressure on defect formation.

Fig. 4.32 shows the relationship of surface defect density (percentage of area covered by optically visible defects) with the chamber pressure. As seen in the figure, the surface defect density was increased from 0.84 % to 5.94 % with increase of the chamber pressure from 0.2 Pa to 1 Pa. The increase in surface defect density was associated with the increase in flake generation. At the higher chamber pressures, plasma volume covers more area of the chamber, which can increase the amount of sputter flux bombardments on chamber components and subsequent flake generation. These flakes can initiate more defect sites and cause further defect formation within the coating. In addition to that, intense re-sputtering at higher chamber pressures can reveal loosely bound defects more and increase the area associated with the defects.
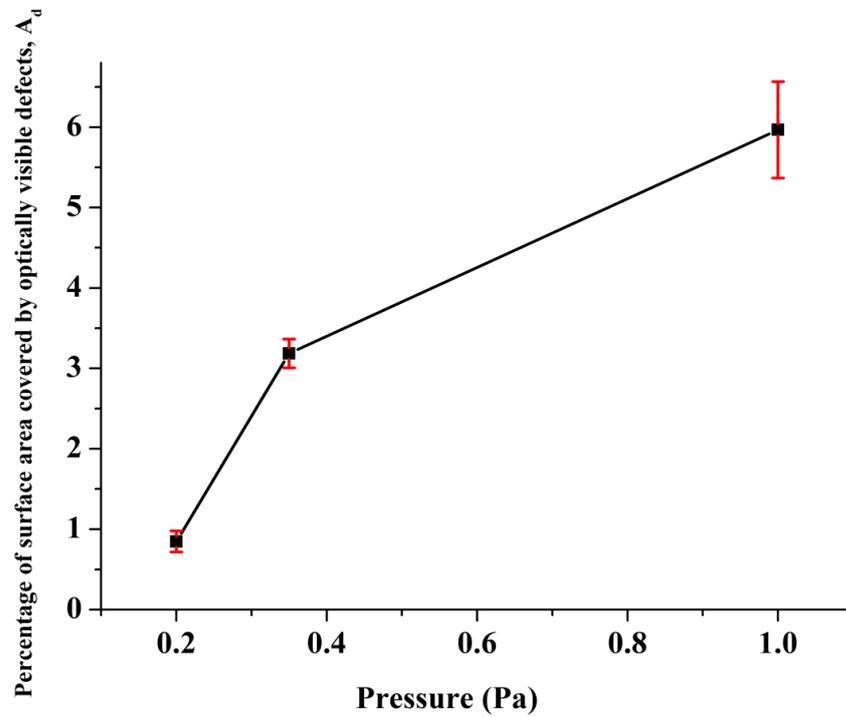
Fig. 4.32. Variation of surface area coved by optically visible defects as a function of chamber pressure.

This study was conducted in a chamber which was not thoroughly cleaned before or between two subsequent coating deposition processes. Although, the easily removable chamber parts were cleaned by sandblasting process and the chamber was cleaned using vacuum cleaner after each process, a complete cleaning of chamber was not possible. The fixed and large chamber parts like heaters; substrate carousel etc. cannot be cleaned on regular basis. The process of removing those parts, cleaning and then again fixing itself is time consuming. Moreover, the total system is needed to shut down in order to clean some parts. And after restarting the system, demo processes are needed to conduct in order to optimise the process, which also requires some time. Thus, frequent thorough cleaning is not expected or sometimes not possible, especially in an industrial environment where many deposition processes run for several hours in order to produce thick coatings.

Here, our result clearly shows that the chamber pressure can be used as an effective tool to control the surface defect density. Therefore, the present study is interesting and could be useful even for industrial processes.

4.3.8 Corrosion resistance

Fig. 4.33 shows the Potentiodynamic polarisation curves of the coatings deposited at various chamber pressures. As seen from the figure, the corrosion resistance exhibited a linear relationship with the chamber pressure.

In the potential range of - 300 mV to + 300 mV, the corrosion current density was significantly higher for the coating produced at the highest chamber pressure of 1 Pa. Thickness values of the coatings deposited at 0.35 Pa and 1 Pa chamber pressure were almost the same (2.15 µm and 2.18 µm respectively); however, surface defect density was higher (A_d = 5.96 %) for the coating deposited at P = 1 Pa. These increased defects are believed to be the reason for lower corrosion resistance. The thickest coating (3.65 µm) with the lowest surface defect density (A_d = 0.84 %) was produced at the lowest chamber pressure of 0.2 Pa. For this coating, pitting resistance was more evident (in the potential range of - 300 mV to + 300 mV). This study confirmed the deleterious effect of coating defects on corrosion performance.
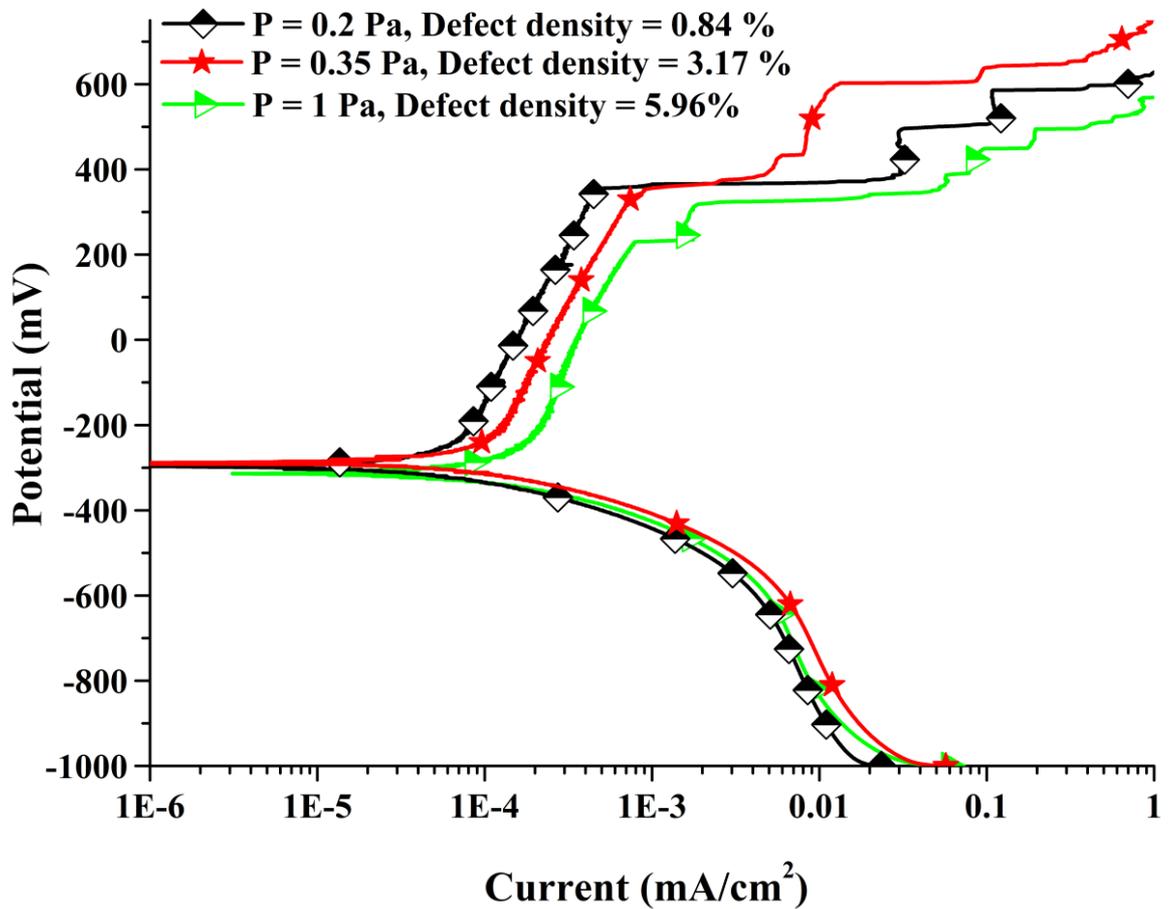
Fig. 4.33. Corrosion curves of the coatings deposited at various chamber pressures.

4.3.9 Tribological properties

4.3.9.1 Determination of wear and friction coefficients

To understand the effect of chamber pressure on wear and friction behaviour, room temperature tribological test in dry sliding conditions were conducted. Fig. 4.34 shows the dependence of friction coefficient on number of revolutions (friction cycles) for the coatings deposited at various chamber pressures.
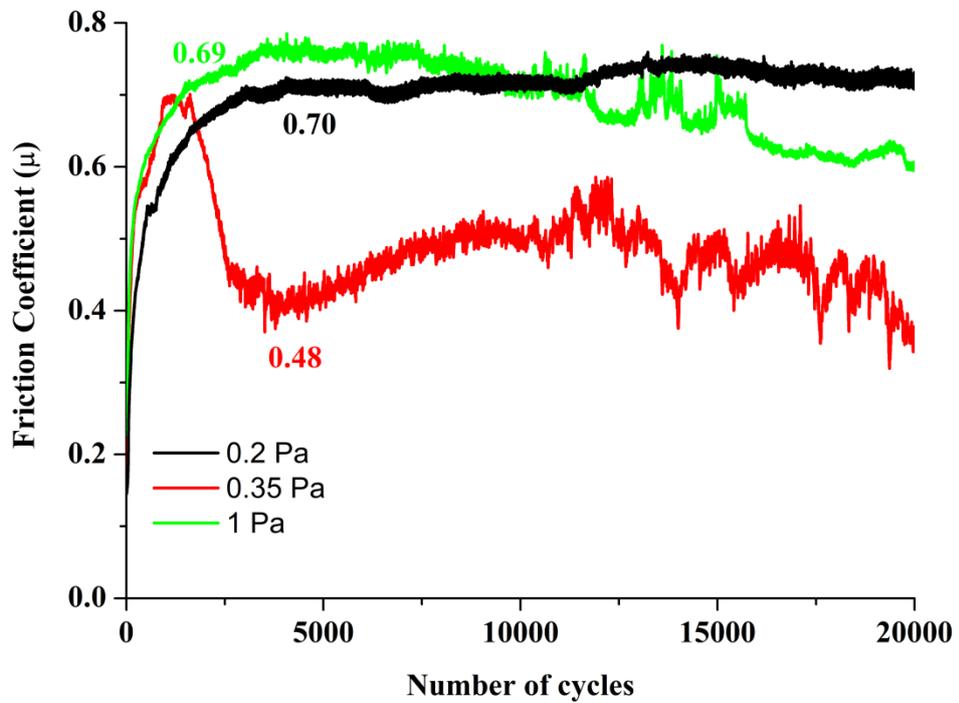
Fig. 4.34. Dependence of friction coefficient on number of revolutions (friction cycles) for the coatings deposited at various chamber pressures.

The coatings deposited at the higher pressures of 0.35 Pa and 1 Pa had the more number of surface defects. As observed in Fig. 4.34, the COF values were fluctuating in the range of 10000 and 20000 cycles. The fluctuation of μ value is common for a sliding wear process with a large amount of debris involved in a three body contact mechanism [104]. This behaviour was consistent with the previous findings (sec 4.1.8, 4.2.9). As discussed earlier, loosely bonded defects could be expunged from the coating during the tribological tests increasing the wear debris formation. Thus, the fluctuations in μ values were more apparent for the coatings with higher defects.

The coating deposited at P= 0.2 Pa, had the lowest surface defect density (A_d = 0.84 %) and the coating deposited at P = 1 Pa had the highest surface defect density (A_d = 5.96 %) but both the coatings showed similar friction coefficient (μ = 0.69 and 0.70 respectively). The coating produced at P = 0.35 Pa showed the best friction value of

0.48. To understand this friction behaviour, optical microscopic and SEM images of the wear tracks were captured (Fig. 4.35).

As observed from the Fig. 4.35, the wear tracks of the coatings deposited at P = 0.2 Pa and 1 Pa evidenced the formation of a tribolayer, whereas the coating produced at P = 0.35 Pa exhibited a clean wear track with no evidence of tribolayer formation. This study suggested that the friction behaviour of the coatings was dominated by the tribolayer formed during the tests.
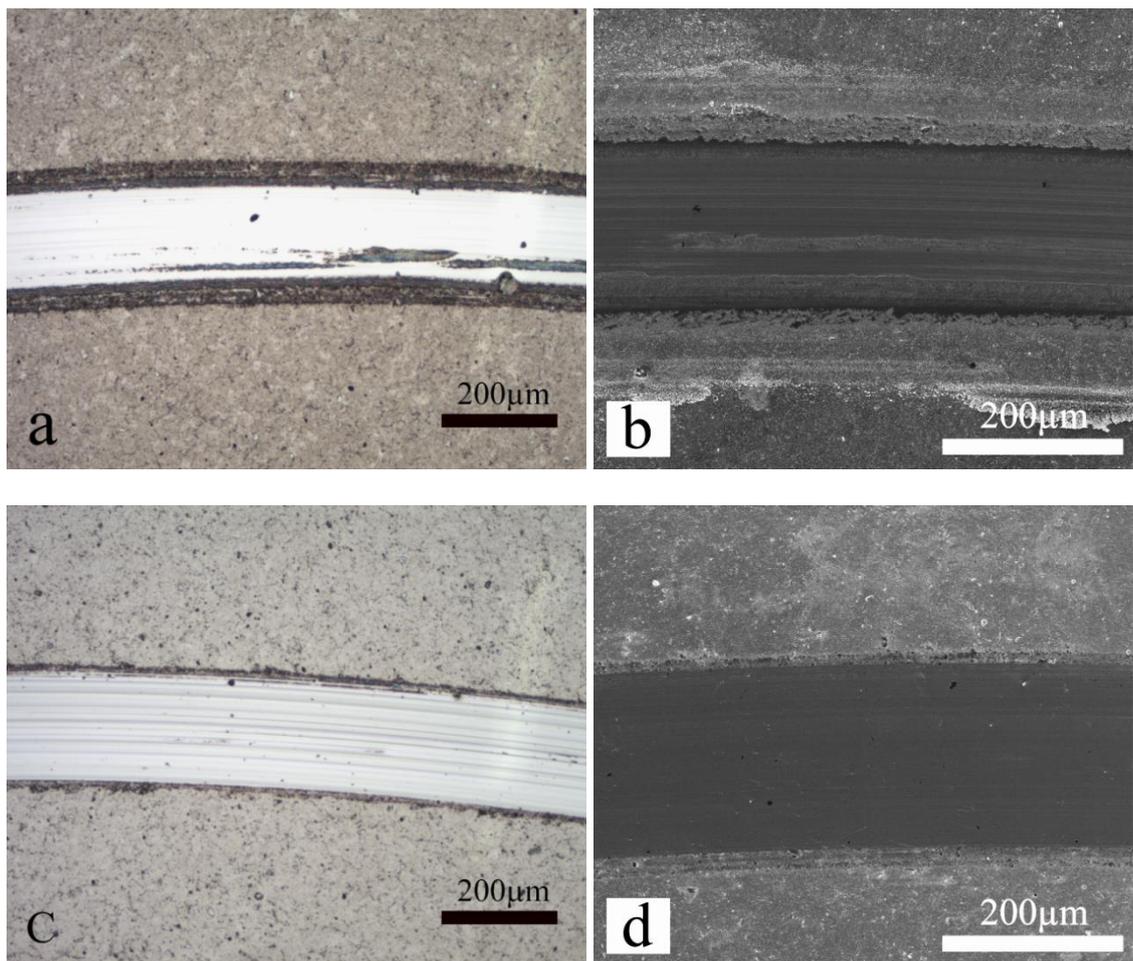
Fig. Fig. 4.35. (continue)
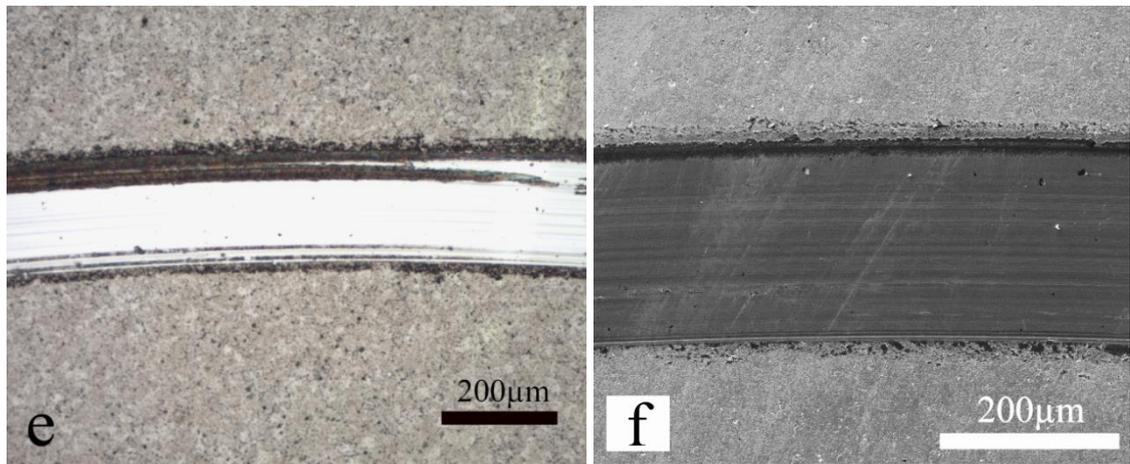
Fig. 4.35. (a) Optical microscopic and (b) SEM image of the wear track of the coating deposited at P = 0.2 Pa; (c) optical microscopic and (d) SEM image of the wear track of the coating deposited at P = 0.35 Pa; (e) optical microscopic and (f) SEM image of the wear track of the coating deposited at P = 1 Pa.
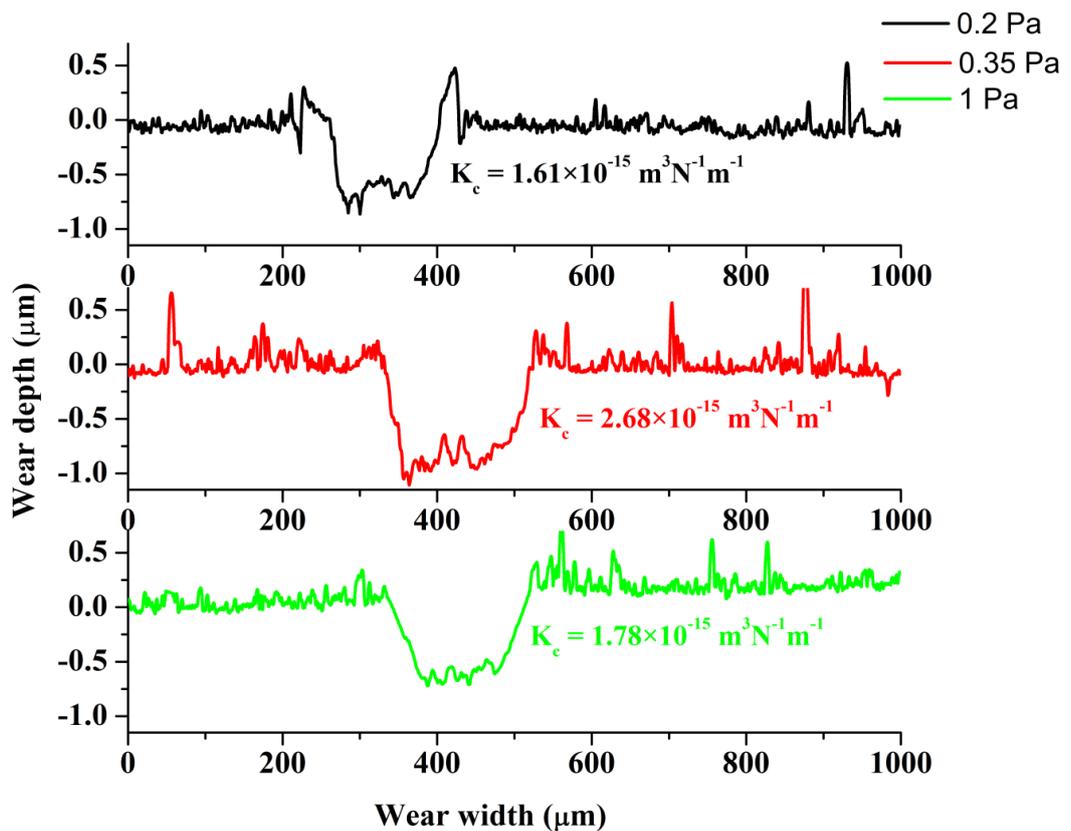
Fig. 4.36. Wear track profiles of the coatings deposited at various chamber pressures.

Fig. 4.36 shows the wear tracks profiles of the coatings. Surprisingly, coatings with the highest μ value of 0.70 exhibited best wear resistance properties ($K_C = 1.61 \times 10^{-15}$ $m^3N^{-1}m^{-1}$). Nevertheless, the coating produced at P = 1 Pa had similar wear value ($K_C = 1.78 \times 10^{-15}$ $m^3N^{-1}m^{-1}$). Although, the effect of higher surface defect density was evident from the fluctuation in μ value, this study suggested that it did not influence the wear rates. Instead, wear rates showed a linear relationship with the bilayer thickness of the coatings. It is well known that wear resistance of multilayer coatings depends on their bilayer thickness [81,86–93]. As found in the sec 4.3.5, the bilayer thickness of the coating deposited at P = 0.2 Pa was the highest (Δ = 39.3 Å). The thicker hard layers of this coating prevented the plastic deformation and the abrasive penetration in the metal layers resulting in the lowest volume loss.

Among all the coatings, the coating deposited at P = 0.35 Pa had the thinnest bilayer (Δ = 27.3 Å) and had the highest wear value ($K_C = 2.68 \times 10^{-15}$ $m^3N^{-1}m^{-1}$). This result showed consistency with the previous findings (sec 4.2.9).

4.3.9.2 Raman Spectroscopy

To study the nature of the oxides produced during the tribo test, Raman data was collected from the wear debris. For the coatings deposited at P = 0.2 Pa and P = 1 Pa, Raman spectra were obtained from the wear debris within the wear tracks. As seen from the Fig. 4.35c,d there was no trace of debris within the wear track of the coating deposited at P = 0.35 Pa. So, in this case Raman data were collected from the wear debris beside the wear track.

The tribolayer produced on the coatings deposited at chamber pressures of 0.2 Pa and 1 Pa exhibited pronounced peaks at around 840 cm^{-1} which corresponds to Nb_2O_5, nH_2O) [118,142]. There was another peak at around 535 cm^{-1} (corresponds to Cr_2O_3) in both cases (P = 0.2 Pa and 1 Pa). Cr_2O_3 belongs to the family of magneli phases and

therefore it is more lubricious [159]. In contrast, Nb_2O_5 has a crystallographic structure which does not contain easily shearable atomic planes and therefore it is less lubricious. Thus, the higher friction coefficient of these coatings can be attributed to the presence of Nb_2O_5 in the tribolayer [118]. In contrast, the coating deposited at P = 0.35 Pa did not have any intense peak and interestingly this coating had the lowest friction coefficient (μ) value, 0.48. This emphasised the fact that the difference in the friction behaviour of these coatings was clearly due to the chemistry of the tribolayer formed within the wear tracks rather than the surface defect density.
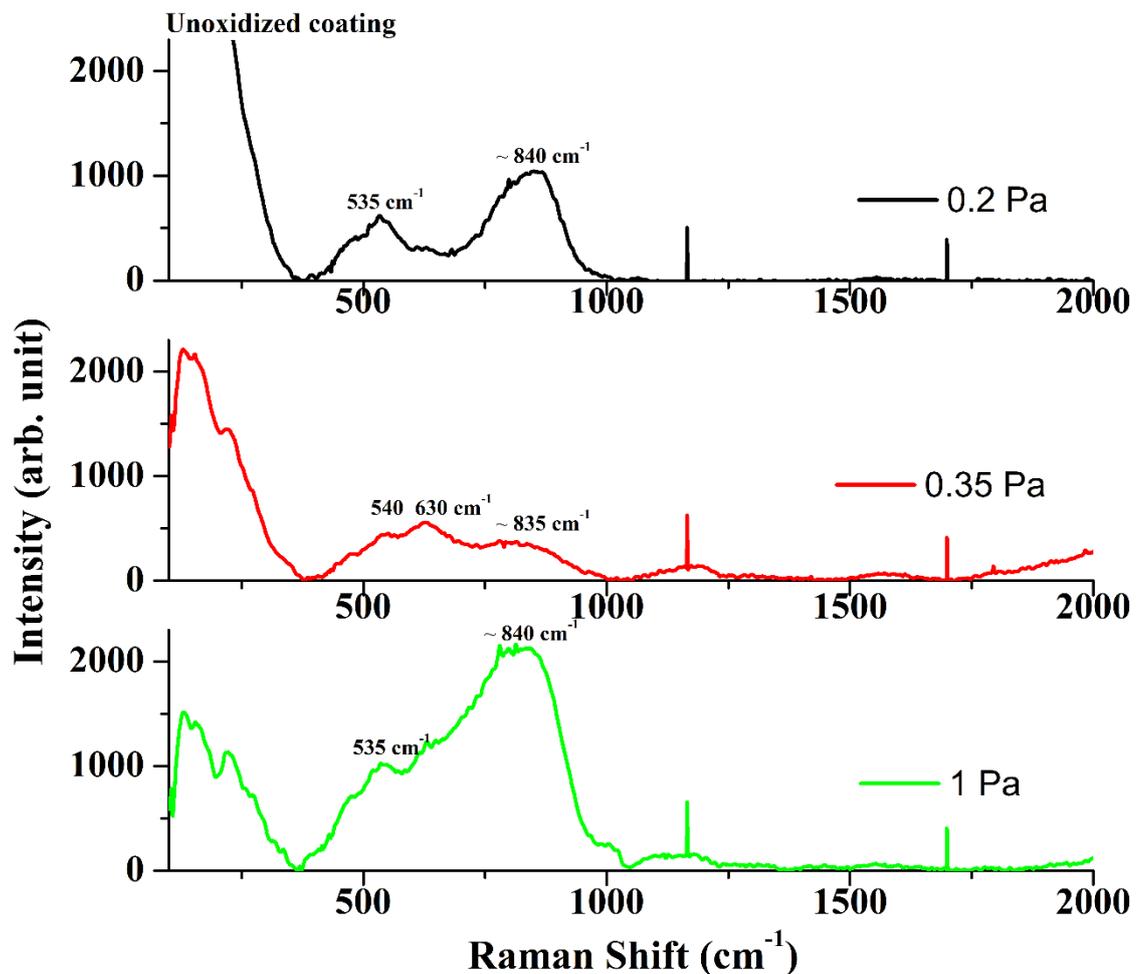
Fig. 4.37. Raman spectra obtained from the wear debris produced during tribo test on the coatings deposited at various chamber pressures.

4.3.10 Summary

- The chamber pressure influenced the microstructures, chemical composition, crystallographic orientation and bilayer thickness of the nanoscale CrN/NbN coatings.

- The study of surface defects indicated that the chamber pressure also influenced the surface defect density. Coatings produced at the lowest chamber pressure (0.2 Pa) had the lowest surface defect density (A_d = 0.84 %).

- The potentiodynamic polarisation study suggested that the surface defect density dominated the coating corrosion behaviour. The coating with the lowest defect (A_d = 0.84 %) and the highest thickness (3.65 µm) had the lowest corrosion current density in the anodic potential ranging from - 300 mV to + 300 mV. Whereas coating with the highest surface defect density (A_d = 5.96 %) had significantly higher corrosion current density compared in the same potential range.

- The coefficients of wear (K_C) were influenced by the bilayer thickness of the coatings. Coatings with the highest bilayer thickness (Δ = 39.3 Å) had the lowest wear rate (K_C = 1.61×10^{-15} $m^3 N^{-1} m^{-1}$), whereas the coatings with the lowest bilayer thickness (Δ = 27.3 Å) exhibited the highest wear rate (K_C = 2.68×10^{-15} $m^3 N^{-1} m^{-1}$).

- The friction value of these coatings was influenced by the nature of oxides formed at the tribological contacts. The coating deposited at P = 0.35 Pa had the lowest friction coefficient (μ = 0.48). Raman spectra of the tribolayer formed on the top of this coating suggested that it contained $CrNbO_4$. In contrast, a Nb_2O_5 based tribolayer in the wear track was formed for the coatings deposited at P = 0.2 Pa and 1 Pa. Both these coatings showed higher friction values (μ = 0.69 and 0.70 respectively) because of the non-lubricious nature of the niobium oxides.

4.4 Influence of chamber cleanliness on HIPIMS/UBM deposited CrN/NbN coatings

4.4.1 Overview of the experiments

CrN/NbN nano-structured multilayer coatings were produced in an industrial sized Hauzer four source PVD machine. To replicate actual deposition conditions, such as those found in an industrial environment, a significant part of this thesis work (sec 4.1, 4.2 and 4.3) was conducted without the chamber being cleaned. Extensive study on coating microstructure and defects indicated that the flakes from chamber components are the reason for most of the defects generated in the case of HIPIMS/UBM coatings. So, this additional study was conducted to investigate the effect of clean environment on the defect formation.

With this objective, two sets of CrN/NbN coatings were produced using HIPIMS/UBM. One set of samples were deposited before cleaning the chamber, while another set of coatings were produced after thoroughly cleaning the chamber. During all the deposition processes, the substrate bias and the chamber pressure were fixed at - 65 V and 0.35 Pa respectively. The deposition time was 120 min for all the coatings.

As observed in the previous sections (4.1, 4.2 and 4.3), the variation in deposition parameters (deposition time, bias voltage and chamber pressure) affected the flake generation resulting in the deviation in surface defect density. At the same time, coating morphology, crystallographic orientation and bilayer thickness were also altered due to the change in ion energies and sputter rates with the variation of deposition parameters (bias voltage and chamber pressure). Also, the thickness of the coatings was changed in each case. As a result, the corrosion and the tribological performances of the coatings

were not only influenced by the surface defect density but also by the coating thickness, structure and morphology.

Thus, this chapter also reports the effect of surface defect density on the corrosion and the tribological performances of the coatings with similar mechanical and chemical properties.

4.4.2 Surface defect density

Fig. 4.38 represents the optical microscopic images of the HIPIMS/UBM coatings deposited before and after cleaning the chamber. It is clear from the figure that the coating deposited after cleaning the chamber had lower defects on its surface than the coating deposited before cleaning. To quantify the density of the defects, these optical microscopic images were converted into black and white binary images. Then using Image J software, percentage of surface area occupied by the defects was evaluated. As anticipated, the surface defect density of the coating produced in a comparatively clean chamber was reduced to 1.37 % from 3.18 %.

This study confirmed our claim that most of the defects found in HIPIMS coatings are associated with the flakes. Cleaning the chamber reduced the sites for flake generation and hence, the surface defect density was reduced after cleaning the chamber.

However, zero surface defect density could not be achieved. This is because the high-energy flux bombardments on chamber wall and other components still produced some flakes and resulted in defect generation in the coatings.
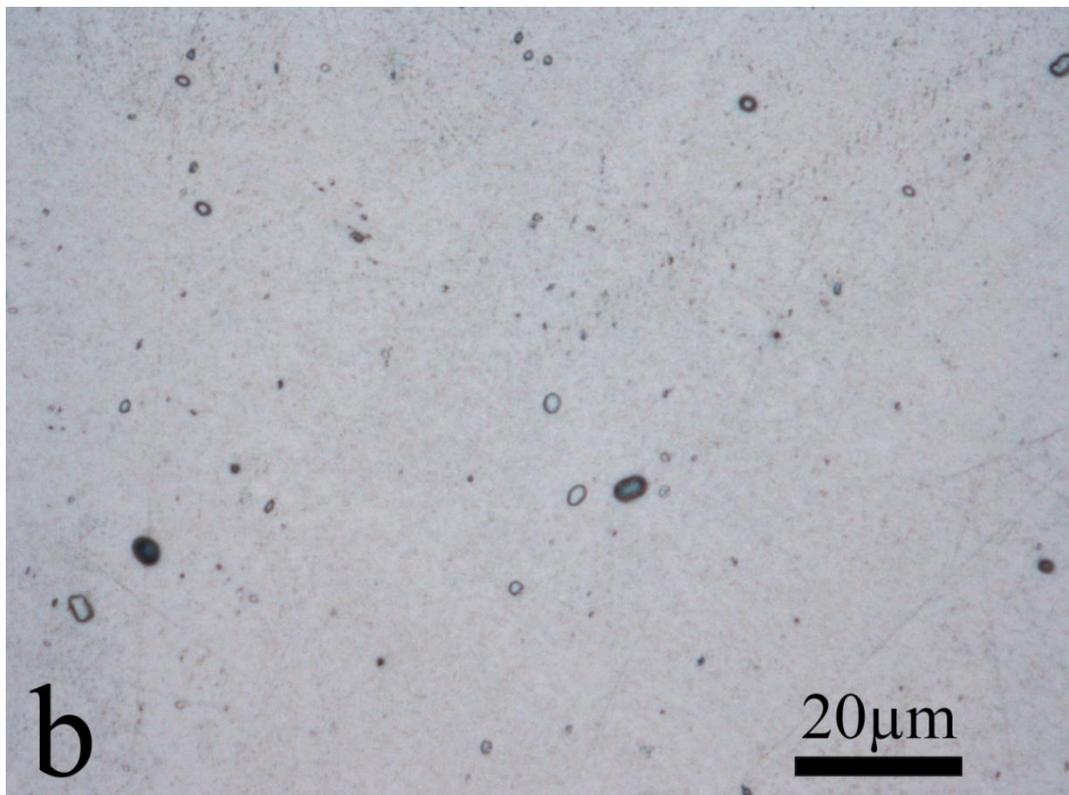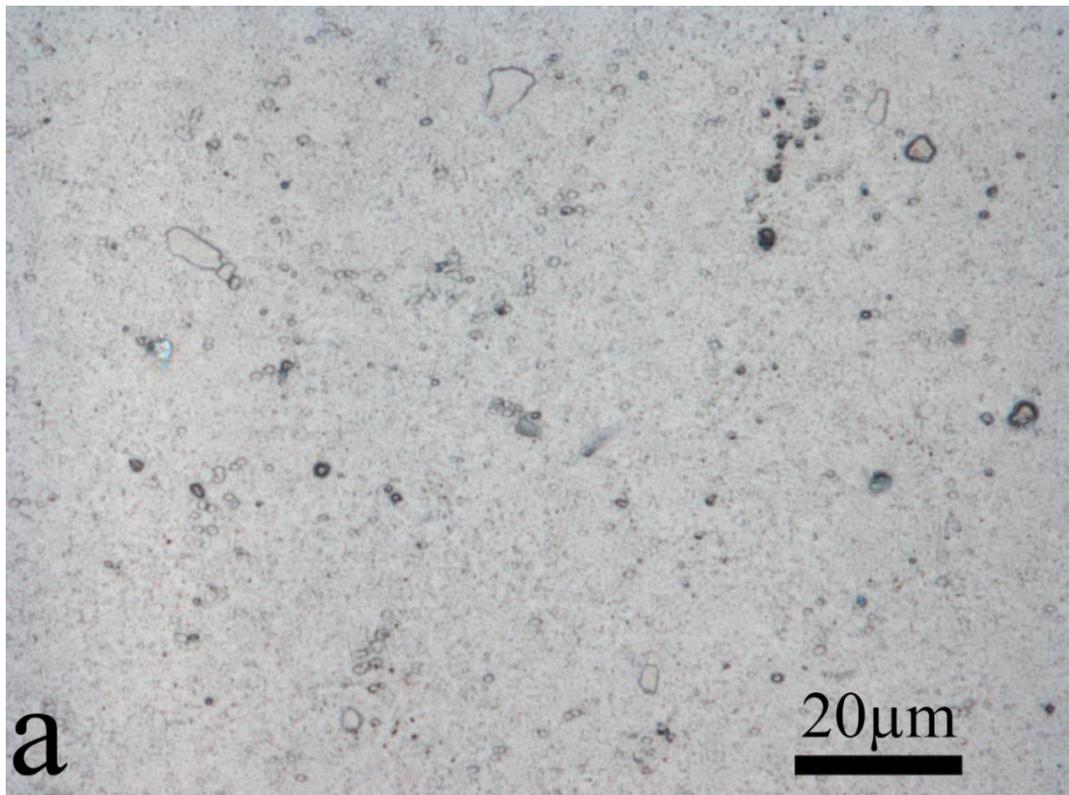
Fig. 4.38. Optical microscopic image of the coating deposited (a) before and (d) after

cleaning the chamber.

4.4.3 Coating roughness

Roughness values of the coatings are summarised in the following table.

Chamber condition (cleanness)	Roughness, Ra (µm)
Before cleaning	0.039 ± 0.002
After cleaning	0.031 ± 0.002

Table 4.11. Roughness values of the coatings deposited before and after cleaning the chamber.

In the sections 4.2.7 and 4.3.6, coating roughness was found to be influenced by the morphology as well as by the surface defect density. However, SEM images (Fig. 4.39) of the coatings exhibited the morphological similarities, which confirmed the reproducibility in the coating deposition. Hence, in this case, the difference in roughness values of the coatings was mainly due to the variation in surface defect density before and after cleaning the chamber. The decrease in surface defect density from 3.18 % to 1.37 % lowered the roughness from 0.039 µm to 0.031 µm.
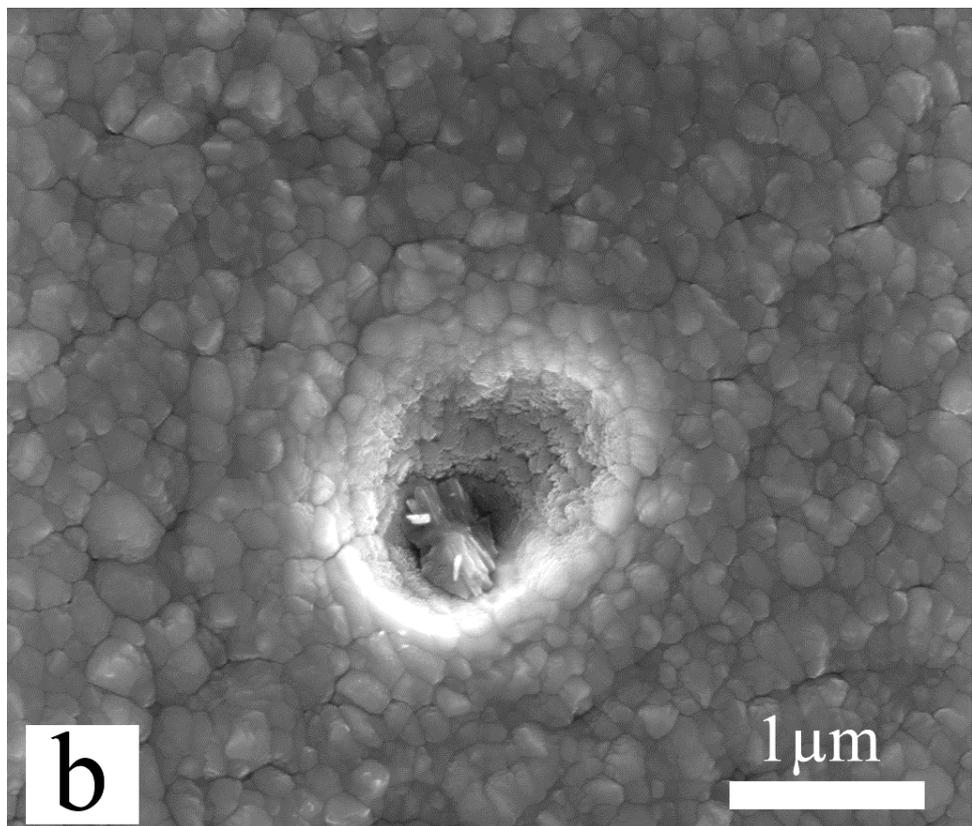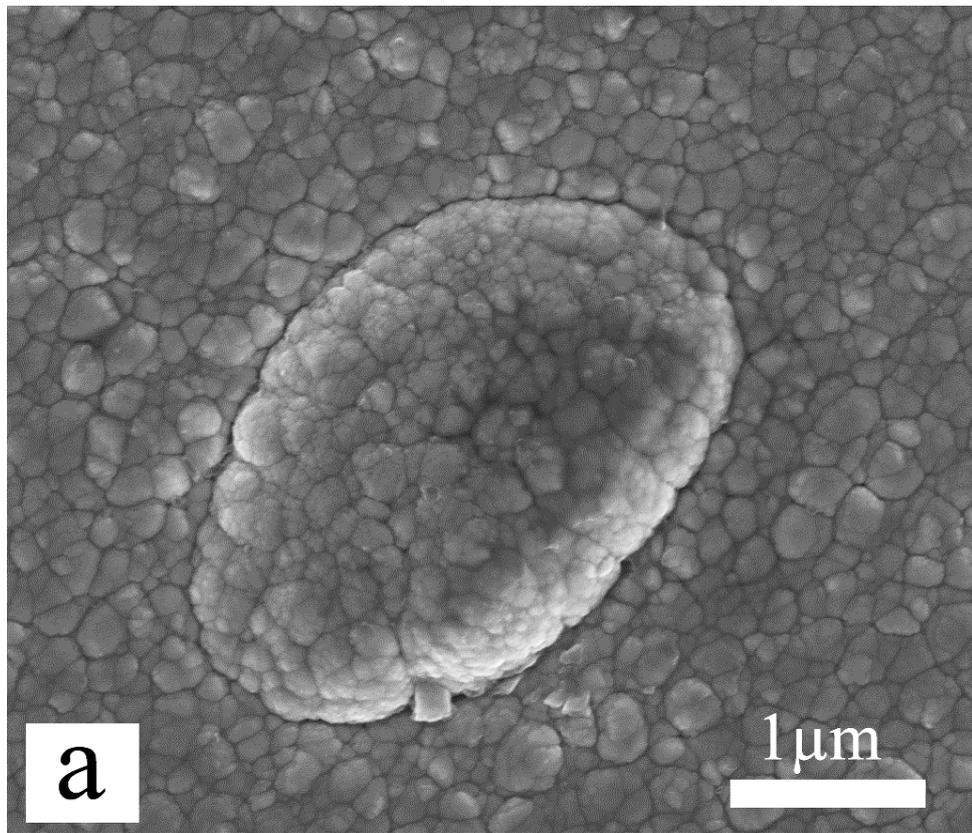
Fig. 4.39. SEM image of the coating deposited (a) before and (d) after cleaning the chamber.

4.4.4 Corrosion resistance

Potentiodynamic corrosion study on CrN/NbN HIPIMS/UBM coatings deposited by varying deposition parameters (deposition time, bias voltage, chamber pressure) revealed the importance of dense microstructure for better corrosion performance. In section 4.2.8, the optimum voltage to produce a coating with sufficient density was found to be - 65 V. Nevertheless, localised coating failure due to the removal of coating defects was also apparent in Fig. 4.22. So, the present study was conducted to investigate the effect of surface defect density on corrosion performance of the coatings with similar dense microstructures as both coatings were produced at U_b = - 65 V, P = 0.35 Pa for t = 120 min.
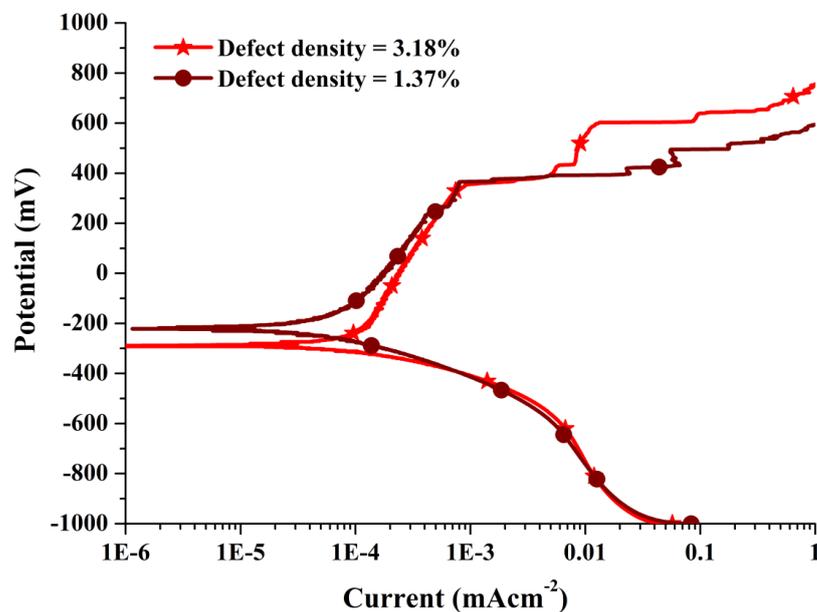
Fig. 4.40. Potentiodynamic polarisation curves of the coatings deposited before and after cleaning the chamber.

As observed from the Fig. 4.40, in the potential range of - 300 mV to + 300 mV, the corrosion current density was little lower for the coating with fewer defects (1.37 %).

Also, the E_{corr} value (- 222 mV) of the coating was more noble. Coating defects like open void defects act as a pathway for corrosive media to reach the substrate resulting in poor corrosion resistance. The higher surface defect density in the coating deposited before cleaning the chamber deteriorated the corrosion properties.

4.4.5 Tribological properties

Fig. 4.41 represents the dependence of friction coefficient on number of revolutions (friction cycles) for the coatings deposited before and after cleaning the chamber. A significant decrease in friction coefficient (μ) was observed for the coating deposited after cleaning the chamber. Moreover, the fluctuation in the μ value was not apparent for this coating. As found in the previous sections (sec 4.2.9 and 4.3.9), removal of defects initiated three body tribo-contact mechanism which subsequently made the friction coefficient behaviour unstable. Thus, due to the presence of higher number of defects, the coating deposited before cleaning the chamber had unstable μ value in the range of 10000 to 20000 cycles.

In sec 4.1.8, 4.2.9 and 4.3.9, μ values were found to be influenced by the oxides produced within the wear tracks during tribological tests. Hence, the Raman spectra were also obtained from the wear track and wear debris. Fig. 4.42 shows that both the tribolayers were similar in nature. This confirmed that the difference in the friction behaviour of these coatings was mainly because of the difference in the surface defect density of the coatings rather than the chemistry of the tribolayers formed in their wear tracks. However, the coefficient of wear values of these coatings were in the similar range ($K_C = 2.68 \times 10^{-15}$ m^{3}N^{-1}m^{-1} for the coating deposited before and $K_C = 2.37 \times 10^{-15}$ m^{3}N^{-1}m^{-1} for the coating deposited after cleaning the chamber). This can be attributed to the similar bilayer thickness of these coatings.
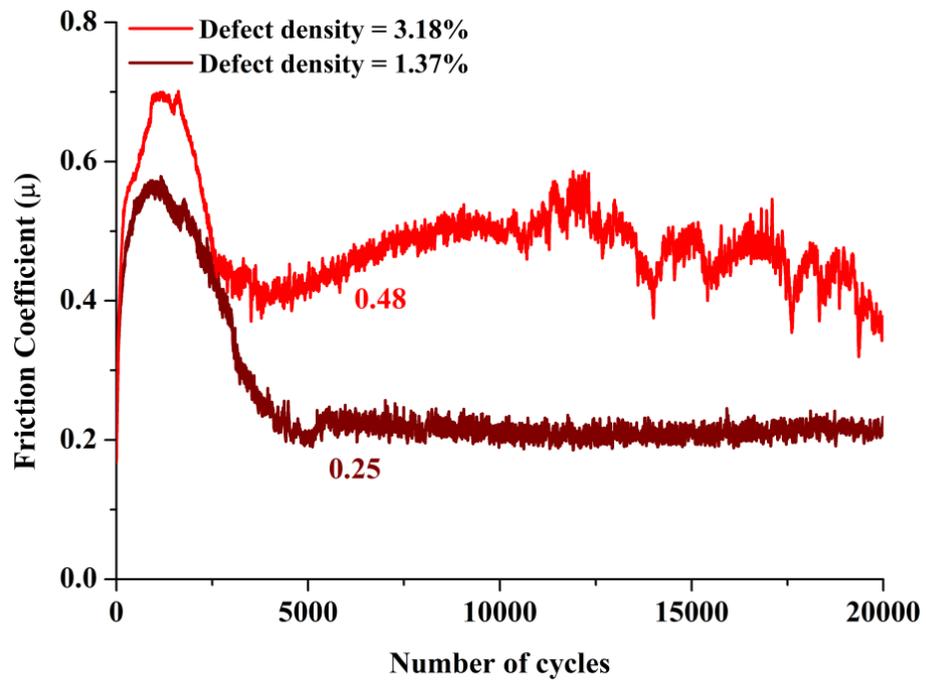
Fig. 4.41. Dependence of friction coefficient on number of revolutions (friction cycles)

for the coatings deposited before and after cleaning the chamber.
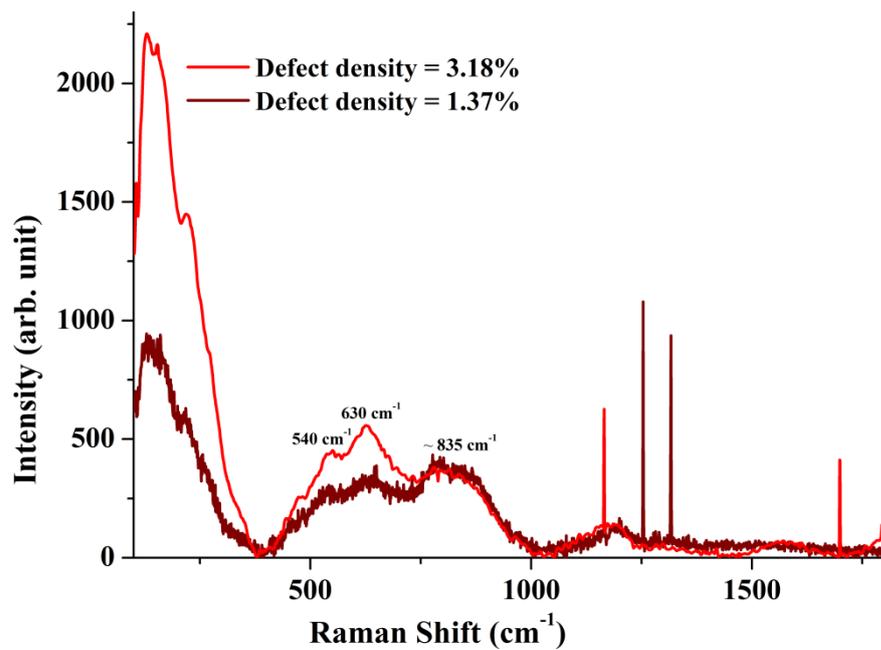
Fig. 4.42. Raman spectra obtained from the wear debris of the coatings deposited before

and after cleaning the chamber.

.4.4.6 Summary

- Coatings produced in a relatively clean chamber had almost three times lower surface defect density of 1.37 % as compared to 3.18 % before cleaning. This confirmed that most of the defects in HIPIMS/UBM coatings generate due to the flakes generation within the coating chamber.

- The E_{corr} value of the coating with less defects (E_{corr} = - 222 mV) was more noble as compared to the coating with higher defects (E_{corr} = - 289 mV). The corrosion resistance of the coating with lower defects was more evident in the potential range of - 300 mV to + 300 mV.

- The pin-on-disk tribological tests confirmed the influence of coating defects on tribological performance. With a decrease in surface defect density from 3.18 % to 1.37 %, the friction coefficient (μ) was reduced from 0.48 to 0.25.

4.5 Comparison between CrN/NbN coatings of similar thickness deposited by pure UBM and HIPIMS/UBM

4.5.1 Overview of the experiments

The aim of this study was to investigate the effect of surface defect density on the coatings deposited by two different physical vapour deposition approaches. One set of CrN/NbN coatings were produced using pure UBM technique and another set of samples were deposited by combined HIPIMS and UBM techniques (HIPIMS/UBM).

For HIPIMS/UBM coating deposition, one Cr and one Nb target were operated in HIPIMS mode, while the other two targets (one Cr and one Nb) were operated in UBM mode. On the other hand, all the four targets were operated in UBM mode in the case of pure UBM coating deposition. During all the deposition processes, the machine was operated in the constant power mode where the average power on the target(s) was always maintained at 8 kW irrespective of the technology (UBM or HIPIMS). The bias voltage was fixed at - 65 V and the chamber pressure was maintained at 0.35 Pa. However, to produce coatings of similar thickness, the deposition time for HIPIMS/UBM coatings was higher (120 min) than that (100 min) for UBM coatings. This difference in deposition time is because of a lower deposition rate of HIPIMS process as compared to conventional magnetron sputtering [46].

4.5.2 Microstructure

SEM was used to study the microstructures of the coatings deposited by two different PVD techniques. Fig. 4.43 represents the SEM images of planar surface view of the UBM and HIPIMS/UBM coatings
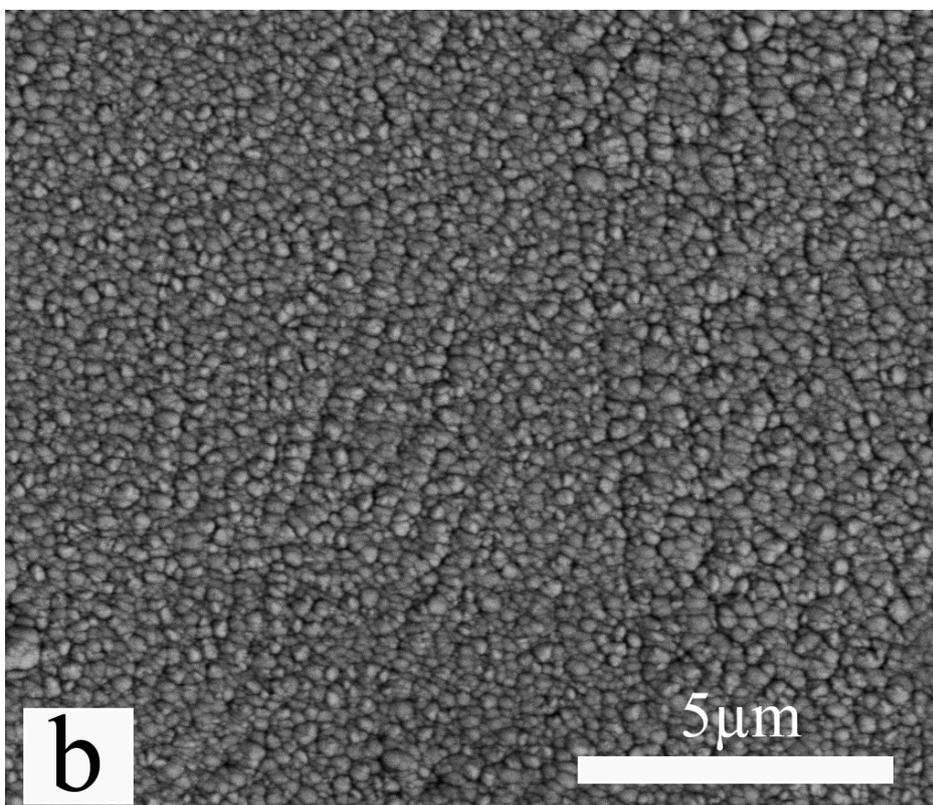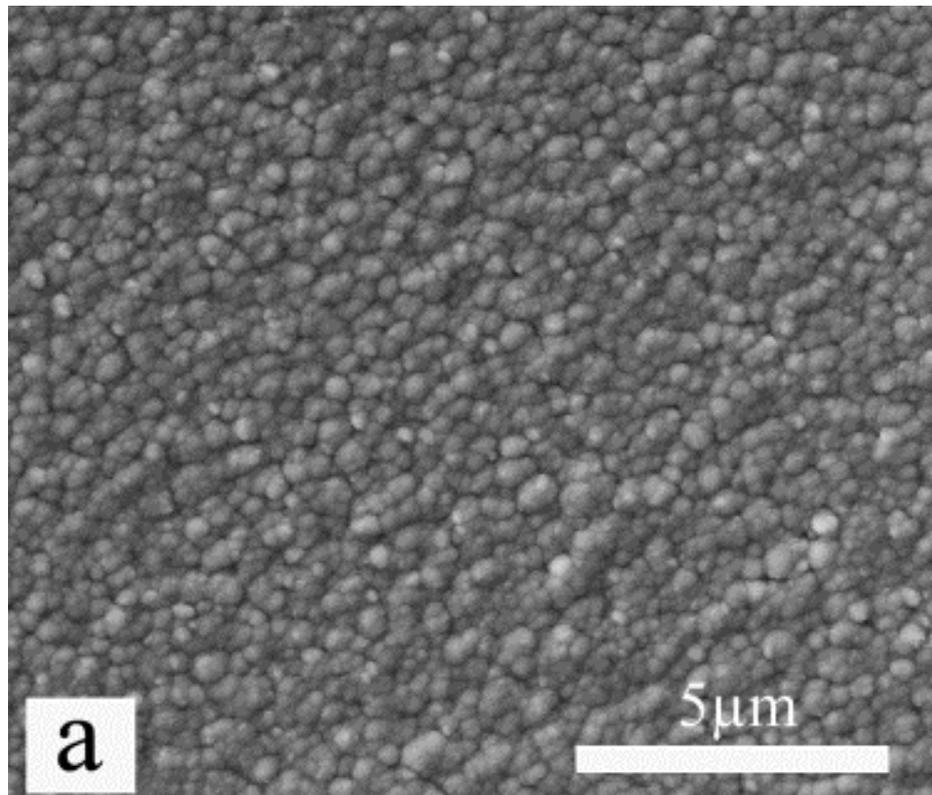
Fig. 4.43. SEM image of (a) UBM and (b) HIPIMS/UBM coating.

In case of UBM coating, dome shaped morphology was more apparent (Fig. 4.43a). The wider and more prominent grain boundary indicates the higher possibility of the space void between the grain columns [102]. Hence, Fig. 4.43a suggested that the UBM coating structure was under dense. In Fig. 4.43b, the advantage of using HIPIMS was clearly visible as the columns were found to be very densely packed compared to the UBM coating.

4.5.3 Coating defects

4.5.3.1 Defect types

Fig. 4.44a-d shows the various types of defects found in UBM and HIPIMS/UBM coatings. The morphologies of the nodular defects found in both UBM and HIPIMS/UBM coatings were very similar (Fig. 4.44a,c). This suggested that the defect growth step was same for both processes and as described earlier (sec 4.1.6), these defects were generated due to the deposition of coating materials on the top of foreign particles attached to the substrate.

However, pinhole defects observed in the coatings were different in size (Fig. 4.44b,d). Several SEM images of the coating surfaces exhibited the existence of larger pinhole defects in case of UBM coatings. In contrast, smaller pinhole defects were observed in HIPIMS/UBM deposited coatings. As seen from the Fig. 4.44e the surface of UBM coating was porous as compared to the surface of HIPIMS/UBM coating (Fig. 44f). The highly ionised HIPIMS plasma during HIPIMS/UMB process helped to overcome the shadowing effect to some extent and produced more dense structures [102] and also resulted in reduction of pinhole defects' size.
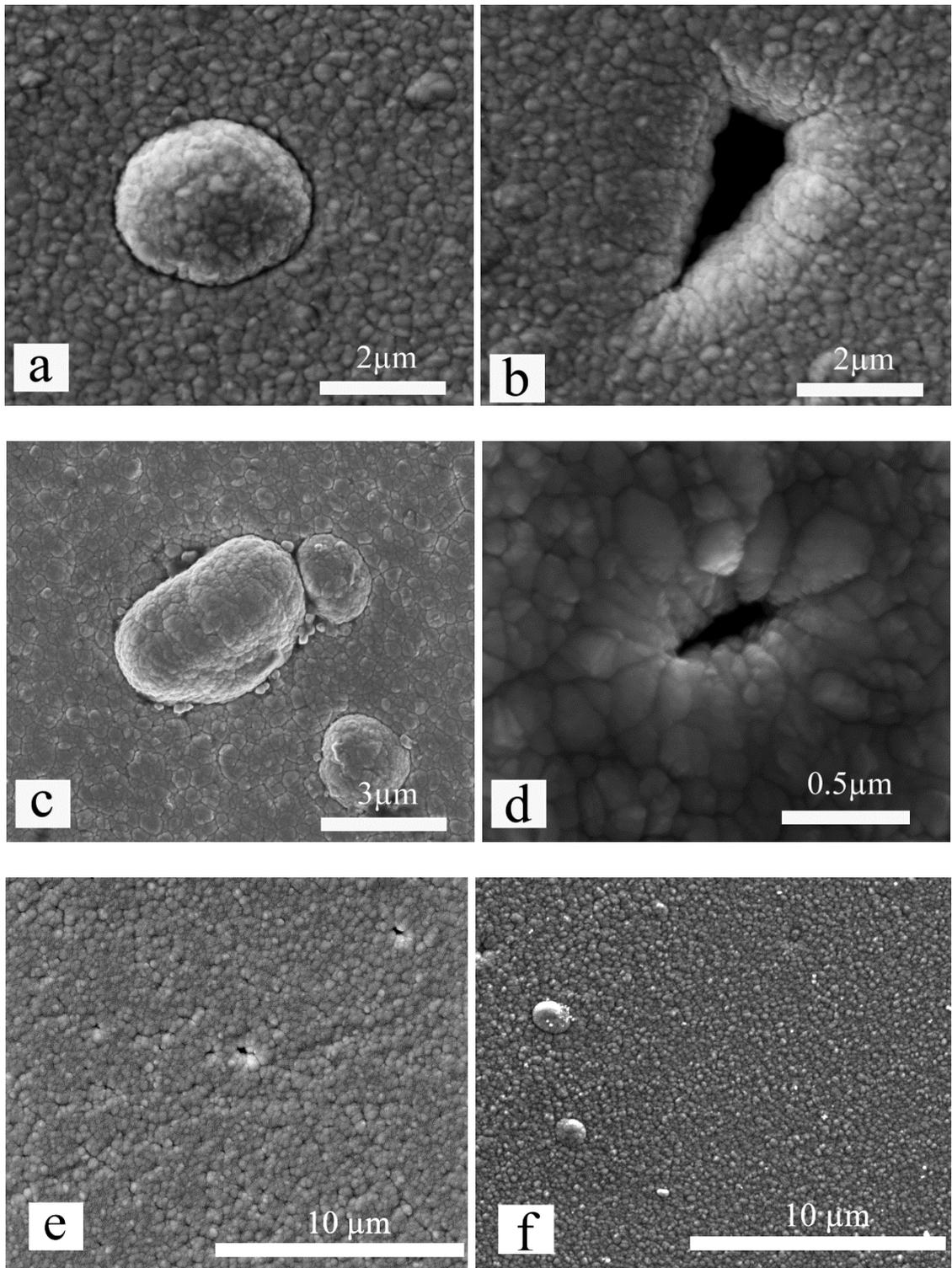
Fig. 4.44. SEM image of (a) nodular and (b) pinhole defect in UBM coating, (c) nodular and (d) pinhole defect in HIPIMS/UBMcoating, (e) UBM coating surface and (f)HIPIMS/UBM coating surface.

Fig. 4.45 shows the FIB-SEM images of a nodular defect. The core structure of the defect clearly revealed the void between the defect and the rest of the coating thickness. Due to the loose bonding of the nodular defects with respect to the rest of the coating, these defects can be easily detached during post deposition applications due to stresses (thermal or mechanical). Nevertheless, in case of UBM coatings, these defects are more likely to be expelled because of the under dense coating structure.
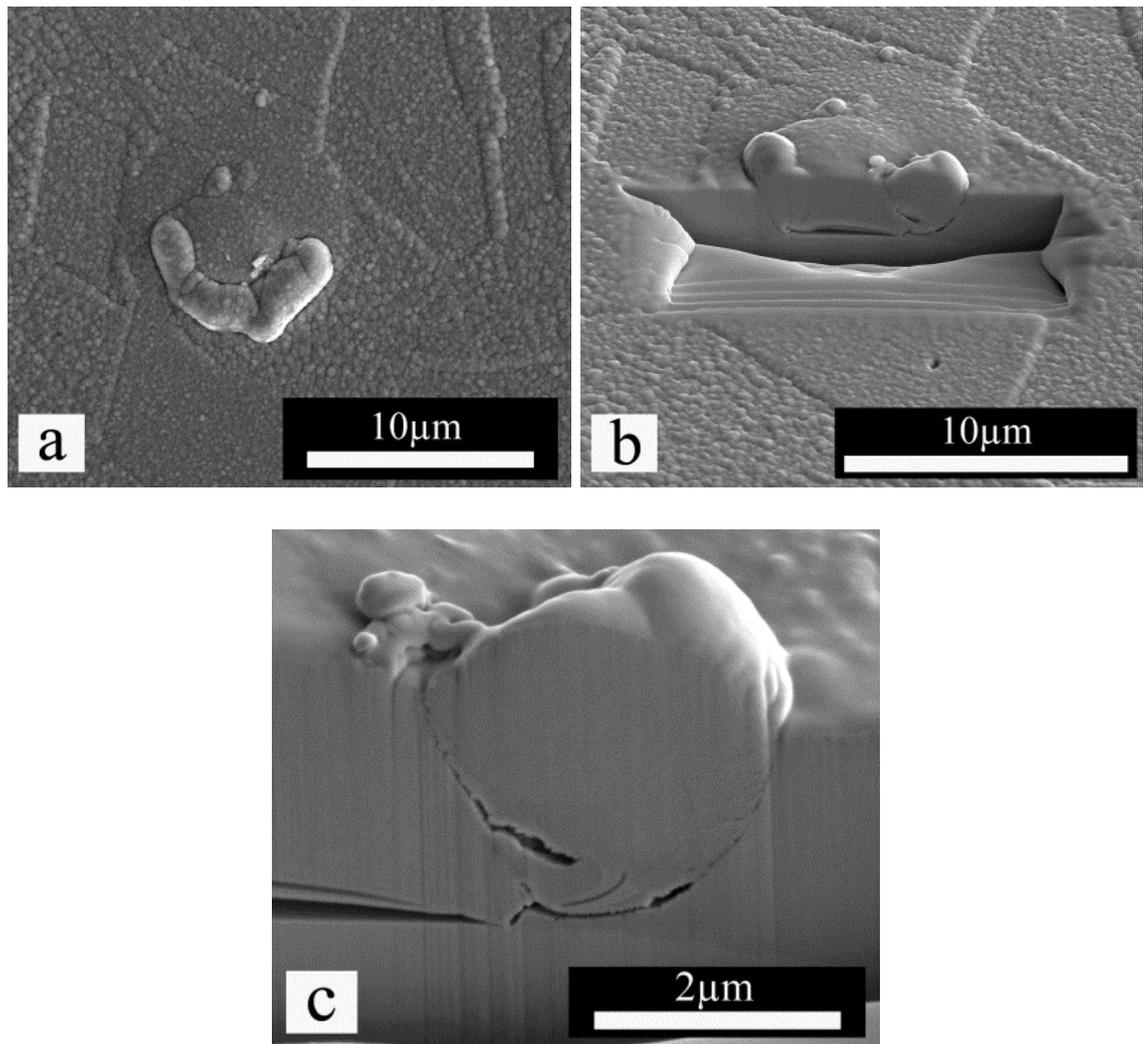
Fig. 4.45. (a) Plan view of the nodular defect, (b) Cross sectional view after ion beam milling, (c) Magnified image of defect cross section.

4.5.3.2 Surface defect density
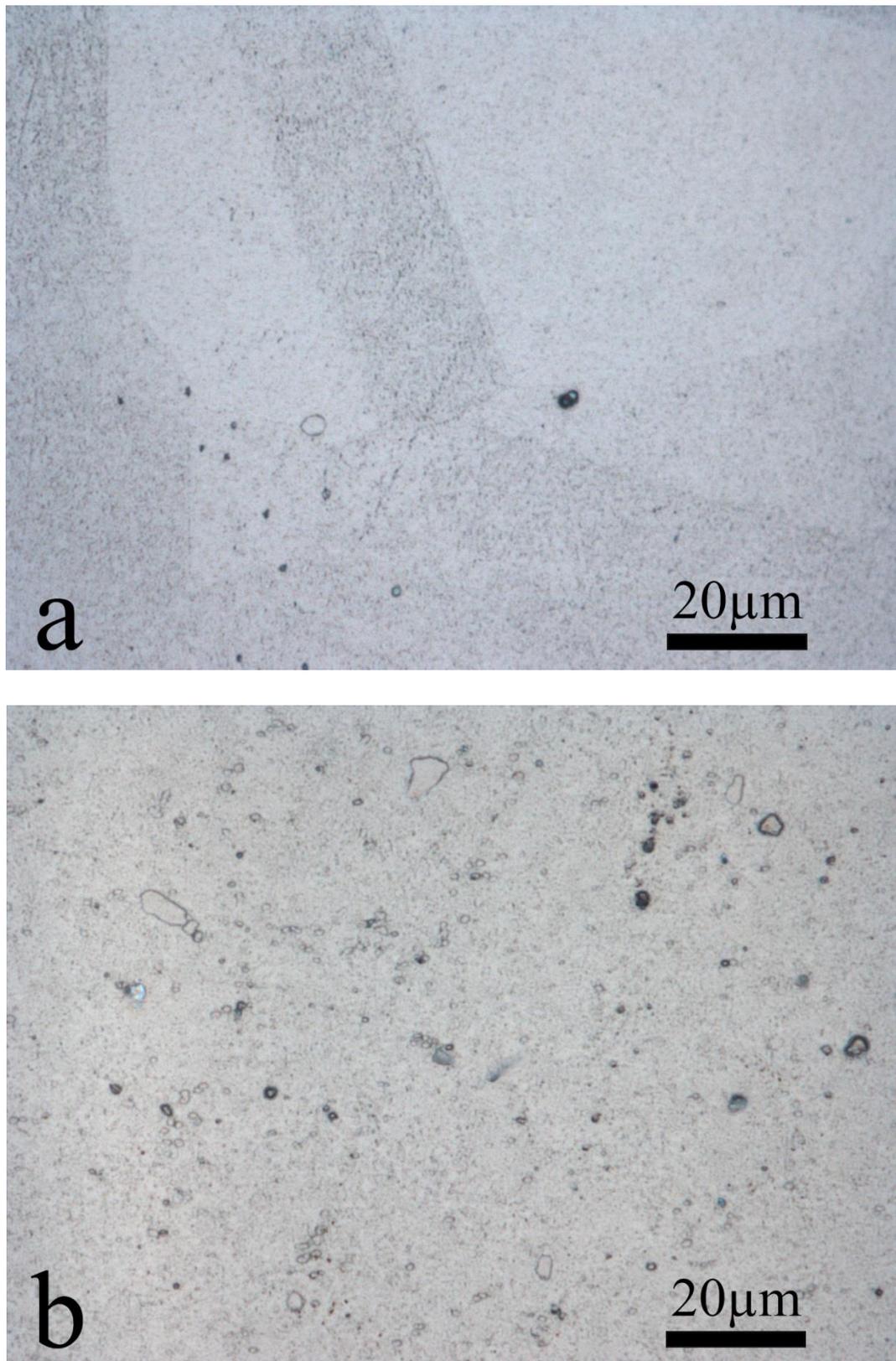
Fig. 4.46. Optical microscopic image of (a) UBM and (b) HIPIMS/UBM coating.

Optical microscopic images of UBM and HIPIMS/UBM coatings (Fig. 4.46) clearly exhibited that the number of defects present on the UBM coating was significantly lower than the HIPIMS/UBM coatings.

The surface defect density calculation releaved that the surface defect density of UBM coating was only 0.21 %, whereas HIPIMS/UBM coating surface was populated with more defects (A_d = 3.18 %). Although the UBM coatings were deposited in a clean chamber, the deference in surface defect density was still significant if compared to the HIPIMS/UBM coatings deposited in the same clean chamber. As found in sec 4.4.2, the surface defect density of HIPIMS/UBM coatings deposited after thoroghly cleaning the chamber was 1.87 %. The lower surface defect density in UBM coating can be attributed to the low energetic particles in the plasma during UBM deposition, which resulted in fewer seed particles generation by the bombardment on the chamber wall. Moreover, the UBM coatings were deposited for less time (100 min) compared to HIPIMS/UBM coatings (120 min). In the section 4.1.6, it was found that the numbers of flakes in the chamber were increased with time during the deposition process. Thus, the lower surface defect density in UBM coatings was also associated with lower deposition time.

4.5.4 Corrosion resistance

Fig. 4.47 shows the potentiodynamic polarisation curve for the UBM coating as well as the HIPIMS/UBM coating of similar thickness. It is clearly visible that in the electrochemical potential range of - 400 mV to + 400 mV, the corrosion current density of UBM coating is significantly higher compared to that of HIPIMS/UBM coating. So, this study indicated that the coating removal rate i.e. the corrosion rate of the HIPIMS/UBM coating was lower than the UBM coating. This result shows the similar trend with the previous study [18]. Interestingly, the surface defect density of the UBM

coatings was much lower than the HIPIMS/UBM coatings. However, the superior microstructure (inter columnar void free) of HIPIMS/UBM coatings made the coating protective despite of having growth defects.
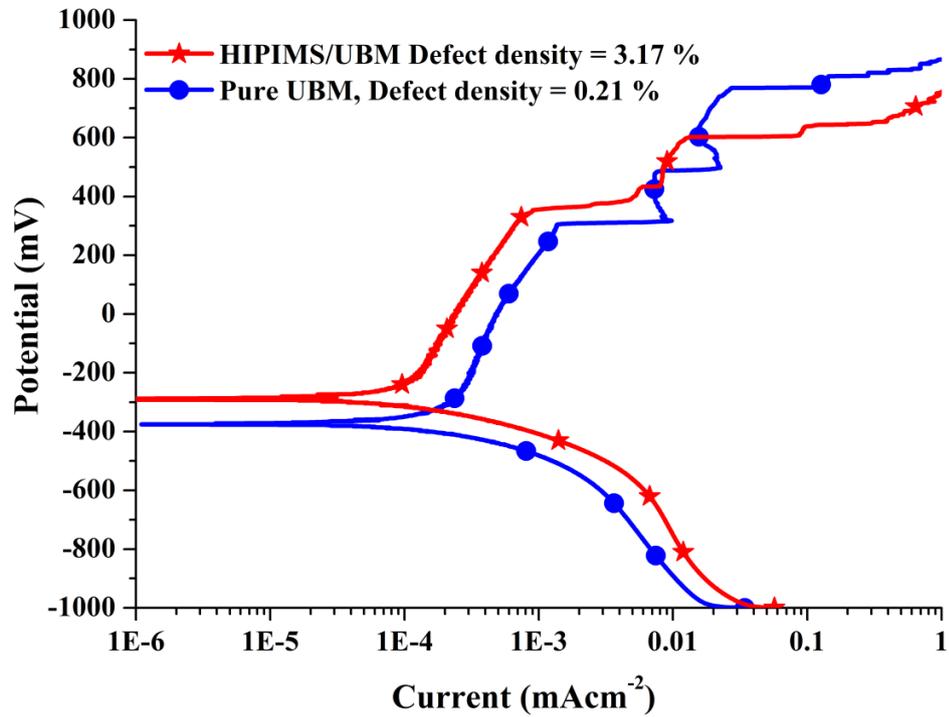
Fig. 4.47. Potentiodynamic polarisation curves of the UBM and HIPIMS/UBM coatings.

4.5.4 Tribological properties

Fig. 4.48 represents the dependence of friction coefficient on number of revolutions (friction cycles) for the coatings deposited by UBM and HIPIMS/UBM technique. The dry sliding friction coefficient of the HIPIMS/UBM coating was lower ($\mu = 0.48$) than the UBM coating ($\mu = 0.59$). It was found in previous sections (4.1.8, 4.2.9 and 4.3.9) that the friction values of the coatings depend on the tribolayer produced during the tribological tests. So, the Raman spectra from the wear tracks of these coatings were collected (Fig. 4.49). There was not much difference between the natures of the

tribolayers formed on both coatings. The wear profiles of the coatings are shown in Fig. 4.50. The wear coefficient of HIPIMS/UBM coating was a factor of 1.25 times smaller than that of UBM coating. Although, the surface defect density of UBM coating was much lower, weak inter-columnar connections (weak bonding among the columns) led to the higher wear rate ($K_C = 3.35 \times 10^{-15}$ m^{3}N^{-1}m^{-1}). Moreover, the production of large amount of debris gradually increased the friction between the coating and the alumina ball. In the range of 1000 to 4000 cycles, the coefficient of friction increased from 0.60 to 0.78. In contrast, the µ value decreased from 0.69 to 0.40 in the same range for HIPIMS/UBM coating. The decrease in µ value can be attributed to uniform multilayer structure and sharp interfaces of HIPIMS/UBM coating which led to the layer by layer material removal mechanism. However, the effect of surface defect density was apparent in the range of 10000 to 20000 cycles. Due to the high stress during sliding, defects were plucked from the coatings, which subsequently made the friction behaviour unsteady and increased the µ value.
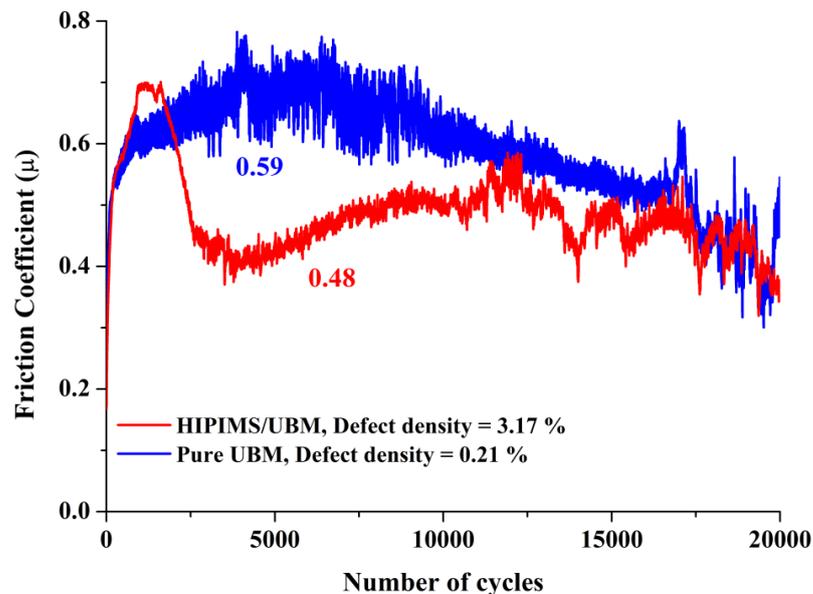
Fig. 4.48. Dependence of friction coefficient on number of revolutions (friction cycles) for the UBM and HIPIMS/UBM coatings.
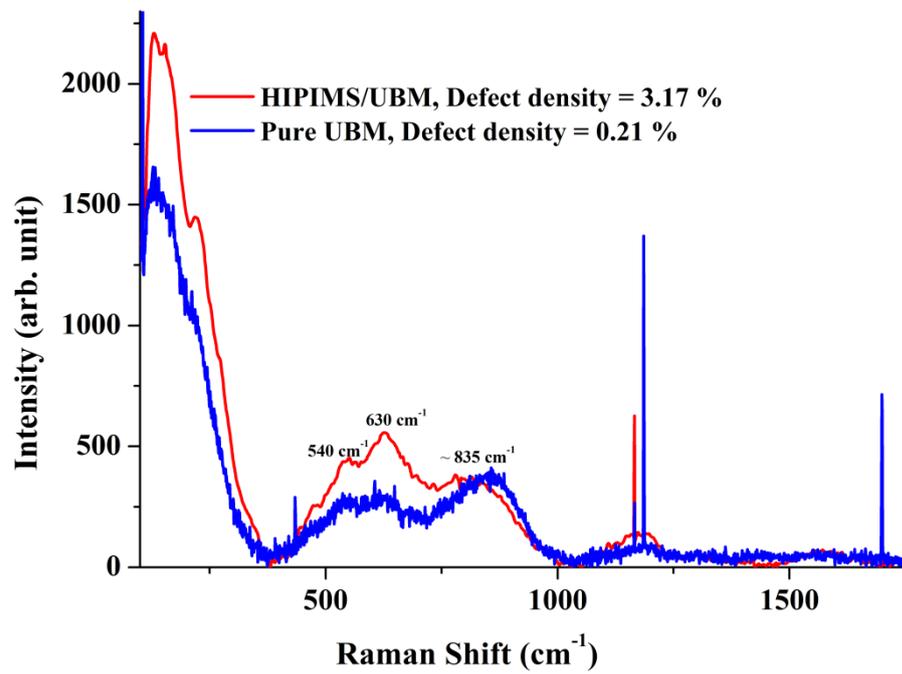
Fig. 4.49. Raman spectra obtained from the wear debris of the UBM and HIPIMS/UBM coatings.
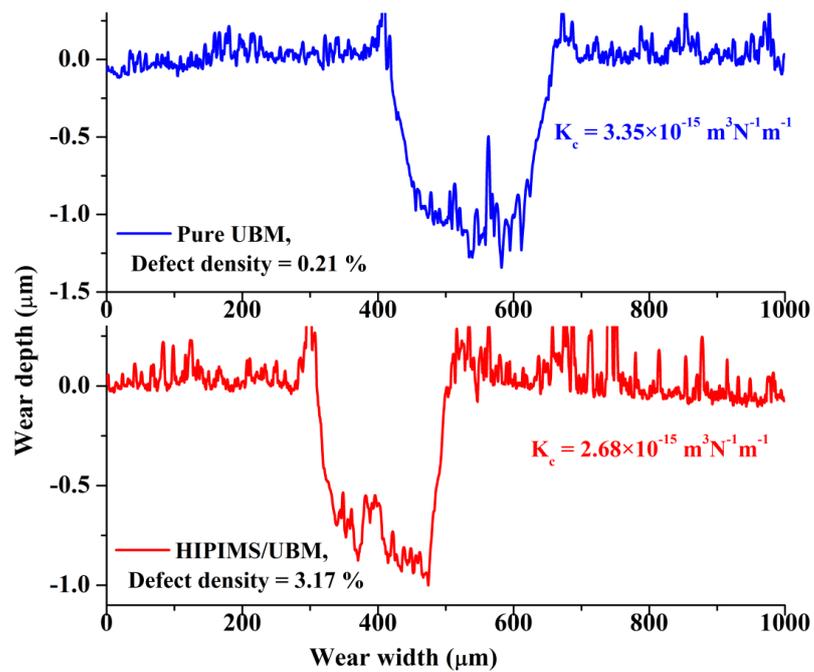
Fig. 4.50. Wear track profiles of the UBM and HIPIMS/UBM coatings.

4.5.5 Summary

- In this study, a significant difference between the defect densities of UBM and HIPIMS/UBM coatings was observed. High-energy flux bombardments on chamber components produced higher numbers of flakes during HIPIMS process and resulted in higher defect generation in the coatings.

- Instead of having more defects, the corrosion resistance of the HIPIMS/UBM coating was higher than the UBM coating. The better corrosion properties of the HIPIMS/UBM coating were associated with its superior microstructure i.e. void free dense microstructure.

- Super dense uniform microstructure of HIPIMS/UBM coating was also beneficial for tribological properties. The coefficient of wear and the coefficient of friction were found to be lower ($K_C = 2.68 \times 10^{-15}$ $m^3N^{-1}m^{-1}$ and $\mu = 0.48$) than those of UBM coating ($K_C = 3.35 \times 10^{-15}$ $m^3N^{-1}m^{-1}$ and $\mu = 0.59$).

- In case of HIPIMS/UBM coating, the effect of defects was apparent in the range of 10000 to 20000 cycles. This particular result suggests that not only the microstructure but the surface defect density also plays a major role in the friction and wear mechanisms. Thus, it is important to reduce surface defect density for better coating performance.

5 Conclusions

This research has been conducted to understand the influence of coating deposition parameters on defect formation during HIPIMS processes. The investigation can be divided into three main sections: effect of deposition time, effect of substrate bias voltage and effect of total chamber pressure on defect formation and their influence on the corrosion and tribological properties of HIPIMS/UBM deposited CrN/NbN coatings. At the end of each section of the investigation, a brief summary has been provided. The general conclusions of the whole study are presented as follows.

1. Coating deposition time had a significant effect on the generation of contamination related defects and on the reduction of the defects associated with substrate pit. With the increase of deposition time from 15 min to 120 min, the surface defect density of the coating increased from 0.48 % to 3.18 %. This increase was due to the formation of contamination related defects. The critical time required for contamination related defects (foreign particles such as flake and chamber dust) to appear was between 30 and 60 min of deposition. Foreign particles were generated from the chamber components of the coating system due to the thermal and structural stresses or the flux-bombardment on them. The rotation of the substrates holders also produced small amount of wear debris. The number of flakes was increased in the chamber with time because of all these continuous processes. Deposition of coating materials on these flakes increased the number of defects in the coatings. Although, the defects associated with substrate pit reduced with the deposition time due to the deposition of coating materials on the pits.

   Deposition time also influenced the corrosion and tribological properties of the coatings. Regardless of having the highest defects (3.18 %), the coating

deposited for the longest time of 120 min exhibited significant improvements in corrosion and tribological performances. This suggests that a critical coating thickness is required to protect the underlying substrate.

2. Increasing substrate bias from - 40 V to - 150 V led to an increase in surface defect density from 3.13 % to 4.30 %. The increase in surface defect density with the increase of substrate bias was associated with two factors, high-energy flux bombardment and re-sputtering phenomena. High-energy flux bombardments on chamber components increased the flakes generation at higher bias voltages. These flakes produced more defects in the coating. Nevertheless, re-sputtering process could also raise the surface defect density. At very high negative bias voltages, the extremely high-energy bombardments of species (Ar and/or coating materials, Cr, Nb and N) on the growing coating surface can expose the already formed defects and hence increase the area under the defects. Also, some loosely bound nodular defects can be expelled from the coatings leaving more visible voids.

    The applied bias voltage also altered the microstructure, chemical composition, crystallographic orientation and bilayer thickness of the coatings. Along with the defects, all these properties influenced the corrosion and tribological performances of the coatings.

    With the increase of bias voltage, the coatings became denser. As a result, corrosion resistance of the coatings was improved. The effect of coating defects was also apparent. Corrosion curves of the coatings with the higher defects exhibited the sudden increase in current densities due to the removal of loosely bound defects.

The wear mechanism of the coatings was dominated by the removal of coating defects during the tests as well as by the bilayer thickness. Coatings with the maximum bilayer thickness had the lowest wear rate.

3. With the increase of chamber pressure from 0.2 Pa to 1 Pa, the surface defect density increased from 0.84 % to 5.94 %. At the higher chamber pressure, plasma volume covered more area of the chamber, which increased the amount of sputter flux bombardments on chamber wall and subsequent flake generation. These flakes promoted further defect formation within the coatings.

   The chamber pressure also influenced the microstructure, chemical composition, crystallographic orientation and bilayer thickness of the coatings. The coating with fewer defects (0.84 %) had better corrosion resistance than the coatings with higher defects. The bilayer thickness of this coating was found to be the highest ($\Delta = 39.3$ Å). The thicker hard layers prevented the plastic deformation and the abrasive penetration in the metal layers resulting in the highest wear resistance ($K_C = 1.61 \times 10^{-15}$ m^{3}N^{-1}m^{-1}).

4. For all the above mentioned coatings deposited by varying deposition time, substrate bias voltage and total chamber pressure, the friction coefficient (μ) was influenced by the nature of oxides formed at the tribological contact. When Nb$_2$O$_5$ based tribolayers in the wear track were formed, the friction coefficient of the coatings reached a value of 0.70. In contrast, the coating deposited for t = 120 min, at U_b = - 65 V and P = 0.35 Pa did not show any significant Raman peak. This coating had the lowest friction coefficient value ($\mu = 0.48$) thanks to the lubricious nature of Cr based tribolayer.

Depending on the tribological and corrosion performances, two coatings were identified for exhibiting improved protective properties among all the coatings deposited for this study. The coating deposited for t = 120 min, at U_b = - 65 V and P = 0.2 Pa had the higher hardness, the lower roughness, surface defect density, corrosion current and wear coefficient than the coating deposited for t = 120 min, at U_b = - 65 V and P = 0.35 Pa. The only disadvantage of the first mentioned coating was the higher value of friction coefficient.

For convenience, the properties of these two coatings are listed in the following table 5.1.

Deposition parameters:	Coating 1	Coating 2
Deposition time (min)	120	120
Bias voltage (V)	- 65	- 65
Chamber pressure (Pa)	0.2	0.35
Deposition technique	HIPIMS/UBM	HIPIMS/UBM
Thickness (µm)	3.65	2.15
Chemical composition (at %) Cr Nb N	 38.41 16.76 44.83	 39.51 14.13 46.36
Crystallographic orientation	(200)	(111)
Bilayer thickness (Å)	39.3	27.3
Hardness (GPa)	26.38	25.85
Roughness (µm)	0.025	0.039
Surface defect density (%)	0.84	3.18
Corrosion current density (mA/cm^2) (In the range of − 200 mV to + 300 mV)	From 7.75×10^{-5} to 4.01×10^{-4}	From 1.41×10^{-4} to 6.8×10^{-4}
Wear coefficient $(m^3 N^{-1} m^{-1})$	1.61×10^{-15}	2.68×10^{-15}
Friction coefficient	0.70	0.48

Table 5.1. Comparison between the properties of the coatings exhibited improved

tribological and corrosion performances.

All these studies on coating defects lead to an important conclusion that HIPIMS does not contribute to the generation of a new category of defect. All the defects found in HIPIMS deposited coatings were generated due to external factors, such as chamber dust or substrate surface imperfections, such as pits. So, an additional study was conducted to investigate the effect of a clean environment on the defect formation. The study revealed that the coating deposited after cleaning the chamber had lower defects on its surface than the coating deposited before cleaning. The corrosion and tribological properties were improved with the decrease in the surface defect density. In addition to that, the comparison between HIPIMS/UBM deposited and pure UBM deposited CrN/NbN coatings confirmed the importance of dense microstructure for better coating performance.

The systematic investigation on coating properties has guided to achieve the objectives set out at the start of the project. The sources of the defects found in HIPIMS deposited coatings have been identified. The study has recommended to minimise the chance of flake generation during deposition in order to reduce defects in the coatings. Surface defect density decreased from 3.18 % to 1.87 % after thoroughly cleaning the chamber components for the deposition processes with t = 120 min, U_b = - 65 V and P = 0.35 Pa. However, the chamber pressure was found to be the most effective tool to control the surface defect density. Reduction in chamber pressure from 0.35 Pa to 0.2 Pa decreased the surface defect density from 3.18 % to 0.84 % for the coatings deposited for t = 120 min and at U_b = - 65 V in the chamber with similar condition in term of cleanliness (note that both the coatings were produced before thoroughly cleaning the chamber).

Although, the defects did not always determine the COF, COW values or affect the corrosion current density of the coatings, the corrosion and tribological studies and the

microscopic studies (optical and SEM) after corrosion and tribological tests suggested that these defects influenced the coating performances to a certain extent depending on their natures (nodular/cone-like defects or pit/void). The loosely bound nodular defects influenced the tribological performance while voids affected the corrosion activities. Nevertheless, the performances of the coatings were also dependent on their microstructure, crystallographic orientation, bilayer thickness, hardness and roughness.

6 Future Works

In this section, the scope for the future work is given based on the knowledge earned during the course of this research:

1. We found that the bilayer thickness influenced the wear mechanism. In this study LAXRD was used to determine the bilayer thickness. However, to analyse the multilayer structure in detail, a transmission electron microscope (TEM) would be useful.

2. Comparison of the coatings showed that the higher bilayer thickness improved the wear resistance. So, one can produce sets of coatings for t = 120 min, at U_b = - 65 V and P = 0.35 Pa by varying the rotation of the substrate holder. It would be advantageous if the rotation of the holder could increase the bilayer thickness and enhance the wear resistance.

3. The friction coefficient values of the coatings were dominated by the oxides produced during tribological tests. Further, the static oxidation test will be useful to understand the behaviour of the coatings during tribological tests.

4. The coating produced for t = 120 min, at U_b = - 65 V and P = 0.2 Pa exhibited the best coating properties if the friction coefficient value (μ) is ignored. The preferred orientation of this coating was (200). Interestingly, all the coatings with (200) orientation had higher friction values (only considering the coatings with thickness higher than 2 μm). In contrast, 2.15 μm thick coating with (111) orientation had much lower friction coefficient. Thus, it would be interesting if the coatings with (111) orientation can be produced by controlling the energies of the depositing materials (i.e. by varying the process parameters, such as peak power, pulses frequency, peak current etc.) at the lower pressure, P = 0.2 Pa.

References

[1]   P.H. Mayrhofer, C. Mitterer, L. Hultman, H. Clemens, Microstructural design of hard coatings, Prog. Mater. Sci. 51 (2006) 1032–1114. doi:10.1016/j.pmatsci.2006.02.002.

[2]   P. Panjan, M. Čekada, M. Panjan, D. Kek-Merl, Growth defects in PVD hard coatings, Vacuum. 84 (2009) 209–214. doi:10.1016/j.vacuum.2009.05.018.

[3]   P. Panjan, M. Čekada, M. Panjan, D. Kek-Merl, F. Zupanič, L. Čurković, S. Paskvale, Surface density of growth defects in different PVD hard coatings prepared by sputtering, Vacuum. 86 (2012) 794–798. doi:10.1016/j.vacuum.2011.07.013.

[4]   A. Drnovšek, P. Panjan, M. Panjan, M. Čekada, The influence of growth defects in sputter-deposited TiAlN hard coatings on their tribological behavior, Surf. Coatings Technol. 288 (2016) 171–178. doi:10.1016/j.surfcoat.2016.01.021.

[5]   W.-D. Münz, I.J. Smith, D.B. Lewis, S. Creasey, Droplet formation on steel substrates during cathodic steered arc metal ion etching, Vacuum. 48 (1997) 473–481. doi:10.1016/S0042-207X(96)00307-7.

[6]   W.-D. Münz, Comparison of TiAlN coatings grown by unbalanced magnetron and arc bond sputtering techniques, J. Vac. Sci. Technol. A Vacuum, Surfaces, Film. 11 (1993) 2583–2589. doi:10.1116/1.578610.

[7]   H.W. Wang, M.M. Stack, S.B. Lyon, P. Hovsepian, W.D. Münz, The corrosion behaviour of macroparticle defects in arc bond-sputtered CrN/NbN superlattice coatings, Surf. Coatings Technol. 126 (2000) 279–287. doi:10.1016/S0257-8972(00)00554-5.

[8]   S.H. Ahn, J.H. Lee, J.G. Kim, J.G. Han, Localized corrosion mechanisms of the multilayered coatings related to growth defects, Surf. Coatings Technol. 177–178 (2004) 638–644. doi:http://dx.doi.org/10.1016/S0257-8972(03)00939-3.

[9]   M. Čekada, P. Panjan, D. Kek-Merl, M. Panjan, G. Kapun, SEM study of defects in PVD hard coatings, Vacuum. 82 (2007) 252–256. doi:10.1016/j.vacuum.2007.07.005.

[10]   P. Panjan, P. Gselman, D. Kek-Merl, M. Čekada, M. Panjan, G. Dražić, T. Bončina, F. Zupanič, Growth defect density in PVD hard coatings prepared by different deposition techniques, Surf. Coatings Technol. 237 (2013) 349–356. doi:10.1016/j.surfcoat.2013.09.020.

[11]   D.D. La Grange, N. Goebbels, A. Santana, R. Heuberger, T. Imwinkelried, L. Eschbach, A. Karimi, Effect of niobium onto the tribological behavior of cathodic arc deposited Nb–Ti–N coatings, Wear. 368–369 (2016) 60–69. doi:10.1016/j.wear.2016.09.003.

[12]   I. Zhirkov, A. Petruhins, J. Rosen, Effect of cathode composition and nitrogen pressure on macroparticle generation and type of arc discharge in a DC arc source with Ti-Al compound cathodes, Surf. Coatings Technol. 281 (2015) 20–26. doi:10.1016/j.surfcoat.2015.09.030.

[13]   A. Anders, Physics of arcing, and implications to sputter deposition, Thin Solid Films. 502 (2006) 22–28. doi:10.1016/j.tsf.2005.07.228.

[14]   D.B. Lewis, S.J. Creasey, C. Wustefeld, A.P. Ehiasarian, P.E. Hovsepian, The role of the growth defects on the corrosion resistance of CrN/NbN superlattice coatings deposited at low temperatures, Thin Solid Films. 503 (2006) 143–148. doi:10.1016/j.tsf.2005.08.375.

[15]   A.P. Ehiasarian, W.D. Münz, High power pulsed magnetron sputtered CrN x films, Surf. Coat. Technol. 163–164 (2003) 267–272. doi:10.1016/S0257-8972(02)00479-6.

[16]   A.P. Ehiasarian, J.G. Wen, I. Petrov, Interface microstructure engineering by

high power impulse magnetron sputtering for the enhancement of adhesion, J. Appl. Phys. 101 (2007). doi:10.1063/1.2697052.

[17] P.E. Hovsepian, D.B. Lewis, W.D. Münz, Recent progress in large scale manufacturing of multilayer/superlattice hard coatings, Surf. Coatings Technol. 133–134 (2000) 166–175. doi:10.1016/S0257-8972(00)00959-2.

[18] Y.P. Purandare, A.P. Ehiasarian, M.M. Stack, P.E. Hovsepian, CrN/NbN coatings deposited by HIPIMS: A preliminary study of erosion-corrosion performance, Surf. Coatings Technol. 204 (2010) 1158–1162. doi:10.1016/j.surfcoat.2009.11.006.

[19] P.E. Hovsepian, D.B. Lewis, W.D. Münz, S.B. Lyon, M. Tomlinson, Combined cathodic arc/unbalanced magnetron grown CrN/NbN superlattice coatings for corrosion resistant applications, Surf. Coatings Technol. 120–121 (1999) 535–541. doi:10.1016/S0257-8972(99)00439-9.

[20] M. Tomlinson, S.B. Lyon, P. Hovsepian, W.D. Munz, Corrosion performance of CrN/NbN superlattice coatings deposited by the combined cathodic arc/unbalanced magnetron technique, Vacuum. 53 (1999) 117–121. doi:10.1016/S0042-207X(98)00405-9.

[21] K.-D. Bouzakis, N. Michailidis, Physical Vapor Deposition (PVD), in: T.I.A. for Produ, L. Laperrière, G. Reinhart (Eds.), CIRP Encycl. Prod. Eng., Springer Berlin Heidelberg, Berlin, Heidelberg, 2014: pp. 1–8. doi:10.1007/978-3-642-35950-7_6489-4.

[22] P. M. Martin, Deposition Technologies: An Overview, Third Edit, Elsevier Ltd., 2010. doi:10.1016/B978-0-8155-2031-3.00001-6.

[23] M. Henini, Handbook of Thin-Film Deposition Processes and Techniques, William Andrew Publishing, 2000. doi:10.1016/S0026-2692(99)00122-6.

[24] A. Anders, Cathodic arc plasma deposition, Vac. Technol. Coat. 3 (2002) 1–26. doi:10.1016/0040-6090(88)90494-4.

[25] T. Solidfilms, P.J. Martin, N. Measurement, D.R. Mckenzie, R.P. Netterfield, P. Swift, S.W. Filipczuk, B. James, Characteristics of titanium arc evaporation processes, 153 (2006) 91–102.

[26] D. M. Mattox, Handbook of physical vapor deposition (PVD) processing, n.d.

[27] M. Ali, E. Hamzah, I.A. Qazi, M.R.M. Toff, Effect of cathodic arc PVD parameters on roughness of TiN coating on steel substrate, Curr. Appl. Phys. 10 (2010) 471–474. doi:10.1016/j.cap.2009.07.007.

[28] D. Depla, S. Mahieu, J. Greene, Sputter deposition processes, Handb. Depos. Technol. Film. Coatings. 281 (1991) 253–296. doi:10.1016/B978-0-8155-2031-3.00005-3.

[29] B. Chapman, Glow discharge processes : sputtering and plasma etching, Wiley, 1980.

[30] B. Window, N. Savvides, Unbalanced dc magnetrons as sources of high ion fluxes, J. Vac. Sci. Technol. A Vacuum, Surfaces, Film. 4 (1986) 453–456. doi:10.1116/1.573904.

[31] J. Musil, Recent advances in magnetron sputtering technology, Surf. Coatings Technol. 100–101 (1998) 280–286. doi:10.1016/S0257-8972(97)00633-6.

[32] D.P. Monaghan, D.G. Teer, P.A. Logan, K.C. Laing, R.I. Bates, R.D. Arnell, An improved method for the deposition of corrosion-resistant aluminium coatings for aerospace applications, Surf. Coatings Technol. 60 (1993) 592–596. doi:10.1016/0257-8972(93)90159-L.

[33] Y.X. Ou, J. Lin, H.L. Che, J.J. Moore, W.D. Sproul, M.K. Lei, Mechanical and tribological properties of CrN/TiN superlattice coatings deposited by a combination of arc-free deep oscillation magnetron sputtering with pulsed dc magnetron sputtering, Thin Solid Films. 594 (2015) 147–155.

doi:10.1016/j.tsf.2015.09.067.

[34] B.R. Peterson, United States Patent [191 â€™ [11] Patent Number: [45], (1994) 3–8.

[35] A.P. Ehiasarian, Fundamentals and applications of HIPIMS, in: R. Wei (Ed.), Plasma Surf. Eng. Res. Its. Pract. Appl. Res. Signpost, Trivandrum, India, 2008: pp. 35–86.

[36] M. Lattemann, A.P. Ehiasarian, J. Bohlmark, P.Å.O. Persson, U. Helmersson, Investigation of high power impulse magnetron sputtering pretreated interfaces for adhesion enhancement of hard coatings on steel, Surf. Coatings Technol. 200 (2006) 6495–6499. doi:10.1016/j.surfcoat.2005.11.082.

[37] J. Lin, J.J. Moore, W.D. Sproul, B. Mishra, J.A. Rees, Z. Wu, R. Chistyakov, B. Abraham, Ion energy and mass distributions of the plasma during modulated pulse power magnetron sputtering, Surf. Coatings Technol. 203 (2009) 3676–3685. doi:10.1016/j.surfcoat.2009.05.048.

[38] A.P. Ehiasarian, J.G. Wen, I. Petrov, Interface microstructure engineering by high power impulse magnetron sputtering for the enhancement of adhesion, J. Appl. Phys. 101 (2007) 54301. doi:10.1063/1.2697052.

[39] J. Alami, P.O.Å. Persson, D. Music, J.T. Gudmundsson, J. Bohlmark, U. Helmersson, Ion-assisted physical vapor deposition for enhanced film properties on nonflat surfaces, J. Vac. Sci. Technol. A Vacuum, Surfaces, Film. 23 (2005) 278–280. doi:10.1116/1.1861049.

[40] T. Shimizu, H. Komiya, Y. Teranishi, K. Morikawa, H. Nagasaka, M. Yang, Pressure dependence of (Ti, Al)N film growth on inner walls of small holes in high-power impulse magnetron sputtering, Thin Solid Films. 624 (2017) 189–196. doi:10.1016/j.tsf.2016.09.041.

[41] Q. Ma, L. Li, Y. Xu, J. Gu, L. Wang, Y. Xu, Effect of bias voltage on TiAlSiN nanocomposite coatings deposited by HiPIMS, Appl. Surf. Sci. 392 (2017) 826–833. doi:10.1016/j.apsusc.2016.09.028.

[42] H. Hoche, S. Groß, M. Oechsner, Development of new PVD coatings for magnesium alloys with improved corrosion properties, Surf. Coatings Technol. 259 (2014) 102–108. doi:10.1016/j.surfcoat.2014.04.038.

[43] J. Lin, J.J. Moore, W.D. Sproul, B. Mishra, Z. Wu, J. Wang, The structure and properties of chromium nitride coatings deposited using dc, pulsed dc and modulated pulse power magnetron sputtering, Surf. Coatings Technol. 204 (2010) 2230–2239. doi:10.1016/j.surfcoat.2009.12.013.

[44] S. Creasey, D.B. Lewis, I.J. Smith, W.-D. Münz, SEM image analysis of droplet formation during metal ion etching by a steered arc discharge, Surf. Coatings Technol. 97 (1997) 163–175. doi:10.1016/S0257-8972(97)00137-0.

[45] A.P. Ehiasarian, P.E. Hovsepian, W.-D. Münz, Combined coating process comprising magnetic field-assisted, high-power, pulsed cathode sputtering and an unbalanced magnetron, Patent US7081186 B2 (25 Jul 2006), EP1260603 A2 (27 Nov 2002), DE10124749 A1 (28 Nov 2002), n.d.

[46] P.E. Hovsepian, A.A. Sugumaran, Y. Purandare, D.A.L. Loch, A.P. Ehiasarian, Effect of the degree of high power impulse magnetron sputtering utilisation on the structure and properties of TiN films, Thin Solid Films. 562 (2014) 132–139. doi:10.1016/j.tsf.2014.04.002.

[47] T. Hurkmans, D.B. Lewis, J.S. Brooks, W.D. Münz, Chromium nitride coatings grown by unbalanced magnetron (UBM) and combined arc/unbalanced magnetron (ABS[TM]) deposition techniques, Surf. Coatings Technol. 86–87 (1996) 192–199. doi:10.1016/S0257-8972(96)02949-0.

[48] A.P. Ehiasarian, Y.A. Gonzalvo, T.D. Whitmore, Time-resolved ionisation studies of the high power impulse magnetron discharge in mixed argon and

nitrogen atmosphere, Plasma Process. Polym. 4 (2007) 309–313. doi:10.1002/ppap.200730806.

[49] F. Magnus, O.B. Sveinsson, S. Olafsson, J.T. Gudmundsson, Current-voltage-time characteristics of the reactive Ar/N2 high power impulse magnetron sputtering discharge, J. Appl. Phys. 110 (2011) 83306. doi:10.1063/1.3653233.

[50] L. Combadiere, J. Machet, Study and control of both target-poisoning mechanisms and reactive phenomenon in reactive planar magnetron cathodic sputtering of TiN, Surf. Coatings Technol. 82 (1996) 145–157. doi:10.1016/0257-8972(95)02671-1.

[51] S. Berg, T. Nyberg, Fundamental understanding and modeling of reactive sputtering processes, Thin Solid Films. 476 (2005) 215–230. doi:10.1016/j.tsf.2004.10.051.

[52] K. Koski, J. Hoelsae, P. Juliet, Surface defects and arc generation in reactive magnetron sputtering of aluminium oxide thin films, Surf. Coatings Technol. 115 (1999) 163–171. doi:10.1016/S0257-8972(99)00172-3.

[53] I. Petrov, P.B. Barna, L. Hultman, J.E. Greene, Microstructural evolution during film growth, J. Vac. Sci. Technol. A Vacuum, Surfaces, Film. 21 (2003) S117. doi:10.1116/1.1601610.

[54] V. Vasanthipillay, K. Vijayalakshmi, Influence of Sputter Deposition Time on the Growth of c-Axis Oriented AlN / Si Thin Films for Microelectronic Application, 2012 (2012) 724–729.

[55] D. Bhaduri, A. Ghosh, S. Gangopadhyay, S. Paul, Effect of target frequency, bias voltage and bias frequency on microstructure and mechanical properties of pulsed DC CFUBM sputtered TiN coating, Surf. Coatings Technol. 204 (2010) 3684–3697. doi:10.1016/j.surfcoat.2010.04.047.

[56] S. Gangopadhyay, R. Acharya, A.K. Chattopadhyay, S. Paul, Effect of substrate bias voltage on structural and mechanical properties of pulsed DC magnetron sputtered TiN-MoSx composite coatings, Vacuum. 84 (2010) 843–850. doi:10.1016/j.vacuum.2009.11.010.

[57] J.-W. Lee, S.-K. Tien, Y.-C. Kuo, C.-M. Chen, The mechanical properties evaluation of the CrN coatings deposited by the pulsed DC reactive magnetron sputtering, Surf. Coatings Technol. 200 (2006) 3330–3335. doi:10.1016/j.surfcoat.2005.07.047.

[58] H. Du, J. Xiong, H. Zhao, Y. Wu, W. Wan, L. Wang, Structure and properties of TiAlLaN films deposited at various bias voltages, Appl. Surf. Sci. 292 (2014) 688–694. doi:10.1016/j.apsusc.2013.12.035.

[59] E. Penilla, J. Wang, Pressure and Temperature Effects on Stoichiometry and Microstructure of Nitrogen-Rich TiN Thin Films Synthesized via Reactive Magnetron DC-Sputtering, J. Nanomater. 2008 (2008) 1–9. doi:10.1155/2008/267161.

[60] L. Shan, Y. Wang, J. Li, J. Chen, Effect of N2 flow rate on microstructure and mechanical properties of PVD CrNx coatings for tribological application in seawater, Surf. Coatings Technol. 242 (2014) 74–82. doi:10.1016/j.surfcoat.2014.01.021.

[61] V.D. Ovcharenko, A.S. Kuprin, G.N. Tolmachova, I.V. Kolodiy, A. Gilewicz, O. Lupicka, J. Rochowicz, B. Warcholinski, Deposition of chromium nitride coatings using vacuum arc plasma in increased negative substrate bias voltage, Vacuum. 117 (2015) 27–34. doi:10.1016/j.vacuum.2015.04.008.

[62] X.S. Wan, S.S. Zhao, Y. Yang, J. Gong, C. Sun, Effects of nitrogen pressure and pulse bias voltage on the properties of Cr-N coatings deposited by arc ion plating, Surf. Coatings Technol. 204 (2010) 1800–1810. doi:10.1016/j.surfcoat.2009.11.021.

[63] A. Anders, A structure zone diagram including plasma-based deposition and ion etching, Thin Solid Films. 518 (2010) 4087–4090. doi:10.1016/j.tsf.2009.10.145.

[64] J.A. Thornton, The microstructure of sputter-deposited coatings, J. Vac. Sci. Technol. A Vacuum, Surfaces, Film. 4 (1986) 3059–3065. doi:10.1116/1.573628.

[65] A.M. Abd El-Rahman, R. Wei, Effect of ion bombardment on structural, mechanical, erosion and corrosion properties of Ti-Si-C-N nanocomposite coatings, Surf. Coatings Technol. 258 (2014) 320–328. doi:10.1016/j.surfcoat.2014.09.006.

[66] M. Panjan, Influence of substrate rotation and target arrangement on the periodicity and uniformity of layered coatings, Surf. Coatings Technol. 235 (2013) 32–44. doi:10.1016/j.surfcoat.2013.06.126.

[67] M.I. Yousaf, V.O. Pelenovich, B. Yang, C.S. Liu, D.J. Fu, Influence of substrate rotation speed on the structure and mechanical properties of nanocrystalline AlTiN/MoN coatings synthesized by cathodic arc ion-plating, Surf. Coatings Technol. 265 (2015) 117–124. doi:10.1016/j.surfcoat.2015.01.049.

[68] B.A. Movchan, A.V. Demchishin, Investigation of the structure and properties of thick vacuum condensates of nickel, titanium, tungsten, and aluminum oxide, Fiz Met. Met. 28 (1969) 653–660.

[69] J. a. Thornton, Influence of apparatus geometry and deposition conditions on the structure and topography of thick sputtered coatings, J. Vac. Sci. Technol. 11 (1974) 666–670. doi:10.1116/1.568682.

[70] R. Messier, A.P. Giri, R.A. Roy, Revised structure zone model for thin film physical structure, J. Vac. Sci. Technol. A Vacuum, Surfaces, Film. 2 (1984) 500–503. doi:10.1116/1.572604.

[71] P.B. Barna, M. Adamik, Fundamental structure forming phenomena of polycrystalline films and the structure zone models, Thin Solid Films. 317 (1998) 27–33. doi:10.1016/S0040-6090(97)00503-8.

[72] P.J. Kelly, R.D. Arnell, Development of a novel structure zone model relating to the closed-field unbalanced magnetron sputtering system, J. Vac. Sci. Technol. A Vacuum, Surfaces, Film. 16 (1998) 2858–2869. doi:10.1116/1.581432.

[73] B. Navinšek, P. Panjan, I. Milošev, Industrial applications of CrN (PVD) coatings, deposited at high and low temperatures, Surf. Coatings Technol. 97 (1997) 182–191. doi:10.1016/S0257-8972(97)00393-9.

[74] I.L. Singer, S. Fayeulle, P.D. Ehni, Friction and wear behavior of TiN in air: The chemistry of transfer films and debris formation, Wear. 149 (1991) 375–394. doi:10.1016/0043-1648(91)90386-9.

[75] Z. Han, X. Hu, J. Tian, G. Li, G. Mingyuan, Magnetron sputtered NbN thin films and mechanical properties, Surf. Coatings Technol. 179 (2004) 188–192. doi:10.1016/S0257-8972(03)00848-X.

[76] H.C. Barshilia, K.S. Rajam, A. Jain, K. Gopinadhan, S. Chaudhary, A comparative study on the structure and properties of nanolayered TiN/NbN and TiAlN/TiN multilayer coatings prepared by reactive direct current magnetron sputtering, Thin Solid Films. 503 (2006) 158–166. doi:10.1016/j.tsf.2005.12.074.

[77] U. Helmersson, S. Todorova, S.A. Barnett, J.E. Sundgren, L.C. Markert, J.E. Greene, Growth of single-crystal TiN/VN strained-layer superlattices with extremely high mechanical hardness, J. Appl. Phys. 62 (1987) 481–484. doi:10.1063/1.339770.

[78] M. Larsson, P. Hollman, P. Hedenqvist, S. Hogmark, U. Wahlström, L. Hultman, Deposition and microstructure of PVD TiN-NbN multilayered coatings by combined reactive electron beam evaporation and DC sputtering, Surf. Coatings Technol. 86–87 (1996) 351–356. doi:10.1016/S0257-8972(96)03026-5.

[79] M. Nordin, M. Herranen, S. Hogmark, Influence of lamellae thickness on the

corrosion behaviour of multilayered PVD TiN/CrN coatings, Thin Solid Films. 348 (1999) 202–209. doi:10.1016/S0040-6090(99)00192-3.

[80] S. Masalovich, Analysis and design of multilayer structures for neutron monochromators and supermirrors, Nucl. Instruments Methods Phys. Res. Sect. A Accel. Spectrometers, Detect. Assoc. Equip. 722 (2013) 71–81. doi:10.1016/j.nima.2013.04.051.

[81] H. Holleck, V. Schier, Multilayer PVD coatings for wear protection, Surf. Coatings Technol. 76–77 (1995) 328–336. doi:10.1016/0257-8972(95)02555-3.

[82] P.E. Hovsepian, D.B. Lewis, W.D. Müunz, A. Rouzaud, P. Juliet, Chromium nitride/niobium nitride superlattice coatings deposited by combined cathodic-arc/unbalanced magnetron technique, Surf. Coatings Technol. 116–119 (1999) 727–734. doi:10.1016/S0257-8972(99)00182-6.

[83] E. Bemporad, C. Pecchio, S. De Rossi, F. Carassiti, Characterisation and wear properties of industrially produced nanoscaled CrN/NbN multilayer coating, Surf. Coatings Technol. 188–189 (2004) 319–330. doi:10.1016/j.surfcoat.2004.08.069.

[84] C. Reinhard, A.P. Ehiasarian, P.E. Hovsepian, CrN/NbN superlattice structured coatings with enhanced corrosion resistance achieved by high power impulse magnetron sputtering interface pre-treatment, Thin Solid Films. 515 (2007) 3685–3692. doi:10.1016/j.tsf.2006.11.014.

[85] J.S. Koehler, Attempt to Design a Strong Solid, Phys. Rev. B. 2 (1970) 547–551. doi:10.1103/PhysRevB.2.547.

[86] Y.J. Kim, T.J. Byun, H.Y. Lee, J.G. Han, Effect of bilayer period on CrN/Cu nanoscale multilayer thin films, Surf. Coatings Technol. 202 (2008) 5508–5511. doi:10.1016/j.surfcoat.2008.06.028.

[87] M.I. Yousaf, V.O. Pelenovich, B. Yang, C.S. Liu, D.J. Fu, Effect of bilayer period on structural and mechanical properties of nanocomposite TiAlN/MoN multilayer films synthesized by cathodic arc ion-plating, Surf. Coatings Technol. 282 (2015) 94–102. doi:10.1016/j.surfcoat.2015.10.018.

[88] L. Chen, Y.X. Xu, Y. Du, Y. Liu, Effect of bilayer period on structure, mechanical and thermal properties of TiAlN/AlTiN multilayer coatings, Thin Solid Films. 592 (2015) 207–214. doi:10.1016/j.tsf.2015.09.029.

[89] M. Kot, W.A. Rakowski, Major, R. Major, J. Morgiel, Effect of bilayer period on properties of Cr/CrN multilayer coatings produced by laser ablation, Surf. Coatings Technol. 202 (2008) 3501–3506. doi:10.1016/j.surfcoat.2007.12.036.

[90] F. Ge, X. Zhou, F. Meng, Q. Xue, F. Huang, Tribological behavior of VC/Ni multilayer coatings prepared by non-reactive magnetron sputtering, Tribol. Int. 99 (2016) 140–150. doi:10.1016/j.triboint.2015.10.019.

[91] S. Kim, E. Kim, D. Kim, J. La, S. Lee, Effects of Bilayer Period on the Microhardness and Its Strengthening Mechanism of CrN / AlN Superlattice Coatings, 45 (2012) 257–263.

[92] Y.J. Kim, T.J. Byun, J.G. Han, Bilayer period dependence of CrN/CrAlN nanoscale multilayer thin films, Superlattices Microstruct. 45 (2009) 73–79. doi:10.1016/j.spmi.2008.12.020.

[93] M.K. Wu, J.W. Lee, Y.C. Chan, H.W. Chen, J.G. Duh, Influence of bilayer period and thickness ratio on the mechanical and tribological properties of CrSiN/TiAlN multilayer coatings, Surf. Coatings Technol. 206 (2011) 1886–1892. doi:10.1016/j.surfcoat.2011.07.045.

[94] D.C. Cameron, R. Aimo, Z.H. Wang, K.A. Pischow, Structural variations in CrN/NbN superlattices, Surf. Coatings Technol. 142 (2001) 567–572. doi:10.1016/S0257-8972(01)01057-X.

[95] S. Barnett, A. Madan, Superhard superlattices, Phys. World. 11 (1998) 45–48. doi:10.1088/2058-7058/11/1/34.

[96] M. Nishibori, How to solve problems of films coated by ARC methods, Surf. Coatings Technol. 52 (1992) 229–233.

[97] G. Hkansson, G. Lööf, H. Ljungcrantz, I.P. Ivanov, Effects of nitrogen pressure on arc-evaporated TiN coatings, Surf. Coatings Technol. 67 (1994) 17–26. doi:10.1016/S0257-8972(05)80022-2.

[98] J.L. Daure, K.T. Voisey, P.H. Shipway, D.A. Stewart, The effect of coating architecture and defects on the corrosion behaviour of a PVD multilayer Inconel 625/Cr coating, Surf. Coatings Technol. 324 (2017) 403–412. doi:10.1016/j.surfcoat.2017.06.009.

[99] C. Mitterer, O. Heuzè, V.-H. Derflinger, Substrate and coating damage by arcing during sputtering, Surf. Coatings Technol. 89 (1997) 233–238. doi:10.1016/S0257-8972(96)02908-8.

[100] G.T.P. Azar, C. Yelkarasi, M. Ürgen, The role of droplets on the cavitation erosion damage of TiN coatings produced with cathodic arc physical vapor deposition, Surf. Coatings Technol. 322 (2017) 211–217. doi:10.1016/j.surfcoat.2017.05.050.

[101] G.S. Selwyn, C.A. Weiss, F. Sequeda, C. Huang, Particle contamination formation in magnetron sputtering processes, J. Vac. Sci. Technol. A Vacuum, Surfaces, Film. 15 (1997) 2023–2028. doi:10.1116/1.580674.

[102] Y.P. Purandare, A.P. Ehiasarian, P.E. Hovsepian, Deposition of nanoscale multilayer CrN/NbN physical vapor deposition coatings by high power impulse magnetron sputtering, J. Vac. Sci. Technol. A Vacuum, Surfaces, Film. 26 (2008) 288–296. doi:10.1116/1.2839855.

[103] M. Tkadletz, C. Mitterer, B. Sartory, I. Letofsky-Papst, C. Czettl, C. Michotte, The effect of droplets in arc evaporated TiAlTaN hard coatings on the wear behavior, Surf. Coatings Technol. 257 (2014) 95–101. doi:10.1016/j.surfcoat.2014.01.010.

[104] A.P. Ehiasarian, P.E. Hovsepian, L. Hultman, U. Helmersson, Comparison of microstructure and mechanical properties of chromium nitride-based coatings deposited by high power impulse magnetron sputtering and by the combined steered cathodic arc/unbalanced magnetron technique, Thin Solid Films. 457 (2004) 270–277. doi:10.1016/j.tsf.2003.11.113.

[105] M. Reichling, a. Bodemann, N. Kaiser, Defect induced laser damage in oxide multilayer coatings for 248nm, Thin Solid Films. 320 (1998) 264–279. doi:10.1016/S0040-6090(97)00399-4.

[106] J.F. DeFord, M.R. Kozlowski, Modeling of electric-field enhancement at nodular defects in dielectric mirror coatings, 24th Annu. Boulder Damage Symp. Proc. -- Laser-Induced Damage Opt. Mater. 1992. (1993) 455–472. doi:10.1117/12.147414.

[107] C.J. Stolz, J.E. Wolfe, P.B. Mirkarimi, J.A. Folta, J.J. Adams, M.G. Menor, N.E. Teslich, R. Soufli, C.S. Menoni, D. Patel, Substrate and coating defect planarization strategies for high-laser-fluence multilayer mirrors, Thin Solid Films. 592 (2015) 216–220. doi:10.1016/j.tsf.2015.04.047.

[108] X. Liu, D. Li, Y. Zhao, X. Li, J. Shao, Characteristics of nodular defect in HfO2/SiO2 multilayer optical coatings, Appl. Surf. Sci. 256 (2010) 3783–3788. doi:10.1016/j.apsusc.2010.01.026.

[109] H.W. Wang, M.M. Stack, P. Hovsepian, W.D. Munz, Macroparticle induced corrosion for arc bond sputtering CrN/NbN superlattice coatings, J. Mater. Sci. Lett. 20 (2001) 1995–1997. doi:10.1023/A:1013111508414.

[110] Y. Purandare, M.M. Stack, P. Hovsepian, A study of the erosion-corrosion of PVD CrN/NbN superlattice coatings in aqueous slurries, Wear. 259 (2005) 256–262. doi:10.1016/j.wear.2005.01.047.

[111] Y.P. Purandare, M.M. Stack, P.E. Hovsepian, Velocity effects on erosion-corrosion of CrN/NbN "superlattice" PVD coatings, Surf. Coatings Technol. 201 (2006) 361–370. doi:10.1016/j.surfcoat.2005.11.143.

[112] P.E. Hovsepian, D.B. Lewis, Q. Luo, A. Farinotti, Corrosion resistance of CrN/NbN superlattice coatings grown by various physical vapour deposition techniques, Thin Solid Films. 488 (2005) 1–8. doi:10.1016/j.tsf.2005.03.016.

[113] J.A. Araujo, G.M. Araujo, R.M. Souza, A.P. Tschiptschin, Effect of periodicity on hardness and scratch resistance of CrN/NbN nanoscale multilayer coating deposited by cathodic arc technique, Wear. 330–331 (2015) 469–477. doi:10.1016/j.wear.2015.01.051.

[114] R. Ramadoss, N. Kumar, S. Dash, D. Arivuoli, A.K. Tyagi, Wear mechanism of CrN/NbN superlattice coating sliding against various counterbodies, Int. J. Refract. Met. Hard Mater. 41 (2013) 547–552. doi:10.1016/j.ijrmhm.2013.07.005.

[115] J.A. Araujo, R.A.R. Giorjao, J. Bettini, R.M. Souza, A.P. Tschiptschin, Modeling intrinsic residual stresses built-up during growth of nanostructured multilayer NbN/CrN coatings, Surf. Coatings Technol. (2016). doi:10.1016/j.surfcoat.2016.07.108.

[116] A. Illana, S. Mato, A. Ehiasarian, Y. Purandare, M.I. Lasanta, M.T. de Miguel, P. Hovsepian, F.J. Pérez-Trujillo, Substrate Finishing and Niobium Content Effects on the High-Temperature Corrosion Resistance in Steam Atmosphere of CrN/NbN Superlattice Coatings Deposited by PVD-HIPIMS, Oxid. Met. 87 (2017) 455–467. doi:10.1007/s11085-016-9701-5.

[117] W. Huang, E. Zalnezhad, F. Musharavati, P. Jahanshahi, Investigation of the tribological and biomechanical properties of CrAlTiN and CrN/NbN coatings on SST 304, Ceram. Int. 43 (2017) 7992–8003. doi:10.1016/j.ceramint.2017.03.081.

[118] J.H. Hsieh, C. Li, A.L.K. Tan, C.K. Poh, N.J. Tan, Study of oxidation and wear behaviors of (Nb,Cr)N thin films using Raman spectroscopy, Surf. Coatings Technol. 177–178 (2004) 299–305. doi:10.1016/j.surfcoat.2003.09.008.

[119] Y.Y. Chang, D.Y. Wang, Corrosion behavior of CrN coatings enhanced by niobium ion implantation, Surf. Coatings Technol. 188–189 (2004) 478–483. doi:10.1016/j.surfcoat.2004.08.057.

[120] A.J.C. Wilson, Elements of x-ray crystallography, Addison-Wesley, 1970.

[121] A.J. Perry, J.A. Sue, P.J. Martin, Practical measurement of the residual stress in coatings, Surf. Coatings Technol. 81 (1996) 17–28. doi:10.1016/0257-8972(95)02531-6.

[122] D.G. Brandon, W.D. Kaplan, Microstructural Characterization of Materials: , John Wiley & Sons Ltd, 2008. https://www.dawsonera.com:443/abstract/9780470727126.

[123] K.L. Briggman, D.D. Bock, Volume electron microscopy for neuronal circuit reconstruction, Curr. Opin. Neurobiol. 22 (2012) 154–161. doi:10.1016/j.conb.2011.10.022.

[124] G. Binnig, C.F. Quate, Atomic Force Microscope, Phys. Rev. Lett. 56 (1986) 930–933. doi:10.1103/PhysRevLett.56.930.

[125] P. Eaton, P. West, Atomic Force Microscopy, Oxford University Press, 2010. doi:10.1093/acprof:oso/9780199570454.001.0001.

[126] Dr. Dmitri Kopeliovich, Metallurgical Microscope, (n.d.). http://www.substech.com/dokuwiki/doku.php?id=metallurgical_microscope (accessed August 8, 2017).

[127] T. V. Vorburger, J. Raja, Surface Finish Metrology Tutorial, (1990) NISTIR 89-4088.

[128] C. Oliver, M. Pharr, An improved technique for determining hardness and elastic

modulus using load and displacement sensing indentation experiments, J. Mater. Res. 7 (1992) 1564–1583. doi:10.1557/JMR.1992.1564.

[129] M.R. VanLandingham, T.F. Juliano, M.J. Hagon, Measuring tip shape for instrumented indentation using atomic force microscopy, Meas. Sci. Technol. 16 (2005) 2173–2185. doi:10.1088/0957-0233/16/11/007.

[130] K.R. Trethewey, Corrosion for science and engineering, 2nd ed. ., Longman, 1996.

[131] J. Soltis, Passivity breakdown, pit initiation and propagation of pits in metallic materials - Review, Corros. Sci. 90 (2015) 5–22. doi:10.1016/j.corsci.2014.10.006.

[132] R.D. Arnell, Tribology : principles and design applications, Macmillan, 1991.

[133] R.P. Nair, D. Griffin, N.X. Randall, The use of the pin-on-disk tribology test method to study three unique industrial applications, Wear. 267 (2009) 823–827. doi:10.1016/j.wear.2009.02.026.

[134] R.L. McCreery, Raman Spectroscopy for Chemical Analysis, Meas. Sci. Technol. 12 (2001) 653. http://stacks.iop.org/0957-0233/12/i=5/a=704.

[135] J.A. Thornton, High Rate Thick Film Growth, Annu. Rev. Mater. Sci. 7 (1977) 239–260. doi:10.1146/annurev.ms.07.080177.001323.

[136] C.H. Ma, J.H. Huang, H. Chen, Residual stress measurement in textured thin film by grazing-incidence X-ray diffraction, Thin Solid Films. 418 (2002) 73–78. doi:10.1016/S0040-6090(02)00680-6.

[137] M. Pourbaix, Atlas of electrochemical equilibria in aqueous solutions, National Association of Corrosion Engineers, Houston, Tex., 1974.

[138] B. Bhushan, Handbook of tribology : materials, coatings and surface treatments, McGraw-Hill, 1991.

[139] V.G. Sargade, S. Gangopadhyay, S. Paul, a. K. Chattopadhyay, Effect of Coating Thickness on the Characteristics and Dry Machining Performance of TiN Film Deposited on Cemented Carbide Inserts Using CFUBMS, Mater. Manuf. Process. 26 (2011) 1028–1033. doi:10.1080/10426914.2010.526978.

[140] D.L.A. de Faria, S. Venâncio Silva, M.T. de Oliveira, Raman microspectroscopy of some iron oxides and oxyhydroxides, J. Raman Spectrosc. 28 (1997) 873–878. doi:10.1002/(SICI)1097-4555(199711)28:11<873::AID-JRS177>3.0.CO;2-B.

[141] S. Bhowmick, A. Banerji, A.T. Alpas, Friction reduction mechanisms in multilayer graphene sliding against hydrogenated diamond-like carbon, Carbon N. Y. 109 (2016) 795–804. doi:10.1016/j.carbon.2016.08.036.

[142] C.P. Constable, J. Yarwood, P. Hovsepian, L.A. Donohue, D.B. Lewis, W.-D. Münz, Structural determination of wear debris generated from sliding wear tests on ceramic coatings using Raman microscopy, J. Vac. Sci. Technol. A Vacuum, Surfaces, Film. 18 (2000) 1681–1689. doi:10.1116/1.582407.

[143] A. Banerji, M.J. Lukitsch, B. McClory, D.R. White, A.T. Alpas, Effect of iron oxides on sliding friction of thermally sprayed 1010 steel coated cylinder bores, Wear. 376–377 (2017) 858–868. doi:10.1016/j.wear.2017.02.032.

[144] T. Hurkmans, D.. Lewis, H. Paritong, J.. Brooks, W.. Münz, Influence of ion bombardment on structure and properties of unbalanced magnetron grown CrNx coatings, Surf. Coatings Technol. 114 (1999) 52–59. doi:10.1016/S0257-8972(99)00031-6.

[145] C.H. Hsu, K.L. Chen, Z.H. Lin, C.Y. Su, C.K. Lin, Bias effects on the tribological behavior of cathodic arc evaporated CrTiAlN coatings on AISI 304 stainless steel, Thin Solid Films. 518 (2010) 3825–3829. doi:10.1016/j.tsf.2010.02.012.

[146] X. Chen, Y. Xi, J. Meng, X. Pang, H. Yang, Effects of substrate bias voltage on mechanical properties and tribological behaviors of RF sputtered multilayer

TiN/CrAlN films, J. Alloys Compd. 665 (2016) 210–217. doi:10.1016/j.jallcom.2015.10.076.

[147] D.M. Devia, E. Restrepo-Parra, P.J. Arango, A.P. Tschiptschin, J.M. Velez, TiAlN coatings deposited by triode magnetron sputtering varying the bias voltage, Appl. Surf. Sci. 257 (2011) 6181–6185. doi:10.1016/j.apsusc.2011.02.027.

[148] M. Farooq, Z.H. Lee, Optimization of the Sputtering Process for Depositing Composite Thin Films, J. Korean Phys. Soc. 40 (2002) 511–515.

[149] E.M. Bachari, G. Baud, S. Ben Amor, M. Jacquet, Structural and optical properties of sputtered ZnO films, Thin Solid Films. 348 (1999) 165–172. doi:10.1016/S0040-6090(99)00060-7.

[150] J. Yan, L. Dong, C. Gao, N. Wang, D. Li, Influence of N2 partial pressure on structure and mechanical properties of tialn/AL2O3 multilayers, Materials (Basel). 6 (2013) 795–804. doi:10.3390/ma6030795.

[151] H. Du, H. Zhao, J. Xiong, W. Wan, Y. Wu, L. Wang, G. Xian, Effect of Ar/N2 flow ratio on oxidation resistance and properties of TiAl(La)N coatings, Int. J. Refract. Met. Hard Mater. 46 (2014) 173–180. doi:10.1016/j.ijrmhm.2014.06.012.

[152] S. Wang, K. Zhang, X. Guo, S.X. Du, M. Wen, W.T. Zheng, Effect of Nitrogen Content on Mechanical and Tribological Properties of WB2 (N) Films Deposited by Reactive Magnetron Sputtering, Mater. Sci. Forum. 817 (2015) 143–149. doi:10.4028/www.scientific.net/MSF.817.143.

[153] C. Chokwatvikul, S. Larpkiattaworn, S. Surinphong, Effect of Nitrogen Partial Pressure on Characteristic and Mechanical Properties of Hard Coating TiAlN Film, J. Met. Mater. Miner. 21 (2011) 115–119.

[154] C.R.D. Priestland, S.D. Hersee, The effects of pressure on the deposition rate in rf sputtering processes, Vacuum. 22 (3) (1972) 103–106.

[155] M. Zhang, K.H. Kim, F. Xu, X. Yang, Structure and oxidation behavior of compositionally gradient CrNx coatings prepared using arc ion plating, Surf. Coatings Technol. 228 (2013) S529–S533. doi:10.1016/j.surfcoat.2012.04.058.

[156] Y.P. Purandare, A.P. Ehiasarian, P. Eh Hovsepian, Target poisoning during CrN deposition by mixed high power impulse magnetron sputtering and unbalanced magnetron sputtering technique, J. Vac. Sci. Technol. A Vacuum, Surfaces, Film. 34 (2016) 41502. doi:10.1116/1.4950886.

[157] D. Depla, R. De Gryse, Target poisoning during reactive magnetron sputtering: Part I: The influence of ion implantation, Surf. Coatings Technol. 183 (2004) 184–189. doi:10.1016/j.surfcoat.2003.10.006.

[158] Z.K. Chang, X.S. Wan, Z.L. Pei, J. Gong, C. Sun, Microstructure and mechanical properties of CrN coating deposited by arc ion plating on Ti6Al4V substrate, Surf. Coatings Technol. 205 (2011) 4690–4696. doi:10.1016/j.surfcoat.2011.04.037.

[159] M.N. Gardos, Magn´eli phases of anion-deficient rutile as lubricious oxides. Part I. Tribological behavior of single-crystal and polycrystalline rutile (Ti_nO_{2n-1}), Tribol. Lett. 8 (2000) 65–78. doi:10.1002/andp.200410099.

Index

Coating morphology: The form or structure of the coating.
Surface roughness: Surface roughness is a measure of unevenness of a surface. It is quantified by the deviations in the direction of the normal vector of a real surface from its ideal form.